Copyright

by

Alex Michael Stafford

2023

The Dissertation Committee for Alex Michael Stafford Certifies that this is the approved version of the following Dissertation:

A Guide to Photocuring Catalyst Selection

Committee:

Zachariah A. Page, Supervisor

Sean T. Roberts

Jonathan L. Sessler

Brian A. Korgel

A Guide to Photocuring Catalyst Selection

by

Alex Michael Stafford

Dissertation

Presented to the Faculty of the Graduate School of

The University of Texas at Austin

in Partial Fulfillment

of the Requirements

for the Degree of

Doctor of Philosophy

The University of Texas at Austin

December 2023

Dedication

To my parents, Cindy and Kevin Stafford, whom without this journey would not have been possible. Thank you for your constant love and support.

Acknowledgements

I would like to give a special thanks to my supervisor, Dr. Zachariah Page. His support and guidance have allowed me to develop and grow as an independent scientist. I would like to thank the members of the ZAP research group for being a welcoming and supportive team. A special thanks to all our collaborators (Dr. Shane Yost at Texas State University, Dr. Tod Grusenmeyer and Dr. Jack Ly at UES/Air Force Research Lab and Dr. Sean Roberts and his research group here at UT Austin: Emily Raulerson, Danielle Cadena, Laura Estergreen, and Seth Allen) whom without this research would not have been as impactful. Lastly, I would like to thank Kristina Kafle for providing us with incredible illustrations for our TOC graphics.

Abstract

A Guide to Photocuring Catalyst Selection

Alex Michael Stafford, Ph.D

The University of Texas at Austin, 2023

Supervisor: Zachariah A. Page

The utilization of light as an energy source to convert liquid resins (termed photopolymers) into solid plastics is a burgeoning field in polymer science. Photopolymerizations have found broad applications in imaging and curing technologies (e.g. photoresists, photolithography, and photocurable coatings) and the driving of rapid polymerizations with visible to near-infrared light will enable nascent technologies in the emerging fields of bio- and composite-3D printing. However, current photopolymerization strategies are limited by long reaction times, high light intensities, and/or large catalyst loadings. The improvement of efficiency remains elusive without a comprehensive, mechanistic evaluation of photocatalysis to better understand how composition relates to polymerization metrics. With this objective in mind, a series of BODIPYs, azaBODIPYs, thiopheneBODIPYs and thionaphthalimides were synthesized and systematically characterized to elucidate key structure–property relationships that correlate to efficient photopolymerization driven by visible to near-IR light. For all these scaffolds, access to longer lived photoexcited states was shown as a general method to increase polymerization rate, quantitatively characterized using a custom real-time infrared spectroscopy setup. Furthermore, a combination of steady-state emission

quenching experiments, electronic structure calculations, and ultrafast transient absorption revealed that efficient intersystem crossing to the lowest excited triplet state was a key mechanistic step to achieving rapid photopolymerization reactions. Unprecedented polymerization rates were achieved with extremely low light intensities (<1 mW/cm^2) and catalyst loadings (<50 μM), exemplified by reaction completion within 60 s of irradiation using green, red, far-red, and near-IR light-emitting diodes. The photoredox catalysts were additionally employed to produce complex 3D structures using high-resolution visible light and near-IR 3D printing, demonstrating the broad utility of these catalysts in additive manufacturing.

Table of Contents

List of Tables

List of Figures

GENERAL INTRODUCTION

Light has been used to rapidly convert liquid resins into solid objects in a process known as photocuring. This process provides control over when and where a reaction occurs (i.e., spatiotemporal control) and has enabled transformative technological advancements in imaging, photolithography, adhesives, coatings and, most recently, stereolithographic 3D printing.[1–7] In particular, enormous growth of the field came at the advent of photolithography, which today has been widely adopted to manufacture modern microelectronics, such as microprocessors and memory chips, ubiquitous in computers, phones, and cars.[8–11] In contemporary photolithography, high energy UV light (<420nm) is used for photocuring, which limits material compatibility due to degradation and attenuation by absorption or scattering of high energy photons. The recent widespread availability of inexpensive visible light emitting diodes (LEDs) offers an alternative method to UV photocuring that provides (1) milder and more cost-effective reaction conditions, (2) larger penetration depths due to reduced scattering and background absorption, and (3) wavelength-selectivity (i.e., the ability to activate different chemical pathways with individual wavelengths/colors of electromagnetic radiation).[12–21] As such, visible light photocuring holds the potential to promote the preparation of, inter alia, biocompatible materials containing UV-absorbing or -sensitive components, strong and lightweight composite structures, and multimaterial objects having predefined functionality embedded in discrete domains. For example, in dentistry, photocurable coatings have shifted to blue irradiation to mitigate risks associated with UV exposure by employing visible light absorbing photoinitiators (e.g., camphorquinone and acylgermanes).[22,23] However, photocuring with longer wavelengths of light (green to near-infrared, NIR) is an ongoing challenge that, to date, has been restricted to long exposure times (>60 s) and/or high intensity irradiation (>50 mW/cm^2), precluding their

utility in photocuring applications.[12–21] To address the grand challenge of efficient photocuring with visible to NIR light, a number of metal and metal-free photosystems have been examined for their ability to induce polymerization.[12,16] These photosystems fall into one of two categories: Type I or Type II and can be seen in **Figure 0.1**. Type I photosystems consist only of a

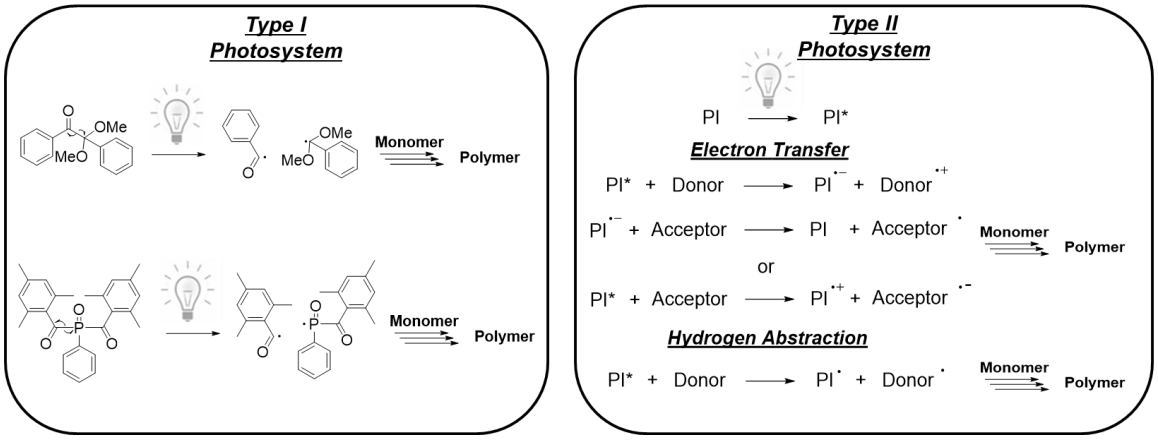

Figure 0.1: General Reaction Scheme of a Type I and Type II Photosystem

photoinitiator that degrades upon light absorption to yield reactive fragments capable of initiating polymerization (e.g., radicals, cations, or anions). Common Type I photoinitiators for radical polymerizations include acyl derivatives like DMPA (2,2-dimethoxy-2-phenylacetophenone) or acyl phosphine oxide derivatives like TPO (trimethylbenzoyldiphenyl phosphine oxide) and BAPO (phenylbis(2,4,6-trimethylbenzoyl) phosphineoxide). Type II systems, on the other hand, require at least two components, an initiator and either a hydrogen donor, photosensitizer, or photoredox catalyst (PRC) to produce reactive units capable of initiating polymerization. While Type I systems rely on a "forbidden" n → π* transition, Type II systems operate through π → π* excitation with characteristically stronger molar absorptivity at longer wavelengths of light (>500 nm, green to NIR). Attractive traits accompanying Type II systems that

activate with low-energy light include being environmentally benign, having minimal side reactions, and not releasing volatile organic compounds.[24,25] However, reactions are often slower for Type II systems in comparison to Type I due to a rate-limiting intermediate atom- or electron-transfer step that relies on an effective collision between an initiator and excited PRC compound to ultimately produce the requisite reactive units. Therefore, we hypothesize that efficiency of a Type II photosystem can be improved by increasing the excited state lifetime of a PRC compound, which in-turn will increase the number of collisions between initiators and excited PRC compounds per photon absorbed. Xanthenes and cyanines have received considerable attention as Type II PRC compounds, with demonstrated photocuring under visible and NIR light, respectively.[24−26] Both Laleveé [16,27,28] and Strehmel[29−31] and their co-workers have elegantly shown visible-to-NIR photocuring of acrylates and epoxies using Type II photosystems. For example, recent reports have shown that NIR polymerization chemistry with PRC loadings of ∼0.02−0.06 mol % can be either rapid (<60 s) when using a high intensity (≥400 mW/cm^2) laser diode at 780 nm,[27] or reactive under low intensity (~30 mW/cm^2) LED light centered at ~790 nm, yet requiring longer exposure times (>100 s).[29] This apparent trade-off between reaction rate and incident light intensity necessitates a closer examination of visible-to-NIR photosystems to advance state-of-the-art photocuring. To this end, an opportunity remains to simultaneously examine critical facets of photocuring by (1) quantifying apparent polymerization rate under normalized irradiation conditions and (2) identifying a modular synthetic photoredox catalyst (PRC) to facilitate a systematic structure−property study.

0.1: REFERENCES

(1) Aguado, B. A.; Grim, J. C.; Rosales, A. M.; Watson-Capps, J. J.; Anseth, K. S. Engineering Precision Biomaterials for Personalized Medicine. *Sci. Transl. Med*. **2018**, *10*, 8645.

(2) Camposeo, A.; Persano, L.; Farsari, M.; Pisignano, D. Additive Manufacturing: Applications and Directions in Photonics and Optoelectronics. *Adv. Opt. Mater*. **2019**, *7* (1), 1800419.

(3) Wallin, T. J.; Pikul, J.; Shepherd, R. F. 3D Printing of Soft Robotic Systems. *Nat. Rev. Mater*. **2018**, *3* (6), 84−100.

(4) Zhang, J.; Xiao, P. 3D Printing of Photopolymers. *Polym. Chem*. **2018**, *9* (13), 1530−1540.

(5) Jung, K.; Corrigan, N.; Ciftci, M.; Xu, J.; Seo, S. E.; Hawker, C. J.; Boyer, C. Designing with Light: Advanced 2D, 3D, and 4D Materials. *Adv. Mater*. **2020**, *32*, 1903850.

(6) Lim, K. S.; Galarraga, J. H.; Cui, X.; Lindberg, G. C. J.; Burdick, J. A.; Woodfield, T. B. F. Fundamentals and Applications of Photo-Cross-Linking in Bioprinting. *Chem. Rev*. **2020**. *120* (19), 10662-10694

(7) Yu, C.; Schimelman, J.; Wang, P.; Miller, K. L.; Ma, X.; You, S.; Guan, J.; Sun, B.; Zhu, W.; Chen, S. Photopolymerizable Biomaterials and Light-Based 3D Printing Strategies for Biomedical Applications. *Chem. Rev*. **2020**. *120* (19) 10695-10743

(8) Willson, C. G.; Dammel, R. R.; Reiser, A. Photoresist Materials: A Historical Perspective. In Advances in Resist Technology and Processing XIV; SPIE, **1997**; Vol. 3049, p 28.

(9) Kozawa, T.; Santillan, J. J.; Itani, T. Relationship between Resolution Blur and Stochastic Defect of Chemically Amplified Resists Used for Extreme Ultraviolet Lithography. *J. Photopolym. Sci. Technol*. **2019**, *32* (1), 161−167.

(10) MacDonald, S. A.; Ito, H.; Willson, C. G. Advances in the Design of Organic Resist Materials. *Microelectron. Eng*. **1983**, *1* (4), 269−293.

(11) Ito, H.; Willson, C. G.; Frechet, J. M. J. New UV Resists with Negative or Positive Tone. In Digest of Technical Papers - Symposium on VLSI Technology; **1982**; pp 86−87.

(12) Dumur, F. Recent Advances on Visible Light Metal-Based Photocatalysts for Polymerization under Low Light Intensity. *Catalysts* **2019**, *9*, 736.

(13) Bagheri, A.; Jin, J. Photopolymerization in 3D Printing. *ACS Appl. Polym. Mater*. **2019**, *1* (4), 593−611.

(14) Corrigan, N.; Yeow, J.; Judzewitsch, P.; Xu, J.; Boyer, C. Seeing the Light: Advancing Materials Chemistry through Photopolymerization. *Angew. Chem., Int. Ed*. **2019**, *58* (16), 5170−5189.

(15) Strehmel, B.; Schmitz, C.; Cremanns, K.; Göttert, J. Photochemistry with Cyanines in the Near Infrared: A Step to Chemistry 4.0 Technologies. *Chem. - Eur. J*. **2019**, *25* (56), 12855− 12864.

(16) Xiao, P.; Zhang, J.; Dumur, F.; Tehfe, M. A.; Morlet-Savary, F.; Graff, B.; Gigmes, D.; Fouassier, J. P.; Lalevee, J. Visible Light́ Sensitive Photoinitiating Systems: Recent Progress in Cationic and Radical Photopolymerization Reactions under Soft Conditions. *Prog. Polym. Sci*. **2015**, *41* (C), 32−66.

(17) Chatani, S.; Kloxin, C. J.; Bowman, C. N. The Power of Light in Polymer Science: Photochemical Processes to Manipulate Polymer Formation, Structure, and Properties. *Polym. Chem*. **2014**, *5* (7), 2187−2201.

(18) Shanmugam, S.; Xu, J.; Boyer, C. Light-Regulated Polymerization under Near-Infrared/Far-Red Irradiation Catalyzed by Bacteriochlorophyll A. *Angew. Chem*. **2016**, *128* (3), 1048−1052.

(19) Corrigan, N.; Xu, J.; Boyer, C. A Photoinitiation System for Conventional and Controlled Radical Polymerization at Visible and NIR Wavelengths. *Macromolecules*. **2016**, *49* (9), 3274−3285.

(20) Wu, Z.; Jung, K.; Boyer, C. Effective Utilization of NIR Wavelengths for Photo-Controlled Polymerization: Penetration Through Thick Barriers and Parallel Solar Syntheses. *Angew. Chem*. **2020**, *132* (5), 2029−2033.

(21) Zhang, Z.; Corrigan, N.; Bagheri, A.; Jin, J.; Boyer, C. A Versatile 3D and 4D Printing System through Photocontrolled RAFT Polymerization. *Angew. Chem*. **2019**, *131* (50), 18122−18131.

(22) Haas, M.; Radebner, J.; Eibel, A.; Gescheidt, G.; Stueger, H. Recent Advances in Germanium-Based Photoinitiator Chemistry. *Chem. - Eur. J*. **2018**, *24* (33), 8258−8267.

(23) Schroeder, W. F.; Vallo, C. I. Effect of Different Photoinitiator Systems on Conversion Profiles of a Model Unfilled Light-Cured Resin. *Dent. Mater*. **2007**, *23* (10), 1313−1321.

(24) Corrigan, N.; Shanmugam, S.; Xu, J.; Boyer, C. Photocatalysis in Organic and Polymer Synthesis. *Chem. Soc. Rev*. **2016**, *45* (22), 6165−6212.

(25) Dadashi-Silab, S.; Doran, S.; Yagci, Y. Photoinduced Electron Transfer Reactions for Macromolecular Syntheses. *Chem. Rev*. **2016**, *116* (17), 10212−10275.

(26) Strehmel, B.; Schmitz, C.; Brömme, T.; Halbhuber, A.; Oprych, D.; Gutmann, J. S. Advances of near Infrared Sensitized Radical and Cationic Photopolymerization:

From Graphic Industry to Traditional Coatings. *J. Photopolym. Sci. Technol*. **2016**, *29* (1), 111−121.

(27) Bonardi, A. H.; Dumur, F.; Grant, T. M.; Noirbent, G.; Gigmes, D.; Lessard, B. H.; Fouassier, J. P.; Lalevee, J. High Performance´ Near-Infrared (NIR) Photoinitiating Systems Operating under Low Light Intensity and in the Presence of Oxygen. *Macromolecules*. **2018**, *51* (4), 1314−1324.

(28) Bonardi, A.; Bonardi, F.; Noirbent, G.; Dumur, F.; Dietlin, C.; Gigmes, D.; Fouassier, J. P.; Lalevee, J. Different NIR Dye Scaffolds´ for Polymerization Reactions under NIR Light. *Polym. Chem*. **2019**, *10* (47), 6505−6514.

(29) Shiraishi, A.; Kimura, H.; Oprych, D.; Schmitz, C.; Strehmel, B. Comparison between NIR and UV-Sensitized Radical and Cationic Reactivity of Iodonium Salts Comprising Anions with Different Coordination Behavior. *J. Photopolym. Sci. Technol*. **2017**, *30* (6), 633−638.

(30) Schmitz, C.; Halbhuber, A.; Keil, D.; Strehmel, B. NIR Sensitized Photoinitiated Radical Polymerization and Proton Generation with Cyanines and LED Arrays. *Prog. Org. Coat*. **2016**, *100*, 32−46.

(31) Schmitz, C.; Pang, Y.; Gülz, A.; Glaser, M.; Horst, J.; Ja¨ger, M.;¨Strehmel, B. New High-Power LEDs Open Photochemistry for NearInfrared- Sensitized Radical and Cationic Photopolymerization. *Angew. Chem*. **2019**, *131* (13), 4445−4450.

Chapter 1: BODIPYs as Green Light Photoredox Catalysts

(J. Am. Chem. Soc. 2020, 142, 34, 14733–14742)

1.1: INTRODUCTION

A series of boron-dipyrromethene (BODIPY) dyes were selected to address the photopolymerization challenges listed above. In spite of the attractive traits of BODIPYs, including tunable optoelectronic properties, high molar extinction, and facile and modular syntheses,[1-3] they have received far less attention as photopolymer catalysts[4-6] in comparison to their xanthene and cyanine counterparts (**Figure 1.1**). However, the

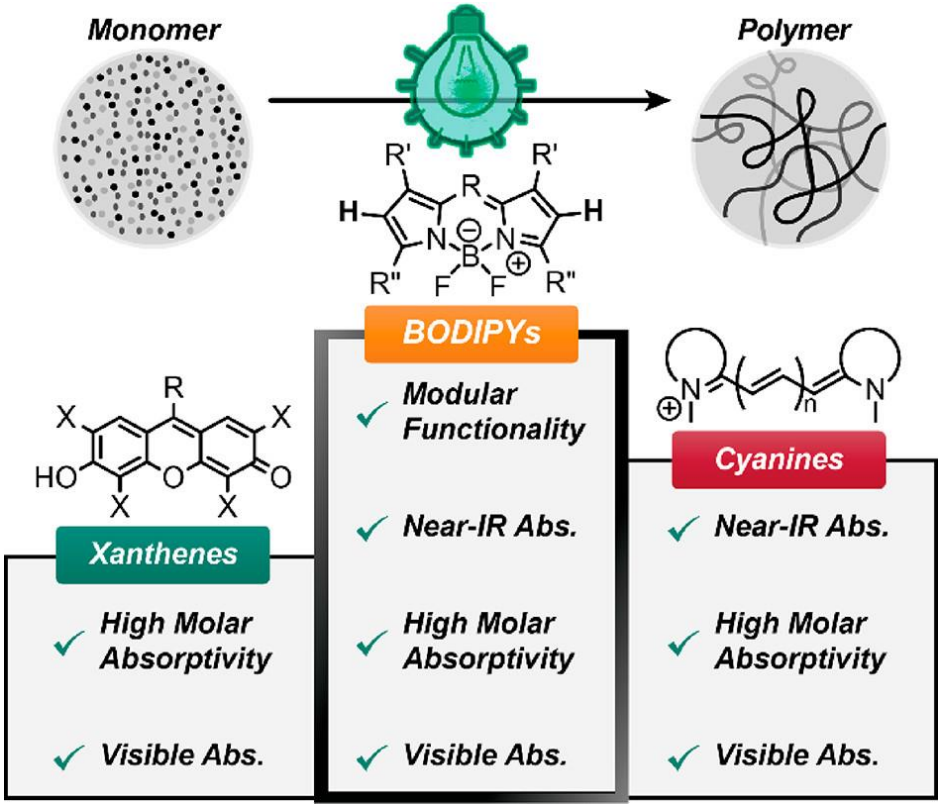

Figure 1.1: Boron Dipyrromethene (BODIPY) as an Attractive Photocatalyst Platform for Visible to NIR Photopolymerizations, in Place of Traditional Xanthene and Cyanine Derivatives

BODIPY platform has been heavily examined for imaging,[7,8] sensing,[9] and photodynamic therapy[10,11] applications. These extensive studies have unveiled a remarkable range of optoelectronic properties for compounds bearing a BODIPY scaffold, showing peak absorption values from 500 to 900 nm (blue/green-NIR), extinction coefficients exceeding 5×10^4 M^{-1} cm^{-2} , and ground state reduction and oxidation potentials that span from −2.40 to −0.35 V and 1.55 to 0.18 V (vs Cp_2Fe/Cp_2Fe^+), respectively.[1-3] Most important for the present application is efficient intersystem crossing (ISC) to long-lived triplet excited states that has been observed for various BODIPYs. Previously, these triplet excited states have played an important role in photodynamic therapy by generating reactive singlet oxygen[12] and are presented here for the first time in photocuring applications. A common method to increase the ISC rate in BODIPYs has been halogenation, which relies on the so-called "heavy atom effect" [13] where spin−orbit coupling is enhanced through incorporation of elements with high atomic number. This impressive versatility in absorption, redox potentials, and excited state dynamics make BODIPY dyes ideal candidates for visible photocuring. Herein, a small library of BODIPYs are synthesized and quantitatively examined using a custom FTIR setup[14] to systematically unveil design parameters that will serve as a guide to advance photopolymer development and associated technologies. Specifically, halogenation is comprehensively examined as a universal method to improve photocuring efficiency, which builds off the hypothesis that longer lived excited states will increase the probability of a successful collision in a Type II initiation process. Triplet state formation is shown to be critical as PRC efficiency increases with ISC rates. PRC halogenation results in a 5−8× rate increase for different BODIPY classes and demonstrates unprecedented photopolymerization sensitivity at low PRC loadings (down to 0.001 mol % = 47 μM) and light intensities for green light (~0.01 mW/cm^2 exposure). Thus,

halogenation to form long-lived excited states is shown to be a general method to effectively increase photopolymerization efficiency, which provides a platform to enable emerging photocuring applications.

1.2: RESULTS AND DISCUSSION

A set of BODIPY dyes were synthesized to contain a mesityl group at the bridgehead position along with 4 methyl substitutions on the periphery, providing both solubility and stability against nucleophilic attack.[15] As shown in **Figure 1.2**, the

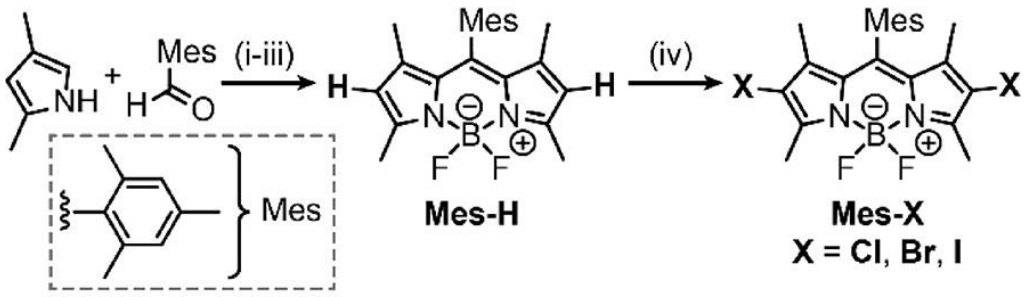

Figure 1.2: Modular Synthetic Procedure to Four Different BODIPY Derivatives. Reagents and Conditions: (i) TFA, DCM, 3 h; (ii) DDQ, 1 h; (iii) NEt_3, $BF_3{\cdot}OEt_2$, 2 h, 65% (two steps); (iv) NCS, DCM (58%) (X = Cl); NBS, DCM (50%) (X = Br); NIS, DCM/MeOH (65%) (X = I).

synthesis of the hydrogen-functionalized derivative (**Mes-H**) was accomplished via reductive coupling between commercially available 2,4-dimethylpyrrole and mesitaldehdye in a facile one pot approach.[16] The resulting modular **Mes-H** derivative served as a framework to study the heavy atom effect with respect to photopolymer catalysis. Subsequent halogenation of **Mes-H** with the respective N-halosuccinimide derivative yielded the desired chloro- (**Mes-Cl**), bromo- (**Mes-Br**), and iodo- **(Mes-I**) substituted BODIPY dyes. Upon isolation, it was immediately apparent by eye that each

compound had a distinct color in solution, ranging from green to deep red (**Figure 1.3**, inset).

To quantitatively compare the photocatalytic activity between different BODIPY derivatives, it was critical to first characterize their optical properties (e.g., absorption profiles and corresponding extinction coefficients). UV–vis absorption spectroscopy in dilute solution revealed that halogenation resulted in a ~30 nm red-shift of the peak absorption wavelength (λ_{max}) (**Figure 1.4**). Specifically, the λ_{max} values were 497, 523,

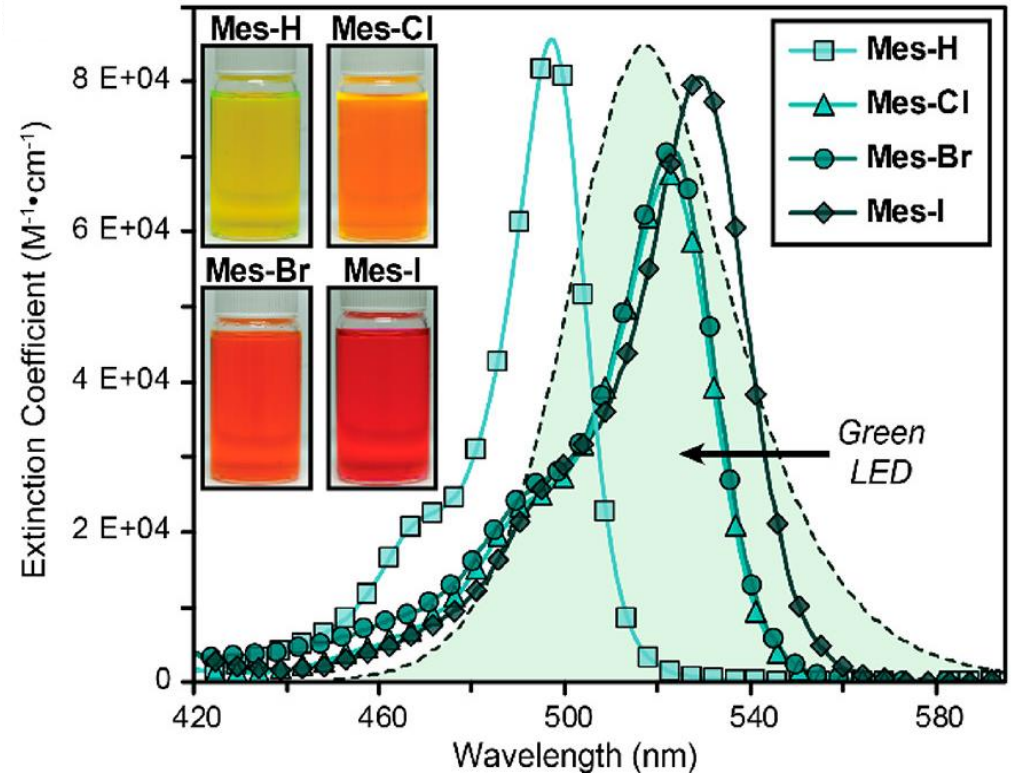

Figure 1.3: UV–Vis Absorption Spectroscopy (5–10 μM in acetonitrile). Normalized Green LED Emission Profile Overlaid with the UV–Vis Absorption Spectra showing Near Full Spectral Overlap with the Halogenated Derivatives and Partial Overlap with Mes-H. Inset: Photographs of Distinctly Colored BODIPYs in Solution.

523, and 529 nm for **Mes-H**. **-Cl**, **-Br**, and **-I** derivatives, respectively (**Table 1.1**). Extinction coefficients were determined using Beer's law with a calibration curve generated from solutions containing different concentrations of each BODIPY derivative. As is typical for BODIPYs, the extinction coefficients at λ_{max} were quite high, ranging from ~67000–86000 M^{-1} cm^{-1} (**Table 1.1**). The strong absorption cross section with respect to the green LED, shown in **Figure 1.3**, for the present derivatives is beneficial for photopolymers as it can facilitate the use of lower catalyst loadings and/or light intensities.

BODIPY	λ_{max} (nm)	ε ($x10^4$ $M^{-1}cm^{-1}$)	Quantum Yield (Φ_f)	τ_{ISC} (ns) (Triplet Yield)	Triplet Lifetime (ns)
Mes-H	497	8.6 ± 0.2	0.94 ± 0.06	-	-
Mes-Cl	523	6.7 ± 0.2	0.70 ± 0.05	7.8 (0.17)	370
Mes-Br	523	6.9 ± 0.3	0.19 ± 0.02	2.9 (0.35)	370
Mes-I	529	7.9 ± 0.3	0.03 ± 0.01	0.2 (0.89)	370

Table 1.1: Optoelectronic Properties of the Mes-BODIPY Photoredox Catalysts

After the isolation of the four BODIPY derivatives, their utility as photosensitizers to induce polymerization was evaluated. The polymerizations were carried out using neat isobornyl acrylate as the monomer, selected for its low volatility and commercial viability. The initiator concentrations used were akin to those reported by Lalevée and co-workers,[6] however, they were reported as mol % in lieu of wt % for direct comparison. Specifically, 0.1 mol % of the BODIPY photosensitizer, 0.1 mol % of

the donor (D) initiator 2-(butyryloxy)-N,N,N-trimethylethan-1-aminium butyltriphenylborate, and 1.0 mol % of the acceptor (A) initiator [4-(octyloxy)phenyl](phenyl)iodonium hexafluoroantimonate (diphenyliodonium) were fully dissolved in the monomer (**Figure 1.4a**). The degassing of the mixture via sparging

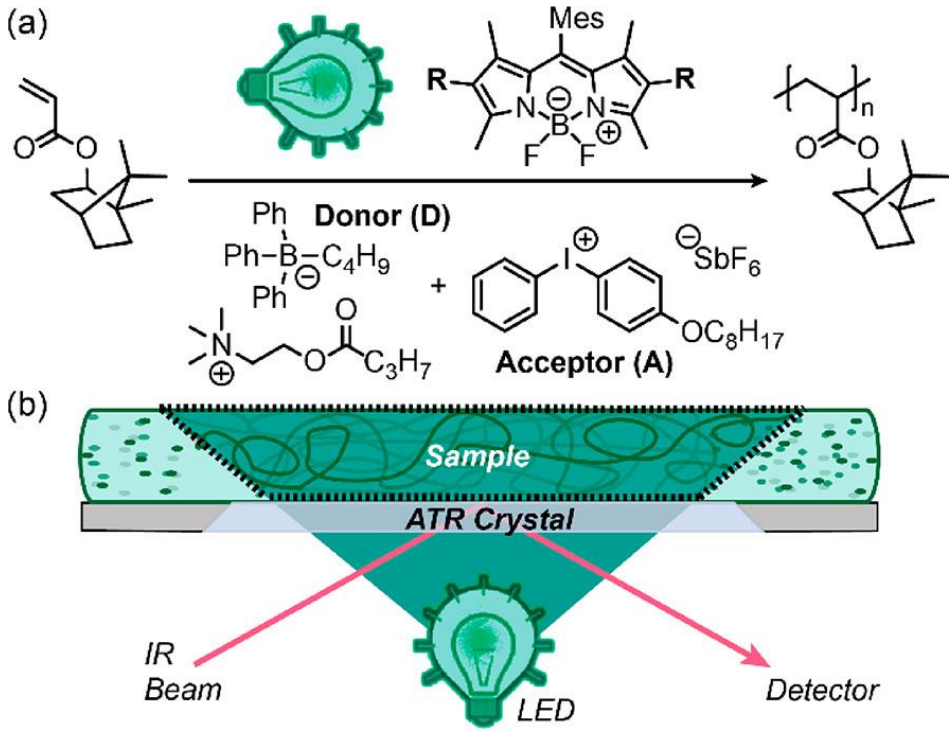

Figure 1.4: (a) Chemical Structures for the Different Components within the Resin Formulation: Isobornyl Acrylate as Monomer, Butyltriphenylborate Salt as Donor, and Diphenyl Iodonium as Acceptor. (b) Schematic Illustration for the Custom Real Time ATR-FTIR Setup with Bottom-Up Irradiation.

with nitrogen or argon was followed by irradiation with a green LED resulted in rapid polymerization, evident by vitrification in less than 60 s. To quantitatively characterize this polymerization process a novel method to monitor reaction kinetics was developed using FTIR spectroscopy.[14] A schematic representation of the attenuated total reflectance

(ATR) FTIR setup is shown in **Figure 1.4b**. Critically, LED and IR irradiation occur from the same face of the ATR crystal (bottom-up). This setup enables precise kinetics data to be rapidly collected for opaque photochemical transformations by providing uniform irradiation and shallow sample measurements. Within the mid-IR region, the depth of measurement ranges from ~0.5–5 μm, depending on the spectral position of the absorption signal. For acrylic polymerizations, the disappearance of the C=C vinylic stretch at 808 cm^{-1} was monitored and used to determine percent double bond conversion,[17] corresponding to a sampling depth of 2.5 μm. Simple glassware was made to encase the sample and purge its surrounding atmosphere with inert gas (e.g., nitrogen) to eliminate oxygen inhibition of the radical polymerization.

To directly compare photocuring efficiency between different BODIPY dyes with distinct absorption profiles, the number of photons absorbed by each sample was normalized. This was accomplished by varying the photon flux from a calibrated green LED after integrating the area of overlap between the absorption profile for each BODIPY derivative with the emission profile of the LED (**Figure 1.3**). The photon flux was calculated based on the following supplemental equations:

$$E = hc/\lambda \quad \textbf{(SE1)}$$

where E = energy (J), h = Plank's constant (=6.626×10^{-34}J s), c = speed of light (3×10^{8} m/s)

$$W = n \times (\frac{E}{t}) \quad \textbf{(SE2)}$$

where W = power, n = number of photons, E = energy of photons, and t = seconds

$$-logT = A = \varepsilon cl \quad \textbf{(SE3)}$$

where T = % transmission, A = absorption, ε = molar extinction coefficient (M^{-1} cm^{-1}), c = concentration (M), and l = path length (cm)

Equation **SE1** and **SE2** are used to convert the intensity output of the LED from (mW/cm^2 nm) into (# of photons/cm^2 s nm). T was calculated from equation **SE3**, followed by the portion of photons absorbed as (1-T). Multiplying the light intensity by (1-T) provides the flux of incident photons that are absorbed by the sample for each photon wavelength. Finally, integrating each curve provided the total absorbed photon flux (or number of photons absorbed) for each sample (**Figure 1.5**). For ATR measurements, a path length of 2.5 μm was used given an effective angle of 45°, a

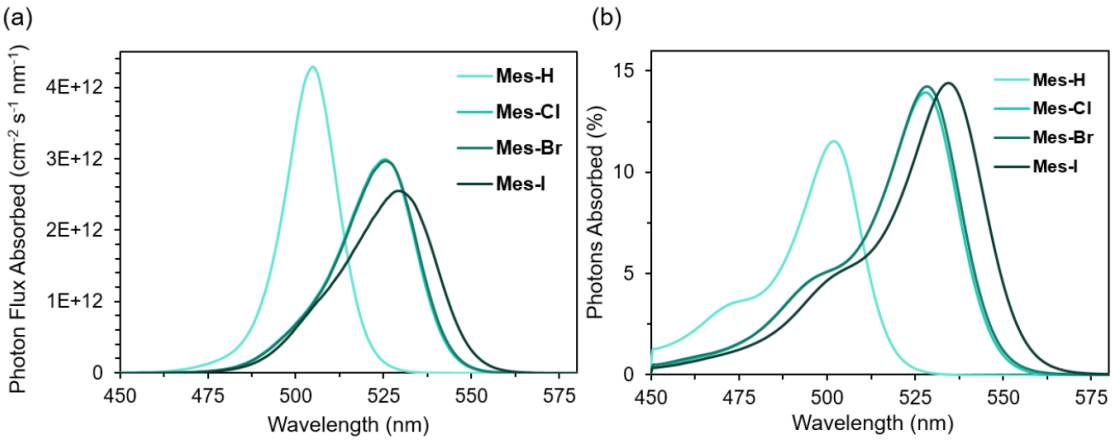

Figure 1.5: Normalized Photons Absorbed for the Mes-BODIPY Derivatives Using a Green LED with a Variable Intensity (1 mW/cm^2, 0.45 mW/cm^2, 0.44 mW/cm^2, and 0.44 mW/cm^2 for Mes-H, -Cl, -Br, and -I respectively) to Normalize the Total Number of Photons Absorbed (~1.1x10^{14} cm^{-2} s^{-1}). (a) Plot of the Photon Flux Absorbed as a Function of Wavelength and (b) Plot of Percent Photons Absorbed of the Green LED as a Function of Wavelength, Showing that Measurements Were Performed Far From Saturation.

wavenumber of 808 cm^{-1} (*vide infra*), a refractive index of 2.4 for the ATR (diamond), and a sample refractive index of 1.5 (estimate). Notably, **Mes-H** has the smallest absorption cross section with the green LED emission compared to the halogenated

BODIPY's, which was compensated by using a 2.2–2.3 times higher photon flux (i.e., light intensity) to equate the number of photons absorbed.

Photopolymerization kinetics were monitored using real time ATR-FTIR to determine the photocatalytic efficiency across the BODIPY series (**Figure 1.6**). A dramatic enhancement in the rate of polymerization was observed (>2×) when employing halogenated vs nonhalogenated derivatives. Furthermore, a trend in the halogenated

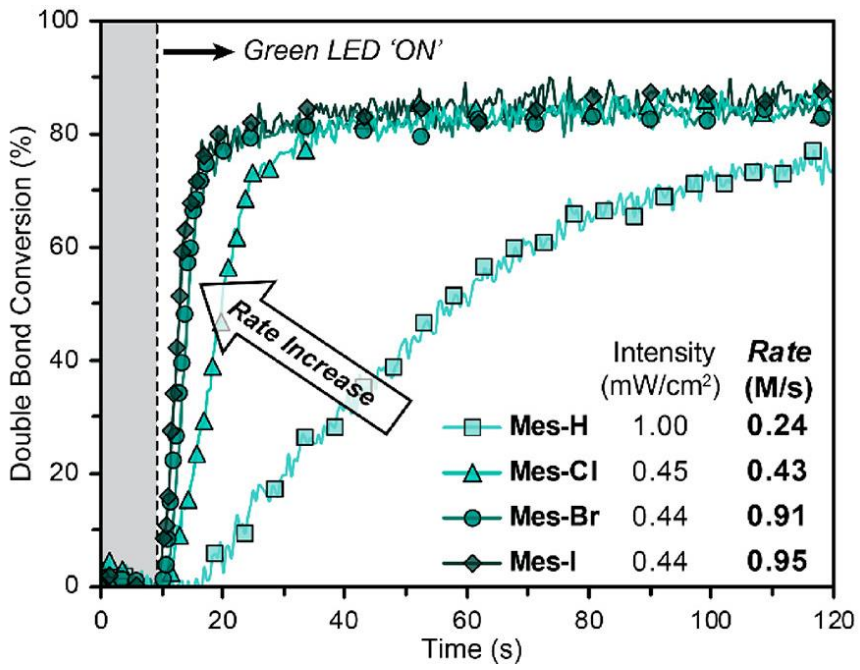

Figure 1.6: Plot of Conversion vs Time Using an Intensity that Normalizes Photons Absorbed Between Different Mes-BODIPY Derivatives. No Polymerization is Observed in the Dark (Gray Region). Upon Irradiation, Polymerization Rates Increase in the Order of **Mes-H**, **-Cl**, **-Br**, and **-I**, respectively.

series was detected, with increasing maximum polymerization rates (0.43 ± 0.03 to 0.91 ± 0.02 to 0.95 ± 0.03 M/s) correlating to an increase in the atomic number of the heavy atom: -Cl to -Br to -I, respectively. As a negative control, no polymerization was observed within the first 10 s prior to light exposure, indicative of resin stability in the

dark and that light is necessary to drive the polymerization. Moreover, resins stored in the dark for ~3 weeks showed no observable loss in activity (**Figure 1.7**). When the light was turned on, all polymerizations were rapidly initiated and reached a maximum monomer to-polymer conversion of ~80%. The ~80% conversion is hypothesized to be an upper limit for this particular mixture due to vitrification of poly(isobornyl acrylate), a glassy polymer (Tg ≈ 94 °C)[18] that "locks" remaining small molecules into place, which is further supported by near quantitative conversion for the less diffusion limited polymerization of 2-hydroxyethyl acrylate (**Figure 1.8**). For **Mes-Br** and **Mes-I**, the time

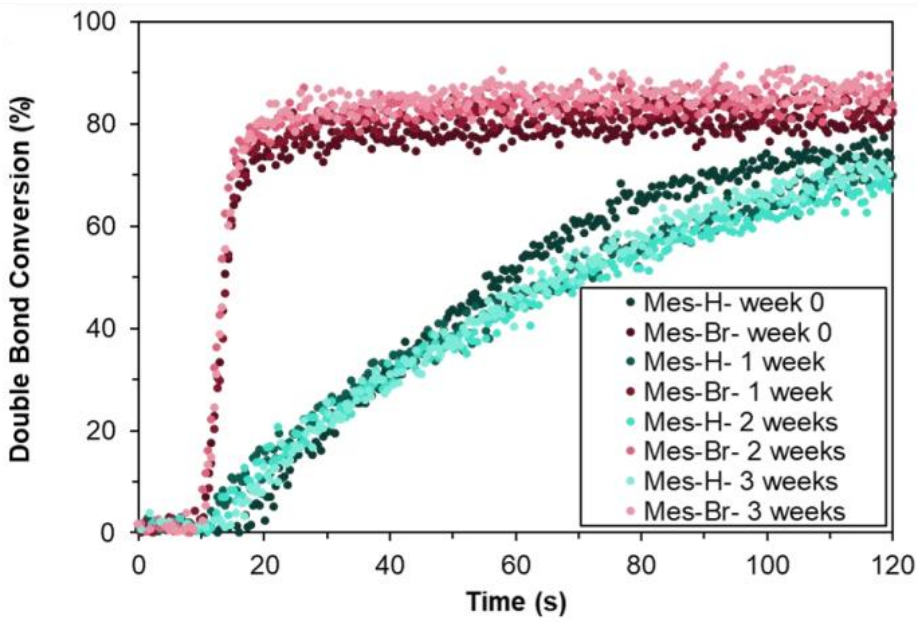

Figure 1.7: BODIPY Isobornyl Acrylate Resin Stability. Mes-H + Donor + Acceptor (0.1, 0.1, 1.0 mol%) and Mes-Br + Donor + Acceptor (0.1, 0.1, 1.0 mol%) Were Stored in Glass Vials Wrapped in Aluminum Foil to Protect from Light and Stored in a -20°C Freezer. Each Resin Was Tested Weekly Using Photo-ATR FTIR with a 530 nm LED at the Normalized Photon Flux Intensities.

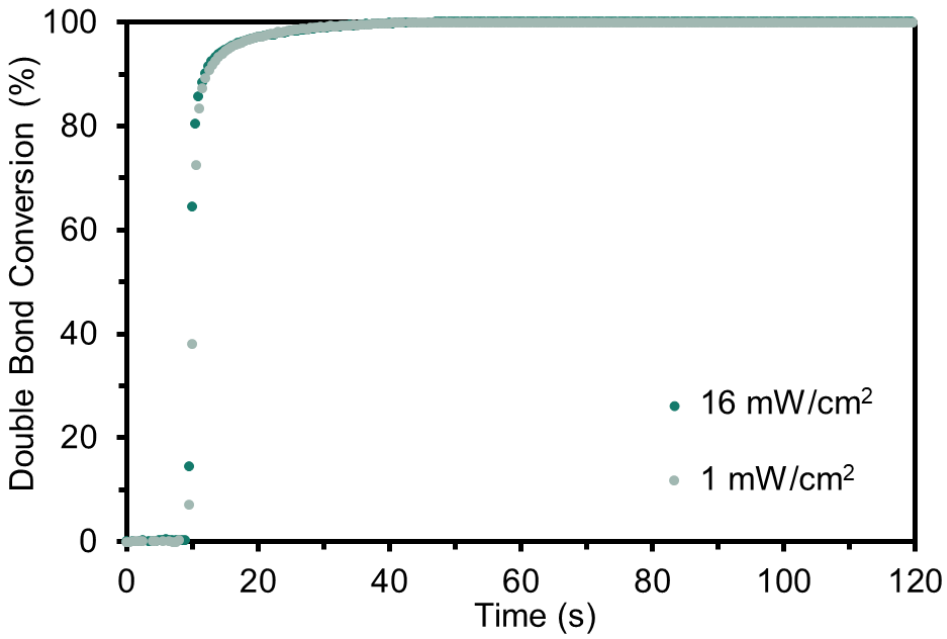

Figure 1.8: HEA Photopolymerization With Mes-I BODIPY Using Resin Formulation: 0.1 mol% BODIPY, 0.1 mol% Borate V (Donor), and 1.0 mol% H-Nu 254 (Acceptor). Irradiated with a 530 nm LED at 16 mW/cm^2 and 1 mW/cm^2.

to reach maximum conversion after turning the light on was 8.5 ± 0.9 s and 6.5 ± 0.3 s, respectively. Impressively, this was achieved under very low light intensity, <0.5 mW/cm^2, which, for comparison, is ~2 orders of magnitude less intense than an unfocused commercial laser pointer (~10–100 mW/cm^2). The ability to react under low light intensity saves energy for photocuring applications, which can enable rapid thin film formation for coatings and adhesives, and 3D printing via digital light processing (DLP), where irradiation at the build plane is typically <20 mW/cm^2. As a testament to the versatility of the present photosystem, *N*,*N*-dimethylacrylamide was also examined and provided similar photopolymerization results to those described above with isobornyl acrylate and 2-hydroxyethyl acrylate (**Figure 1.9**).

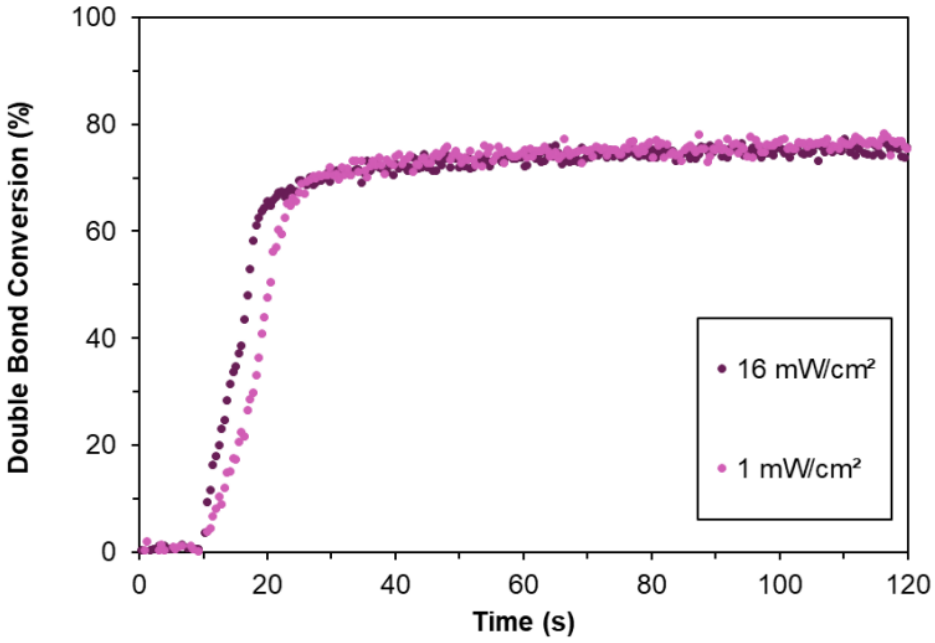

Figure 1.9: DMA Photopolymerization With Mes-I BODIPY Using Resin Formulation: 0.1 mol% BODIPY, 0.1 mol% Borate V (Donor), and 1.0 mol% H-Nu 254 (Acceptor). Irradiated with a 530 nm LED at 16 mW/cm^2 (Polymerization Rate: 5.7± 0.2 %Conv/s) and 1 mW/cm^2 (Polymerization Rate: 3.1 ± 0.4 %Conv/s).

Up to this point, the photopolymerizations examined have all been performed under an inert atmosphere with degassing. As a final demonstration of the flexibility of this photosystem, the polymerizations were conducted without degassing and under aerobic conditions. As can be seen in **Figure 1.10**, the photosystem is able to achieve rapid polymerization even in the presence of oxygen. Due to the ability of BODIPY triplet excited states being able to undergo triplet-triplet energy transfer to generate singlet oxygen, we observe a shift in overall efficiency with **Mes-Cl** outperforming the other halogenated derivatives. The triplet yield of **Mes-Cl** is only 17% whereas **Mes-I** is 89%, thus **Mes-I** is more impacted by the presence of oxygen and therefore the decrease

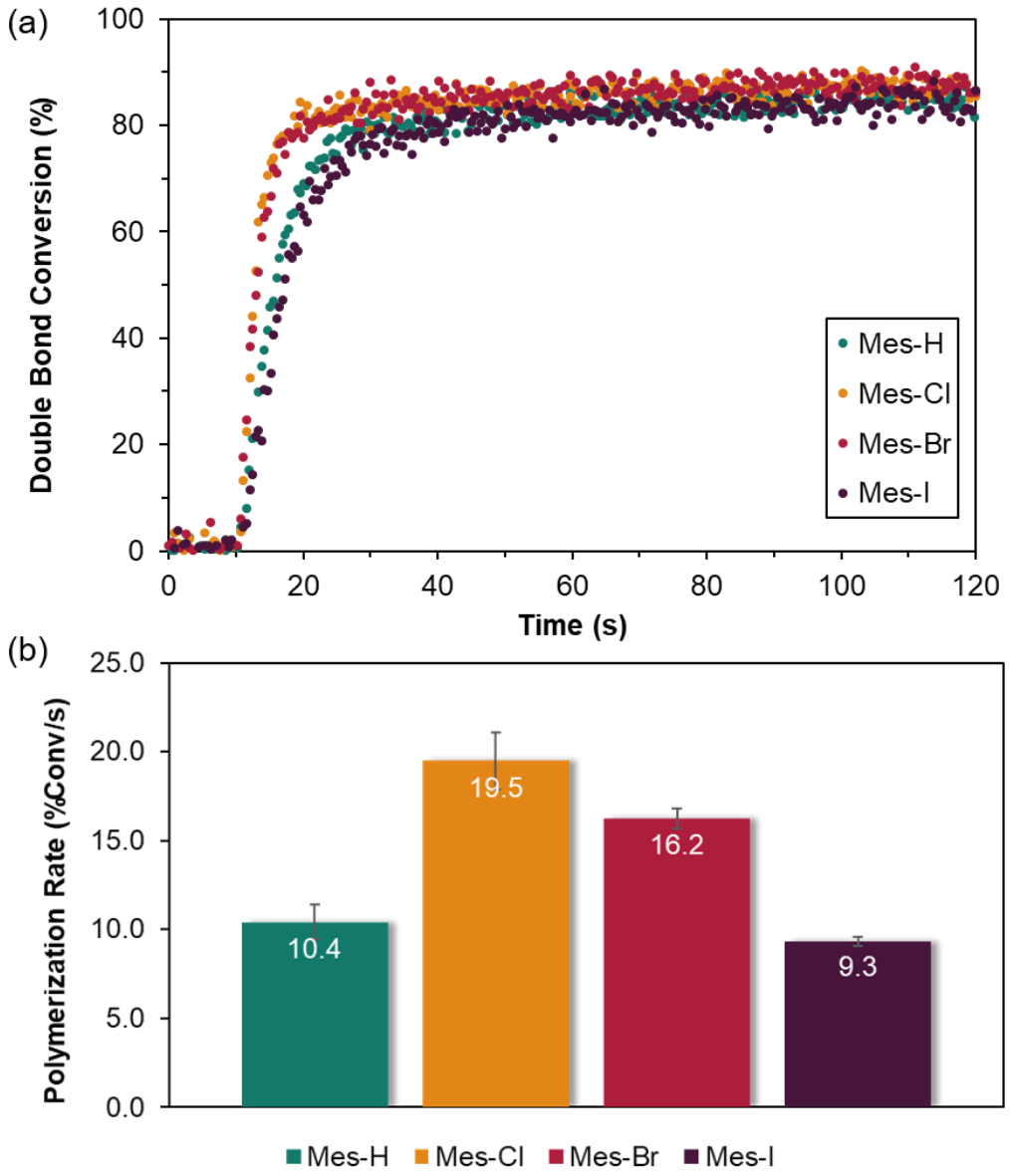

Figure 1.10: BODIPY Isobornyl Acrylate Photopolymerizations Aerobic Tests. (a) Mes-H, -Cl, -Br, -I in the Optimized Resin Formulation (0.1 mol% Mes-X ,0.1 mol% Donor,1.0 mol% Acceptor) Were Tested on the Photo-ATR-FTIR With a 530 nm LED at 16 mW/cm^2. The Samples Were Not Degassed Prior to Polymerization and the Polymerizations Were Carried Out Under Ambient environmental conditions. (b) Polymerization Rate in %Conversion/second of Optimized Resin Formulation. Error Bars Represent ± 1 standard deviation.

in its rate.

Fluorescence spectroscopy was used to probe the steady-state photophysics of the Mes-BODIPY derivatives and better understand the mechanism(s) that lead to faster polymerization rates. The fluorescence quantum yield (QY) was determined following literature precedent[19] in acetonitrile with Rhodamine 6G as a reference dye (**Figure 1.11**). The fluorescence QY values were inversely related to the polymerization rate, specifically 0.94 ± 0.06, 0.70 ± 0.05, 0.19 ± 0.02, and 0.03 ± 0.01 for **Mes-H**, **-Cl**, **-Br**, and **-I** derivatives, respectively (**Table 1**). The decreased QY for halogenated derivatives in dilute solution suggests that an intramolecular nonradiative quenching pathway outcompetes fluorescence, such as ISC.

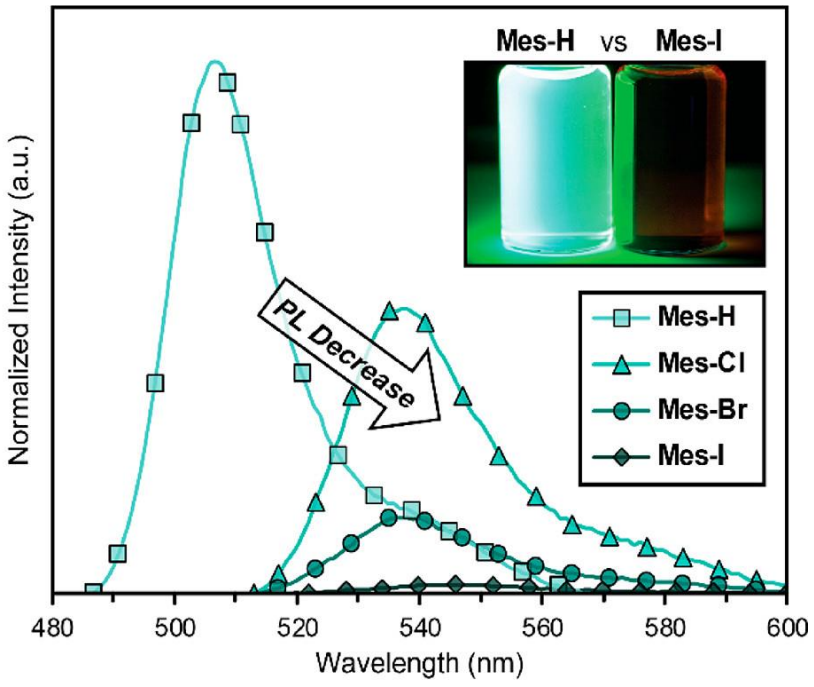

Figure 1.11: Photoluminescence (PL) of Mes-BODIPY Series, Showing a Decrease in Emission Upon Halogenation, Suggestive of a Nonradiative Intramolecular Process. Inset: Photographs of **Mes-H** and **Mes-I** in Acetonitrile (0.3 mM) Irradiated with a Hand-Held 365 nm UV lamp.

Subsequently, intermolecular fluorescence (i.e., singlet) quenching by D and A initiators was probed to elucidate the mechanisms for radical generation (**Figure 1.12**). The Stern–Volmer plot for **Mes-H** and **Mes-Br** shows quenching by both D and A compounds, represented as an increase in the ratio between initial fluorescence intensity (I_0) and intensity (I) at a particular concentration of D or A (i.e., I_0/I). This suggests that some contribution toward polymerization derives from the singlet photoexcited state for both **Mes-H** and **Mes-Br**, although to a lesser extent for **Mes-Br** as represented by the weaker quenching. Consecutive additions of D result in a steeper slope relative to equimolar additions of A for both Mes-BODIPY derivatives. This indicates that

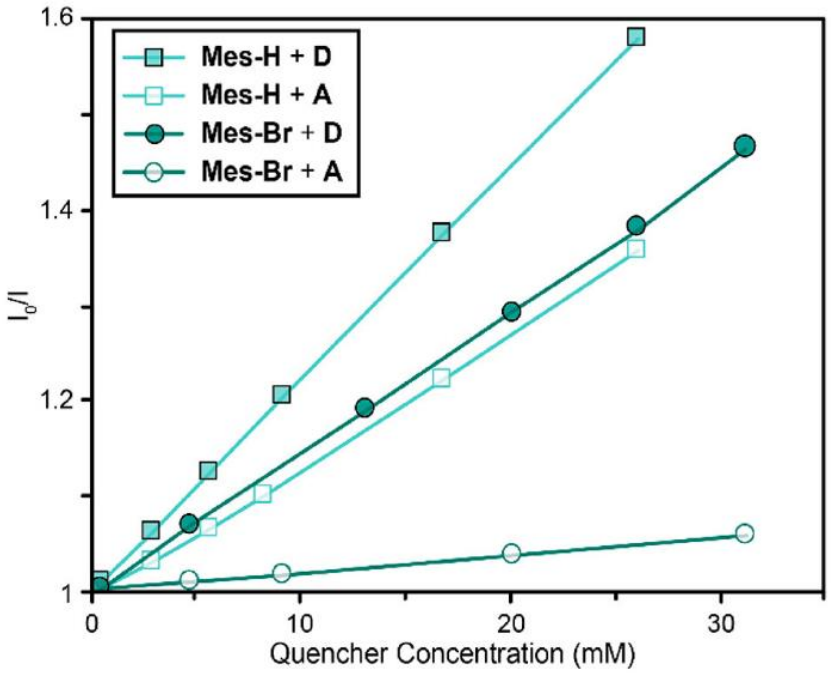

Figure 1.12: Stern–Volmer Plot of **Mes-H** (1 mM) and **Mes-Br** (1 mM) in the Presence of **D** and **A**, Showing that **D** Results in More Efficient Quenching for Both Dyes.

photoexcited Mes-BODIPY dyes more readily accept an electron from D, as opposed to donating an electron to A in the singlet excited state. Thus, the major mechanistic pathway for this photosystem is thought to follow reductive quenching, which would result in a radical anion of the respective Mes-BODIPY and a butyl radical[20] from the oxidized triphenylalkyl borate salt, D (**Figure 1.13**). Importantly, while the **Mes-Br** results in faster polymerization rates, the Stern–Volmer plot suggests that **Mes-H** reacts faster with both D and A, suggesting a secondary pathway is contributing to polymerization for **Mes-Br**.

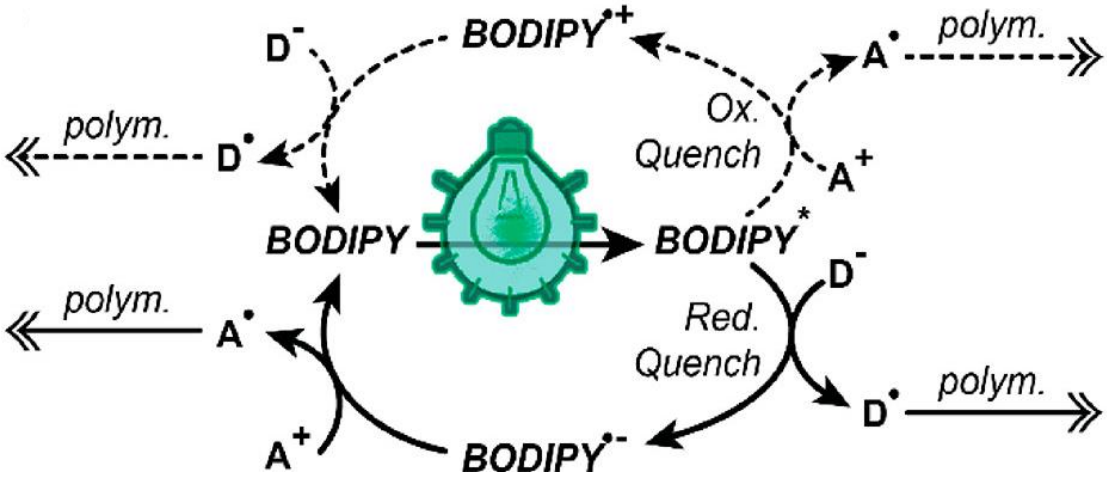

Figure 1.13: Proposed Photosystem Mechanisms with Oxidative Quenching, Top, and Reductive Quenching (Primary Pathway), Bottom

Prior to an investigation of the secondary pathway, cyclic voltammetry (CV) and computational studies were performed to probe the electronic energy states of the different photosystem components for corroboration of the mechanistic hypothesis that reductive quenching is favored over oxidative quenching. CV data was collected to determine the highest occupied molecular orbital (HOMO) and lowest unoccupied molecular orbital (LUMO) energy levels, as provided in **Table 1.2**. Halogenation stabilized both the LUMO and HOMO energy levels, although to a greater extent for the

LUMO (~0.3 eV decrease vs ≲0.15 eV decrease, respectively). This shift correlates to a decrease in the electronic energy gap ($E_g = E_{HOMO} - E_{LUMO}$), which is consistent with the red-shift in absorption (i.e., decrease in optical energy gap) observed previously (**Figure 1.3**). The decrease in both HOMO and LUMO energy levels in going from **Mes-H** to **-Br** increases the driving force for reductive quenching and decreases it for oxidative quenching (**Figure 1.13**), in support of the Stern–Volmer analysis. Additionally, density functional theory was used to support the relative electronic functional level trends

Compound	E_{ox} (V vs. $Ag/AgNO_3$	E_{red} (V vs. $Ag/AgNO_3$)	HOMO[a] (eV)	LUMO[a] (eV)
Mes-H	0.939	-1.542	-5.64 (-5.42)	-3.16 (-3.06)
Mes-Cl	1.103	-1.292	-5.81 (-5.59)	-3.41 (-3.25)
Mes-Br	1.111	-1.294	-5.81 (-5.60)	-3.41 (-3.23)
Mes-I	1.124	-1.334	-5.82 (-5.54)	-3.37 (-3.29)
HNu 254	1.562	-1.194	-6.27	-3.51 (-3.91)
Borate V	0.434	-	-5.14 (-5.43)	-

Table 1.2: Cyclic Voltammetry Data of Mes-BODIPY Photocatalysts and Donor (Borate V) and Acceptor (HNu 254). [a]Values in parentheses are computed energy levels using a def2-tzvp basis set and cam-b3lyp functional.

observed with CV and demonstrate that computational methods may be used as a predictive tool in the future. Specifically, the def2-tzvp basis set and cam-b3lyp functional were used in an implicit solvation model to compute the HOMO and LUMO energy levels. Following literature precedent for diphenyliodinium,[21,22] accurate

estimations for the D and A initiators were achieved by using a concerted ionization and bond cleaving process. The geometries for all molecules were optimized with the 6-31G* basis set and B3LYP functional in the gas phase. The energies were computed as follows:

$$E_{LUMO} = -(E_{Anion} - E_{Ground})$$ (**SE6**)

$$E_{HOMO} = E_{Cation} - E_{Ground}$$ (**SE7**)

$E_{\_Ground}$ is the energy of the neutral ground state, E_{Anion} is the energy of the anion, and E_{Cation} is the energy of the cation. Equation **SE6** yields the vertical electron affinity and equation **SE7** yields the vertical ionization potential. For these calculations an implicit solvation model, SMD, was used with acetonitrile as the implicit solvent.[23] Linear response TDDFT was used to compute the singlet excited state energies, and the triplet excited states were modeled by setting the spin multiplicity to 3 to converge on the lowest triplet state. For the two co-initiators, the donor D, and the acceptor A, the HOMO and LUMO levels were computed via a concerted electron transfer and bond cleavage mechanism. This mechanism was first used on diphenyliodinium.[21,22] It was shown that simultaneous addition of an electron and cleavage of the C-I bond was necessary to reproduce experimental results. Assuming only an electron transfer event yielded 5.88 and 2.25 eV for D HOMO and A LUMO, respectively. The diabatic electronic transfer event HOMO and LUMO values are off by over 1.0 eV. The equations used for the A LUMO (equation **SE8**) and the D HOMO (equation **SE9**) are:

$$E_{Ar2I+\,/\,Ar\cdot+ArI} = E_{LUMO,Ad} - E_{BDE}$$ (**SE8**)

$$E_{Ar3RB-\,/\,Ar\cdot+Ar2RB} = E_{HOMO,Ad} + E_{BDE}$$ (**SE9**)

E_{BDE} is the bond dissociation energy of the C-I or C-B bond. This was computed by optimizing the geometry of the dissociated fragments and computing their energy within

the SMD implicit solvent model. The bond dissociation energy was then obtained by $E_{BDE} = E_{frag,1} + E_{frag,2} - E_{mol}$. For both A and D there are two unique bonds that can be cleaved. In the case of A one of the two aromatic rings has an ether while the other does not. In the case of D there are the aromatic rings (Ar) or the alkane chain (R) that are bonded to the boron. $E_{HOMO,Ad}$ and $E_{LUMO,Ad}$ are the adiabatic ionization potential and electron affinity, respectively. The adiabatic HOMO and LUMO use the optimized geometry of the iodine fragment or boron fragment after bond cleavage. For example, $E_{LUMO,Ad}$ for A is the adiabatic electron affinity of the ArI^+ fragment. These were computed in the SMD implicit solvation model. An adiabatic ionization potential/electron affinity is computed by taking the difference in energy between the minimized geometry of the ground state and the minimized geometry of the reduced/oxidized state. This is different from the commonly used diabatic ionization potential where only the minimized ground state geometry is used for both electronic states. In **Table 1.3**, there are two values listed for the HOMO and LUMO energies of the initiators because there are two

HNu 254	$E_{LUMO,Ad}$ (eV)	E_{BDE} (eV)	$E_{Ar2I+ / Ar• +ArI}$ (eV)
Ar• + ArOI	5.89	1.94	3.95
ArO• + ArI	6.53	2.62	3.91
Borate V	$E_{LUMO,Ad}$ (eV)	E_{BDE} (eV)	$E_{Ar3RB- / Ar• + Ar2RB}$ (eV)
Ar• + Ar_2RB	2.07	3.36	5.43
R• + Ar_3B	2.40	2.58	4.98

Table 1.3: Breakdown of the Energies Involved in the Concerted Electron Attachment/Detachment and Bond Cleavage of the Co-Initiators.

unique C-I or C-B bonds to cleave. In the case of the borate donor, the C-B bond with the aromatic ring vs alkane has significant differences. The Ar_3B fragment has a larger ionization potential, but the R-B bond is significantly weaker than the Ar-B bond. Based on the bond dissociation energies, cleavage of an aromatic group requires more energy than the alkane chain, and thus a larger ionization potential. Interestingly, for the diphenyl iodonium acceptor (H-Nu 254) there are significant differences in the electron affinity and bond dissociation energy between the two aromatic groups, but they cancel with each other to yield almost identical electron affinities. In comparison, if we use equations **SE6** and **SE7** for the co-initiators we get 5.88 and 2.25 eV for the D HOMO and the A LUMO, respectively. This is in agreement with other work on similar co-initiators showing that the electron transfer process occurs with the bond cleavage and not independently of each other. As can be seen in **Table 1.2**, the computational values for the HOMO and LUMO energies are within 0.2 eV of the experimental values. Surprisingly, it is very consistent across all values that we underestimate by 0.2 eV, suggesting that for future screening a shift of 0.2 eV to the current computational protocol might yield more accurate results. The singlet excited state energies were computed using TDDFT. They follow the same trends as the experimental values but are roughly 0.4-0.5 eV higher than the experimental values. All the singlet excited states were 99% from a HOMO -> LUMO excitation. This supports the correlation between the excitation energies and the redox energies. Both CV and computation confirm that there is a larger energetic driving force for reductive over oxidative quenching in the present photosystems, substantiating the preference for electron transfer from D to photoexcited Mes-BODIPY.

So far, optoelectronic characterization has focused on the lowest excited singlet (S_1) state of the Mes-BODIPY dyes, but fluorescence quenching experiments suggest that

halogenation provides an additional mechanism to facilitate higher polymerization rates. Transient absorption (TA) spectroscopy was employed to better assess the connection between Mes-BODIPY excited state dynamics and photocatalytic efficiency. **Figure 1.14** plots the TA spectra of the halogenated BODIPY series dissolved in acetonitrile

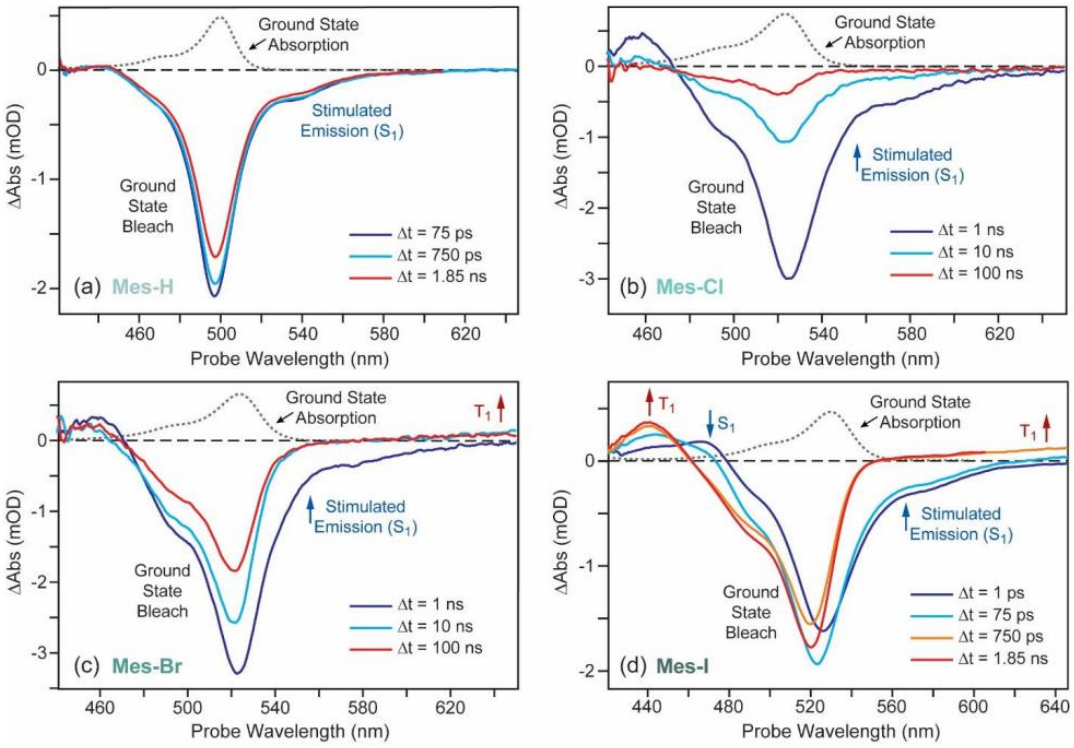

Figure 1.14: TA Spectra of **Mes-H** (a), **Mes-Cl** (b), **Mes-Br** (c), and **Mes-I** (d) in Acetonitrile. Excitation Pulses Centered at 525 nm Derived from the Output of a NOPA Were Used to Collect Spectra of **Mes-H** and **Mes-I** While Spectra of **Mes-Cl** and **Mes-Br** Were Taken Following Excitation at 532 nm Using the Output of a Frequency-Doubled Nd:YAG Laser. The Polarization of the Pump and Probe Pulses Were Set Perpendicular to One Another.

following photoexcitation at 530 nm. Upon photoexcitation of **Mes-I**, a broad negative signal appears from 480 to 540 nm that corresponds to a bleaching of its ground state absorption while stimulated emission can be seen at longer probe wavelengths and tracks the shape of **Mes-I**'s steady-state emission spectrum. Together, these features indicate

excitation of **Mes-I** to its S_1 state. Over time, the stimulated emission is gradually replaced by a weak induced absorption band while the ground state bleach shows little evolution, signaling conversion of the S_1 state to a new excited state. Concomitant with this change is growth of an induced absorption band centered at 440 nm attributed to **Mes-I**'s lowest excited triplet (T_1) state on the basis of prior photoinduced absorption spectra of BODIPY dyes.[24–27] Global target analysis of this data is used to extract an ISC rate of 197 ps (k_{ISC} = 5.1 × 10^9 s^{-1}). Briefly, TA data sets, $\Delta Abs(t, \lambda_{probe})$, were decomposed into a linear combination of species associated decay spectra (SADS), $\{\sigma_n(\lambda_{probe})\}$, with time-dependent weights, $\{c_n(t)\}$, whose values are the solutions to a set of sequential first-order rate equations:

$$\Delta Abs(t, \lambda_{probe}) = \sum_n c_n(t)\sigma_n(\lambda_{probe}) \text{ (SE10)}$$

$$\frac{dc1(t)}{dt} = I_0 - k_1c_1(t) \text{ (SE11)}$$

$$\frac{dcn(t)}{dt} = k_{n-1}c_{n-1}(t) - k_nc_n(t),\ n > 1 \text{ (SE12)}$$

Here, the set of SADS, $\{\sigma_n(\lambda_{probe})\}$, represent spectroscopically distinct configurations of the system that include singlet and triplet excited states of the BODIPY molecules we examine. I_0 describes the photoexcited population prepared by the excitation pulse while the set of rate constants, $\{k_n(t)\}$, describe the exchange of this population between the configurations associated with each $\sigma_n(\lambda_{probe})$. TA spectra of **Mes-Cl** and **Mes-Br** show similar spectral evolution, albeit with lower ISC rates (**Table 1**). Following ISC, the T_1 states of **Mes-I**, **Mes-Br**, and **Mes-Cl** display similar excited state lifetimes of 370 ns. In contrast, no evidence for T_1 state formation is seen for **Mes-H**, which returns directly from the S_1 state to its ground state over the course of a few nanoseconds. Importantly, the comparable rates for ISC and S_1 relaxation to the ground state for **Mes-Br** and **Mes-**

Cl indicate these two processes compete with one another following photoexcitation. Based on the ratio of time constants measured for these processes, we estimate 35% of photoexcited **Mes-Br** molecules successfully intersystem cross to their T_1 state while the triplet yield is even lower for **Mes-Cl**, 17%. In contrast, the fast ISC rate of **Mes-I** ensures that the majority of its photoexcited population (89%) convert to its T_1 state. We ascribe the observed enhancement in photopolymerization rate in moving from **Mes-H** to **Mes-I** to this difference in triplet production yield. As photopolymerization requires the diffusive encounter of a photoexcited Mes-BODIPY molecule and an electron donor or acceptor, the longer lifetime of the Mes-BODIPY T_1 state increases the likelihood that a photoexcited molecule will encounter a suitable partner before it deactivates to the ground state. The increased triplet production yield of **Mes-I** over those of **Mes-Cl** and **Mes-Br** ensures more photoexcitation events will result in triplet formation, thereby increasing the rate of photopolymerization.

To test the limits of photopolymerization, light intensity and catalyst loading were independently decreased for **Mes-I** under green light (**Figure 1.15**) until it took ~60 s to reach maximum conversion. Impressively, using the optimized formulations, light intensities of 0.01 mW/cm^2 corresponding to an absorbed photon flux of 0.3×10^{13} cm^{-2}s^{-1}, were found to be the lower bounds for green irradiation **(Figure 1.15a**). For context, the light intensity emitted at the screen of an iPhone 8 was measured to be ~0.1 mW/cm^2 at full brightness. Using an intensity of 16 mW/cm^2, lower limits of 0.001 mol % (= 47 μM) catalyst loading, corresponding to an absorbed photon flux of 4.2×10^{13} cm^{-2}s^{-1}, were found for **Mes-I** (**Figure 1.15b**). Therefore, rapid photopolymerization can be achieved with extremely low irradiation intensity or catalyst loading, which is conducive to a variety of applications and ultimately will save on energy and/or material costs. Additional intensity sweep measurements with the 530 nm LED were conducted for the

Mes-X series as another testament of efficiency and can be seen in **Figure 1.16** and **Figure 1.17**. Halogenation of the photocatalyst maintains rapid polymerization rates at lower and lower light intensities with **Mes-Cl** at 0.4 mW/cm^2 and both **Mes-Br** and **Mes-I** at 0.01 mW/cm^2.

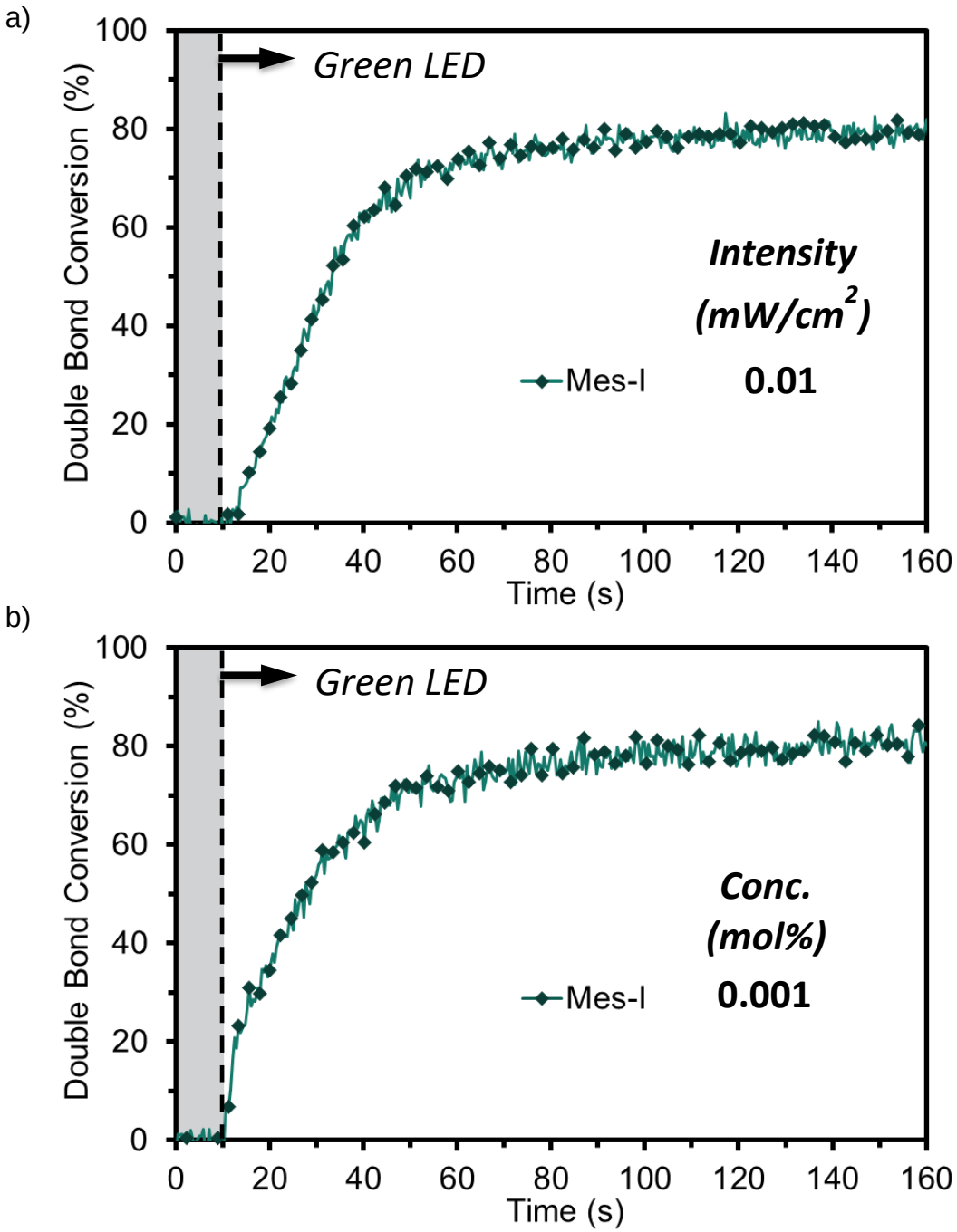

Figure 1.15: Photopolymerization Limits for **Mes-I** Under Green (530 nm) Irradiation, While Maintaining Near Complete Conversion Within ~60 s. Minimum (a) Exposure Intensity and (b) Photosensitizer Concentration

a)

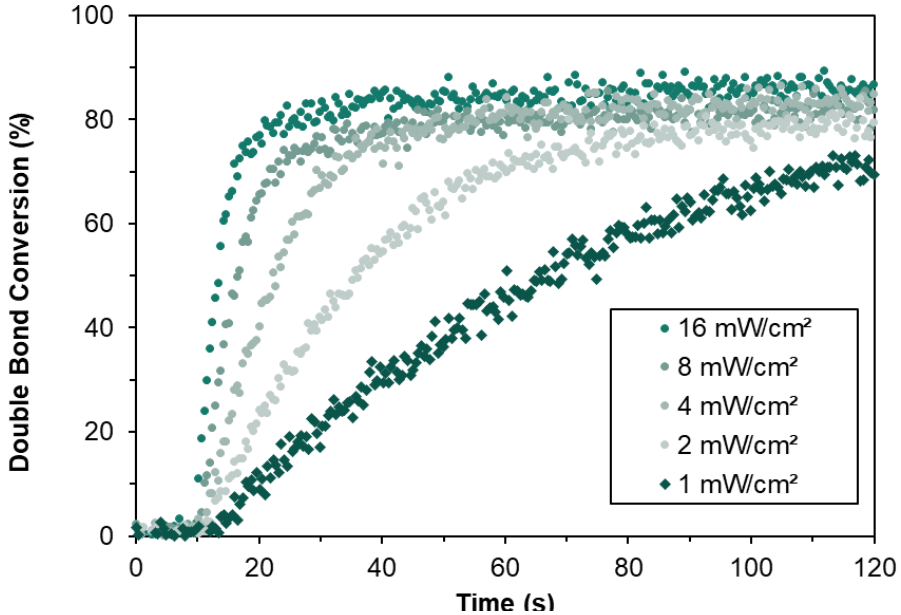

b)

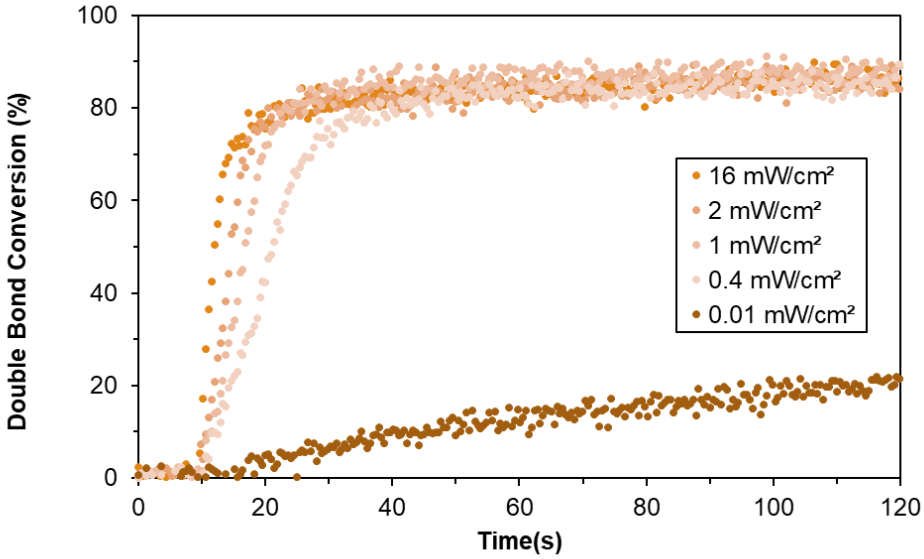

Figure 1.16: (a) Photopolymerization of Isobornyl Acrylate with **Mes-H** and a 530 nm LED At Varying Intensities Using the Optimized Resin Formulation. (b) Photopolymerization of Isobornyl Acrylate with **Mes-Cl** and a 530 nm LED At Varying Intensities Using the Optimized Resin Formulation.

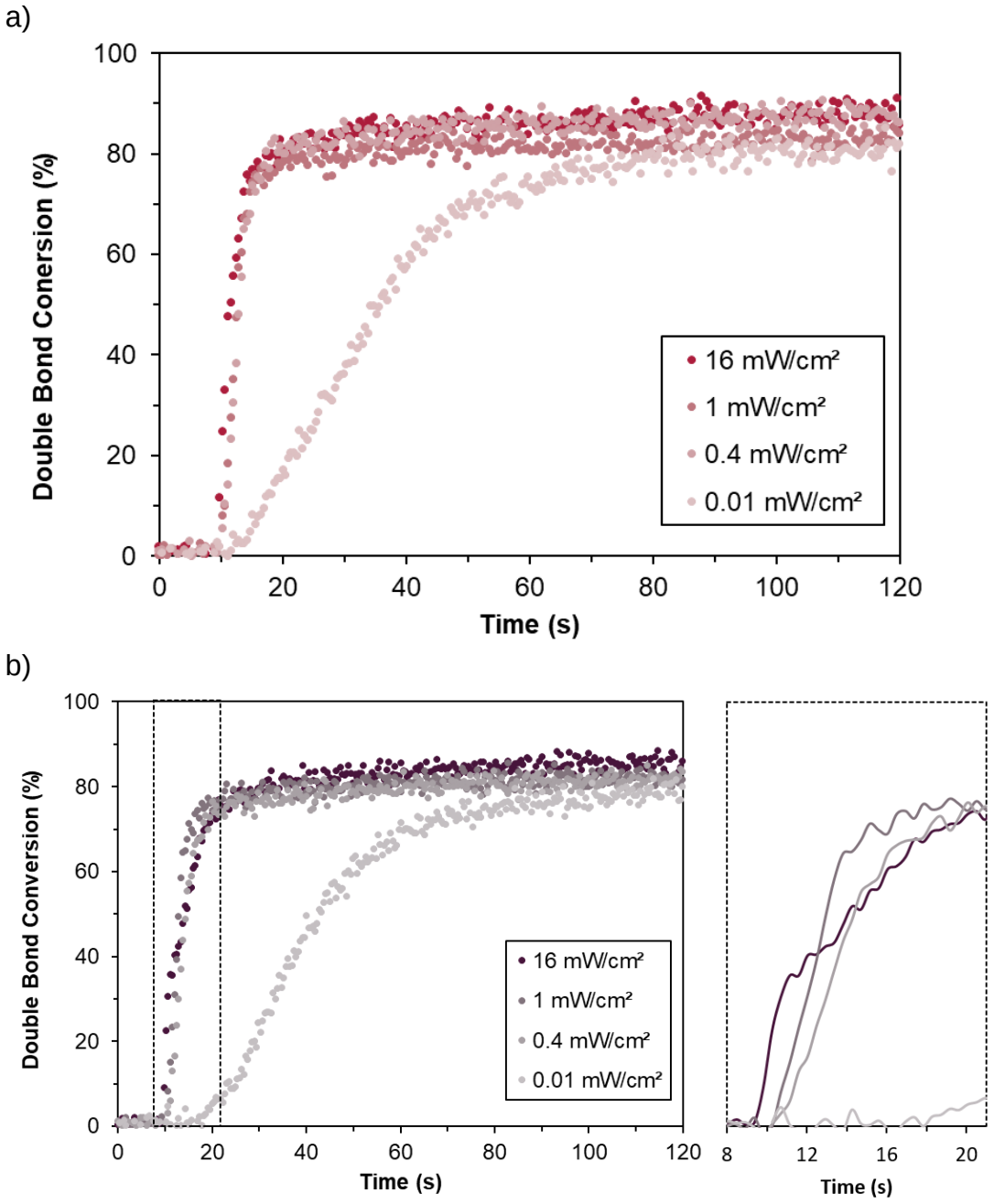

Figure 1.17: (a) Photopolymerization of Isobornyl Acrylate with **Mes-Br** and a 530 nm LED At Varying Intensities Using the Optimized Resin Formulation. (b) Photopolymerization of Isobornyl Acrylate with **Mes-I** and a 530 nm LED At Varying Intensities Using the Optimized Resin Formulation.

As a final demonstration, rapid high resolution DLP 3D printing with visible light was performed using **Mes-Br** at 530 nm (~1.8 mW/cm^2). The selected photocurable resin comprised the same photosystem components described above and replaced isobornyl acrylate with *N*,*N*-dimethyl acrylamide and trimethylolpropane triacrylate as the monomer and cross-linker in a 4:1 ratio, respectively, which was found to provide a good combination of solubility and little adhesion to the resin vat during prints. To ensure homogeneity the samples were vigorously mixed using a Vortex mixer, followed by sonication for 10 min. Prior to printing the resins were sparged with nitrogen gas, and 3D printing was conducted under a nitrogen atmosphere to prevent oxygen inhibition. **Figure 1.18** shows digital and scanning electron microscopy images for a complex 3D printed structure with custom form factors, namely an octet-truss lattice. Notably, the final part is photoluminescent, indicating that some amount of the BODIPY chromophore remains intact (e.g., incomplete bleaching) (**Figure 1.18b**). The selected layer thickness was 25 μm (measured to be 25.5 ± 1.3 μm by SEM), and an exposure time of 10 s/layer was found to provide good resolution. This exposure time correlates to a fast build rate of 9 mm/h (without recoating process), competing with state-of-the-art DLP 3D printers on the market that rely on high energy UV to violet light (~385–405 nm) for photocuring.[28]

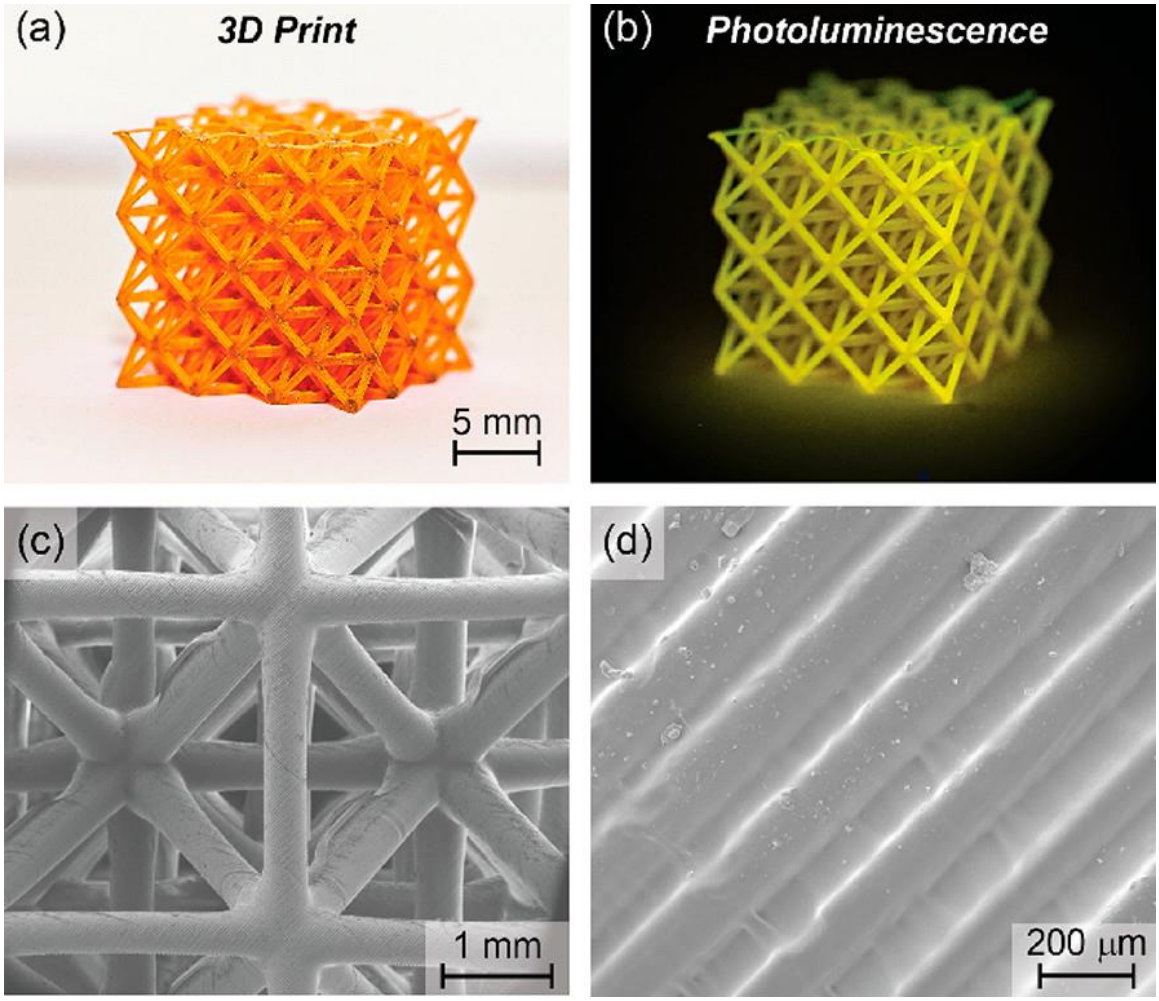

Figure 1.18: Rapid High Resolution Digital Light Processing (DLP) 3D Print of a Hierarchical Octet-Truss Lattice Using **Mes-Br** as the Photosensitizer and a Green LED Centered at 530 nm as the Projection Source. Photographs Under Room Light (a) and Hand-Held UV Light (b). (c, d) Scanning Electron Microscopy Images at Different Magnifications, Showing High Resolution Features.

1.3: EXPERIMENTAL

1.31: MATERIALS

Chemicals: 2,4-Dimethyl-1H-pyrrole 97% and 1-chloropyrrolidine-2,5-dione (NCS) 97% were purchased from Ark Pharm. 2,4,6-trimethyl-benzaldehyde 97%, dichloromethane (DCM) 99.9%, anhydrous, potassium hydroxide (KOH) (certified ACS), methanol (MeOH) (certified ACS), and toluene (Certified ACS) were purchased from Fisher Scientific. Trifluoroacetic acid (TFA) >99.9%, 2,3-dichloro-5,6-dicyano-1,4-benzoquinone (DDQ) 99.15%, N-bromosuccinimide (NBS) 99.98% were purchased from Chem-Impex. Triethylamine ≥99.5%, 3,4,5-trimethoxybenzaldehyde 98%, and Uvasol® acetonitrile for spectroscopy was purchased were purchased from Sigma-Aldrich. Boron trifluoride diethyl etherate 98% was purchased from Oakwood Chemical. Niodosuccinimide (NIS) was purchased from Combi-Blocks. 4'-tert-butylacetophenone 95% was purchased from Matrix Scientific. Nitromethane >98% was purchased from TCI Chemicals. Ammonium acetate ≥97.0% was purchased from Alfa Aesar. Rhodamine 6G, 99%, pure, laser grade, was purchased from ACROS Organics. H-Nu 254, Onium Salt and Borate V were purchased from Spectra Group Limited, Inc. $CDCl_3$ 99.8% was purchased from Cambridge Isotope Laboratories. All chemicals were used as received without additional purification, unless otherwise noted.

1.32: EQUIPMENT AND INSTRUMENTATION

Nuclear Magnetic Resonance (NMR) Spectroscopy

NMR spectra were recorded on an Agilent MR 400 MHz spectrometer utilizing $CDCl_3$ as the solvent. ^{1}H NMR were carried out coupled and referenced to the $CDCl_3$ chemical shift at 7.26 ppm. ^{13}C NMR were carried out decoupled and referenced to the $CDCl_3$ chemical shift at 77.16 ppm.

High Resolution Mass Spectrometry (HRMS)

HRMS was performed on an Agilent Technologies 6530 Accurate-Mass Q-TOF LC/MS using ESI and the data was subsequently analyzed using Agilent MassHunter Qualitative Analysis Software.

Real-Time Fourier-Transform Infrared Spectroscopy (RT-FTIR)

RT-FTIR was recorded utilizing an INVENIO-R FT-IR Spectrometer from Bruker (**Figure 1.19**) and controlled via OPUS Spectroscopy Software. A liquid nitrogen cooled (LN-MCT Mid) detector was used for measurements. A modified GladiATR Illuminate ATR accessory[14] from PIKE Technologies was used to analyze chemical composition and monitor photocuring of liquid resins upon exposure to light. Collimated LED light source 530 nm-P/N LCS-0530-15-22 from Mightex Systems along with Lightguide Adapters were utilized to irradiate resins with visible light (see photopolymerization procedure for more details). LED Controller M/N SLC-MA02-U was used with a 3 mm liquid light guide (LLG-3- 4H).

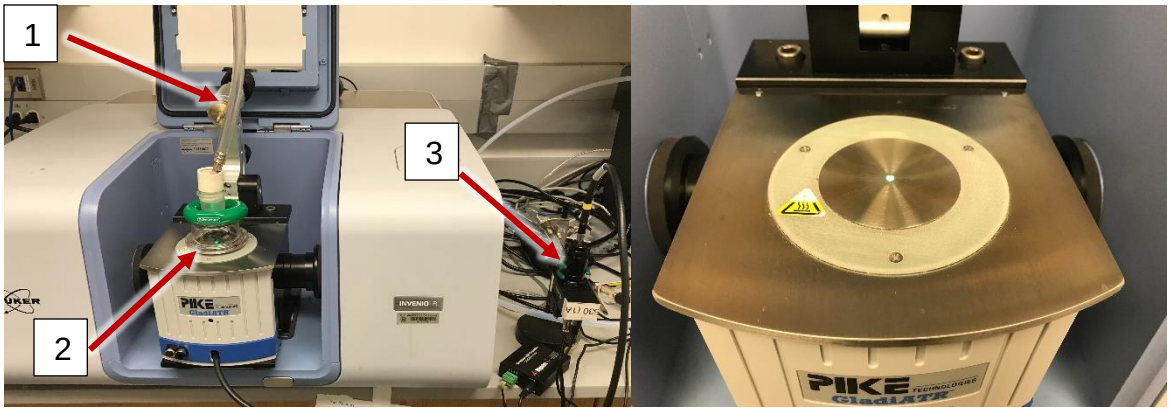

Figure 1.19: Photo-ATR FTIR Setup (1) Argon/Nitrogen Gas Line (2) Custom Glass Top With O-Ring to Create Oxygen Free Atmosphere (3) LED and Liquid Light Guide. Close-Up Image of Custom ATR Accessory With Green LED On.

1.33: STEADY-STATE OPTICAL CHARACTERIZATION

UV-visible absorption spectra were recorded on an Ocean Optics QE PRO-ABS Fiber Optic Spectrometer utilizing deuterium-tungsten halogen light sources (DH-2000-BAL). 600 μm fiberoptic cables (QP600-025-SR) were coupled to the detector with a slit width of 5 μm. Dilute absorption data was collected in acetonitrile utilizing quartz cuvettes and a qpod sample holder (QNW qpod2e).

1.34: THIN-FILM ABSORPTION

The absorption data for the BODIPY dyes was acquired using the following general resin formulation: 0.1 mol% BODIPY, 0.1 mol% Borate V (Donor), and 1.0 mol% H-Nu 254 (Acceptor) to more accurately represent the conditions used during photopolymerization measurements. Plastic shims were used as spacers to create a gap of known thickness between two glass slides. Due to the high extinction coefficient of the BODIPY dyes the samples were measured within a thickness range from 13-100 μm on an Ocean Optics Stage RTL-T. All absorption data was collected within the limits of Beer's Law with respect to the max emission peak for each corresponding LED (i.e., 530 nm for the green LED). The extinction coefficient values determined from this data were used to calculate the number of equivalent photons between samples to normalize the number of photons absorbed.

1.35: TRANSIENT ABSORPTION CHARACTERIZATION

Femtosecond time-resolved experiments: Transient absorption (TA) spectra that monitored photoexcited sample dynamics on femtosecond to sub-nanosecond timescales were performed using an experimental layout described in prior work.[29,30] Briefly, excitation and probe pulses were derived from the output of a Ti:sapphire regenerative amplifier (Coherent Legend Elite Duo: 3 kHz repetition rate, ~4.2 mJ, ~90 fs). Excitation pulses centered at 525 nm used to photoexcite Mes-BODIPY derivatives were produced

by using the Ti:sapphire laser to pump a home-built noncollinear optical parametric amplifier (NOPA). Spectrally-broad probe pulses (450 – 800 nm) were derived via self-phase modulation by focusing a small portion of the Ti:sapphire output into a 3 mm thick c-cut sapphire window. A computer controlled optical delay stage (Newport ILS300LM) was used to scan the time of arrival of the probe at the sample with respect to the pump. Pump-induced changes in probe transmission through each sample solution were detected using a Si CCD (Princeton Instruments, PyLoN 100BR) interfaced with a Czerny-Turner spectrometer (Acton Instruments SP-2556). Sample solutions were prepared by dissolving dry powder of each compound in acetonitrile. Sample solutions were housed in 1 mm path length quartz cuvettes and degassed using nitrogen prior to experiments. Nanosecond time-resolved experiments: For experiments that probed the photoexcited dynamics of **Mes-Cl**, **Mes-Br**, and **Mes-I** over nanosecond-to-microsecond timescales, the probe pulse and generation and detection setup was identical to that used for femtosecond resolution experiments. However, the excitation pulse was replaced by the frequency-doubled output of a Q-switched Nd:YAG laser (Alphalas Pulselas-A: 532 nm, <1 ns, 8.7 μJ). Scanning of the time delay between the pump and probe was achieved by using an electronic delay generator (Stanford Research Systems DG535) to synchronize the operation of the Ti:sapphire and Q-switched Nd:YAG lasers.

1.36: FLUORESCENCE MEASUREMENTS

All fluorescence measurements were recorded on an Agilent Cary Eclipse Fluorescence Spectrophotometer. The fluorometer is equipped with a Unique Agilent Xenon flash lamp (190 nm – 1100 nm) as the light source, and a high performance R928 photomultiplier (PMT) (200 nm – 900 nm) detector. The sensitivity of this system is >4000:1 RMS (350 nm) and >1400:1 RMS (500 nm) after the calibration.

1.37: ELECTRONIC CHARACTERIZATION

Cyclic voltammetry (CV) was performed in an argon-filled MBraun glovebox using the CHI 660D Electrochemistry Workstation housed within the Center for Electrochemistry at The University of Texas at Austin. A single-compartment three-electrode cell was used with glassy carbon as the working electrode, a platinum wire as the counter electrode, and an $Ag/AgNO_3$ (0.01 M) nonaqueous reference electrode calibrated versus Fc/Fc^+ in 0.1 M tetrabutylammonium hexafluorophosphate ($TBAPF_6$) acetonitrile solutions ($E½(Fc/Fc^+)$ = 0.1 V vs Ag/Ag^+) with a 0.1 V/s scan rate. Oxidation onsets were utilized to calculate the highest occupied molecular orbital (HOMO) energy levels -(4.8 eV $–E_{ox}$ (Ferrocene) + E_{ox}) and reduction onsets to calculate the lowest unoccupied molecular orbital (LUMO) energy levels -(4.8 eV $–E_{ox}$ (Ferrocene) + E_{red})[31].

1.38: LED LIGHT SOURCES

All LEDs used were purchased from Mightex Systems. The emission profile for each LED was measured using a calibrated UV-Vis Ocean Insight system. Irradiation intensities were measured with a Thorlabs PM100D photometer equipped with a silicon-based photodiode power sensor (S120VC, Thorlabs). Emission profiles were recorded with a QE pro spectrometer, in which the LED was connected to the fiber optic system using a 3 mm liquid lightguide from Mightex Systems (serial #: LLG-03-59-340-0800-1).

1.39: 3D PRINTER

3D printing was performed using a custom, digital light processing (DLP) 3D printer (Monoprinter, MA, USA) (**Figure 1.20**). The printer was equipped with a green LED (Luminus PT-120-G) that has a peak emission wavelength at 525 nm. The light intensity measured at the resin vat floor was ~1.8 mW/cm^2, which was used for all prints in this study. Custom software (MonoWare) was used to import STL design files and digitally slice them into a sequence of 2D image files for projection. The projector resolution was

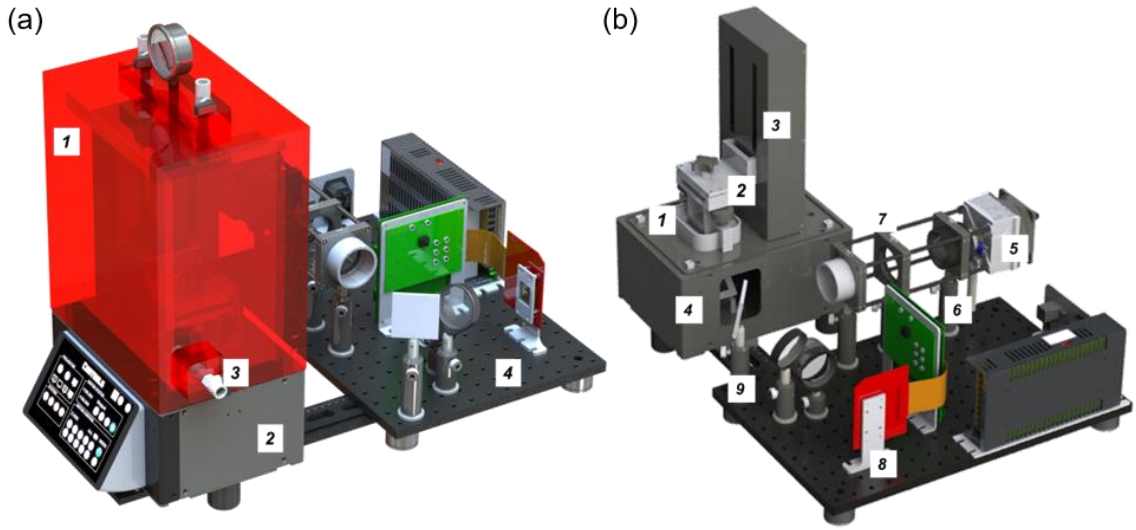

Figure 1.20: (a) 3D printer With Acrylic Housing for Inert Gas Purging. Components: (1) N2 Chamber, (2) DLD 3D Printer, (3) N_2 Inlet, and (4) Visible LEDs Projector. (b) 3D Printer Without Acrylic Housing. Mechanical Components: (1) Resin Vat, (2) Build Platform, (3) Arduino Stage. Optical Components: (4) Mirror, (5) LED With Heat Sink, (6) Collimation Lens, (7) Diffuser, (8) Digital Mirror Device (DMD), and (9) Mirror.

1920 × 1080 pixels, with each pixel being 20 µm × 20 µm at the image plane. The maximum build plane for the printer in its current configuration is 38.4 mm × 21.6 mm, and a vat with the dimensions of 56 mm × 35 mm × 25 mm (length × width × height) was used. A transparent fluorinated polymer film (Teflon FEP film, DuPont, 127 µm thick) was used as the base of the resin tank to provide a non-stick and flexible surface. The octet truss model was selected to demonstrate the utility of BODIPY photocatalysts in rapid high resolution visible light 3D printing. The predetermined layer thickness for each slice of the 3D print was 25 µm, with an exposure time of 12 s for the first layer and 10 s for all subsequent layers. An opaque acrylic chamber containing a nitrogen inlet near the resin vat and an outlet at the top of the housing facilitated a light purge with nitrogen during the print to minimize oxygen inhibition. After completion of the 3D print, the

printed object was post-cured for 10 minutes using a UV nail lamp (JH-818, Junhao) with a maximum emission wavelength at 370 nm and an average intensity of 4.3 mW/cm^2.

1.310: SCANNING ELECTRON MICROSCOPE (SEM)

SEM (Fei Quanta 650, ThermoFisher) was used to examine the surface characteristics of the 3D printed octet truss and measure the average layer thickness (25.5 ± 1.3 μm). For improved imaging, the sample was sputtered with Au using an EMS sputter coater (Electron Microscopy Science). Sputtering was conducted for 1.5 min at 40 mA.

1.311: SYNTHESIS

The syntheses of Mes-BODIPY derivatives were accomplished in an analogous fashion to that previously reported in literature.[32,33]

5,5-difluoro-10-mesityl-1,3,7,9-tetramethyl-5H-4l4,5l4-dipyrrolo[1,2-c:2',1'-f][1,3,2]diazaborinine (**Mes-H**).

2,4-dimethyl-1H-pyrrole (1.18 g, 1.28 mL, 1 Eq, 12.4 mmol) was added to 250 mL of DCM in a dry 500 mL 2-neck round bottom flask in a nitrogen filled glovebox. 2,4,6-trimethylbenzaldehyde (0.73 g, .73 mL, 0.40 Eq, 5.0 mmol) was added to the solution. The round bottom was removed from the glovebox and placed under N_2. 50 μL of TFA in 2.5 mL of dry DCM was added slowly to the reaction flask while stirring and after complete addition the reaction was stirred for 3 hr. The reaction was monitored via thin layer chromatography (TLC) (1:1 DCM:hexane). After reaction completion, the round bottom was placed in an ice bath and 1.13 g of DDQ (0.40 Eq, 5.0 mmol) was added to the flask and stirred for 10 min while on ice then 1 hr at room temp. 10 mL of NEt_3 (5.8 Eq, 72 mmol) was added to the reaction mixture and stirred for 10 min. 10 mL of BF_3•OEt_2 (6.5 Eq, 81 mmol) was added slowly to the reaction flask and stirred for 2 hr. Crude product was washed with sat. Na_2CO_3 (3 x 50mL) and the organic layer subsequently dried with anh. $MgSO_4$, filtered, concentrated under reduced pressure using

rotary evaporation, and purified via column chromatography (1:1 DCM:hexane) to yield the desired product as an orange solid (1.170 g, 65%). ^{1}H NMR (400 MHz, CDCl3) δ 6.94 (s, 2H), 5.96 (s, 2H), 2.56 (s, 6H), 2.33 (s, 3H), 2.09 (s, 6H), 1.38 (s, 6H); ^{13}C NMR (100 MHz, CDCl3) δ 155.0, 142.3, 141.6, 138.5, 134.9, 131.1, 130.6, 128.9, 120.8, 21.2, 19.5, 14.6, 13.4; IR (ATR): 2950, 2918, 2858, 1537, 1501, 1463, 1435, 1406, 1362, 1303, 1187, 1152, 1122, 1103, 1083, 1061, 1046, 970, 702 cm^{-1} ; HRMS (ESI): exact mass calculated for $C_{22}H_{25}BF_2N_2$ [M+Na] + 389.1976, found 389.1980

2,8-dichloro-5,5-difluoro-10-mesityl-1,3,7,9-tetramethyl-5H-4l4,5l4-dipyrrolo[1,2-c:2',1'- f][1,3,2]diazaborinine (**Mes-Cl**).

5,5-difluoro-10-mesityl-1,3,7,9-tetramethyl-5H-4l4,5l4-dipyrrolo[1,2-c:2',1'-f][1,3,2]diazaborinine (Mes-H) (100 mg, 1 Eq, 273 µmol) was dissolved in 10 mL of dry DCM in a 100 mL 2-neck round bottom. 1-chloropyrrolidine-2,5-dione (80.2 mg, 2.2 Eq, 601 µmol) in 5 mL of DCM was added to the flask under N_2 at room temp. The reaction was monitored via TLC (1:1 DCM:hexane) until completion. The crude product was washed with 1 M NaOH (3 x 10mL) and the organic layer was subsequently dried with anh. $MgSO_4$, filtered, concentrated under reduced pressure using rotary evaporation, and purified via column chromatography (1:1 DCM:hexane) to yield the desired product as a red-orange solid (69 mg, 58%). ^{1}H NMR (400 MHz, CDCl3) δ 6.97 (s, 2H), 2.58 (s, 6H), 2.35 (s, 3H), 2.07 (s, 6H), 1.37 (s, 6H); ^{13}C NMR (100 MHz, CDCl3) δ 152.3, 142.8, 139.4, 137.3, 134.9, 130.4, 129.4, 129.0, 122.3, 21.4, 19.6, 12.6, 11.0; IR (ATR): 2962, 2922, 2852, 1531, 1500, 1466, 1405, 1382, 1350, 1309, 1166, 1122, 1085, 1062, 994, 923, 774, 702, 604 cm^{-1} ; HRMS (ESI): exact mass calculated for $C_{22}H_{23}BCl_2F_2N_2$ [M+Na]+ 457.1196, found 457.1202

2,8-dibromo-5,5-difluoro-10-mesityl-1,3,7,9-tetramethyl-5H-4l4,5l4-dipyrrolo[1,2-c:2',1'- f][1,3,2]diazaborinine (**Mes-Br**).

5,5-difluoro-10-mesityl-1,3,7,9-tetramethyl-5H-4l4,5l4-dipyrrolo[1,2-c:2',1'-f][1,3,2]diazaborinine (Mes-H) (200 mg, 1 Eq, 0.27 mmol) was dissolved in 20 mL of dry DCM in a 100 mL 2-neck round bottom. NBS (214 mg, 2.2 Eq, 1.20 mmol) in 5 mL of dry DCM was added to the flask under N_2 at room temp. The reaction was monitored via TLC (1:1 DCM:hexane). The crude product was washed with 1 M NaOH (3 x 10mL), and the organic layer was dried with anh. $MgSO_4$, filtered, concentrated under reduced pressure using rotary evaporation, and purified via column chromatography (1:1 DCM:hexane) to yield the desired product as a red solid (150mg, 52%). ^{1}H NMR (400 MHz, CDCl3) δ 6.98 (s, 2H), 2.61 (s, 6H), 2.36 (s, 3H), 2.07 (s, 6H), 1.38 (s, 6H); ^{13}C NMR (100 MHz, CDCl3) δ 153.6, 142.4, 139.8, 139.3, 134.8, 130.5, 129.6, 129.3, 111.4, 21.2, 19.5, 13.7, 12.6; IR (ATR): 2956, 2919, 2854, 1529, 1462, 1400, 1383, 1345, 1314, 1175, 1118, 1099, 1084, 1060, 996, 851, 774, 701, 592 cm^{-1} ; HRMS (ESI): exact mass calculated for $C_{22}H_{23}BBr_2F_2N_2$ [M+Na]+ 545.0186, found 545.0189

5,5-difluoro-2,8-diiodo-10-mesityl-1,3,7,9-tetramethyl-5H-4l4,5l4-dipyrrolo[1,2-c:2',1'- f][1,3,2]diazaborinine (**Mes-I**).

5,5-difluoro-10-mesityl-1,3,7,9-tetramethyl-5H-4l4,5l4-dipyrrolo[1,2-c:2',1'f][1,3,2]diazaborinine (Mes-H) (100 mg, 1 Eq, 273 µmol) was dissolved in 10 mL of DCM in a 100 mL 2-neck round bottom. NIS (135 mg, 2.2 Eq, 601 µmol) in 10 mL of methanol was added to the flask under N_2 at room temp. The reaction was monitored via TLC (1:1 DCM:hexane). The crude product was washed with 1 M NaOH (3 x 10mL) and the organic layer was dried with anh. $MgSO_4$, filtered, concentrated under reduced pressure using rotary evaporation, and purified via column chromatography (1:1 DCM:hexane) to yield the desired product as a purple solid (110 mg, 65%).^{1}H NMR (400 MHz, CDCl3) δ 6.97 (s, 2H), 2.65 (s, 6H), 2.36 (s, 3H), 2.06 (s, 6H), 1.40 (s, 6H); ^{13}C NMR (100 MHz, CDCl3) δ 156.4, 144.6, 141.7, 139.3, 134.8, 130.8, 130.5, 129.3, 85.3,

21.2, 19.5, 16.0, 15.8; IR (ATR): 2953, 2917, 2852, 1519, 1475, 1455, 1397, 1340, 1308, 1176, 1135, 1115, 1092, 1080, 993, 850, 775, 701, 586 cm^{-1} ; HRMS (ESI): exact mass calculated for $C_{22}H_{23}BF_2I_2N_2$ [M+Na]+ 640.9909, found 640.9908

1.312: CHARACTERIZATION

^{1}H NMR Spectra

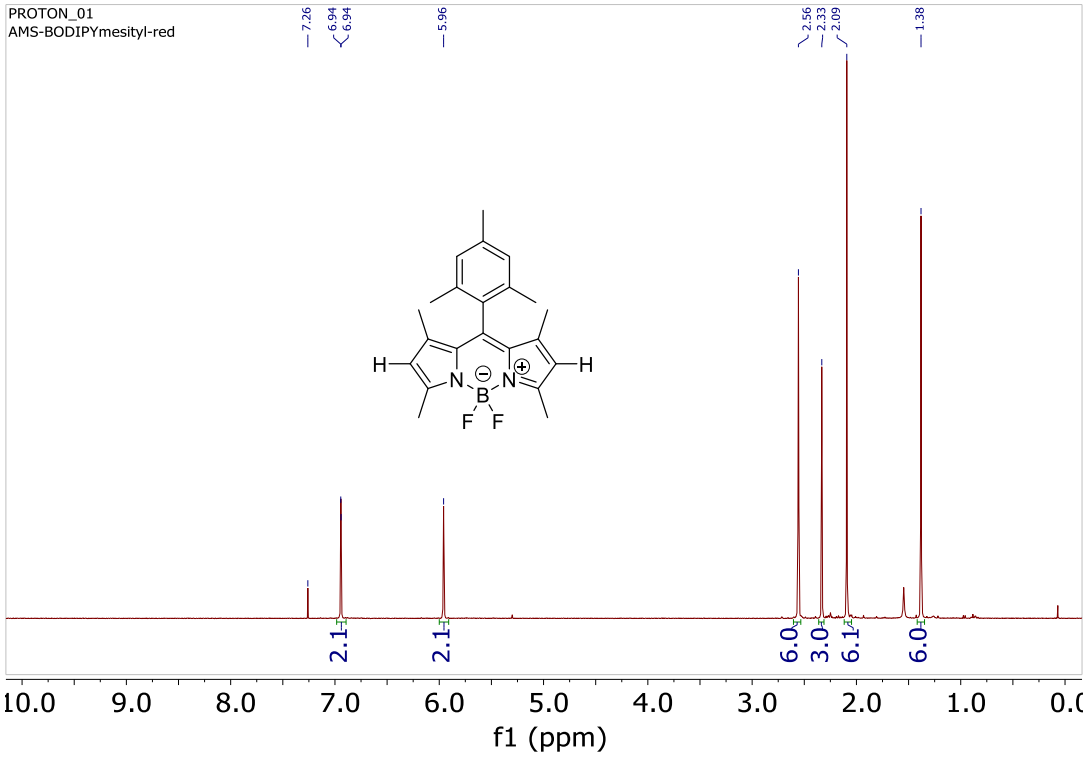

Figure 1.21: ^{1}H NMR of **Mes-H** (S1) BODIPY in $CDCl_3$

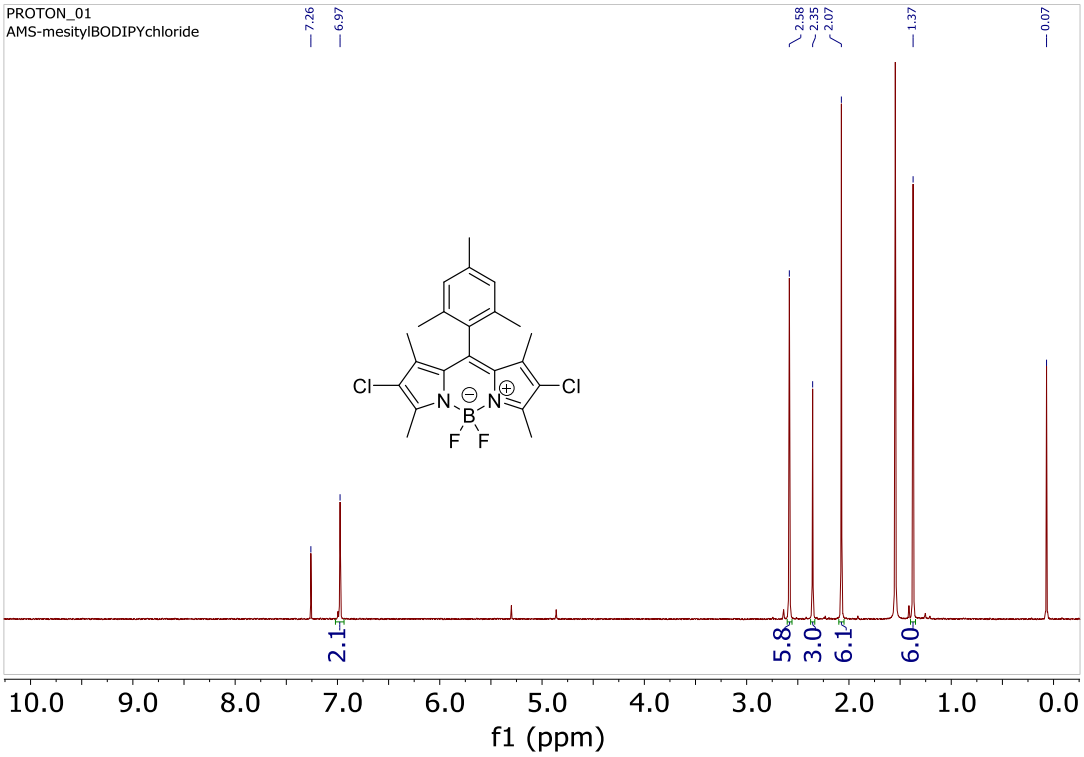

Figure 1.22: ^{1}H NMR of **Mes-Cl** (S2) BODIPY in $CDCl_3$

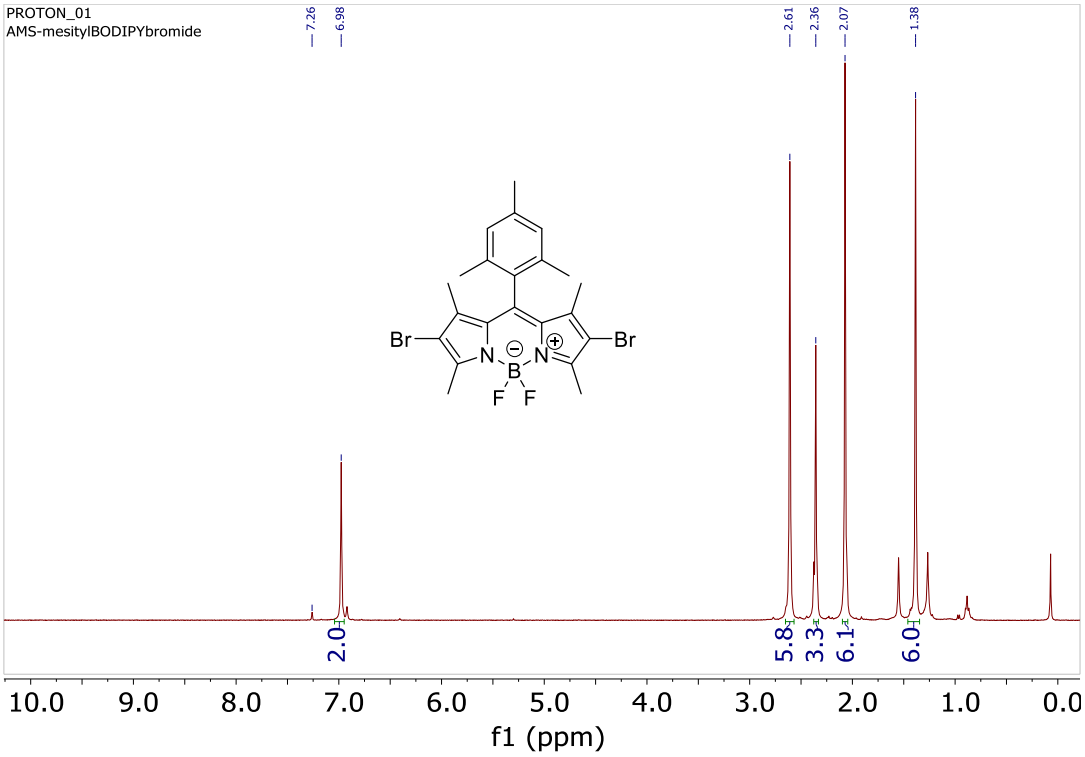

Figure 1.23: ^{1}H NMR of **Mes-Br** (S3) BODIPY in $CDCl_3$

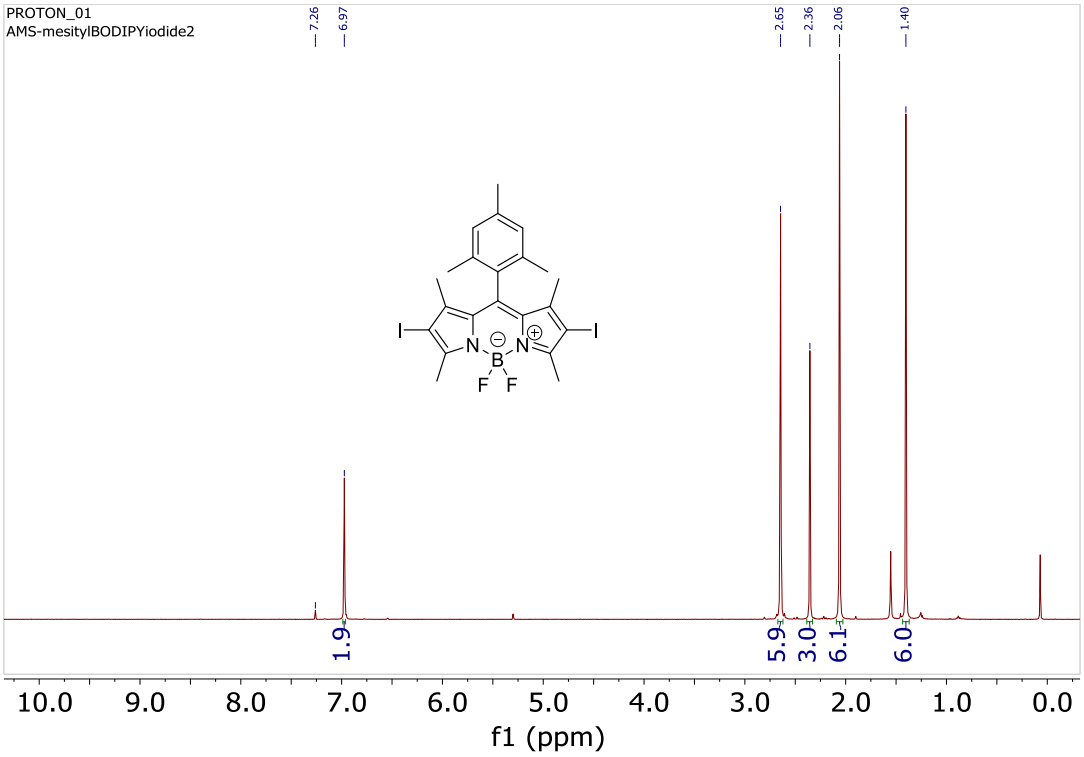

Figure 1.24: ^{1}H NMR of **Mes-I** (S4) BODIPY in $CDCl_3$

1.4: CONCLUSION

Halogenation of BODIPY dyes was demonstrated to be an effective strategy to improve the efficiency of light-driven polymerizations. Systematic kinetic and optoelectronic characterizations of a series of halogenated BODIPY derivatives unveiled critical structure property insights for the explanation of observable efficiency enhancement. Real time ATR-FTIR with custom bottom-up irradiation was used to quantitatively characterize polymerization rate, showing that halogenation of BODIPY dyes with either mesityl or nitrogen functionality at the meso bridgehead position resulted in 5–8× higher polymerization rates upon exposure to green light. Fluorescence quenching studies suggested that electron donation into the photoexcited BODIPY dyes (i.e., reductive quenching) was the primary mechanistic pathway for radical generation. This mechanism was also supported by a larger energetic driving force identified from cyclic voltammetry and density functional theory. Transient absorption spectroscopy confirmed that the presence of "heavy atoms" (e.g., halogens) results in faster intersystem crossing rates, which corresponds to higher triplet yields and longer excited state lifetimes. In turn, the longer lifetimes improve photocatalytic efficiency by increasing the number of collisions that occur per photon absorbed between BODIPY in the excited state and an initiator. Furthermore, the halogenated BODIPY derivatives were shown to provide unprecedented photopolymerization rates (complete conversion within ~60 s) given extremely low catalyst loadings (~0.001 mol %) or light intensities (~0.01 mW/cm^2 green light). The rapid kinetics were exploited for high resolution DLP 3D printing using a low-energy green LED. These results are particularly exciting to inform the future development of more efficient far-red and NIR photoredox catalysts that absorb between 700-780 nm and beyond 780 nm, respectively, which can extend the

utility of photopolymers to include the formation of strong and lightweight hybrid composites and biocompatible tissue scaffolds.

1.5: REFERENCES

(1) Lu, H.; MacK, J.; Yang, Y.; Shen, Z. Structural Modification Strategies for the Rational Design of Red/NIR Region BODIPYs. *Chem. Soc. Rev*. **2014**, *43* (13), 4778−4823.

(2) Loudet, A.; Burgess, K. BODIPY Dyes and Their Derivatives: Syntheses and Spectroscopic Properties. *Chem. Rev*. **2007**, *107* (11), 4891−4932.

(3) L. Thompson, B.; Heiden, Z. Redox Chemistry of BODIPY Dyes. In BODIPY Dyes - A Privilege Molecular Scaffold with Tunable Properties; **2019**.

(4) Bonardi, A.; Bonardi, F.; Noirbent, G.; Dumur, F.; Dietlin, C.; Gigmes, D.; Fouassier, J. P.; Lalevee, J. Different NIR Dye Scaffolds´ for Polymerization Reactions under NIR Light. *Polym. Chem*. **2019**, *10* (47), 6505−6514.

(5) Telitel, S.; Blanchard, N.; Schweizer, S.; Morlet-Savary, F.; Graff, B.; Fouassier, J. P.; Lalevee, J. BODIPY Derivatives and Boranil´ as New Photoinitiating Systems of Cationic Polymerization Exhibiting a Tunable Absorption in the 400−600 Nm Spectral Range. *Polymer*. **2013**, *54* (8), 2071−2076.

(6) Telitel, S.; Lalevee, J.; Blanchard, N.; Kavalli, T.; Tehfe, M. A.;´ Schweizer, S.; Morlet-Savary, F.; Graff, B.; Fouassier, J. P. Photopolymerization of Cationic Monomers and Acrylate/Divinylether Blends under Visible Light Using Pyrromethene Dyes. *Macromolecules*. **2012**, *45* (17), 6864−6868.

(7) Costa, P.; Sandrin, D.; Scaiano, J. C. Real-Time Fluorescence Imaging of a Heterogeneously Catalysed Suzuki−Miyaura Reaction. *Nat. Catal*. **2020**, *3*, 427−437.

(8) Qiu, H.; Gao, Y.; Boott, C. E.; Gould, O. E. C.; Harniman, R. L.; Miles, M. J.; Webb, S. E. D.; Winnik, M. A.; Manners, I. Uniform Patchy and Hollow Rectangular Platelet Micelles from Crystallizable Polymer Blends. *Science* (Washington, DC, U. S.) **2016**, *352* (6286), 697−701.

(9) Haldar, U.; Lee, H. Il. BODIPY-Derived Polymeric Chemosensor Appended with Thiosemicarbazone Units for the Simultaneous Detection and Separation of Hg(II) Ions in Pure Aqueous Media. *ACS Appl. Mater. Interfaces*. **2019**, *11* (14), 13685−13693.

(10) Kamkaew, A.; Lim, S. H.; Lee, H. B.; Kiew, L. V.; Chung, L. Y.; Burgess, K. BODIPY Dyes in Photodynamic Therapy. *Chem. Soc. Rev*. **2013**, *42* (1), 77−88.

(11) Miao, X.; Hu, W.; He, T.; Tao, H.; Wang, Q.; Chen, R.; Jin, L.; Zhao, H.; Lu, X.; Fan, Q.; Huang, W. Deciphering the Intersystem Crossing in Near-Infrared BODIPY Photosensitizers for Highly Efficient Photodynamic Therapy. *Chem. Sci*. **2019**, *10* (10), 3096− 3102.

(12) Zhao, J.; Xu, K.; Yang, W.; Wang, Z.; Zhong, F. The Triplet Excited State of Bodipy: Formation, Modulation and Application. *Chem. Soc. Rev*. **2015**, *44* (24), 8904−8939.

(13) Koziar, J. C.; Cowan, D. O. Photochemical Heavy-Atom Effects. *Acc. Chem. Res*. **1978**, *11*, 334−341.

(14) Allen, M. J.; Page, Z. A. Tracking Photocuring via ATR-FT-IR with Illumination through the ATR Element. Spectrosc. *Appl. Noteb*. **2020**, *35* (2), 78.

(15) Boens, N.; Verbelen, B.; Ortiz, M. J.; Jiao, L.; Dehaen, W. Synthesis of BODIPY Dyes through Postfunctionalization of the Boron Dipyrromethene Core. *Coord. Chem. Rev*. **2019**, *399*, 213024.

(16) Wang, X. F.; Yu, S. S.; Wang, C.; Xue, D.; Xiao, J. BODIPY Catalyzed Amide Synthesis Promoted by BHT and Air under Visible Light. *Org. Biomol. Chem*. **2016**, *14* (29), 7028−7037.

(17) Lovell, L. G.; Berchtold, K. A.; Elliott, J. E.; Lu, H.; Bowman, C. N. Understanding the Kinetics and Network Formation of Dimethacrylate Dental Resins. *Polym. Adv. Technol*. **2001**, *12* (6), 335−345.

(18) Thermal Transitions of Homopolymers: Glass Transition & Melting Point https://www.sigmaaldrich.com/technical-documents/ articles/materials-science/polymer-science/thermal-transitions-ofhomopolymers.html.

(19) Würth, C.; Grabolle, M.; Pauli, J.; Spieles, M.; Resch-Genger, U. Relative and Absolute Determination of Fluorescence Quantum Yields of Transparent Samples. *Nat. Protoc*. **2013**, *8* (8), 1535−1550.

(20) Polykarpov, A. Y.; Neckers, D. C. Tetramethylammonium Phenyltrialkylborates in the Photoinduced Electron Transfer Reaction with Benzophenone. Generation of Alkyl Radicals and Their Addition to Activated Alkenes. *Tetrahedron Lett*. **1995**, *36* (31), 5483−5486.

(21) Romanczyk, P. P.; Kurek, S. S. Reliable Reduction Potentials of Diaryliodonium Cations and Aryl Radicals in Acetonitrile from HighLevel Ab Initio Computations. *Electrochim. Acta*. **2020**, *351*, 136404.

(22) Romanczyk, P. P.; Kurek, S. S. The Reduction Potential of Diphenyliodonium Polymerisation Photoinitiator Is Not − 0.2 V vs. SCE. A Computational Study. *Electrochim. Acta*. **2017**, *255*, 482−485.

(23) Marenich, A. V.; Cramer, C. J.; Truhlar, D. G. Universal Solvation Model Based on Solute Electron Density and on a Continuum Model of the Solvent Defined by the

Bulk Dielectric Constant and Atomic Surface Tensions. *J. Phys. Chem. B*. **2009**, *113* (18), 6378–6396.

(24) Sabatini, R. P.; McCormick, T. M.; Lazarides, T.; Wilson, K. C.; Eisenberg, R.; McCamant, D. W. Intersystem Crossing in Halogenated Bodipy Chromophores Used for Solar Hydrogen Production. *J. Phys. Chem. Lett*. **2011**, *2* (3), 223−227.

(25) Rachford, A. A.; Ziessel, R.; Bura, T.; Retailleau, P.; Castellano, F. N. Boron Dipyrromethene (Bodipy) Phosphorescence Revealed in [Ir(Ppy) 2(Bpy-C - C-Bodipy)]+. *Inorg. Chem*. **2010**, *49* (8), 3730− 3736.

(26) Whited, M. T.; Djurovich, P. I.; Roberts, S. T.; Durrell, A. C.; Schlenker, C. W.; Bradforth, S. E.; Thompson, M. E. Singlet and Triplet Excitation Management in a Bichromophoric Near-InfraredPhosphorescent BODIPY-Benzoporphyrin Platinum Complex. *J. Am. Chem. Soc*. **2011**, *133* (1), 88−96.

(27) Lee, Y.; Malamakal, R. M.; Chenoweth, D. M.; Anna, J. M. Halogen Bonding Facilitates Intersystem Crossing in Iodo-BODIPY Chromophores. *J. Phys. Chem. Lett*. **2020**, *11* (3), 877−884.

(28) Wallin, T. J.; Pikul, J.; Shepherd, R. F. 3D Printing of Soft Robotic Systems. *Nat. Rev. Mater*. **2018**, *3* (6), 84−100.

(29) Le, A. K.; Bender, J. A.; Arias, D. H.; Cotton, D. E.; Johnson, J. C.; Roberts, S. T. Singlet Fission Involves an Interplay between Energetic Driving Force and Electronic Coupling in Perylenediimide Films. *J. Am. Chem. Soc*. **2018**, *140* (2), 814–826.

(30) Azzaro, M. S.; Le, A. K.; Wang, H.; Roberts, S. T. Ligand-Enhanced Energy Transport in Nanocrystal Solids Viewed with Two-Dimensional Electronic Spectroscopy. *J. Phys. Chem. Lett*. **2019**, *10* (18), 5602–5608.

(31) Thorat, K. G.; Kamble, P.; Ray, A. K.; Sekar, N. Novel Pyrromethene Dyes with N-Ethyl Carbazole at the Meso Position: A Comprehensive Photophysical, Lasing, Photostability and TD-DFT Study. *Phys. Chem. Chem. Phys*. **2015**, *17* (26), 17221–17236.

(32) Wang, X. F.; Yu, S. S.; Wang, C.; Xue, D.; Xiao, J. BODIPY Catalyzed Amide Synthesis Promoted by BHT and Air under Visible Light. *Org. Biomol. Chem*. **2016**, *14* (29), 7028–7037.

(33) Lu, H.; MacK, J.; Yang, Y.; Shen, Z. Structural Modification Strategies for the Rational Design of Red/NIR Region BODIPYs. *Chem. Soc. Rev*. **2014**, *43* (13), 4778–4823.

Chapter 2: Aza-BODIPYs as Far-Red and Near-IR Light Photoredox Catalysts

(J. Am. Chem. Soc. 2020, 142, 34, 14733–14742)
(Macromolecules. 2023, XX, XX, XXXX DOI: 10.1021/acs.macromol.3c02004*)*

2.1: INTRODUCTION

The utility of light as an energy source to rapidly convert liquid resins into solid structures has found broad applications in imaging and curing technologies, such as photolithography, adhesives, coatings, and most recently light-based 3D printing (e.g., stereolithography and volumetric printing).[1–4] The rapid growth of photocuring began with photolithography, which has been widely exploited for the development of modern optoelectronics. With the advent of additive manufacturing (3D printing) rapidly changing the industrial fabrication of goods, the same methodologies utilized in photolithography have been extended to light-based 3D printing, which enables some of the shortest build times and smallest resolved features of any 3D printing platform to-date.[5–8] However, contemporary light-based 3D printers rely on high-energy UV light, which limits the scope of materials that can be produced due to pervasive absorption and scattering. For example, UV (<400 nm) light is often incompatible with biomedical applications due to shallow penetration depths through tissue and the risk of cellular damage upon absorption.[9] Thus, photocuring with lower energy visible (400-780 nm) and near infrared (NIR) (≥780 nm) light poses an attractive alternative to UV.

The benefits of photocuring with visible and NIR light include **1**) mild and more cost-effective reaction conditions, **2)** high penetration depth resulting in fast reactions for optimal resolution, **3)** benign conditions for 3D bioprinting, and **4)** enabling spectral control (i.e., the ability to activate discrete chemical pathways with individual wavelengths/colors of light).[10–12] However, as the wavelength of light increases the

energy packed within each photon decreases, which concomittantly reduces the driving force for photocuring and results in longer times to solidification. As a result, the slower reactions have precluded the utility of visible-to-NIR light in the aforementioned applications that require curing in under ~60 seconds for practicality. Although recent progress has been made in improving the efficiency (e.g., speed and sensitivity) of visible-to-NIR photocuring,[13–19] including for use in 3D printing[20–22], novel photocatalyst systems and greater fundamental insight into their design principles are required to consider implementation in commercially relevant photocuring technology.

To place the present work into context, state-of-the-art visible-to-NIR photocuring metrics are detailed below, emphasizing the wavelength and intensity of light used. Photocuring with light at wavelengths ≥500 nm (green light) are highlighted given that photosystems activated in this region operate by photoinduced electron/energy transfer (PET) mechanisms (Type II reactions), in contrast to direct photolysis (Type I reactions) that occur under shorter wavelengths of light (primarily UV). To facilitate (PET), two or three component photosystems are common. These multicomponent photosystems comprise a photocatalyst (PC) and an electron rich donor (D) and/or electron difficient acceptor (A) that act as (co-)initiators to generate reactive radical species upon irradiation with light.

Traditionally, xanthenes and cyanines have dominated the literature for use as green- and red-light activated PCs, respectively.[18,23,24] For example, Lalevée and coworkers[25,26] recently showed that a cyanine-borate salt could be used for rapid polymerization upon exposure to a NIR laser diode (785 nm) at an intensity of 2.55 W/cm^2; ~40 s to reach maximum monomer conversion. For the same NIR laser diode at an intensity of 400 mW/cm^2 they demonstrated polymerizations with squaraine, squarylium, and BODIPY dyes reaching maximum monomer conversion after ~140 s,

~120 s, and ~200 s, respectively. There exists a tradeoff between light intensity and polymerization rate, which prohibits incorporation into modern 3D printing platforms, particularly the economical projection- and display-based printers that offer short build times over large areas yet operate with low light intensities <40 mW/cm^2. In tandem with our work, Allonas and coworkers,[27] synthesized a penta-methine cyanine dye that could achieve NIR photopolymerization within ~10 s at 40 mW/cm^2 using a NIR LED at 850 nm. Unfortunately the solubility of the photocatalyst in the monomer resin was poor and required the addition of DMSO to dissolve but a promising photocatalyst nonetheless.

To combat the photocuring intensity-reactivty paradox we examined in Chaper 1 a unique three component photosystem comprised of halogenated boron dipyromethene (BODIPY) dyes as PCs and a triphenyl(*n*-butyl) borate salt donor and diphenyliodonium salt acceptor.[28] Upon exposure to narrow-band LEDs (~30 nm FWHM) centered at 525 nm (green) a maximum monomer conversion was achieved within ~60 seconds using a light intensity as low as 0.01 mW/cm^2. Critically, the halogens (Br and I) facilitated intersystem crossing (ISC) to a long-lived triplet excited state, which in-turn improved photocuring efficiency. While this enabled rapid visible light photocuring, a photosystem operable at NIR wavelengths (≥780 nm) and low light intensity (≤40 mW/cm^2) from energy-efficient LEDs remains elusive. As such, we sought to red-shift our green-light photosystem by utilizing the tunable aza-BODIPY scaffold.

Herein, the effect of electron donating groups (EDGs) on photocuring efficiency with aza-BODIPY PCs was systematically examined in conjuction with pyrrole halogenation and boron methylation to achieve rapid red and far-red photopolymerizations (**Figure 2.1**). Inspired by the work of Zhao and coworkers[29] as well as Nowakowska and coworkers[30], we also hoped to take advantage of a unique

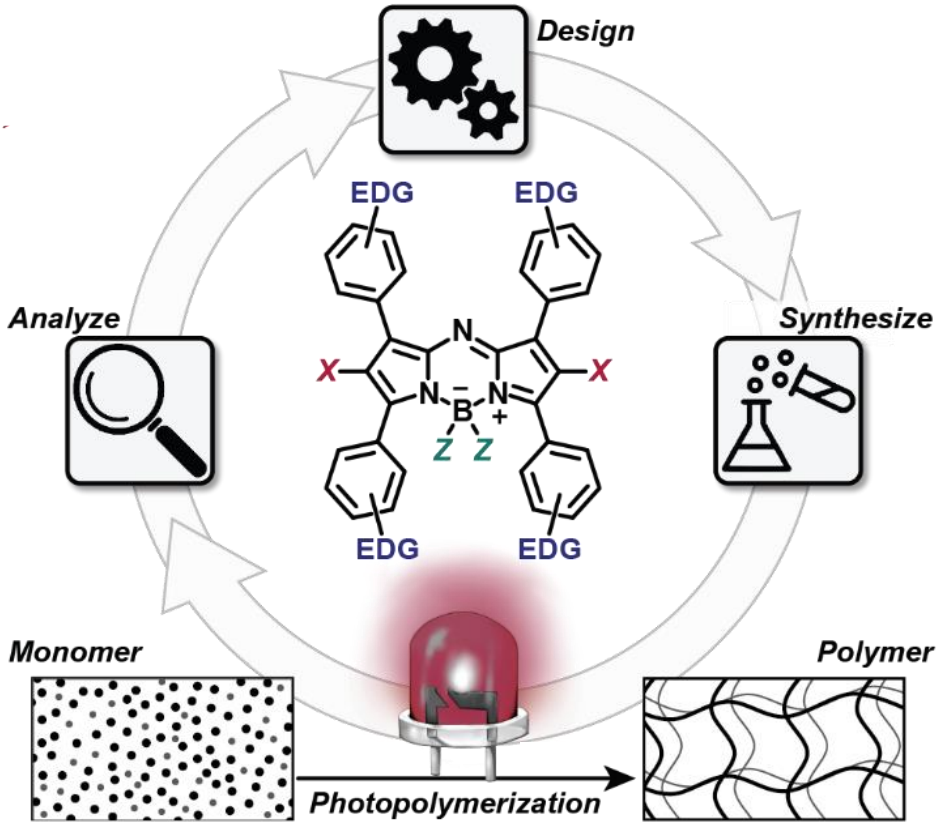

Figure 2.1: Enhancing Photopolymerization Efficiency with Far-Red and near-IR Light. Systematic Design-Synthesis-Analysis Circularity with aza-BODIPY Derivatives as Photocatalysts Enabled Rapid Apparent Polymerization Rates Using Low Intensity (I) Light Emitting Diodes (LEDs) Having a Wavelength Maximum (λ_{max}) of 740 nm.

charge-transfer within Aza-BODPYs to achieve efficient NIR photopolymerization. Overall, Aza-BODIPYs with EDGs provide strong far-red (~700-780 nm) and NIR (≥780 nm) absorption, while heavy atoms and boron methylation enhance ISC to longer lived excited states that facilitate efficient conversion of the low energy photons to reactive free radicals to initiate polymerization. Unprecedented sensitivity to red, far-red, and NIR light is revealed while maintaining excellent temporal control (no initial dark polymerization).

2.2: Results and Discussion

Given the demonstrated significance of the heavy atom effect, our next aim was to develop BODIPY PRCs that operate effectively under irradiation from a far-red LED. To this end, the mesityl group at the meso bridgehead position was replaced with a nitrogen, and the methyl substituents off the pyrrole units were replaced with phenyl rings[31,32]. Analogous to the modular Mes-BODIPY syntheses, acetophenone and benzaldehyde derivatives as well as N-bromosuccinimide were employed to provide both the hydrogen, aza-H, and bromine, aza-Br, functionalized dyes (**Figure 2.2**).

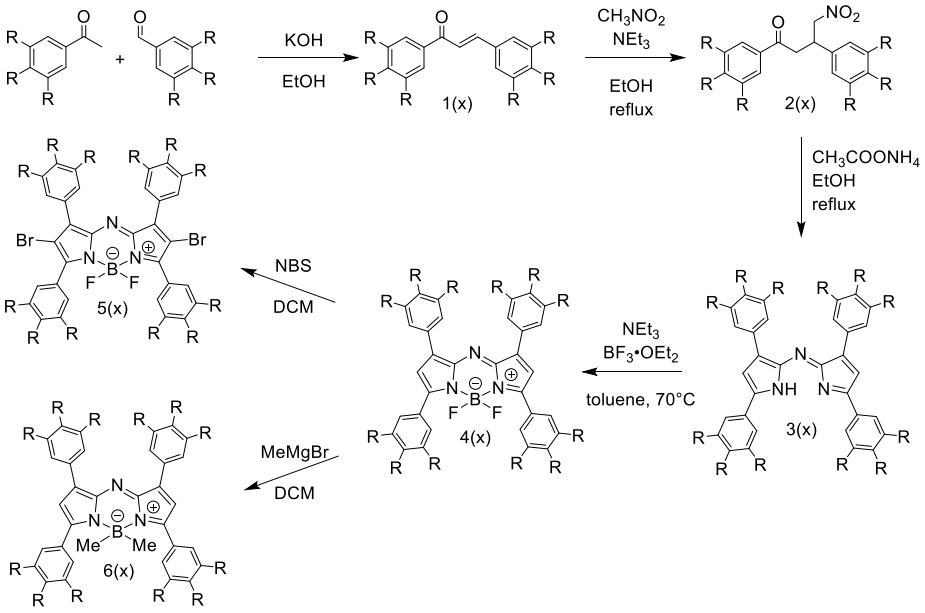

Figure 2.2: General Synthesis of EDG Aza-BODIPY Series

As shown in **Figure 2.3**, the combination of a nitrogen bridgehead and electron rich phenyl substituents resulted in a ~135 nm λ_{max} red shift compared to the mesityl BODIPY dyes: from ~525 nm (**Mes-Br**) to ~660 nm (**aza-Br**). Interestingly, halogenation of the aza-BODIPY resulted in a slight blue shift (~15 nm) in contrast to that observed for the green-light Mes-BODIPY dyes. This blue shift requires a higher photon flux to be used in order to normalize the number of photons absorbed when exciting with a far-red LED. Using an analogous tricomponent photosystem with aza-BODIPY as the photosensitizer, the polymerization of isobornyl acrylate was carried out under 656 nm (red) and 740 nm (far-red) LEDs. The overlap between aza-BODIPY absorbance and LED emission was again used to normalize the number of photons by tuning the 740 nm LED intensity, providing a means to directly compare photopolymerization efficiency, with the total number of photons absorbed equaling 2.9 x 10^{14} $cm^{-2}s^{-1}$ (**Figure 2.4**).

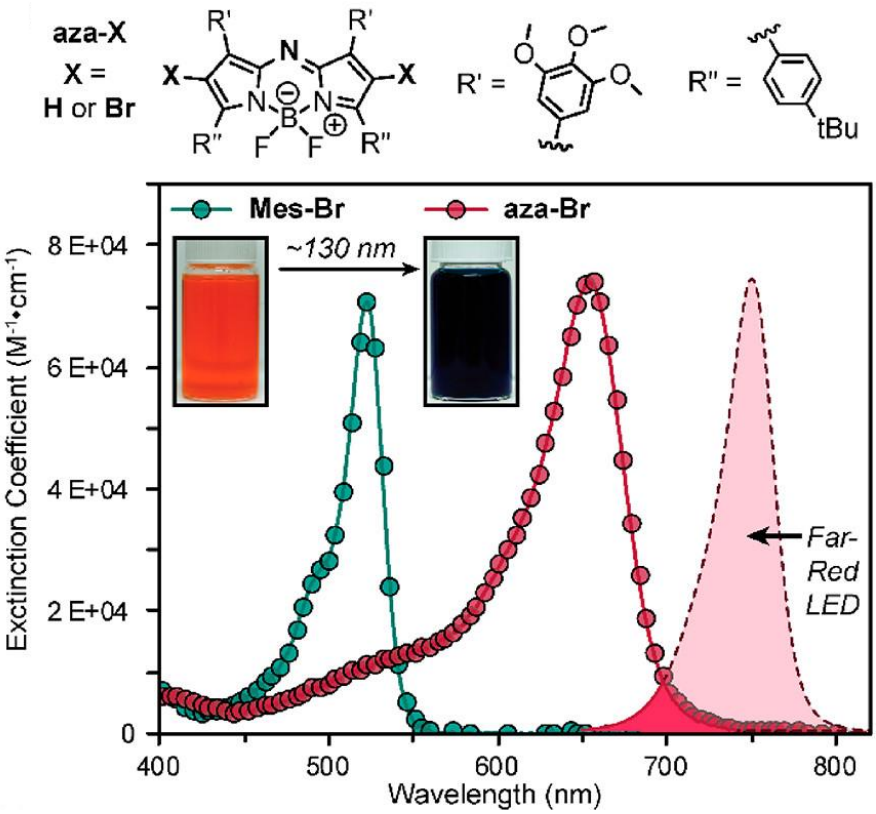

Figure 2.3: Chemical Structures for **Aza-H** and **Aza-Br** and UV–Vis Absorption Spectra for **Mes-Br** and **Aza-Br** (4–6 μM in acetonitrile) Overlayed with Emission Profile of 740 nm LED. Inset: Photographs of Distinctly Colored **Mes-Br** and **Aza-Br** in Solution.

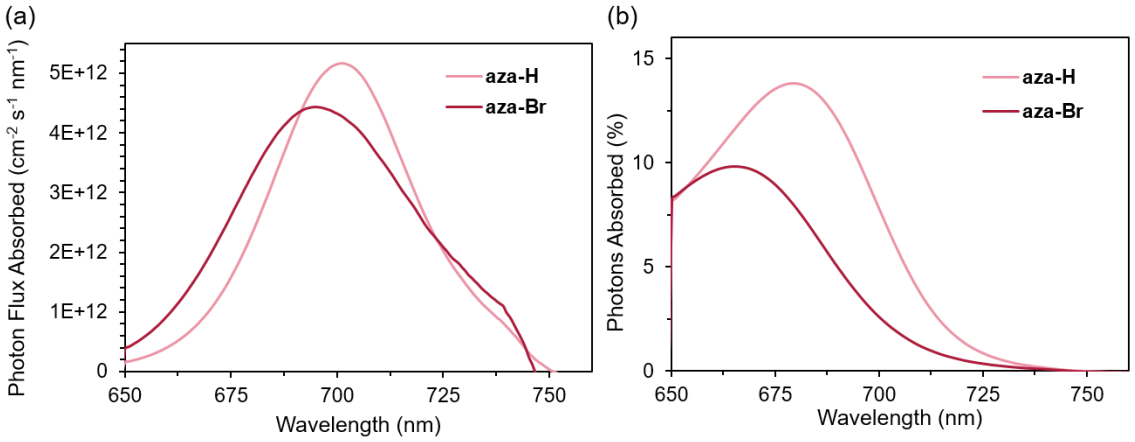

Figure 2.4: Normalized Photons Absorbed for the Aza-BODIPY Derivatives Using a Far-Red LED with a Variable Intensity (6.36 mW/cm^2 and 16 mW/cm^2 for Aza-H and Aza-Br respectively) to Normalize the Total Number of Photons Absorbed (~2.9x10^{14} cm^{-2} s^{-1}). (a) Plot of the Photon Flux Absorbed as a Function of Wavelength and (b) Plot of Percent Photons Absorbed of the Far-Red LED as a Function of Wavelength, Showing that Measurements Were Performed Far From Saturation.

Monitoring the kinetics using the custom ATR-FTIR setup revealed a dramatic enhancement in polymerization rate when using **aza-Br** compared to **aza-H**, under both red (**Figure 2.5**) and far-red irradiation **(Figure 2.6**). As can be seen in **Figure 2.5**, the brominated aza-BODIPY is able to achieve max conversion within 10 seconds at 1 mW/cm^2 using a 656 nm LED whereas the non-brominated aza-BODIPY can only achieve max conversion within 30 seconds at 16 mW/cm^2. Under far-red light, as can be seen in **Figure 2.6**, **aza-Br** resulted in polymerizations that were ~8× faster than those of **aza-H** (0.66 ± 0.03 M/s vs 0.08 ± 0.02 M/s), which corresponded to reaching maximum conversion in 11.4 ± 0.9 s. Such rapid far-red photopolymerization is, to the best of our knowledge, unprecedented.

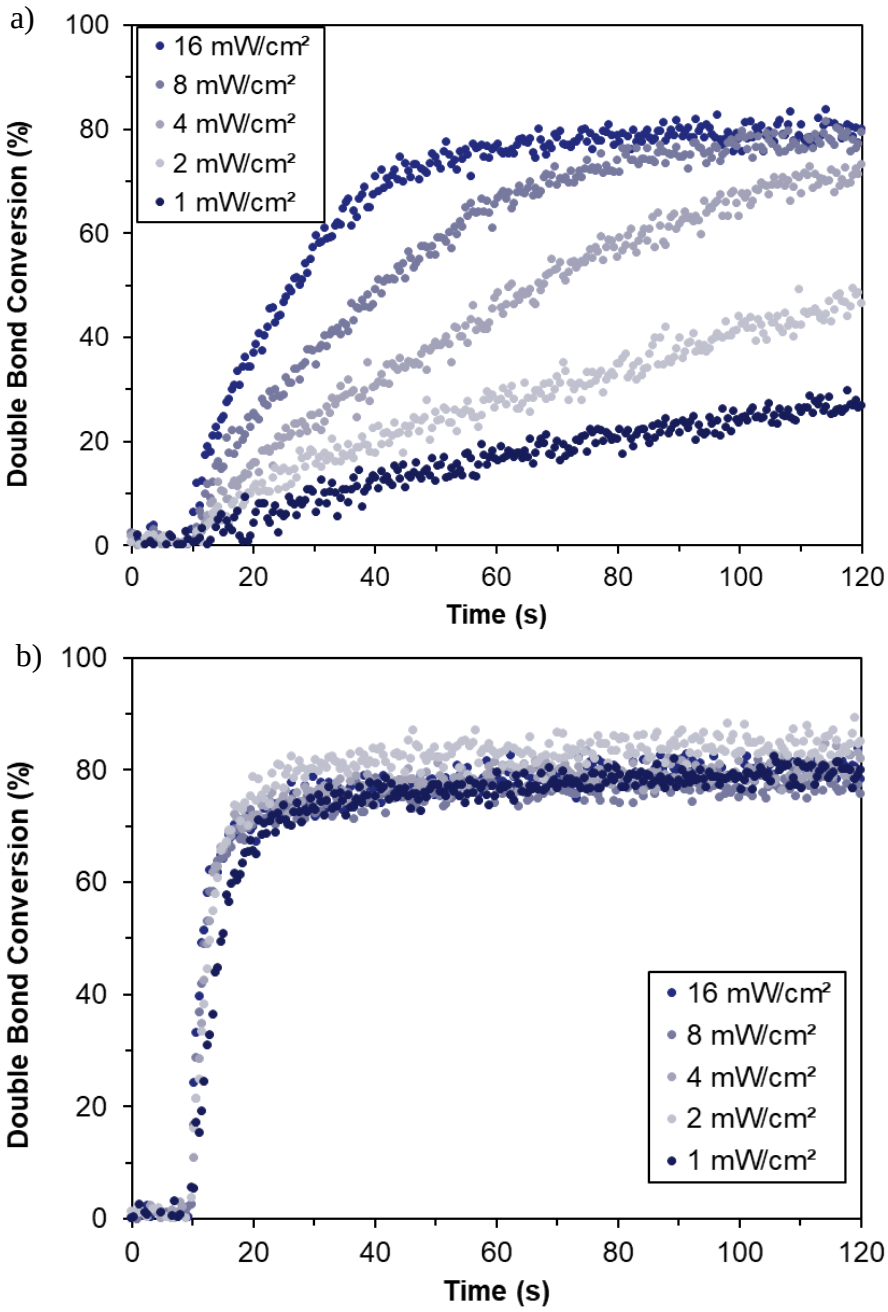

Figure 2.5: (a) Photopolymerization of Isobornyl Acrylate with **Aza-H** and a 656 nm LED at Different Intensities in the Optimized Resin Formulation. (b). Photopolymerization of Isobornyl Acrylate with **Aza-Br** and a 656 nm LED at Different Intensities in the Optimized Resin Formulation.

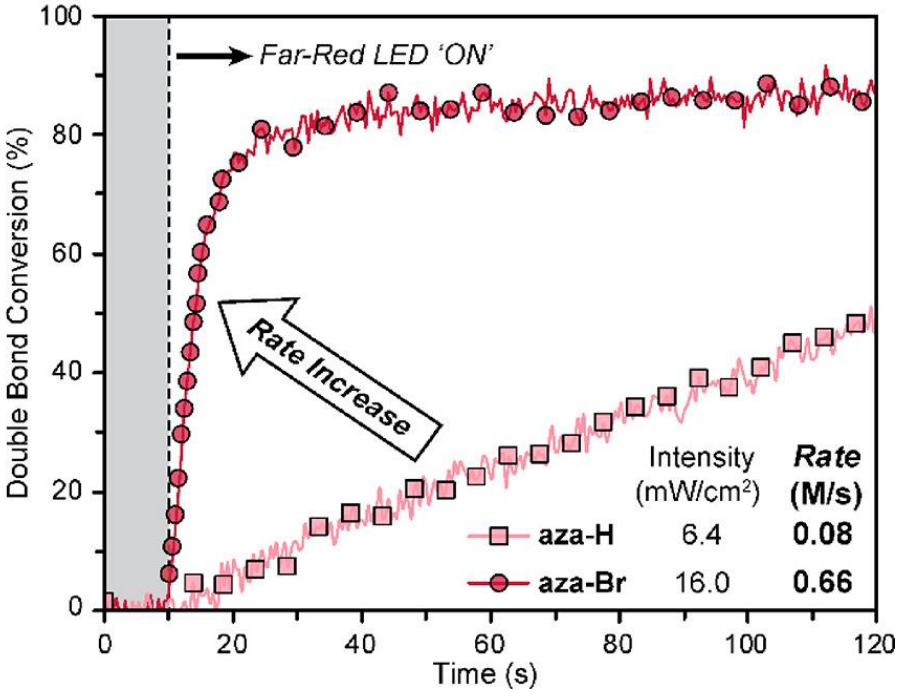

Figure 2.6: Plot of Conversion vs Time Using an Irradiation Intensity that Normalizes Photons Absorbed Between the Two Aza-BODIPY Derivatives. No Polymerization is Observed in the Dark (Gray Region). Upon Irradiation **Aza-Br** Polymerizes at a Rate ~8× Faster Than **Aza-H**.

Similar to our green-light Mes-BODIPY photosystem, we wanted to test light intensity and catalyst loading limitations while reaching full conversion within ~60 seconds. As can be seen in **Figure 2.7**, using the optimized resin formulation, a light intensity of 1 mW/cm^2, corresponding to an absorbed photon flux of 1.8×10^{13} cm^{-2}s^{-1}, was found to be the lower bound for far-red irradiation. Using an intensity of 16 mW/cm^2 for far-red light, a lower limit of 0.004 mol% (= 188 μM) catalyst loading, corresponding to an absorbed photon flux of 1.2×10^{13} cm^{-2}s^{-1}, was found for **aza-Br**.

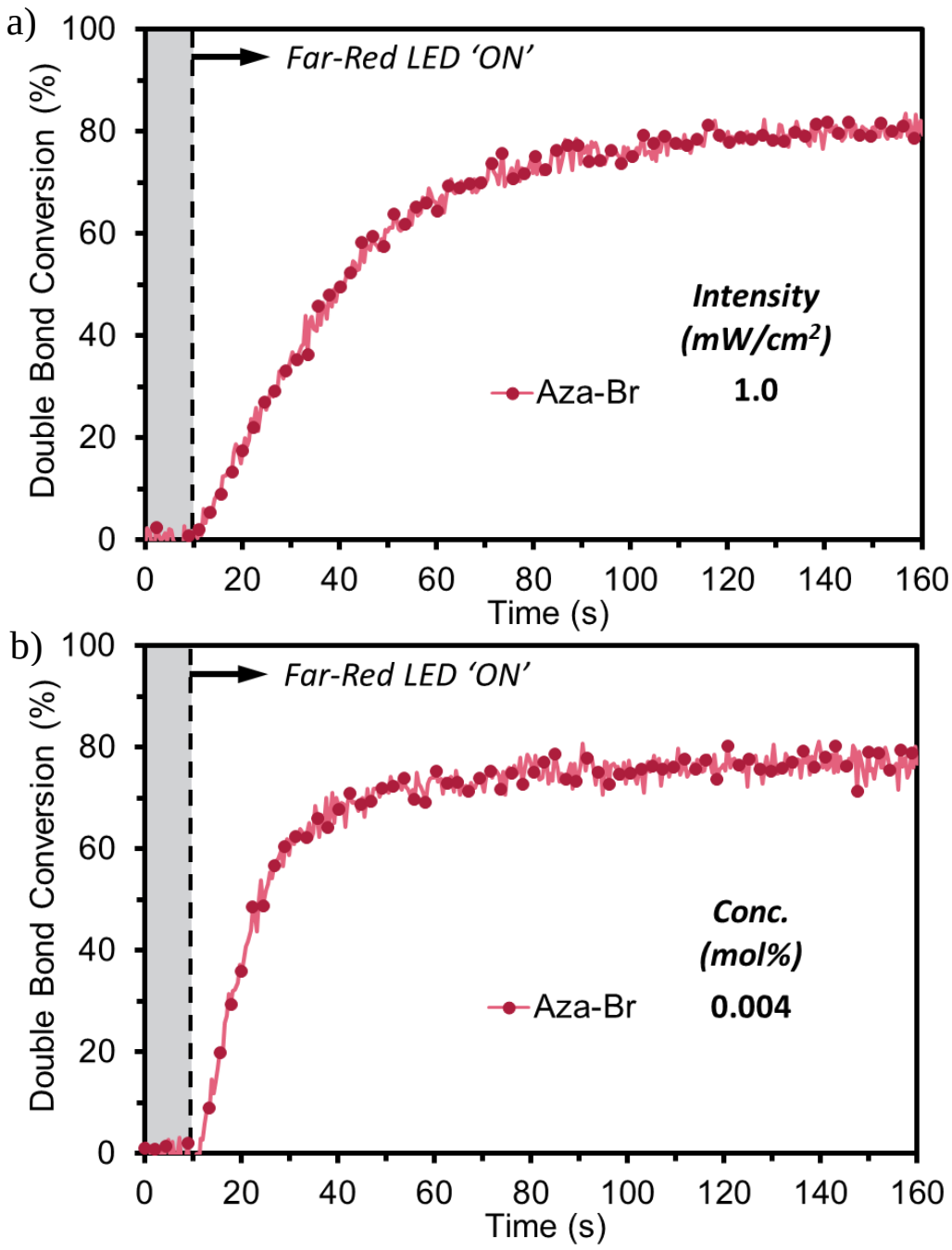

Figure 2.7: Photopolymerization Limits for **Aza-Br** Under Far-Red (740 nm) Irradiation, While Maintaining Near Complete Conversion within ~60 s. Minimum (a) Exposure Intensity and (b) Photosensitizer Concentration

Transient absorption spectra of **aza-Br** and **aza-H** was also collected and indicates bromination leads to triplet formation via ISC that is competitive with decay of the BODIPY S_1 state to its ground state (**Figure 2.8**). While aza-Br undergoes ISC with a rate constant of $k_{ISC} = 6.1 \times 10^9\ s^{-1}$ (τ_{ISC} = 164 ps), no appreciable triplet formation via ISC (<1% yield) is observed for **aza-H**. This leads to a longer-lived triplet population

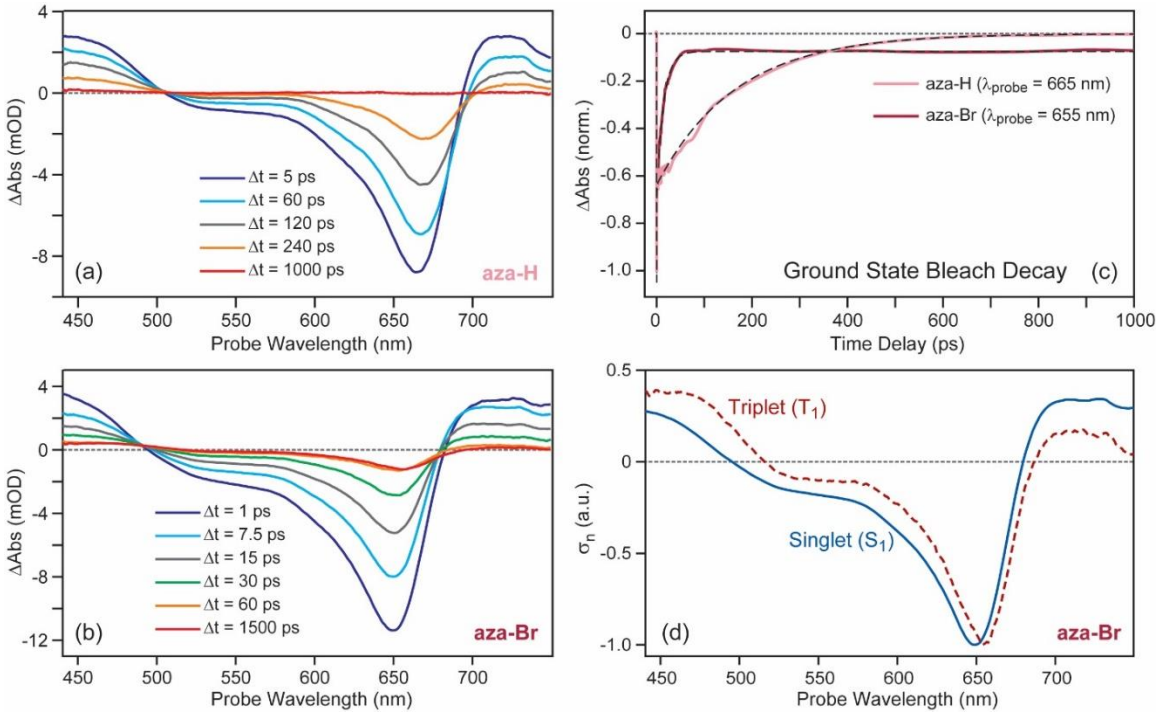

Figure 2.8: TA Spectra of **Aza-H** (a) and **Aza-Br** (b) in Acetonitrile Recorded Following Photoexcitation at 645 nm. The Relative Polarization of the Pump and Probe Pulses Was Set at the Magic Angle (54.7º) to Suppress Signal Contributions From Molecular Reorientation. (c) Ground State Bleach Relaxation Kinetics Recorded at a Probe Wavelength of 665 nm for **Aza-H** and 655 nm for **Aza-Br**. A Persistent Non-Zero Amplitude is Seen for **Aza-Br**, Signaling T_1 State Formation. (d) SADS, $\sigma_n(\lambda_{probe})$, Assigned to the Lowest Excited Singlet (S_1) and Triplet (T_1) States of **Aza-Br** Using Global Target Analysis.

upon photoexcitation of **aza-Br** that can initiate polymerization, while it remains absent for **aza-H**. Thus, as we previously explored, we conclude that halogenation to enhance

triplet formation via ISC is a general method that can improve photopolymerization efficiency. Notably, the TA spectra of **aza-Br** suggests there is additional room to optimize performance of this material as deactivation of **aza-Br** from its S_1 state to its ground state is found to significantly compete with ISC. Such competition was not seen for our green-light Mes-BODIPY dyes, suggesting modification of the functional groups that adorn **aza-Br** could be used to improve its ISC yield, potentially lowering the photopolymerization threshold intensity. As such, the next phase of our aza-BODIPY photocatalyst development begins with the exploration of electron donating groups on the aza-BODIPY scaffold.

A library of azaBODIPY derivatives bearing EDGs were selected for their ease of synthesis and high extinction coeffecients (> 5 x 10^4 M^{-1} cm^{-2}) in the far-red to NIR spectral region (≥700 nm).[33–35] Specifically, the azaBODIPYs contained phenyl rings with tertiary-butyl, methoxy, and/or dimethylamino functionality (**Figure 2.9a**). The naming convention used herein is as follows: (top EDGs)-(bottom EDGs)-azaX, where top refers to the same side as the nitrogen bridgehead and X to hydrogen (H) or bromine (Br). For example, $(MeO)_3$-*t*Bu-azaBr represents the first azaBODIPY compound that we examined. A modular four- or five-step synthetic protocol was followed to harness each derivative. Briefly, an aldol condensation of the respective EDG benzaldehdye and acetophenone was performed in basic conditions, followed by a michael addition with nitromethane. The aza-dipyrromethene was obtained in one-pot using ammonium acetate in ethanol under reflux. Reaction with BF_3•OEt_2 yielded the aza-BODIPY. Subsequent reaction with either NBS or MeMgBr resulted in the brominated or methylated aza-BODIPY, respectively. (see **Figure 2.1**)

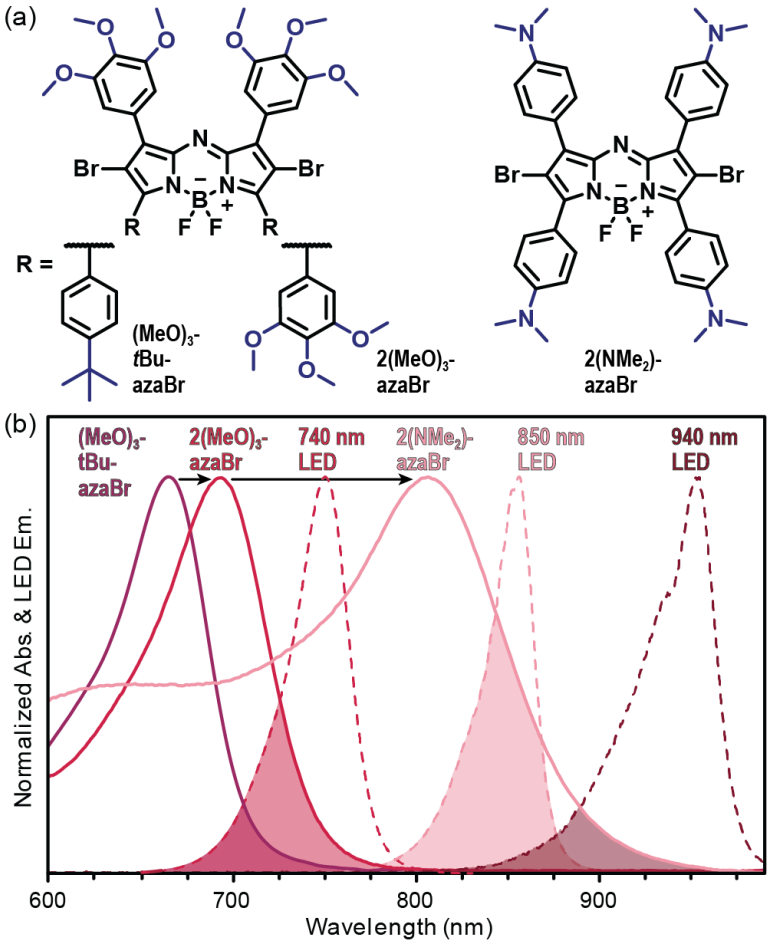

Figure 2.9: Chemical Structures (a) and Absorption Profiles (b) for Halogenated Aza-BODIPYs. Normalized Absorbance Profiles Overlayed With 740, 850, and 940 nm LED Emission Profiles; Cross-Sections Are Shaded.

The absorption profiles and associated extinction coefficients were characterized using UV-vis absorption spectroscopy to determine spectral overlap with far-red and NIR light emitting diodes (**Figure 2.9b**). Increasing the number and strength (OMe to NMe_2) of EDGs resulted in a notable red-shift in peak absorbance, particularly for those containing dimethylamino substituents; >100 nm red-shift relative to methoxy-functionalized. This dramatic red-shift was postulated to result from intramolecular charge transfer between the electron rich amines as donors and the electron deficient

BODIPY core as an acceptor[19,20]. **Figure 2.9b** shows representative absorption profiles for brominated aza-BODIPYs (R-azaBr) given precedent for halogenation to improve photopolymerization efficiency.[28] In-general halogenation resulted in a slight blue shift in peak absorption for MeO-azaBODIPYs (~10 nm), and no significant change for NMe_2-azaBODIPYs. All derivatives showed strong peak absorption with extinction coefficiencts in excess of 1 x 10^4 M^{-1} cm^{-2}. Complete absorbance information for all reported aza-BODIPYs can be found in **Table 2.1** as well as structures in **Figure 2.10**. In accord with spectral overlap between aza-BODIPY absorption and LED emission $(MeO)_x$-aza-BODIPYs were primarily assessed as PCs under far-red light centered at 740 nm (FWHM ≈ 36 nm), and NMe_2-azaBODIPYs under NIR light centered at 850 and 940 nm (FWHM ≈ 28 and 43 nm, respectively). With this aza-BODIPY series covering the far-red to NIR spectral range, their viability as low energy photoinitiators could be examined. To evaluate the efficiency of these dyes, we utilize the same three-component type II photosystem as our green-light BODIPYs in Chapter 1 with a borate salt as a donor and an iodonium salt as an acceptor (**Figure 2.11a**), the only modification being the wavelength of the LED. The polymerizations were carried out using the resin formulation of 0.1 mol% aza-BODIPY, 0.1 mol% donor, and 1.0 mol% acceptor in isobornyl acrylate as the monomer due to its low volatility and preparation from a renewable resource. A representation of the ATR-FTIR setup used can be seen in **Figure 2.11b**. This photoATR from PIKE technologies enables irradiation from both the LED and IR light source to occur on the same side of the sample, which enables very precise kinetics data as we no longer must worry about the light penetration depth on polymerization rate. In addition, an inert atmosphere can be obtained by encasing the surface of the ATR crystal, where the sample sits, with air-free glassware and purging with nitrogen or argon. This eliminates oxygen inhibition of the radical polymerization

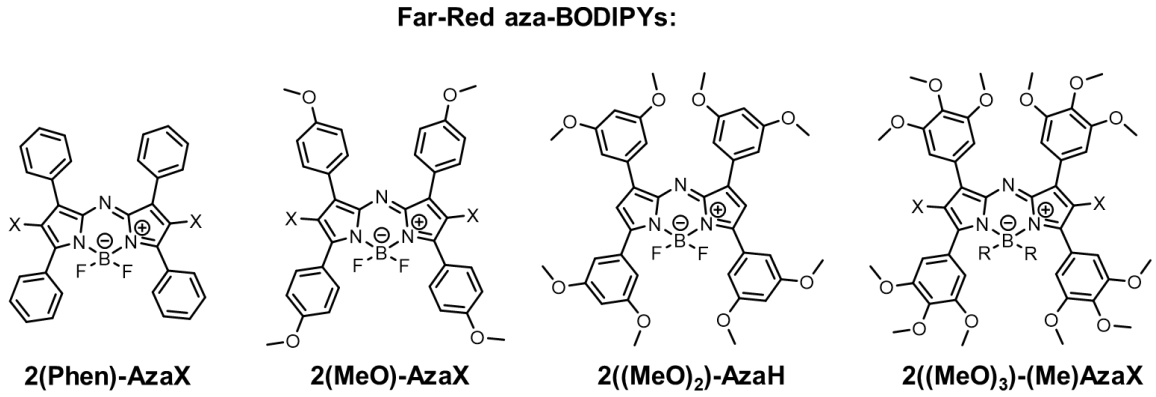

Figure 2.10: Chemical Structures of Far-Red Aza-BODIPY Photoredox Catalysts

Aza-BODIPY	λ_{max} (nm)	ε ($M^{-1}cm^{-1}$)	HOMO (eV)	LUMO (eV)
2(Phen)-AzaH	647	27550 ± 8830	-5.71	-4.08
2(Phen)-AzaBr	643	34530 ± 790	-5.82	-4.14
2(MeO)-AzaH	694	27820 ± 740	-5.40	-3.93
2(MeO)-AzaBr	680	37790 ± 1100	-5.67	-4.13
$2((MeO)_2)$-AzaH	668	18150 ± 420	-5.66	-4.11
$(MeO)_3$-tBu-AzaH	680	60810 ± 5000	-5.57	-3.96
$(MeO)_3$-tBu-AzaBr	654	74110 ± 4410	-5.97	-4.03
$2((MeO)_3)$-AzaH	701	18000 ± 3930	-5.58	-4.03
$2((MeO)_3)$-AzaBr	694	34920 ± 4680	-5.70	-4.21
$2((MeO)_3)$-MeAzaH	626	38740 ± 1890	-5.46	-3.77

Table 2.1: Optoelectronic Properties of the Far-Red Aza-BODIPY Photoredox Catalysts

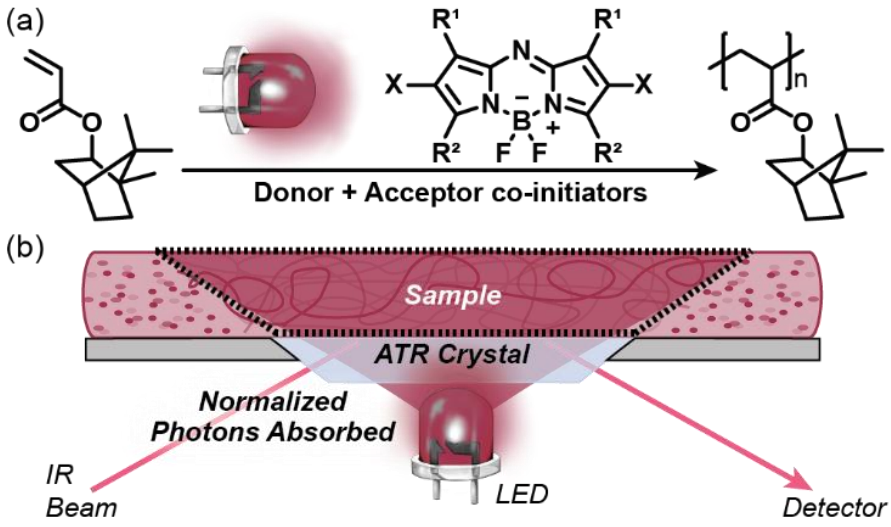

Figure 2.11: (a) Photopolymerization Resin Mixture Consisting of Monomer (Isobornyl Acrylate), 0.1 mol% Photocatalyst (Aza-BODIPY), 0.1 mol% Donor (Borate V), and 1.0 mol% Acceptor (HNu 254). (b) Photo ATR-FTIR Setup.

and provides good consistency in the measurements. Lastly, with with respect to analyzing photocuring efficiency, we followed the same protocol as Chapter 1 by utilizing photon flux. Direct comparisons between different dyes is challenging as each dye has a unique absorption profile which will affect how much light it will be able to absorb from a given LED. Utilizing the absorption profile of each dye vs. the emission profile of the LED, the number of photons being absorbed at any given intensity can be determined by integrating the area of overlap between the two plots. From there, the number of photons being absorbed across the experiment was normalized such that each dye absorbed the same number of photons. This results in the intensity of the calibrated LED having to be adjusted for each dye. As a result, we are evaluating photoinitiator efficiency relative to equal number of photons absorbed rather than the intensity of the LED. Our first comparison will examine the impact of -methoxy group substitution on

the aza-BODIPY core and can be seen in **Figure 2.12**. This analysis was done using a red LED at 656 nm on the AzaH derivatives for two reasons: 1) we wanted to ensure any efficiency differences were due to the -methoxy substituents and not any other substituent effects (like halogenation) and 2) synthesizing the $2(MeO)_2$-AzaBr proved to be incredibly difficult due to uncontrolled bromination on the phenyl ring -C between the two -methoxy substituents. By normalizing the total number of photons absorbed, we observe a ~2x increase in polymerization rate from the base 2(Phen)-AzaH to the 2(MeO)-AzaH. Akin to halogenation, this performance enhancement plateaus as we increase the quantity of -methoxy substituents where we observe $2((MeO)_2)$-AzaH and $2((MeO)_3)$-AzaH having almost identical rates of polymerization.

An additional modification was made to the $2((MeO)_3)$-AzaH derivative given its intrinsic efficiency and that was looking at the impact of boron methylation (**Figure 2.13**). This comparison was done using the same resin formulation but with the 740 nm LED. We observe that methylation of the far-red derivative results in a significant decrease in polymerization rate. As previously discussed, we see a ~4x increase in polymerization rate upon bromination, but methylation results in an almost ~3x decrease in polymerization rate.

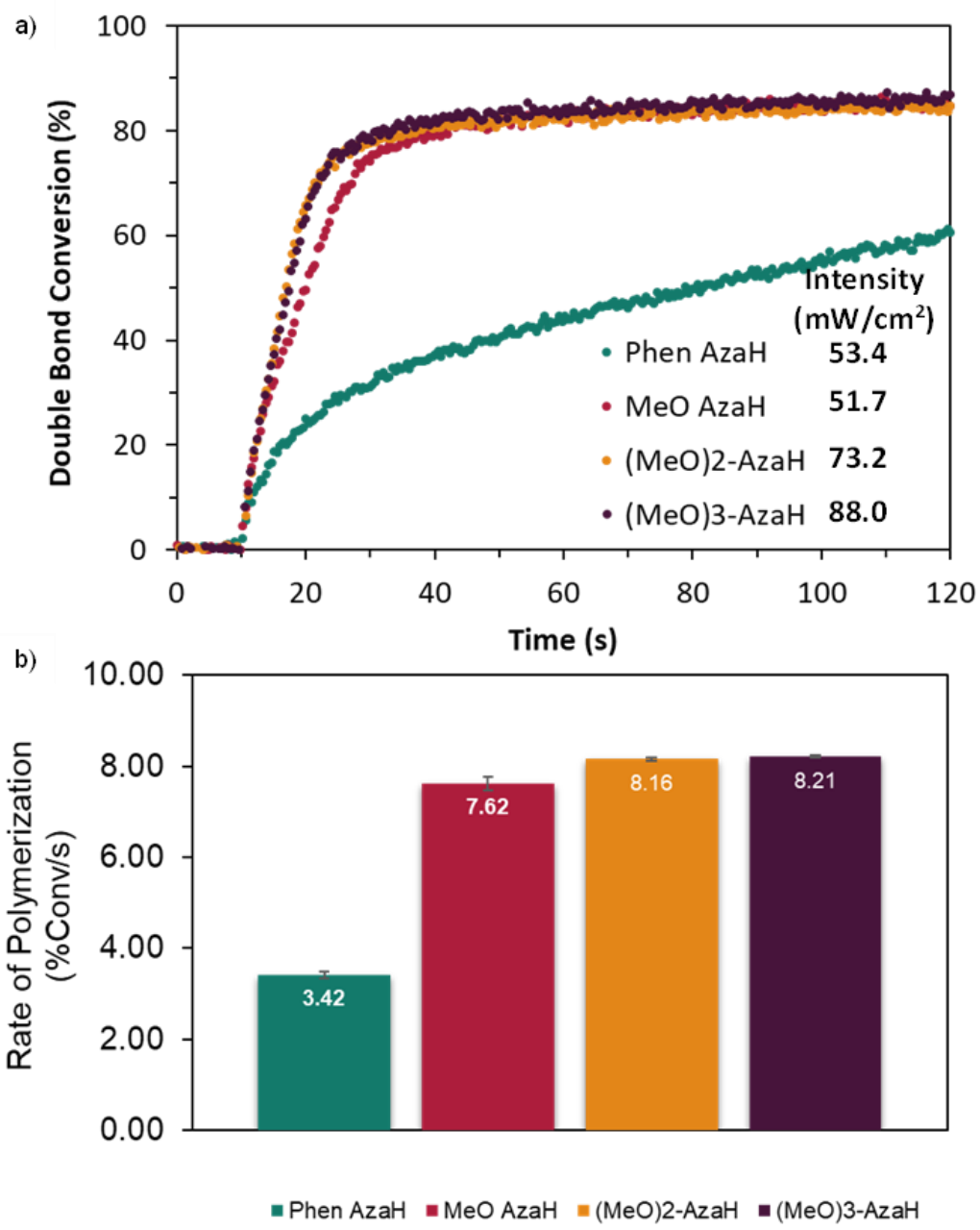

Figure 2.12: Normalized Photon Flux Photopolymerizations of EDG-AzaH With a 656 nm LED. (a) Double Bond Conversion vs Time ATR-FTIR Data at Varying Intensities. (b) Polymerization Rate in % Conversion/second at the Different LED Intensities. Error Bars Represent ± 1 Standard Deviation.

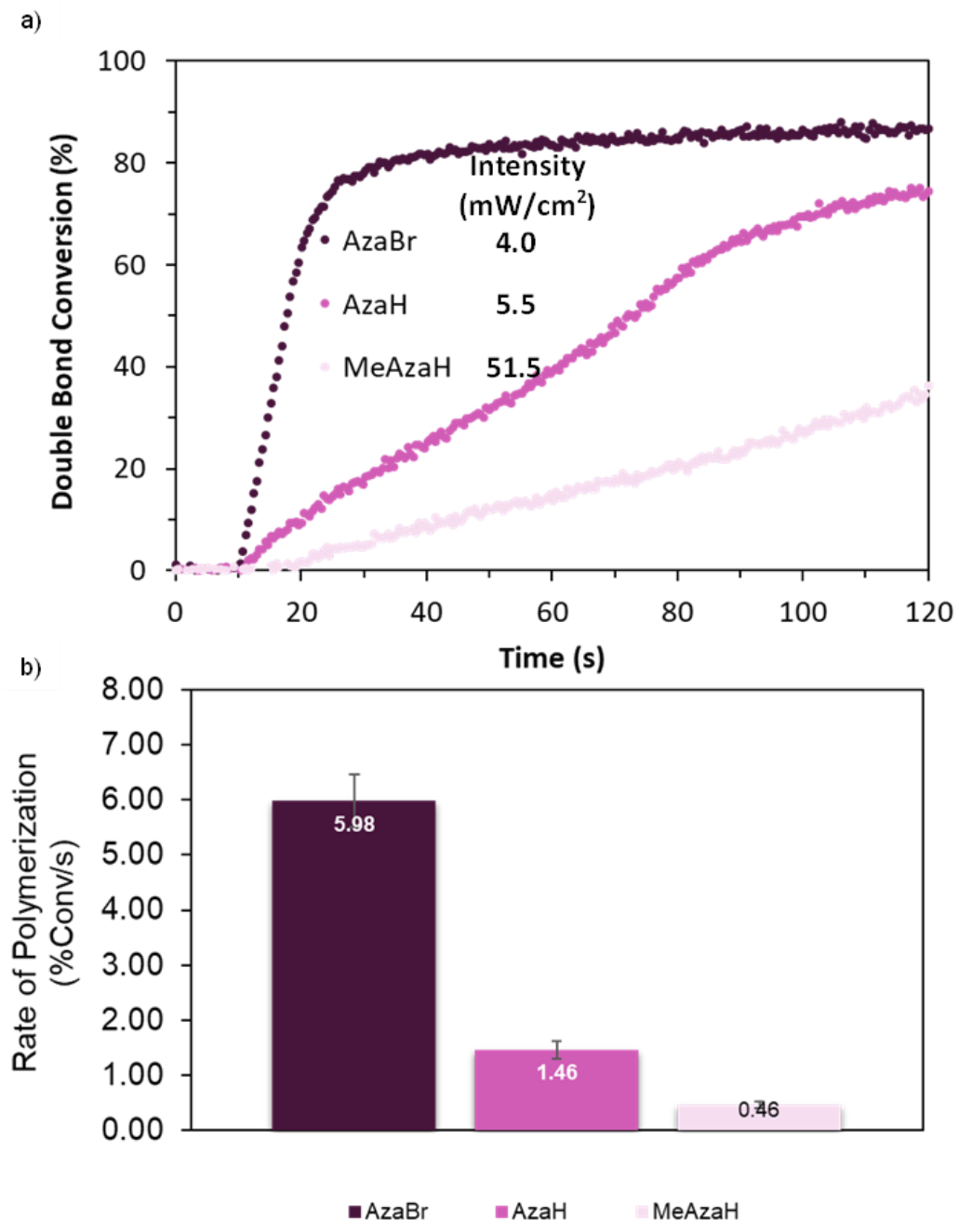

Figure 2.13: Normalized Photon Flux Photopolymerizations of 2((MeO)$_3$)-AzaH + AzaBr + MeAzaH With a 740 nm LED. (a) Double Bond Conversion vs Time ATR-FTIR Data at Varying Intensities. (b) Polymerization Rate in %Conversion/second at the Different LED Intensities. Error Bars Represent ± 1 Standard Deviation.

With these uncovered design parameters, we wanted to test the far-red intensity limit we could achieve with our newly designed aza-BODIPY. As can be seen in **Figure 2.14**, when comparing the first aza-BODIPY we studied, $(MeO)_3$-tBu AzaBr, we see a significant increase in the rate of polymerization with the new 2($(MeO)_3$) AzaBr at the very low light intensity of 0.66 mW/cm^2, which is the lowest intensity we can achieve with our current LED setup. The new derivative is able to absorb more photons from the 740 nm LED due to its red-shifted absorbance (**Table 2.1**) and combined with the intrinsic efficiency of the brominated aza-BODIPY scaffold and slight improvement with EDG substitution, we are able to achieve an even lower intensity while maintaining fast polymerization rates.

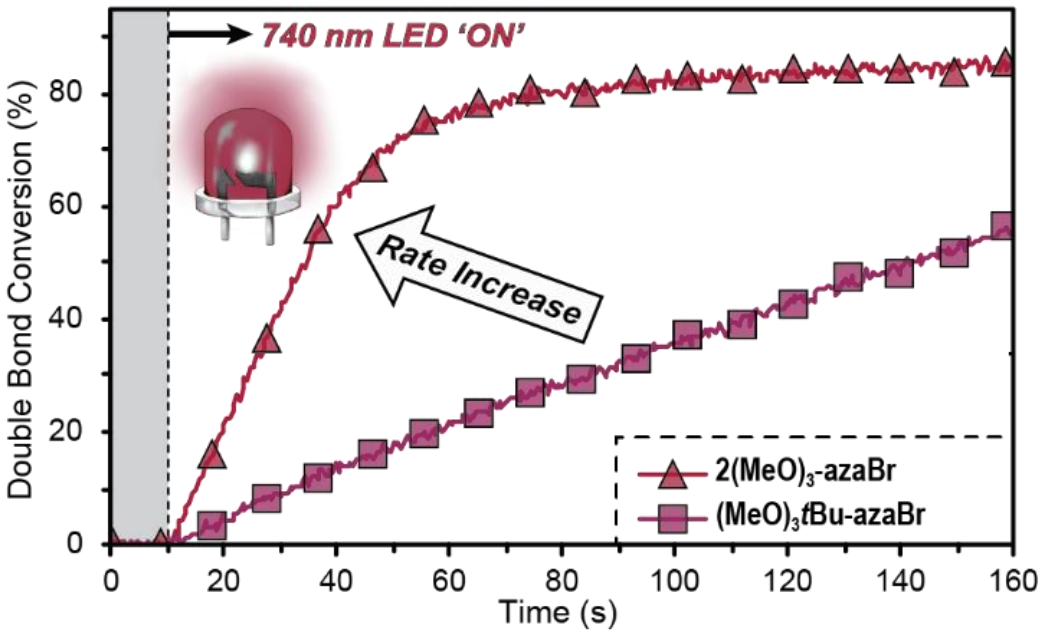

Figure 2.14: Photopolymerization Rate of Isobornyl Acrylate With Far-Red 2($(MeO)_3$)AzaBr and $(MeO)_3$-tBu AzaBr Using a 740 nm LED at 0.66 mW/cm^2 Using the Optimized Resin Formulation.

As a final demonstration, we tested our far-red photosystem in the polymerization of 2-hydroxyethylacrylate (HEA) in order to show the versatility in both hydrophilic and hydrophobic monomers. As can be seen in **Figure 2.15**, the polymerization proceeds rapidly at both high (88 mW/cm^2) and low (0.66 mW/cm^2) light intensities reaching full conversion within 10 s and 90 s, respectively. Through the analysis of EDG substituent

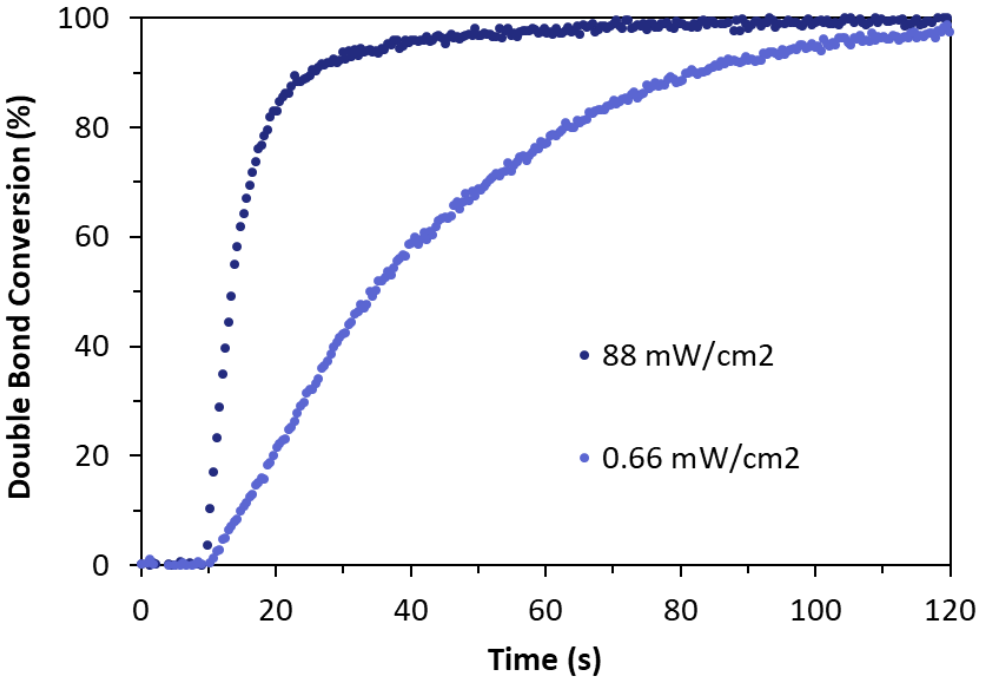

Figure 2.15: Photopolymerization of HEA With 2((MeO)$_3$)-AzaBr Using a 740 nm LED at a High (88 mW/cm^2) and Low (0.66 mW/cm^2) Light Intensity in the Optimized Resin Formulation.

effects, we were able to push a red and far-red aza-BODIPY photosystem to unprecedented reactivity at very low light intensities using a 740 nm LED. As such, our sights are now focused on pushing the limits of near-IR photocatalysts in a similar manner to our visible light photosystems.

To that end, we continued with further modifications to the aza-BODIPY scaffold via the incorporation of -dimethylamino (-NMe_2) substituents. A total of five NIR aza-BODIPYs were synthesized and can be found in **Figure 2.16** along with their respective photophysical properties in **Table 2.2**. The impact of halogenation, boron methylation,

NIR aza-BODIPYs:

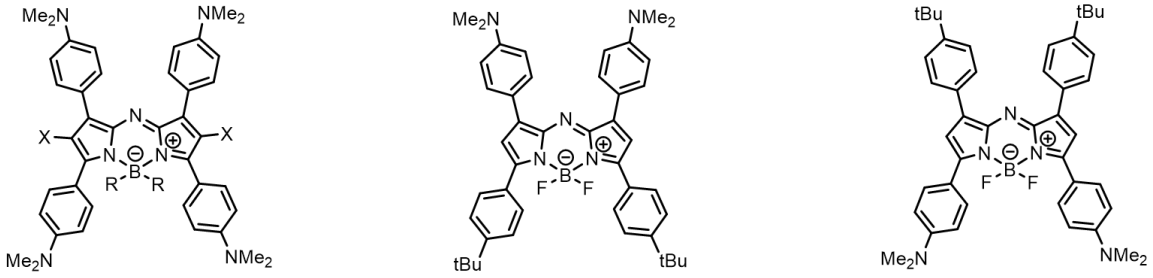

2(NMe_2)-(Me)AzaX **NMe_2-tBu-AzaH** **tBu-NMe_2-AzaH**

Figure 2.16: Chemical Structures of NIR Aza-BODIPY Photoredox Catalysts

BODIPY	λ_{max} (nm)	ε ($M^{-1}cm^{-1}$)	HOMO (eV)	LUMO (eV)
2(NMe_2)-AzaH	804	18590 ± 2350	-5.02	-3.70
2(NMe_2)-AzaBr	810	13130 ± 1430	-5.45	-3.96
2(NMe_2)-MeAzaH	719	14990 ± 1000	-5.36	-3.51
NMe_2-tBu-AzaH	627 (763)	25230 ± 1330	-4.97	-3.84
tBu-NMe_2-AzaH	790	11780 ± 1230	-5.06	-3.79

Table 2.2: Optoelectronic Properties of the NIR Aza-BODIPY Photoredox Catalysts

and -NMe_2 substitution position were all examined. By modifying the -NMe_2 position, we observe a unique shift in the absorbance profile of the aza-BODIPY dye (**Figure 2.17**). The dramatic red-shift (~100 nm) from the far-red aza-BODIPYs is the result of an

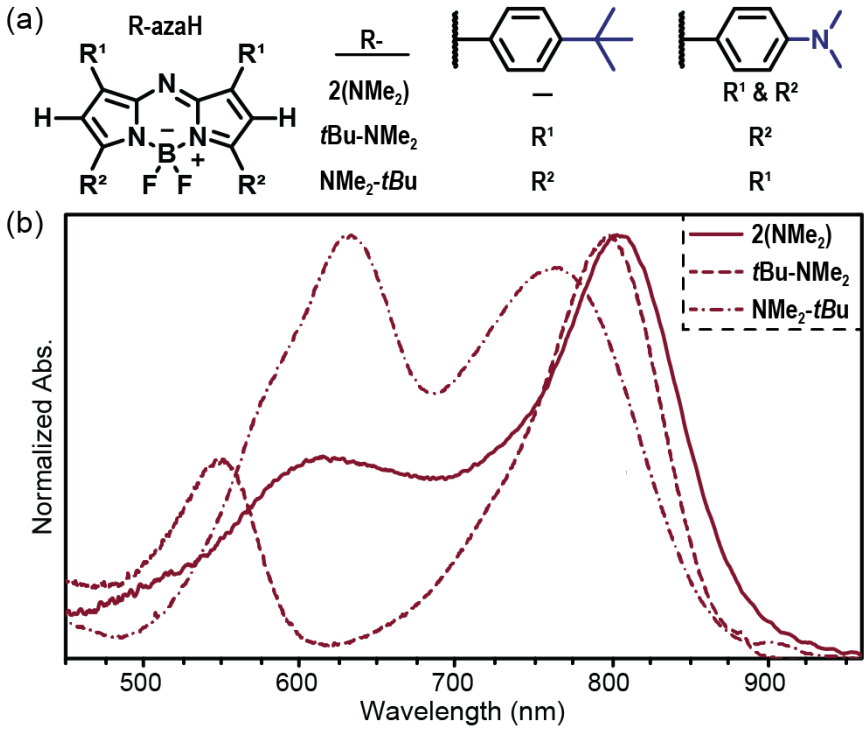

Figure 2.17: (a) Structure of NIR Aza-BODIPYs. (b) Absorbance Profile of NIR Aza-BODIPYs.

intramolecular photoinduced electron transfer (PET). This charge-transfer state gives rise to the NIR absorption band and can be tuned by -NMe_2 substitution position. The absorption profile of NMe_2-tBu-AzaH in **Figure 2.17** has a much more prominent bimodal absorption peak and its CT absorbance is slightly blue shifted relative to 2(NMe_2)-AzaH and tBu-NMe_2-AzaH. This shift in absorbance has a direct influence on the ability of the photocatalyst to initiate polymerization (**Figure 2.18**). Utilizing the same resin formulation as the far-red photosystem with isobornyl acrylate, the rate of

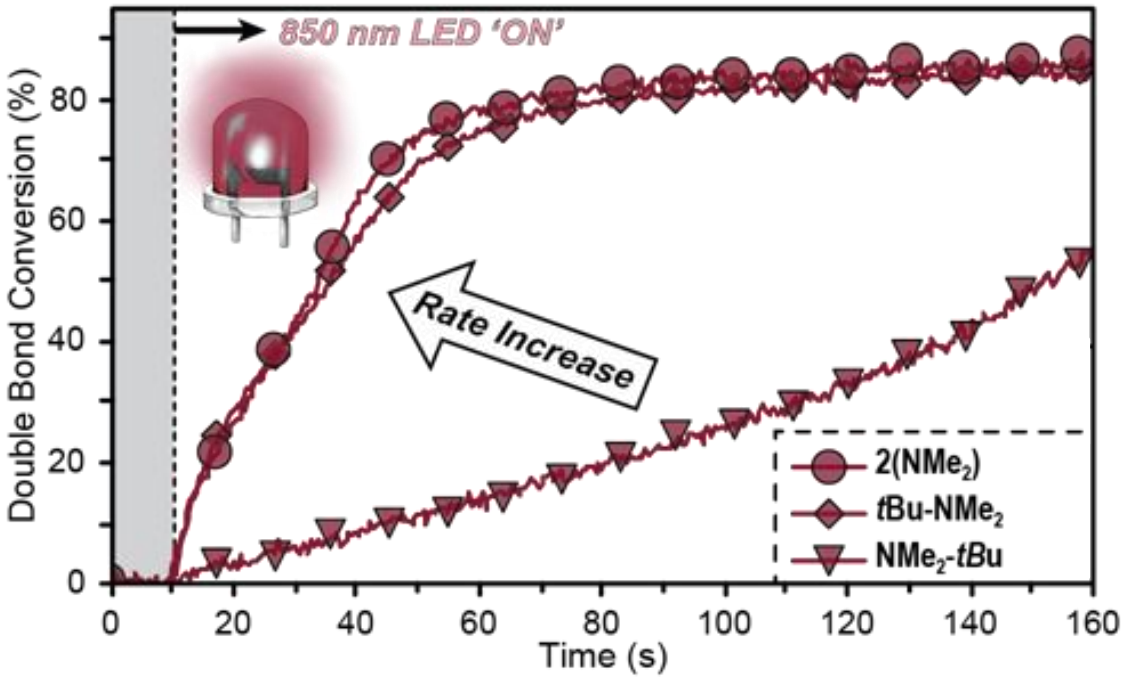

Figure 2.18: Photopolymerization Rate of Isobornyl Acrylate With 0.1 mol% NIR Aza-BODIPYs, 0.1 mol% donor (Borate V), and 1.0 mol% HNu 254 Using an 850 nm LED at 55 mW/cm^2.

polymerization was monitored using the ATR-FTIR with an 850 nm LED at 55 mW/cm^2. We observe a dramatic decrease in polymerization efficiency when -NMe_2 substitution occurs on only the top phenyl rings (above meso-N bridgehead), whereas when -NMe_2 substitution is on the bottom phenyl rings, rapid polymerization occurs. The charge-transfer in the NMe_2-tBu-AzaH derivative likely leads to rapid internal conversion that inhibits electron transfer within the photosystem. As such, when utilizing photocatalysts that possess this kind of intramolecular photoinduced electron transfer, it is important to avoid this type of bimodal absorption when aiming to develop highly efficient photosystems.

Further studies on light intensity with the 2(NMe_2)-(Me)-AzaX series using an 850 nm LED were performed to test the limits of these NIR photocatalysts. **Figure 2.19**

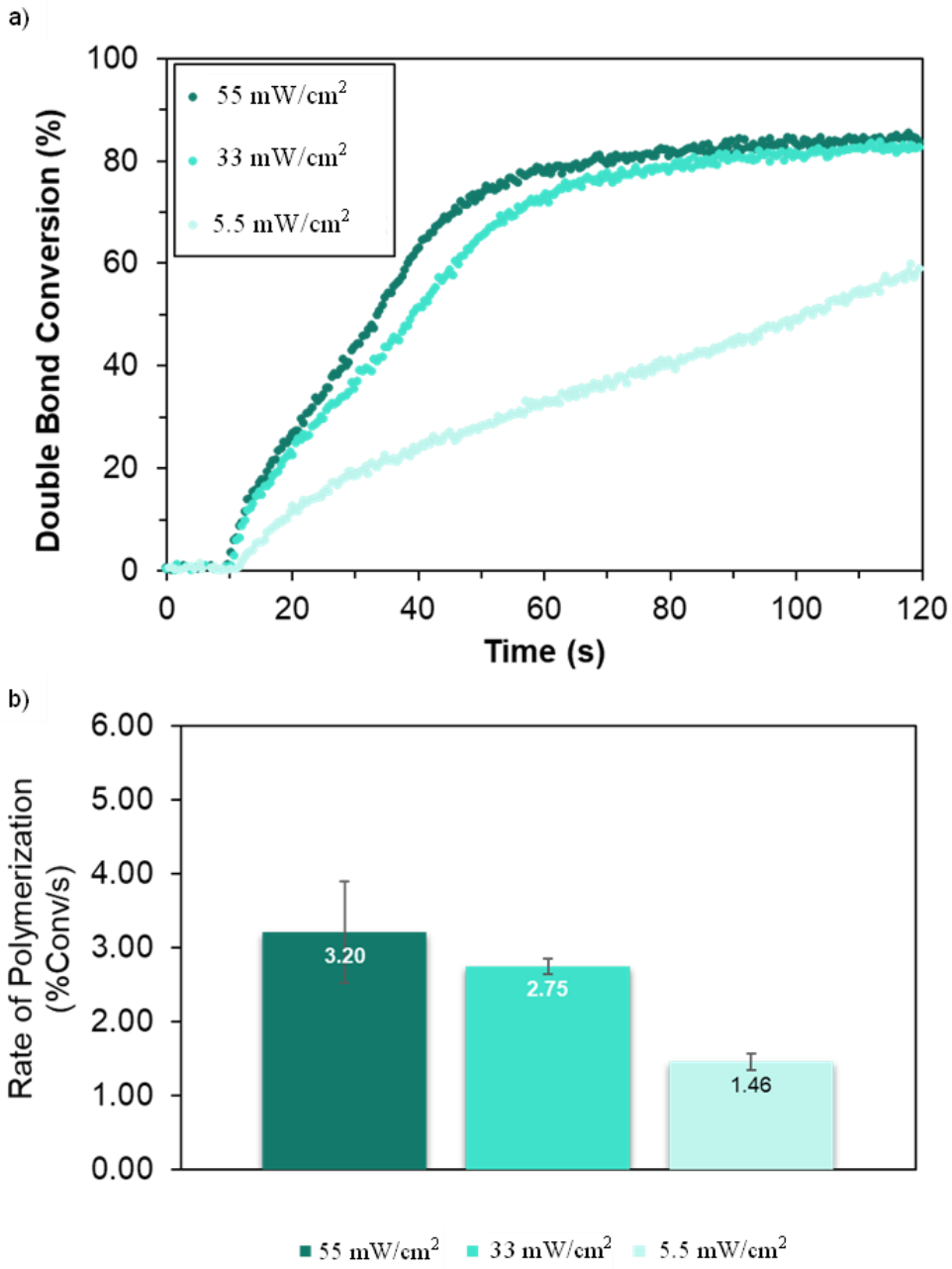

Figure 2.19: (a) Photopolymerization Rate of Isobornyl Acrylate With 0.1 mol% 2(NMe_2)-AzaH, 0.1 mol% Donor (Borate V), and 1.0 mol% HNu 254 using an 850 nm LED at Varying Intensities. (b) Polymerization Rate in %Conversion/second at the Different LED Intensities. Error Bars Represent ± 1 Standard Deviation.

showcases the polymerization of 2(NMe_2)-AzaH. Max conversion was observed to occur within 50 s at 33 mW/cm^2. Given the unprecedented reactivity of the AzaH derivative at 850 nm, we were optimistic about 2(NMe_2)-AzaBr as halogenation has proven to be an effective design parameter to enhance polymerization rate. However, as observed in **Figure 2.20**, the rate of polymerization upon bromination did not drastically improve. The rates of polymerization for 2(NMe_2)-AzaBr and 2(NMe_2)-AzaH are almost identical at 55 mW/cm^2 (3.68 %Conv/s vs. 3.20 %Conv/s, respectively), but the rate of 2(NMe_2)-AzaBr drops more as the intensity of the light decreases. This result can be explained by examining the TA data (**Figure 2.21**) for these two derivatives. Both 2(NMe_2)-AzaBr and 2(NMe_2)-AzaH upon irradiation first go to the excited S_1 state, but very rapidly ISC to a photoexcited CT state. Even upon bromination, the rate of ISC to a T_1 state is slower than the rate of transfer to the CT state and thus the impact of halogenation is not felt. This photosystem is not generating a significant amount of the longer lived T_1 state and therefore not receiving the enhancement in polymerization rate.

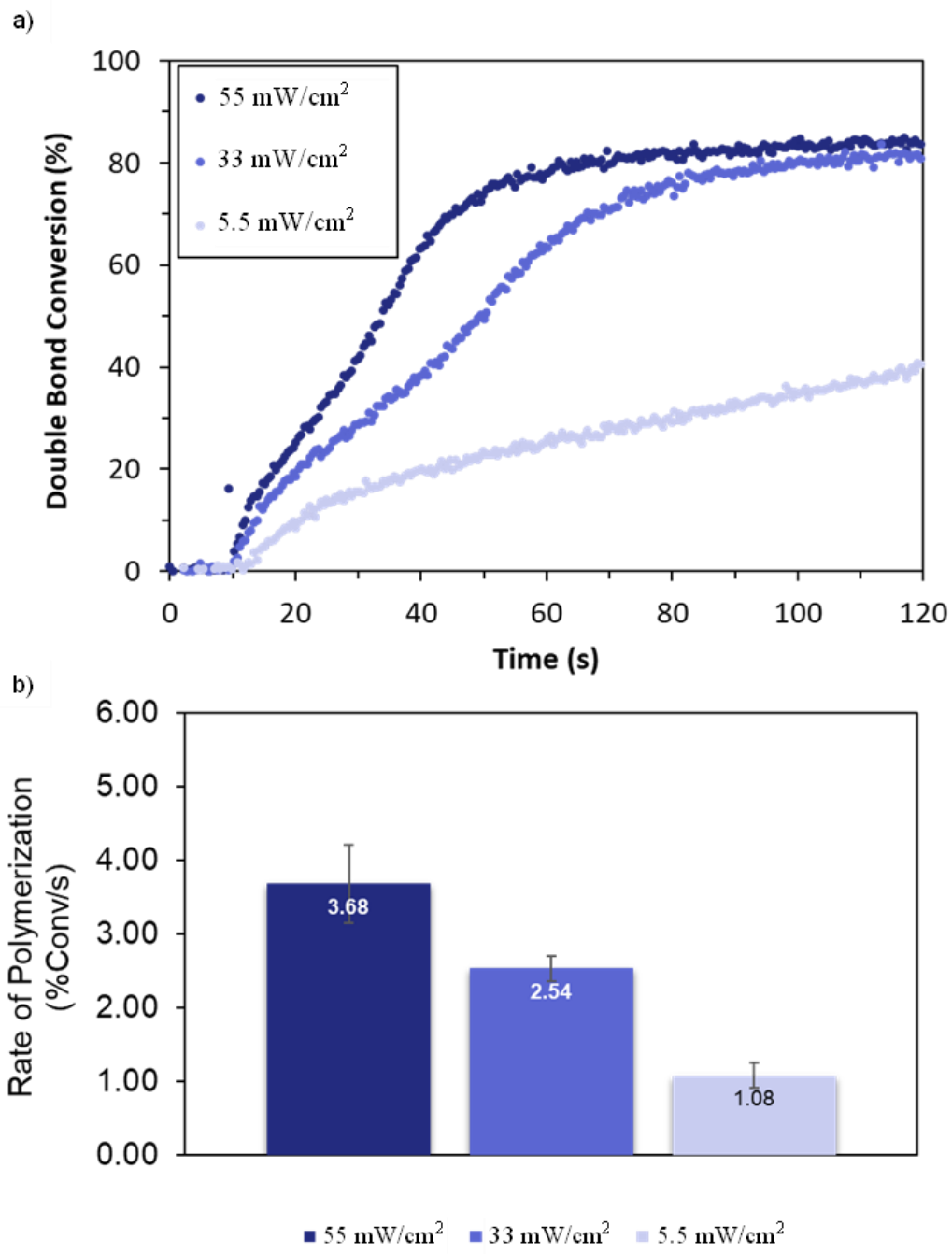

Figure 2.20: (a) Photopolymerization Rate of Isobornyl Acrylate With 0.1 mol% 2(NMe_2)-AzaBr, 0.1 mol% Donor (Borate V), and 1.0 mol% HNu 254 using an 850 nm LED at Varying Intensities. (b) Polymerization Rate in %Conversion/second at the Different LED Intensities. Error Bars Represent ± 1 Standard Deviation.

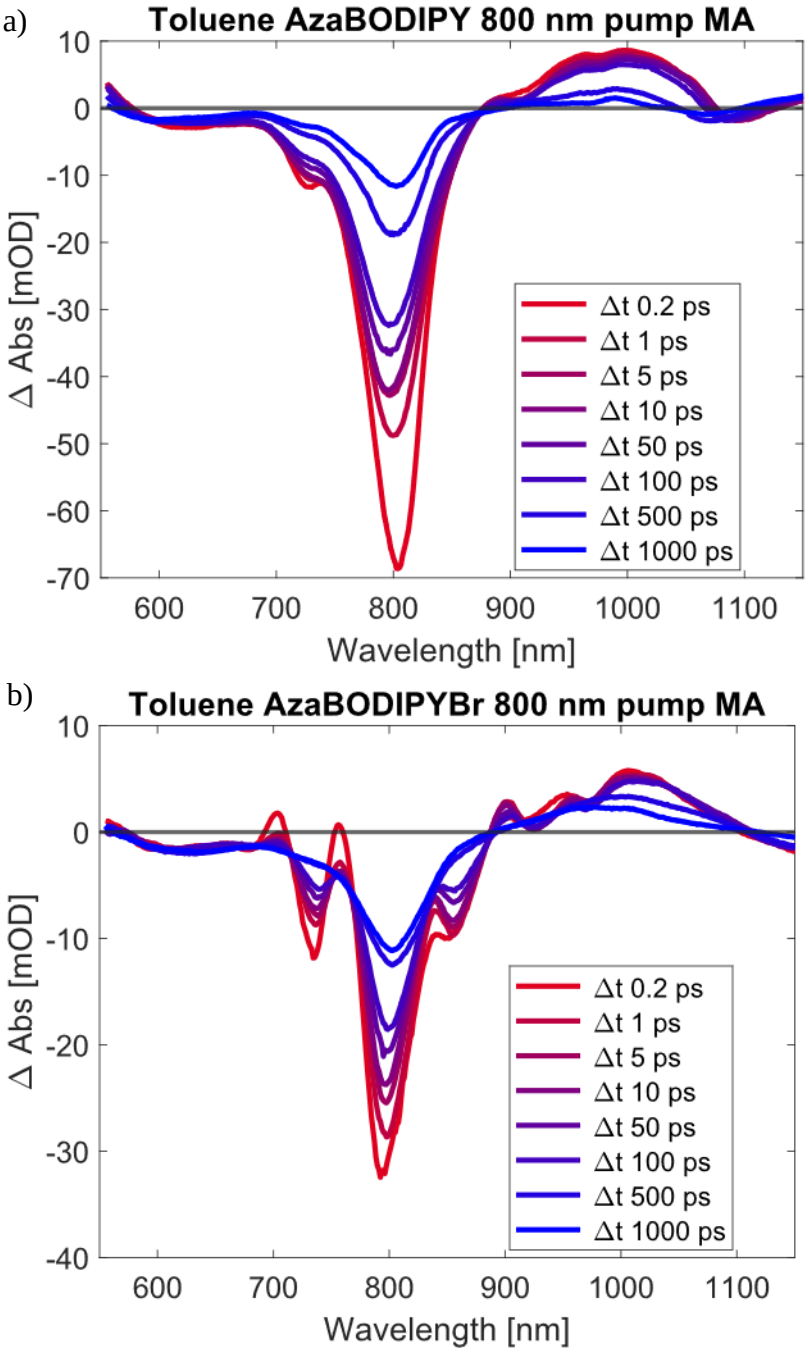

Figure 2.21: (a) TA Spectrum of 2(NMe_2)-AzaH in Toluene. (b) TA spectrum of 2(NMe_2)-AzaBr in Toluene

Given this deviation in behavior due to the CT state, we hypothesized that the impact of boron methylation would also change with this NIR aza-BODIPY. Thus, 2(NMe_2)-MeAzaH was synthesized and a significant blue-shift in maximum absorbance was observed (**Table 2.2**). Replacing the -F with -Me adds more electron density to the aza-BODIPY core and likely diminishes the charge-transfer effect. Despite this blue-shift, the absorbance profile still possesses some overlap with the emission profile of the 850 nm LED. The rates of polymerization at different light intensities were measured and can be found in **Figure 2.22**. 2(NMe_2)-MeAzaH has slightly slower rates of polymerization at 55 mW/cm^2 than 2(NMe_2)-AzaH and 2(NMe_2)-AzaBr. That being said, this slower rate is likely due to poor overlap of the 850 nm LED. We account for this by normalizing the total number of photons absorbed by doing a photon flux comparison with the 850 nm LED (**Figure 2.23**). We observe that the intrinsic efficiency of the MeAzaH derivative is higher than that of the AzaH and AzaBr with AzaBr performing the worst.

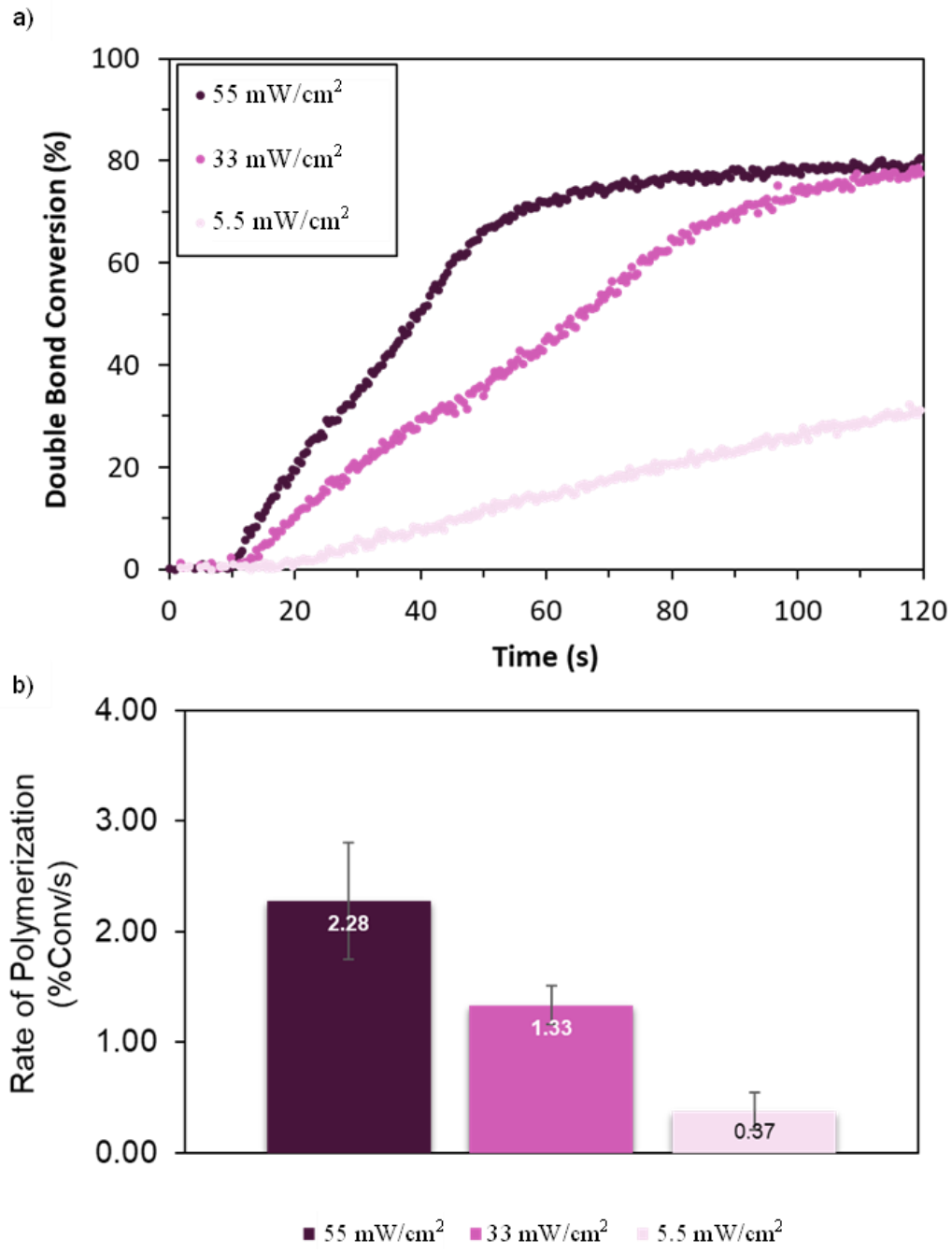

Figure 2.22: (a) Photopolymerization Rate of Isobornyl Acrylate With 0.1 mol% 2(NMe_2)-MeAzaH, 0.1 mol% Donor (Borate V), and 1.0 mol% HNu 254 Using an 850 nm LED at Varying Intensities. (b) Polymerization Rate in %Conversion/second at the Different LED Intensities. Error Bars Represent ± 1 Standard Deviation.

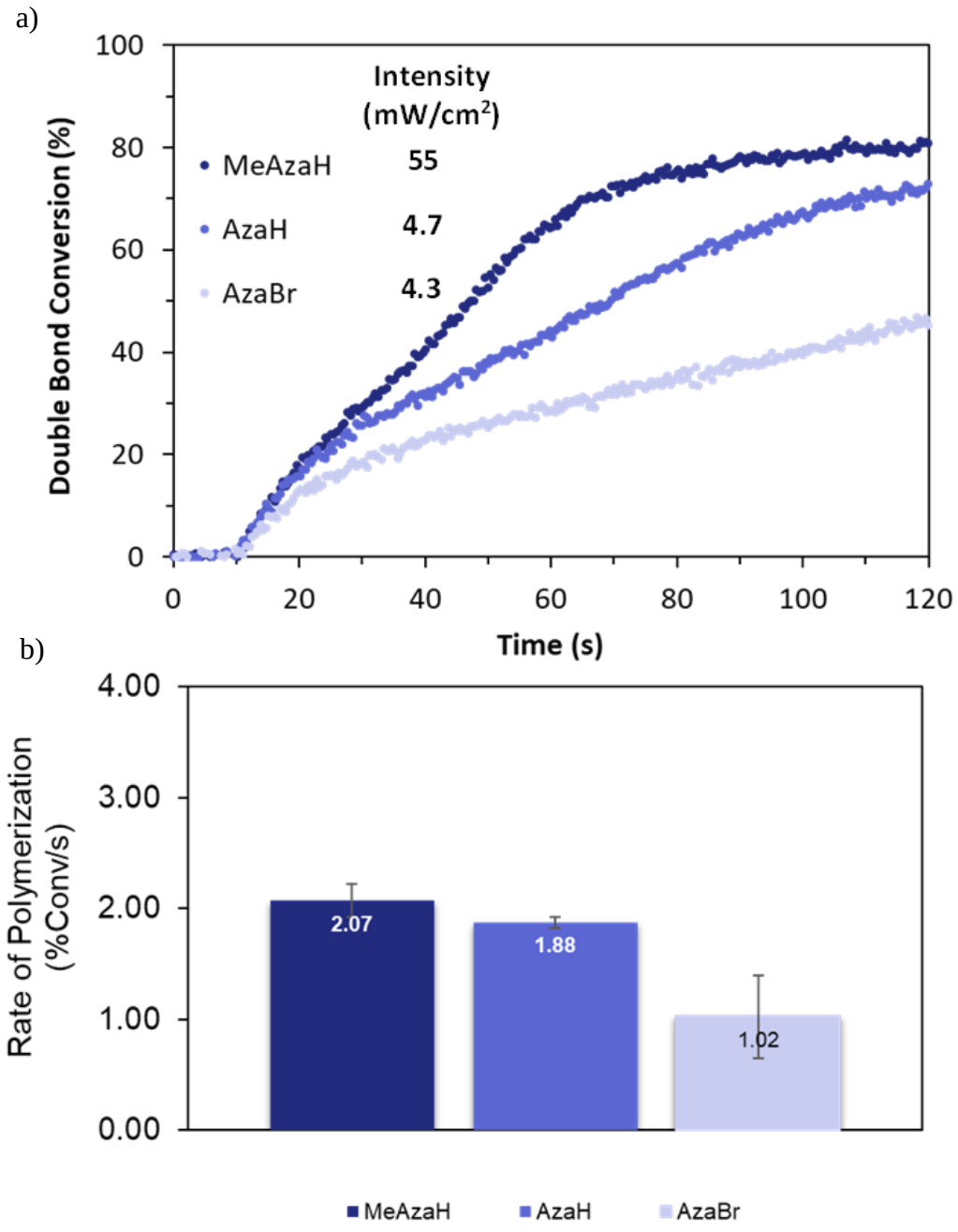

Figure 2.23: (a) Normalized Photon Flux Photopolymerizations of Isobornyl Acrylate With 2(NMe_2)-AzaH + AzaBr + MeAzaH with an 850 nm LED. (a) Double Bond Conversion vs Time ATR-FTIR Data at Varying Intensities. (b) Polymerization Rate in %Conversion/second at the Different LED Intensities. Error Bars Represent ± 1 Standard Deviation.

As a final demonstration of the utility of these NIR-azaBODIPYs, we performed rapid high resolution DLP 3D printing with NIR light using 2(NMe_2)-AzaH at 850 nm (~4 mW/cm^2). The selected photocurable resin comprised the same photosystem components described above as well as the addition of 0.005 wt% TEMPO and replaced isobornyl acrylate with 1,6-hexanediol diacrylate and trimethylolpropane triacrylate as the monomer and cross-linker in a 10:1 ratio, respectively. TEMPO was added to help avoid curing the resin bath. As the rate of polymerization for this system is slower, it reuires a longer exposure time than our green-light 3D print and thus a greater chance for curing the bath. Utilziing a resolution print (**Figure 2.24**), we determined the ideal exposure time was 30 s/layer and a layer thickness of 25 μm. With this setup, we were able to successfully 3D print a gecko (**Figure 2.24b**) and demonstrate NIR 3D printing with an LED for the first time.

a)

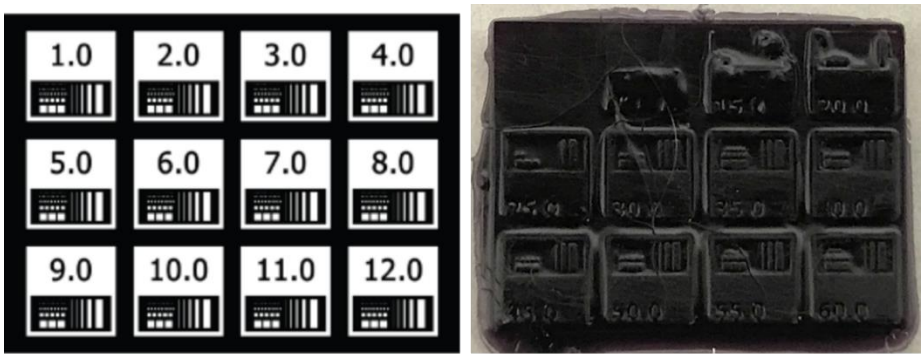

b)

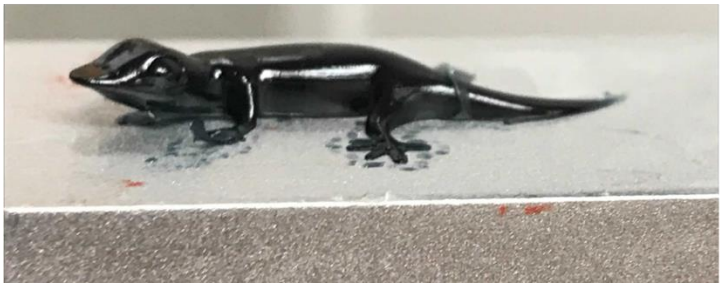

Figure 2.24: (a) Resolution Print of 2(NMe_2)-AzaH With a NIR LED at 850 nm. (b) 3D Print of a Gecko With NIR light

2.3: EXPERIMENTAL

2.31: MATERIALS

Chemicals: 3,5-dimethoxybenzaldehyde 98% was purchased from AK Scientific Inc. 4-dimethylaminoacetophenone 98.0+%, methyl magnesium bromide (MeMgBr), (3M in diethyl ether), dichloromethane (DCM) 99.9%, anhydrous, potassium hydroxide (KOH) (certified ACS), methanol (MeOH) (certified ACS), ethanol, anhydrous (EtOH),1,2-dichloroethane 99.8% (DCE), and toluene (Certified ACS) were purchased from Fisher Scientific. Acetophenone ≥99%, N-bromosuccinimide (NBS) 99.98% were purchased from Chem-Impex. 3,4,5-trimethoxyacetophenone 98%, triethylamine ≥99.5%, 3,4,5-trimethoxybenzaldehyde 98% were purchased from Sigma-Aldrich. Boron trifluoride diethyl etherate 98% was purchased from Oakwood Chemical. 3,5-dimethoxyacetophenone 95% was purchased from Combi-Blocks. 4-dimethylaminobenzaldehyde ≥98.0%, p-Anisaldehyde >99%, nitromethane >98% were purchased from TCI Chemicals. 4-methoxyacetophenone 99%, benzaldehyde 99+% and ammonium acetate ≥97.0% were purchased from Alfa Aesar. H-Nu 254, Onium Salt and Borate V were purchased from Spectra Group Limited, Inc. $CDCl_3$ 99.8% was purchased from Cambridge Isotope Laboratories. All chemicals were used as received without additional purification, unless otherwise noted.

2.32: EQUIPMENT AND INSTRUMENTATION

NUCLEAR MAGNETIC RESONANCE (NMR) SPECTROSCOPY

NMR spectra were recorded on an Agilent MR 400 MHz spectrometer utilizing $CDCl_3$ as the solvent. ^{1}H NMR were carried out coupled and referenced to the $CDCl_3$ chemical shift at 7.26 ppm. ^{13}C NMR were carried out decoupled and referenced to the $CDCl_3$ chemical shift at 77.16 ppm.

HIGH RESOLUTION MASS SPECTROMETRY (HRMS)

HRMS was performed on an Agilent Technologies 6530 Accurate-Mass Q-TOF LC/MS using ESI and the data was subsequently analyzed using Agilent MassHunter Qualitative Analysis Software.

REAL-TIME FOURIER-TRANSFORM INFRARED SPECTROSCOPY (RT-FTIR)

RT-FTIR was recorded utilizing an INVENIO-R FT-IR Spectrometer from Bruker (Figure S1) and controlled via OPUS Spectroscopy Software. A liquid nitrogen cooled (LN-MCT Mid) detector was used for measurements. A modified GladiATR Illuminate ATR accessory[36] from PIKE Technologies was used to analyze chemical composition and monitor photocuring of liquid resins upon exposure to light. Collimated LED light sources (656 nm-P/N LCS-0656-07-22, 740 nm-P/N LCS-0740-10-22, 810 nm-P/N LCS-0810-02-22, 850 nm-P/N LCS-0850-03-22, 940 nm-P/N LCS-0940-02-38) from Mightex Systems along with Lightguide Adapters were utilized to irradiate resins with visible light (see photopolymerization procedure for more details). LED Controller M/N SLC-MA02-U was used with a 3 mm liquid light guide (LLG-3- 4H).

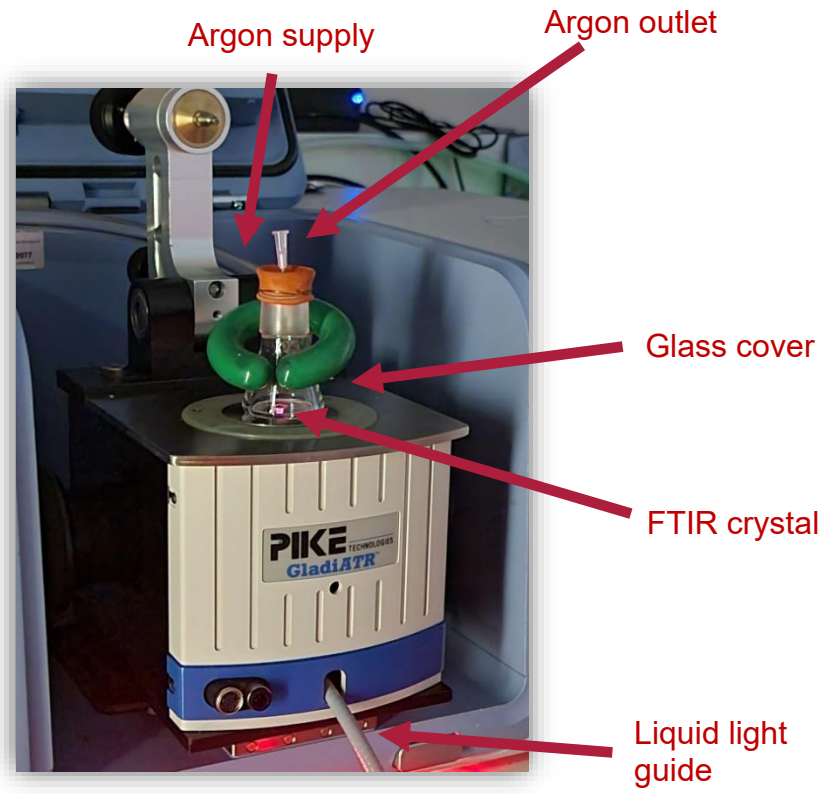

Figure 2.25: PhotoATR-FTIR Setup With Air-Free Glassware

2.33: STEADY-STATE OPTICAL CHARACTERIZATION

UV-visible absorption spectra were recorded on an Ocean Optics QE PRO-ABS Fiber Optic Spectrometer utilizing deuterium-tungsten halogen light sources (DH-2000-BAL). 600 μm fiberoptic cables (QP600-025-SR) were coupled to the detector with a slit width of 5 μm. Dilute absorption data was collected in acetonitrile utilizing quartz cuvettes and a qpod sample holder (QNW qpod2e). Thin-film absorption data was collected in the resin formulation (see photopolymerization conditions) utilizing the Ocean Optics Stage RTL-T.

2.34: TRANSIENT ABSORPTION CHARACTERIZATION

Femtosecond time-resolved experiments: Transient absorption (TA) spectra that monitored photoexcited sample dynamics on femtosecond to sub-nanosecond timescales were performed using an experimental layout described in prior work.[37,38] Briefly, excitation and probe pulses were derived from the output of a Ti:sapphire regenerative amplifier (Coherent Legend Elite Duo: 3 kHz repetition rate, ~4.2 mJ, ~90 fs). Pulses centered at 645 nm used to excite aza-H and aza-Br were created by using a β-barium borate (BBO) crystal to frequency double the signal output of a commercial optical parametric amplifier (Light Conversion, TOPAS-prime). Spectrally-broad probe pulses (450 – 800 nm) were derived via self-phase modulation by focusing a small portion of the Ti:sapphire output into a 3 mm thick c-cut sapphire window. Probe pulses were also generated by using an OPA (optical parametric amplifier) to generate a signal field at ~1200 nm that was then used to generate a continuum extending from ~550 – 1150 nm. A computer controlled optical delay stage (Newport ILS300LM) was used to scan the time of arrival of the probe at the sample with respect to the pump. Pump induced changes in probe transmission through each sample solution were detected using a Si CCD (Princeton Instruments, PyLoN 100BR) interfaced with a Czerny-Turner spectrometer (Acton Instruments SP-2556). Sample solutions were prepared by dissolving dry powder of each compound in acetonitrile. Sample solutions were housed in 1 mm path length quartz cuvettes and degassed using nitrogen prior to experiments.

2.35: ELECTRONIC CHARACTERIZATION

Cyclic voltammetry (CV) was performed in an argon-filled MBraun glovebox using the CHI 660D Electrochemistry Workstation housed within the Center for Electrochemistry at The University of Texas at Austin. A single-compartment three-electrode cell was used

with glassy carbon as the working electrode, a platinum wire as the counter electrode, and an $Ag/AgNO_3$ (0.01 M) nonaqueous reference electrode calibrated versus Fc/Fc^+ in 0.1 M tetrabutylammonium hexafluorophosphate ($TBAPF_6$) acetonitrile solutions ($E_{½}(Fc/Fc^+)$ = 0.1 V vs Ag/Ag^+) with a 0.1 V/s scan rate. Oxidation onsets were utilized to calculate the highest occupied molecular orbital (HOMO) energy levels -(4.8 eV $–E_{ox}$ (Ferrocene) + E_{ox}) and reduction onsets to calculate the lowest unoccupied molecular orbital (LUMO) energy levels -(4.8 eV $–E_{ox}$ (Ferrocene) + E_{red})[39].

2.36: LED LIGHT SOURCES

All LEDs used were purchased from Mightex Systems. The product numbers for the LEDs listed are 656 nm-P/N LCS-0656-07-22, 740 nm-P/N LCS-0740-10-22, 810 nm-P/N LCS-0810-02-22, 850 nm-P/N LCS-0850-03-22, 940 nm-P/N LCS-0940-02-38. The emission profile for each LED was measured using a calibrated UV-Vis Ocean Insight system. Irradiation intensities were measured with a Thorlabs PM100D photometer equipped with a silicon-based photodiode power sensor (S120VC, Thorlabs). Emission profiles were recorded with a QE pro spectrometer, in which the LED was connected to the fiber optic system using a 3 mm liquid lightguide from Mightex Systems (serial #: LLG-03-59-340-0800-1)

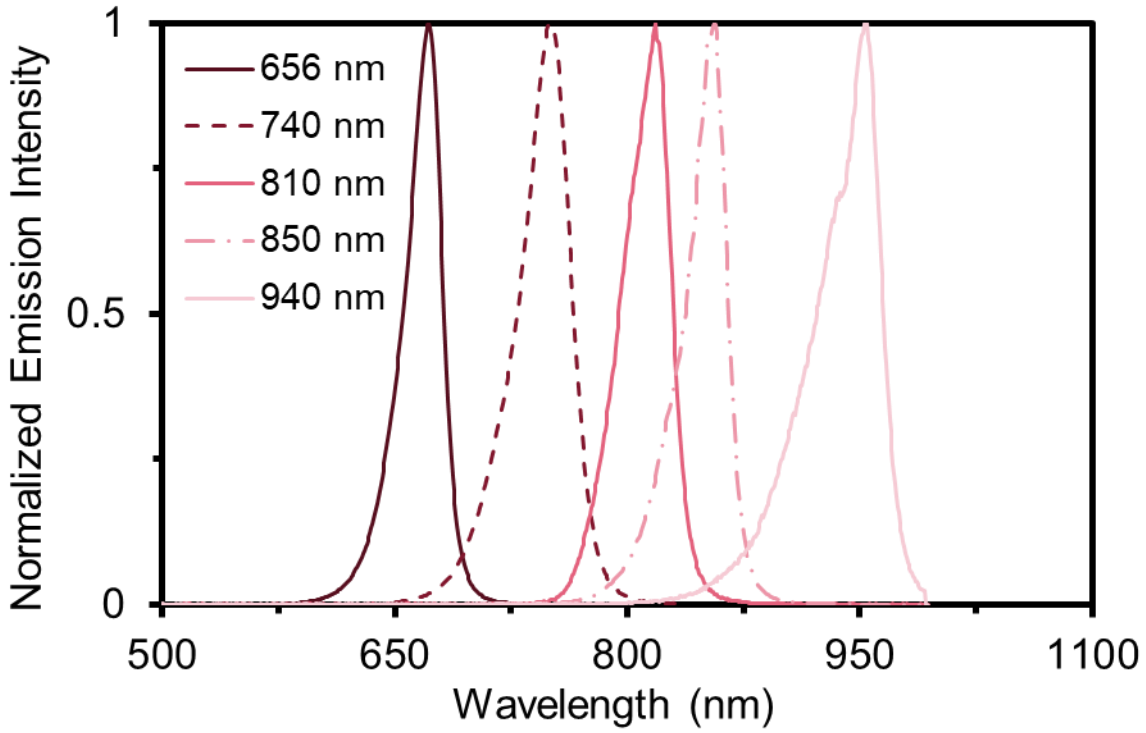

Figure 2.26: LED Emission Profiles of Red, Far-Red, and Near-IR Light Sources

2.37: 3D PRINTER

3D printing was performed using a custom, digital light processing (DLP) 3D printer (Monoprinter, MA, USA) (**Figure 1.21**). The printer was equipped with a green LED (Luminus PT-120-G) that has a peak emission wavelength at 525 nm. The light intensity measured at the resin vat floor was ~1.8 mW/cm^2, which was used for all prints in this study. Custom software (MonoWare) was used to import STL design files and digitally slice them into a sequence of 2D image files for projection. The projector resolution was 1920 × 1080 pixels, with each pixel being 20 μm x 20 μm at the image plane. The maximum build plane for the printer in its current configuration is 38.4 mm x 21.6 mm, and a vat with the dimensions of 56 mm × 35 mm × 25 mm (length × width × height) was

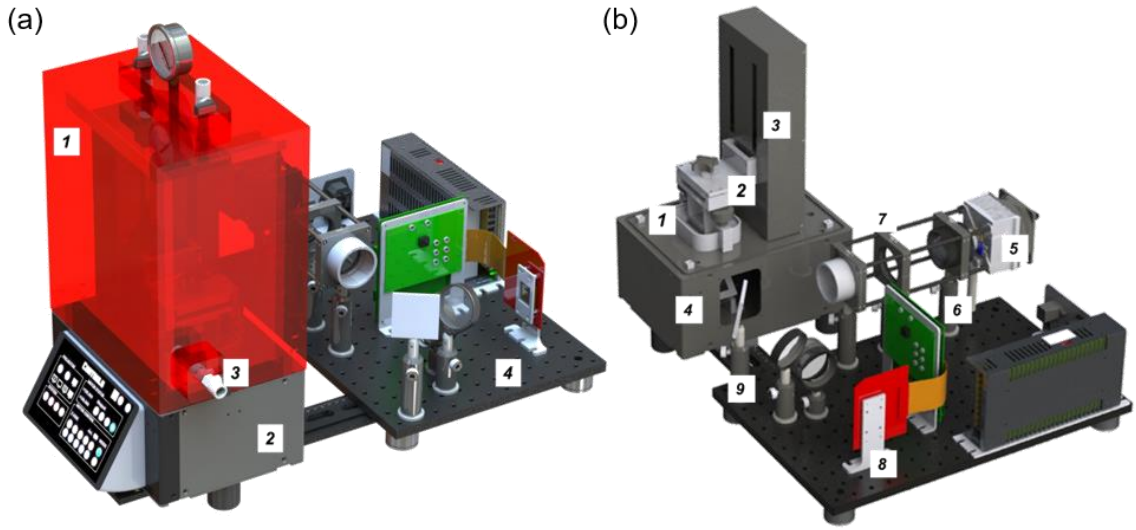

Figure 2.27: (a) 3D Printer With Acrylic Housing For Inert Gas Purging. Components: (1) N2 Chamber, (2) DLP 3D Printer, (3) N_2 Inlet, and (4) Visible LEDs Projector. (b) 3D Printer Without Acrylic Housing. Mechanical Components: (1) Resin Vat, (2) Build Platform, (3) Arduino Stage. Optical Components: (4) Mirror, (5) LED with Heat Sink, (6) Collimation lens, (7) Diffuser, (8) Digital Mirror Device (DMD), and (9) Mirror.

used. A transparent fluorinated polymer film (Teflon FEP film, DuPont, 127 µm thick) was used as the base of the resin tank to provide a non-stick and flexible surface. The octet truss model was selected to demonstrate the utility of BODIPY photocatalysts in rapid high resolution visible light 3D printing. The predetermined layer thickness for each slice of the 3D print was 25 µm, with an exposure time of 12 s for the first layer and 10 s for all subsequent layers. An opaque acrylic chamber containing a nitrogen inlet near the resin vat and an outlet at the top of the housing facilitated a light purge with nitrogen during the print to minimize oxygen inhibition. After completion of the 3D print, the printed object was post-cured for 10 minutes using a UV nail lamp (JH-818, Junhao) with a maximum emission wavelength at 370 nm and an average intensity of 4.3 mW/cm^2.

2.38: SYNTHESIS

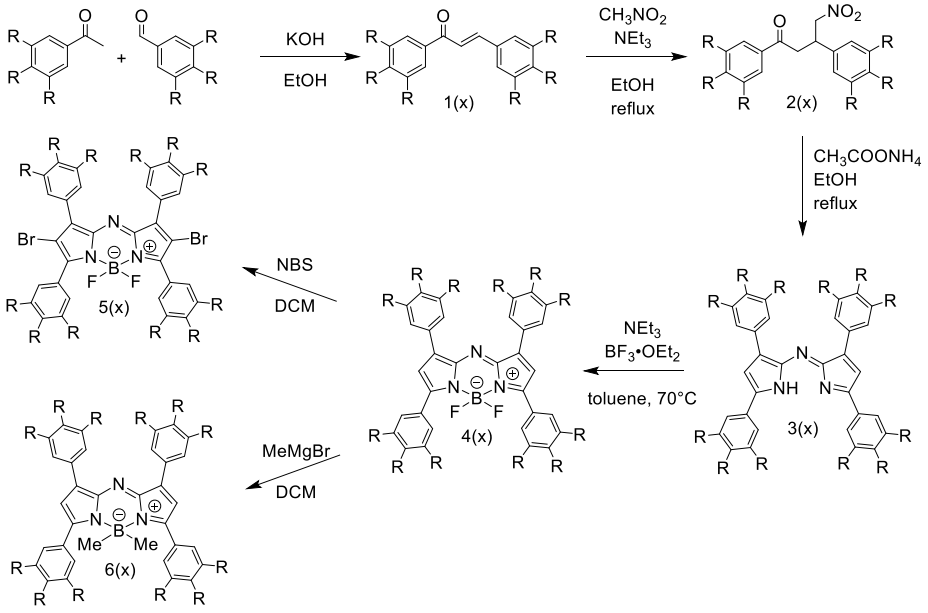

Figure 2.28: General Synthesis of EDG Aza-BODIPY Series

(E)-chalcone (1a)

Sodium hydroxide (7.33 g, 3.81 Eq, 183 mmol) in 70 mL of water and 40 mL of EtOH was added to a 250 mL round bottom flask with stir bar. The flask was subsequently placed in an ice bath. Acetophenone (17.33 g, 16.8 mL, 3 Eq, 144.2 mmol) was added to flask with stirring and then benzaldehyde (15.33 g, 14.7 mL, 3.005 Eq, 144.5 mmol). The temperature of the mixture was kept at about 25°C and the reaction mixture was stirred vigorously (2-3 hr). The stir bar was removed and the flask was placed in a -20°C freezer overnight. The resultant solid was filtered and recrystallized in EtOH at 50°C to yield 23.686 g (79%).^{1}H NMR (400 MHz, $CDCl_3$) δ 8.02-8.04 (m, 2H), 7.80-7.84 (d, *J* = 16 Hz, 1H), 7.63-7.66 (m, 2H), 7.48-7.61 (m, 4H), 7.41-7.42 (m, 3H); ^{13}C NMR (100 MHz, $CDCl_3$) δ 190.4, 144.8, 138.1, 134.8, 132.8, 130.5, 128.9, 128.6, 128.5, 128.4, 122.0; IR

(ATR): 3035, 1662, 1604, 1573, 1494, 1447, 1334, 1285, 1205, 1177, 1155, 1012, 986, 926, 864, 809, 784, 685, 658 cm^{-1}; HRMS (APCI): exact mass calculated for $C_{15}H_{12}O$ $[M+H]^+$ 209.0966, found 209.0961

(E)-1,3-bis(4-methoxyphenyl)prop-2-en-1-one (1b)

1-(4-methoxyphenyl)ethan-1-one (8.00 g, 1 Eq, 53.3 mmol) and potassium hydroxide (9.00 g, 3.01 Eq, 160 mmol) in 30 mL of ethanol was slowly added to 4-methoxybenzaldehyde (8.00 g, 7.14 mL, 1.10 Eq, 58.8 mmol) in 20 mL of ethanol. The mixture was stirred at room temperature for 1 h and filtered under vacuum. The resultant faint yellow solid was collected, washed twice with ethanol and water to yield 12.685 g (89%).^{1}H NMR (400 MHz, $CDCl_3$) δ 8.02-8.04 (d, *J* = 8 Hz, 2H), 7.76-7.80 (d, *J* = 16 Hz, 1H), 7.59-7.61 (d, *J* = 8 Hz, 2H), 7.41-7.46 (d, *J* = 20 Hz, 1H), 6.96-6.99 (d, *J* = 12 Hz, 2H), 6.92-6.94 (d, *J* = 8 Hz, 2H), 3.88 (s, 3H), 3.85 (s, 3H); ^{13}C NMR (100 MHz, $CDCl_3$) δ 188.7, 163.2, 161.5, 143.8, 131.2, 130.7, 130.1, 127.7, 119.4, 114.3, 113.8, 55.4, 50.6; IR (ATR): 2996, 2842, 1653, 1590, 1570, 1507, 1417, 1334, 1300, 1250, 1211, 1177, 1165, 1109, 1033, 1013, 984, 846, 823, 810, 748, 714, 673, 635, 607 cm^{-1}; HRMS (APCI): exact mass calculated for $C_{17}H_{16}O_3$ $[M+H]^+$ 269.1177, found 269.1171

(E)-1,3-bis(3,5-dimethoxyphenyl)prop-2-en-1-one (1c)

1-(3,5-dimethoxyphenyl)ethan-1-one (4.00 g, 1 Eq, 22.2 mmol) and potassium hydroxide (4.50 g, 3.61 Eq, 80.1 mmol) in 30 mL of ethanol was slowly added to 3,5-dimethoxybenzaldehyde (3.98 g, 1.08 Eq, 24.0 mmol) in 10 mL of ethanol. The mixture was stirred at room temperature for 1 h and filtered under vacuum. The resultant faint yellow solid was collected, washed twice with ethanol and water to yield 6.499 g (89%).^{1}H NMR (400 MHz, $CDCl_3$) δ 7.69-7.72 (d, *J* = 12 Hz, 1H), 7.38-7.42 (d, *J* = 16 Hz, 1H), 7.13-7.14 (d, *J* = 4 Hz, 2H), 6.76-6.77 (d, *J* = 4 Hz, 2H), 6.66-6.67 (t, *J* = 4 Hz, 1H), 6.51-6.52 (t, *J* = 4 Hz, 1H), 3.85 (s, 6H), 3.83 (s, 6H); ^{13}C NMR (100 MHz, $CDCl_3$)

δ 189.7, 160.9, 160.7, 144.7, 139.9, 136.6, 122.2, 106.3, 106.2, 104.8, 102.6, 55.4, 55.3; IR (ATR): 3000, 2971, 2938, 2840, 1658, 1580, 1454, 1425, 1345, 1294, 1278, 1204, 1154, 1064, 1052, 1031, 978, 921, 839, 828, 769, 677, 630, 607 cm^{-1}; HRMS (APCI): exact mass calculated for $C_{19}H_{20}O_5$ $[M+H]^+$ 329.1389, found 329.1386

(E)-1,3-bis(3,4,5-trimethoxyphenyl)prop-2-en-1-one (1d)

1-(3,4,5-trimethoxyphenyl)ethan-1-one (8.00 g, 1 Eq, 38.1 mmol) and potassium hydroxide (9.00 g, 4.22 Eq, 160 mmol) in 30 mL of ethanol was slowly added to 3,4,5-trimethoxybenzaldehyde (8.00 g, 1.07 Eq, 40.8 mmol) in 20 mL of ethanol. The mixture was stirred at room temperature for 1 h and filtered under vacuum. The resultant faint yellow solid was collected, washed twice with ethanol and water to yield 14.421 g (98%).^{1}H NMR (400 MHz, $CDCl_3$) δ 7.69-7.73 (d, *J* = 16 Hz, 1H), 7.30-7.34 (d, *J* = 16 Hz, 1H), 7.25 (s, 2H), 6.86 (s, 2H), 3.94 (s, 6H), 3.93 (s, 3H), 3.92 (s, 6H), 3.89 (s, 3H); ^{13}C NMR (100 MHz, $CDCl_3$) δ 189.4, 153.4, 153.0, 144.8, 142.4, 140.4, 133.5, 130.3, 121.4, 106.4, 105.8, 61.0, 60.8, 56.5, 56.3; IR (ATR): 3003, 2948, 2832, 1661, 1578, 1502, 1466, 1450, 1411, 1325, 1305, 1267, 1243, 1225, 1149, 1119, 1072, 993, 972, 812, 726, 609 cm^{-1}; HRMS (APCI): exact mass calculated for $C_{21}H_{24}O_7$ $[M+H]^+$ 389.1600, found 389.1596

(E)-1,3-bis(4-(dimethylamino)phenyl)prop-2-en-1-one (1e)

4-(dimethylamino)benzaldehyde (7.31 g, 1 Eq, 49.0 mmol) and 1-(4 (dimethylamino)phenyl)ethan-1-one (8.00 g, 1 Eq, 49.0 mmol) were added in EtOH (40 mL), and then an NaOH solution (8.0 g in 20 mL H2O) was added. The reaction mixture was stirred overnight, neutralized with dil. HCl and filtered. The orange solid was washed with EtOH/H20 to yield 11.376 g (79%).^{1}H NMR (400 MHz, $CDCl_3$) δ 7.97-7.99 (d, *J* = 8 Hz, 2H), 7.73-7.77 (d, *J* = 16 Hz, 1H), 7.52-7.54 (d, *J* = 8 Hz, 2H), 7.37-7.41 (d, *J* = 16 Hz, 1H), 6.69-6.70 (d, *J* = 4 Hz, 2H), 6.66-6.67 (d, *J* = 4 Hz, 2H), 3.05 (s, 6H), 3.01 (s,

6H); ^{13}C NMR (100 MHz, $CDCl_3$) δ 188.2, 153.0, 151.6, 143.7, 130.4, 129.9, 126.0, 122.8, 116.4, 111.6, 110.6, 39.8, 39.7; IR (ATR): 2973, 2893, 2801, 1637, 1595, 1570, 1547, 1520, 1431, 1366, 1340, 1234, 1162, 1049, 1025, 983, 803, 746, 677, 590 cm^{-1}; HRMS (APCI): exact mass calculated for $C_{19}H_{22}N_2O$ $[M+H]^+$ 295.1810, found 295.1811

(E)-1-(4-(tert-butyl)phenyl)-3-(4-(dimethylamino)phenyl)prop-2-en-1-one (1f)

1-(4-(tert-butyl)phenyl)ethan-1-one (8.00 g, 8.30 mL, 1 Eq, 45.4 mmol) and potassium hydroxide (9.00 g, 3.53 Eq, 160 mmol) in 30 mL of methanol was slowly added to 4-(dimethylamino)benzaldehyde (8.00 g, 1.18 Eq, 53.6 mmol) in 20 mL of methanol. The mixture was stirred at room temperature for 1 hr and filtered under vacuum. The resultant faint yellow solid was collected, washed twice with methanol and water to yield 14.0 g (100%). ^{1}H NMR (400 MHz, $CDCl_3$) δ 7.95-7.97 (d, *J* = 8.6 Hz, 2H), 7.77-7.81 (d, *J* = 15.5 Hz, 1H), 7.54-7.56 (d, *J* = 8.7 Hz, 2H), 7.49-7.51 (d, *J* = 8.3 Hz, 2H), 7.33-7.37 (d, *J* = 15.5 Hz, 1H), 6.69-6.71 (d, *J* = 8.6 Hz, 2H), 3.05 (s, 6H), 1.36 (s, 9H); ^{13}C NMR (100 MHz, $CDCl_3$) δ 190.2, 155.9, 152.0, 145.5, 136.4, 130.4, 128.3, 125.5, 122.7, 117.0, 111.9, 40.2, 35.1, 31.2; IR (ATR): 2960, 2901, 1642, 1604, 1566, 1542, 1462, 1431, 1410, 1368, 1342, 1309, 1292, 1227, 1164, 1128, 1037, 1000, 808, 683 cm^{-1}; HRMS (APCI): exact mass calculated for $C_{21}H_{25}NO$ $[M+H]^+$ 308.1936, found 308.2011

(E)-3-(4-(tert-butyl)phenyl)-1-(4-(dimethylamino)phenyl)prop-2-en-1-one (1g)

1-(4-(dimethylamino)phenyl)ethan-1-one (8.00 g, 1 Eq, 49.0 mmol) and potassium hydroxide (9.00 g, 3.27 Eq, 160 mmol) in 30 mL of methanol was slowly added to 4-(tert-butyl)benzaldehyde (8.00 g, 8.2 mL, 1.01 Eq, 49.3 mmol) in 20 mL of methanol. The mixture was stirred at room temperature for 1 hr and filtered under vacuum. The resultant orange solid was collected, washed twice with methanol and water to yield 8.635 g (57%). ^{1}H NMR (400 MHz, $CDCl_3$) δ 7.99-8.02 (d, *J* = 8.7 Hz, 2H), 7.76-7.80 (d, *J* = 15.5 Hz, 1H), 7.53-7.61 (m, 3H), 7.42-7.44 (d, *J* = 8.1 Hz, 2H), 6.70-6.72 (d, *J* =

8.6 Hz, 2H), 3.08 (s, 6H), 1.34 (s, 9H); ^{13}C NMR (100 MHz, $CDCl_3$) δ 188.1, 153.6, 142.6, 132.8, 130.9, 128.2, 126.1, 125.9, 121.5, 110.9, 40.1, 35.0, 31.3; IR (ATR): 2949, 2900, 2863, 1698, 1644, 1596, 1583, 1542, 1464, 1434, 1376, 1305, 1233, 1169, 1107, 1019, 946, 829, 755, 744 cm^{-1}; HRMS (APCI): exact mass calculated for $C_{21}H_{25}NO$ $[M+H]^+$ 308.1936, found 308.2015

(E)-1-(4-(tert-butyl)phenyl)-3-(3,4,5-trimethoxyphenyl)prop-2-en-1-one (1h).

1-(4-(tertbutyl)phenyl)ethan-1-one (8.00 g, 8.30 mL, 1 Eq, 45.4 mmol) and potassium hydroxide (9.00 g, 3.53 Eq, 160 mmol) in 30 mL of methanol was slowly added to 3,4,5-trimethoxybenzaldehyde S8 (8.00 g, 0.898 Eq, 40.8 mmol) in 20 mL of methanol. The mixture was stirred at room temperature for 1 h and filtered under vacuum. The resultant faint yellow solid was collected and washed twice with methanol and water to yield the desired product as a faint yellow solid (12.880 g, 89%). ^{1}H NMR (400 MHz, $CDCl_3$) δ 7.95-7.98 (d, J = 8.8 Hz, 2H), 7.69-7.73 (d, J = 15.6 Hz, 1H), 7.51-7.53 (d, J = 8.8 Hz, 2H), 7.39-7.43 (d, J = 15.6 Hz, 1H), 6.86 (s, 2H), 3.92 (s, 6H), 3.90 (s, 3H), 1.36 (s, 9H); ^{13}C NMR (100 MHz, $CDCl_3$) δ 190.1, 156.5, 153.4, 144.5, 140.3, 135.6, 130.5, 128.5, 125.6, 121.6, 105.6, 60.9, 56.2, 35.1, 31.1; IR (ATR): 2962, 2938, 2905, 1651, 1580, 1501, 1451, 1417, 1327, 1318, 1278, 1245, 1218, 1191, 1153, 1004, 825, 525, 516 cm^{-1}; HRMS (ESI): exact mass calculated for $C_{22}H_{26}O_4$ $[M+H]^+$ 355.1909, found 355.1904

4-nitro-1,3-diphenylbutan-1-one (2a)

1a (8.00 g, 1 Eq, 38.4 mmol), triethylamine (16.3 g, 22.5 mL, 4.2 Eq, 161 mmol), and nitromethane (14.3 g, 12.5 mL, 6.1 Eq, 234 mmol) were dissolved in 80 mL of MeOH. Reaction mixture was refluxed @65°C overnight. Solvent was removed via rotavap to yield 8.972 g (87%) of a brown solid.^{1}H NMR (400 MHz, $CDCl_3$) δ 7.87-7.88 (d, *J* = 4 Hz, 2H), 7.52-7.55 (t, *J* = 6 Hz, 1H), 7.39-7.43 (t, *J* = 8 Hz, 2H), 7.22-7.31 (m, 5H), 4.77-4.82 (dd, *J* = 8, 12 Hz, 1H), 4.62-4.68 (dd, *J* = 8, 12 Hz, 1H), 4.15-4.22 (p, *J* = 12 Hz,

1H), 3.35-3.48 (m, 2H); ^{13}C NMR (100 MHz, $CDCl_3$) δ 197.1, 139.0, 136.2, 133.1, 129.1, 128.8, 127.9, 127.6, 127.3, 79.4, 41.4, 39.2; IR (ATR): 2975, 2939, 2826, 1689, 1542, 1449, 1370, 1195, 1028, 771, 757, 743, 702, 683, 627, 606 cm^{-1}; HRMS (APCI): exact mass calculated for $C_{16}H_{15}NO_3$ $[M+H]^+$ 270.1130, found 270.1124

1,3-bis(4-methoxyphenyl)-4-nitrobutan-1-one (2b)

1b (5.00 g, 1 Eq, 18.6 mmol) was dissolved in a mixture of ethanol (40 mL), triethylamine (30 mL, 11.5 Eq, 215 mmol) and nitromethane (16 mL, 16.0 Eq, 299 mmol), and then they reacted under reflux for 24 h. The solution was cooled and neutralized with 1 M HCl, and CH_2Cl_2 (3×100 mL) was used to extract the crude product. $MgSO_4$ was used to dry the combined organics. The solvent was reduced via rotavap and purified via column chromatography (Hexane:EtOAc) to yield 2.576 g (42%) of a light yellow solid. ^{1}H NMR (400 MHz, $CDCl_3$) δ 7.86-7.89 (d, *J* = 12 Hz, 2H), 7.16-7.19 (d, *J* = 12 Hz, 2H), 6.88-6.91 (d, *J* = 12 Hz, 2H), 6.81-6.84 (d, *J* = 12 Hz, 2H), 4.76-4.80 (dd, *J* = 4, 12 Hz, 1H), 4.58-4.64 (dd, *J* = 8, 14 Hz, 1H), 4.10-4.17 (p, *J* = 8 Hz, 1H), 3.83 (s, 3H), 3.74 (s, 3H), 3.27-3.39 (m, 2H); ^{13}C NMR (100 MHz, $CDCl_3$) δ 195.6, 163.7, 158.3, 131.1, 130.2, 129.3, 128.4, 114.2, 113.7, 79.8, 55.4, 55.0, 41.1, 38.7; IR (ATR): 3002, 2959, 2839, 1672, 1598, 1575, 1547, 1511, 1461, 1420, 1377, 1305, 1248, 1210, 1168, 1114, 1026, 994, 977, 828, 809, 603, 561 cm^{-1}; HRMS (APCI): exact mass calculated for $C_{18}H_{19}NO_5$ $[M+H]^+$ 330.1341, found 330.1340

1,3-bis(3,5-dimethoxyphenyl)-4-nitrobutan-1-one (2c)

1c (3.00 g, 1 Eq, 9.14 mmol), triethylamine (3.07 g, 4.3 mL, 4.6 Eq, 42.0 mmol), and nitromethane (3.68 g, 3.23 mL, 6.6 Eq, 60.3 mmol) were dissolved in 20 mL of EtOH. Reaction mixture was refluxed at 85°C overnight. The solvent was reduced via rotavap and purified via column chromatography (Hexane:EtOAc) to yield 3.478 g (98%) of a light yellow solid. ^{1}H NMR (400 MHz, $CDCl_3$) δ 7.03-7.04 (d, *J* = 4 Hz, 2H), 6.64-6.65

(t, *J* = 4 Hz, 1H), 6.40-6.41 (d, *J* = 4 Hz, 2H), 6.34-6.35 (t, *J* = 4 Hz, 1H), 4.74-4.79 (dd, *J* = 8, 12 Hz, 1H), 4.61-4.66 (dd, *J* = 8, 12 Hz, 1H), 4.10-4.17 (m, 1H), 3.81 (s, 6H), 3.76 (s, 6H), 3.29-3.43 (m, 2H); ^{13}C NMR (100 MHz, $CDCl_3$) δ 196.4, 160.9, 160.7, 141.5, 138.0, 105.6, 105.5, 105.3, 98.9, 79.1, 55.2, 55.0, 41.3, 39.4; IR (ATR): 2978, 2946, 2882, 1596, 1551, 1475, 1443, 1397, 1384, 1364, 1205, 1171, 1071, 1035, 850, 807 cm^{-1}; HRMS (APCI): exact mass calculated for $C_{20}H_{23}NO_7$ $[M+H]^+$ 390.1553, found 390.1553

4-nitro-1,3-bis(3,4,5-trimethoxyphenyl)butan-1-one (2d)

1d (5.00 g, 1 Eq, 12.9 mmol) was dissolved in a mixture of ethanol (40 mL), triethylamine (30 mL, 17 Eq, 220 mmol) and nitromethane (16 mL, 23 Eq., 300 mmol), and then they reacted under reflux for 24 h. The solution was cooled and neutralized with 1 M HCl, and CH_2Cl_2 (3×100 mL) was used to extract the crude product. $MgSO_4$ was used to dry the combined organics. The solvent was cleaned up under reduced pressure to yield 4.965 g (86%) of a brown solid. ^{1}H NMR (400 MHz, $CDCl_3$) δ 7.11 (s, 2H), 6.44 (s, 2H), 4.76-4.81 (dd, *J* = 8, 14 Hz, 1H), 4.63-4.68 (dd, *J* = 8, 12 Hz, 1H), 4.07-4.14 (p, *J* = 8 Hz, 1H), 3.86 (s, 3H), 3.85 (s, 6H), 3.79 (s, 6H), 3.76 (s, 3H), 3.27-3.40 (m, 2H); ^{13}C NMR (100 MHz, $CDCl_3$) δ 195.7, 153.2, 152.8, 142.6, 137.1, 134.7, 131.4, 105.4, 104.4, 79.1, 60.7, 60.5, 56.1, 56.0, 41.3, 39.8; IR (ATR): 2939, 2906, 2837, 1673, 1583, 1540, 1504, 1463, 1429, 1368, 1322, 1253, 1164, 1121, 1057, 1000, 889, 840, 778, 662 cm^{-1}; HRMS (APCI): exact mass calculated for $C_{22}H_{27}NO_9$ $[M+H]^+$ 450.1764, found 450.1771

1,3-bis(4-(dimethylamino)phenyl)-4-nitrobutan-1-one (2e)

1e (6.100 g, 1 Eq, 20.72 mmol) was dissolved in a mixture of ethanol (40 mL), triethylamine (10.9 mL, 4.6 Eq., 78.13 mmol) and nitromethane (6.00 mL, 6.6 Eq., 112.1 mmol), and then they reacted under reflux for 24 h. The solution was cooled and neutralized with 1 M HCl, and CH_2Cl_2 (3×100 mL) was used to extract the crude product. $MgSO_4$ was used to dry the combined organics. The solvent was cleaned up under

reduced pressure to yield 4.068 g (55%) of a brown solid. ^{1}H NMR (400 MHz, $CDCl_3$) δ 7.82-7.84 (d, *J* = 8 Hz, 2H), 7.12-7.14 (d, *J* = 8 Hz, 2H), 6.66-6.68 (d, *J* = 8 Hz, 2H), 6.61-6.63 (d, *J* = 8 Hz, 2H), 4.78-4.83 (dd, *J* = 8, 12 Hz, 1H), 4.58-4.63 (dd, *J* = 8, 12 Hz, 1H), 4.05-4.12 (m, 1H), 3.21-3.34 (m, 2H), 3.05 (s, 6H), 2.91 (s, 6H); ^{13}C NMR (100 MHz, $CDCl_3$) δ 195.2, 153.6, 150.0, 130.3, 128.1, 127.0, 124.5, 112.8, 110.7, 80.2, 41.1, 40.5, 40.0, 39.0; IR (ATR): 2878, 2809, 1661, 1598, 1547, 1525, 1482, 1433, 1373, 1354, 1270, 1231, 1169, 1125, 1064, 983, 946, 804, 785, 682, 566 cm^{-1}; HRMS (APCI): exact mass calculated for $C_{20}H_{25}N_3O_3$ $[M+H]^+$ 356.1974, found 356.1970

1-(4-(tert-butyl)phenyl)-3-(4-(dimethylamino)phenyl)-4-nitrobutan-1-one (2f)

1f (7.000 g, 1 Eq, 22.77 mmol) was dissolved in a mixture of ethanol (40 mL), triethylamine (14.6 mL, 4.6 Eq., 104.7 mmol) and nitromethane (8.05 mL, 6.6 Eq., 150.3 mmol) and was subsequently reacted under reflux for 24 hr. The solution was cooled and neutralized with 1 M HCl, and CH_2Cl_2 (3×100 mL) was used to extract the crude product. $MgSO_4$ was used to dry the combined organics. The solvent was removed under reduced pressure to yield __ g of a brown solid (%). ^{1}H NMR (400 MHz, $CDCl_3$) δ 7.85-7.87 (d, *J* = 8.4 Hz, 2H), 7.45-7.47 (d, *J* = 8.4 Hz, 2H), 7.12-7.14 (d, *J* = 8.7 Hz, 2H), 6.66-6.68 (d, *J* = 8.8 Hz, 2H), 4.76-4.80 (dd, *J* = 12.1, 6.7 Hz, 1H), 4.60-4.65 (dd, *J* = 12.1, 8.0 Hz, 1H), 4.08-4.15 (q, *J* = 7.1 Hz, 1H), 3.36-3.40 (dd, *J* = 8.8, 7.0 Hz, 2H) 2.92 (s, 6H), 1.33 (s, 9H); ^{13}C NMR (100 MHz, $CDCl_3$) δ 197.0, 157.4, 150.1, 134.1, 128.2, 128.1, 126.6, 125.8, 112.9, 80.2, 45.7, 41.8, 40.6, 38.7, 35.3, 31.2; IR (ATR): 2964, 2889, 2809, 1672, 1605, 1543, 1525, 1476, 1444, 1374, 1299, 1239, 1191, 1124, 1060, 1003, 868, 797, 643, 632 cm^{-1}; HRMS (APCI): exact mass calculated for $C_{22}H_{28}N_2O_3$ $[M+H]^+$ 369.2099, found 369.2176

3-(4-(tert-butyl)phenyl)-1-(4-(dimethylamino)phenyl)-4-nitrobutan-1-one (2g)

1g (5.00 g, 1 Eq, 16.3 mmol) was dissolved in a mixture of ethanol (40 mL), triethylamine (10.4 mL, 4.6 Eq., 74.8 mmol) and nitromethane (5.75 mL, 6.6 Eq., 107 mmol) and was subsequently reacted under reflux for 24 hr. The solution was cooled and neutralized with 1 M HCl, and CH_2Cl_2 (3×100 mL) was used to extract the crude product. $MgSO_4$ was used to dry the combined organics. The solvent was removed under reduced pressure to yield __ g of a brown solid (%). ^{1}H NMR (400 MHz, $CDCl_3$) δ 7.68-7.71 (d, *J* = 9.1 Hz, 2H), 7.19-7.21 (d, *J* = 8.1 Hz, 2H), 7.07-7.09 (d, *J* = 8.2 Hz, 2H), 6.49-6.51 (d, *J* = 8.9 Hz, 2H), 4.69-4.73 (dd, *J* = 12.6, 6.1 Hz, 1H), 4.51-4.57 (dd, *J* = 12.5, 8.7 Hz, 1H), 4.02-4.07 (m, 1H), 3.11-3.26 (m, 2H), 2.92 (s, 6H), 1.15 (s, 9H); ^{13}C NMR (100 MHz, $CDCl_3$) δ 195.0, 153.7, 150.5, 136.7, 130.4, 127.2, 126.0, 124.5, 110.8, 79.8, 41.0, 40.1, 39.2, 34.6, 31.4; IR (ATR): 2960, 2882, 1655, 1598, 1547, 1513, 1479, 1432, 1408, 1378, 1336, 1314, 1270, 1182, 1067, 1004, 981, 833, 809, 581 cm^{-1}; HRMS (APCI): exact mass calculated for $C_{22}H_{28}N_2O_3$ $[M+H]^+$ 369.2099, found 369.2180

1-(4-(tert-butyl)phenyl)-4-nitro-3-(3,4,5-trimethoxyphenyl)butan-1-one (2h)

1h (10.796 g, 1 Eq, 30.458 mmol), triethylamine (13 g, 18 mL, 4.2 Eq, 0.13 mol), and nitromethane (11 g, 10 mL, 6.1 Eq, 0.19 mol) were dissolved in 80 mL of MeOH. The reaction mixture was refluxed at 65°C overnight. Upon cooling the reaction, solvent was removed under reduced pressure using rotary evaporation, followed by recrystallization of the crude product in MeOH to yield the desired product as a white solid (12.035 g, 95%). ^{1}H NMR (400 MHz, $CDCl_3$) δ 7.85-7.87 (d, J = 8.8 Hz, 2H), 7.46-7.48 (d, J = 8.8 Hz, 2H), 6.46 (s, 2H), 4.79-4.84 (dd, J = 12.5, 6.6 Hz, 1H), 4.65-4.70 (dd, J = 12.5, 8.1 Hz, 1H), 4.12-4.21 (m, 1H), 3.84 (s, 6H), 3.81 (s, 3H), 3.32-3.47 (qd, J = 17.5, 6.9 Hz, 2H), 1.33 (s, 9H); ^{13}C NMR (100 MHz, $CDCl_3$) δ 196.9, 157.6, 153.5, 137.5, 134.9, 133.9, 128.1, 125.8, 104.6, 79.5, 60.8, 56.2, 50.6, 41.6, 39.8, 35.2, 31.0; IR (ATR): 2959, 2841, 1681, 1592, 1545, 1513, 1462, 1427, 1406, 1378, 1358, 1321, 1272, 1251, 1236,

1159, 993, 826, 658 cm^{-1}; HRMS (ESI): exact mass calculated for $C_{23}H_{29}NO_6$ $[M+Na]^+$ 438.1892, found 438.1894

(Z)-N-(3,5-diphenyl-1H-pyrrol-2-yl)-3,5-diphenyl-2H-pyrrol-2-imine (3a)

2a (4.10 g, 1 Eq, 15.2 mmol) and ammonium acetate (18.8 g, 16 Eq, 244 mmol) were dissolved in 100 mL of ethanol and were refluxed for 24 h. After cooling down to room temperature, the reaction mixture was filtered to give a metallic dark red solid, which was washed with ethanol followed by water to yield 0.951 g (14%).^{1}H NMR (400 MHz, $CDCl_3$) δ 8.05-8.07 (d, *J* = 8 Hz, 4H), 7.95-7.97 (d, *J* = 8 Hz, 4H), 7.36-7.56 (m, 12H), 7.21 (s, 2H); ^{13}C NMR (100 MHz, $CDCl_3$) δ 150.8, 142.8, 131.6, 130.2, 129.3, 129.2, 129.0, 128.4, 128.3, 128.2, 126.7, 115.1; IR (ATR): 3047, 1541, 1487, 1464, 1438, 1408, 1348, 1316, 1289, 1261, 1230, 1168, 1137, 1073, 1009, 960, 929, 902, 797, 755, 684, 656 cm^{-1}; HRMS (APCI): exact mass calculated for $C_{32}H_{23}N_3$ $[M+H]^+$ 450.1970, found 450.1972

(Z)-N-(3,5-bis(4-methoxyphenyl)-1H-pyrrol-2-yl)-3,5-bis(4-methoxyphenyl)-2H-pyrrol-2-imine (3b)

The mixture of 2b (2.576 g, 1 Eq, 7.821 mmol), ammonium acetate (9.50 g, 15.8 Eq, 123 mmol) and ethanol (40 mL) reacted under reflux for 24 h. The reaction mixture was cooled to room temp and subsequently filtered and the solid washed with cold ethanol to yield 0.834 g (19%) of a dark blue solid. ^{1}H NMR (400 MHz, $CDCl_3$) δ 8.01-8.03 (br, 4H), 7.87-7.89 (br, 4H), 7.03-7.05 (br, 6H), 6.95-6.96 (br, 4H), 3.91 (s, 6H), 3.88 (s, 6H); ^{13}C NMR (100 MHz, $CDCl_3$) δ 161.2, 159.6, 154.1, 141.7, 130.4, 128.1, 125.2, 114.6, 114.1, 113.7, 112.9, 55.5, 55.4; IR (ATR): 2991, 2949, 2830, 1598, 1495, 1451, 1420, 1247, 1176, 1163, 1140, 1106, 1032, 1000, 962, 903, 838, 802, 784, 769, 645, 620, 590, 568 cm^{-1}; HRMS (APCI): exact mass calculated for $C_{36}H_{31}N_3O_4$ $[M+H]^+$ 570.2393, found 570.2387

(Z)-N-(3,5-bis(3,5-dimethoxyphenyl)-1H-pyrrol-2-yl)-3,5-bis(3,5-dimethoxyphenyl)-2H-pyrrol-2-imine (3c)

The mixture of 2c (3.478 g, 1 Eq, 8.932 mmol), ammonium acetate (14.1 g, 20.5 Eq, 183 mmol) and EtOH (40 mL) were reacted under reflux for 24 hr. The reaction mixture was cooled to room temperature and the residue was filtered and subsequently washed with cold ethanol to yield 0.786 g (13%) of a dark blue solid. ^{1}H NMR (400 MHz, $CDCl_3$) δ 7.08-7.11 (m, 10H), 6.55-6.56 (t, *J* = 4 Hz, 2H), 6.47-6.48 (t, *J* = 4 Hz, 2H), 3.90 (s, 12H), 3.70 (s, 12H); ^{13}C NMR (100 MHz, $CDCl_3$) δ 161.4, 160.7, 160.2, 155.0, 149.5, 142.9, 135.7, 133.9, 116.0, 107.0, 105.6, 104.7, 102.3, 101.0, 55.7, 55.4; IR (ATR): 3002, 2936, 2836, 1587, 1546, 1453, 1423, 1296, 1198, 1150, 1062, 1008, 946, 925, 835, 807, 765, 745, 694, 673, 638 cm^{-1}; HRMS (APCI): exact mass calculated for $C_{40}H_{39}N_3O_8$ $[M+H]^+$ 690.2815, found 690.2822

(Z)-N-(3,5-bis(3,4,5-trimethoxyphenyl)-1H-pyrrol-2-yl)-3,5-bis(3,4,5-trimethoxyphenyl)-2H-pyrrol-2-imine (3d)

The mixture of 2d (5.79 g, 1 Eq, 12.9 mmol), ammonium acetate (29.7 g, 29.9 Eq, 385 mmol) and EtOH (40 mL) reacted under reflux for 24. The reaction mixture was cooled to room temperature and the residue was filtered and subsequently washed with cold ethanol to yield 2.085 g (20%) of a dark blue solid. ^{1}H NMR (400 MHz, $CDCl_3$) δ 7.15-7.16 (d, *J* = 4 Hz, 8H), 7.03 (s, 2H), 3.97(s, 12H), 3.94 (s, 6H), 3.91 (s, 6H), 3.72 (s, 12H); ^{13}C NMR (100 MHz, $CDCl_3$) δ 154.9, 154.0, 153.2, 149.5, 143.0, 141.2, 138.4, 129.5, 128.0, 115.2, 106.9, 106.2, 105.5, 104.8, 61.2, 57.1, 57.0, 56.2, 55.9; IR (ATR): 3001, 2937, 2823, 1562, 1500, 1468, 1445, 1415, 1328, 1118, 1064, 997, 956, 875, 851, 809, 792, 783, 761, 753, 720, 616 cm^{-1}; HRMS (APCI): exact mass calculated for $C_{44}H_{47}N_3O_{12}$ $[M+H]^+$ 810.3238, found 810.3250

(Z)-4,4'-(2-((3,5-bis(4-(dimethylamino)phenyl)-1H-pyrrol-2-yl)imino)-2H-pyrrole-3,5-diyl)bis(N,N-dimethylaniline) (3e)

The mixture of 2e (6.00 g, 1 Eq, 16.9 mmol), ammonium acetate (38.9 g, 29.9 Eq, 505 mmol) and ethanol (40 mL) reacted under reflux for 24 hr. The reaction mixture was cooled to room temperature and residue was filtered and subsequently washed with cold ethanol to yield 1.233 g (12%) of a dark blue solid. ^{1}H NMR (400 MHz, $CDCl_3$) δ 8.04-8.06 (d, *J* = 8 Hz, 4H), 7.84-7.86 (d, *J* = 8 Hz, 4H), 6.98 (s, 2H), 6.77-6.81 (t, *J* = 8 Hz, 8H), 3.07 (s, 12H), 3.03 (s, 12H); ^{13}C NMR (100 MHz, $CDCl_3$) δ 151.0, 149.8, 131.5, 130.2, 130.1, 130.0, 128.1, 127.9, 127.7, 126.9, 112.1, 112.0, 111.8, 110.8, 110.6, 40.4, 40.2; IR (ATR): 2881, 2845, 2792, 1596, 1503, 1426, 1343, 1321, 1244, 1184, 1159, 1137, 1112, 1055, 942, 898, 792, 740, 613, 563 cm^{-1}; HRMS (APCI): exact mass calculated for $C_{40}H_{43}N_7$ $[M+H]^+$ 622.3658, found 622.3656

(Z)-4-(5-(4-(tert-butyl)phenyl)-2-((5-(4-(tert-butyl)phenyl)-3-(4-(dimethylamino)phenyl)-1H-pyrrol-2-yl)imino)-2H-pyrrol-3-yl)-N,N-dimethylaniline (3f)

The mixture of 2f (8.390 g, 1 Eq, 22.77 mmol), ammonium acetate (28.08 g, 16 Eq, 364.3 mmol) and ethanol (40 mL) reacted under reflux for 24 hr. The reaction mixture was cooled to room temperature and the residue was filtered and subsequently washed with cold ethanol to yield 3.399 g (23%) of a dark blue solid. ^{1}H NMR (400 MHz, $CDCl_3$) δ 8.04-8.06 (d, *J* = 8.9 Hz, 4H), 7.88-7.90 (d, *J* = 8.4 Hz, 4H), 7.54-7.56 (d, *J* = 8.4 Hz, 4H), 7.04 (s, 2H), 6.78-6.80 (d, *J* = 8.9 Hz, 4H), 3.04 (s, 12H), 1.41 (s, 18H); ^{13}C NMR (100 MHz, $CDCl_3$) δ 150.3, 130.4, 126.4, 126.2, 112.2, 111.9, 40.6, 35.1, 31.4; IR (ATR): 2961, 2865, 1606, 1576, 1538, 1504, 1460, 1429, 1412, 1341, 1298, 1241, 1167, 1139, 1047, 1011, 906, 832, 795, 745 cm^{-1}; HRMS (APCI): exact mass calculated for $C_{44}H_{49}N_5$ $[M+H]^+$ 648.3988, found 648.4056

(Z)-4-(3-(4-(tert-butyl)phenyl)-2-((3-(4-(tert-butyl)phenyl)-5-(4-(dimethylamino)phenyl)-1H-pyrrol-2-yl)imino)-2H-pyrrol-5-yl)-N,N-dimethylaniline (3g)

The mixture of 2g (5.99 g, 1 Eq, 16.3 mmol), ammonium acetate (20.0 g, 16 Eq, 260 mmol) and ethanol (40 mL) reacted under reflux for 24 hr. The reaction mixture was cooled to room temperature and the residue was filtered and subsequently washed with cold ethanol to yield 2.279 g (22%) of a dark blue solid. ^{1}H NMR (400 MHz, $CDCl_3$) δ 8.01-8.03 (d, *J* = 8.5 Hz, 4H), 7.84-7.86 (d, *J* = 8.6 Hz, 4H), 7.43-7.45 (d, *J* = 8.5 Hz, 4H), 7.08 (s, 2H), 6.81-6.83 (d, *J* = 9.0 Hz, 4H), 3.09 (s, 12H), 1.39 (s, 18H); ^{13}C NMR (100 MHz, $CDCl_3$) δ 153.9, 151.4, 150.4, 149.4, 141.2, 131.8, 129.0, 128.0, 125.0, 120.4, 113.3, 112.3, 40.4, 34.7, 31.5; IR (ATR): 2954, 2899, 2861, 1653, 1596, 1572, 1541, 1508, 1459, 1407, 1359, 1296, 1202, 1184, 1106, 1020, 970, 820, 788, 717 cm^{-1}; HRMS (APCI): exact mass calculated for $C_{44}H_{49}N_5$ $[M+H]^+$ 648.3988, found 648.4060

(Z)-5-(4-(tert-butyl)phenyl)-N-(5-(4-(tert-butyl)phenyl)-3-(3,4,5-trimethoxyphenyl)-1Hpyrrol-2-yl)-3-(3,4,5-trimethoxyphenyl)-2H-pyrrol-2-imine (3h)

2h (2.00 g, 1 Eq, 4.81 mmol) and ammonium acetate (5.94 g, 16 Eq, 77.0 mmol) were dissolved in 100 mL of methanol and refluxed for 24 h. After cooling down to room temperature, the reaction mixture was filtered under reduced pressure to give a metallic dark black solid, which was washed with methanol followed by water to yield the desired product as a black solid (422 mg, 12%). ^{1}H NMR (400 MHz, $CDCl_3$) δ 7.90-7.92 (d, J = 8.5 Hz, 4H), 7.57-7.59 (d, J = 8.5 Hz, 4H), 7.16 (s, 4H), 7.11 (s, 2H), 3.91 (s, 6H), 3.72 (s, 12H), 1.42 (s, 18H); ^{13}C NMR (100 MHz, $CDCl_3$) δ 154.9, 153.8, 153.1, 149.4, 142.7, 138.1, 129.7, 129.4, 126.5, 126.3, 114.9, 106.4, 61.0, 56.0, 35.1, 31.3; IR (ATR): 2998, 2962, 2825, 1567, 1545, 1493, 1461, 1411, 1363, 1321, 1306, 1281, 1264, 1239, 1186,

1031, 796, 713, 650 cm^{-1}; HRMS (ESI): exact mass calculated for $C_{46}H_{51}N_3O_6$ $[M+H]^+$ 742.3856, found 742.3854

5,5-difluoro-1,3,7,9-tetraphenyl-5H-4l4,5l4-dipyrrolo[1,2-c:2',1'-f][1,3,5,2]triazaborinine (4a)

Boron trifluoride diethyl etherate (1.03 mL, 15.0 Eq, 8.34 mmol) was slowly added into the mixture of dry CH_2Cl_2 (20 mL), 3a (250 mg, 1 Eq, 556 µmol) and DIPEA (2.52 mL, 26 Eq, 14.5 mmol), which then reacted at 25 °C for 4 h to yield 187 mg (68%) of a dark blue solid. ^{1}H NMR (400 MHz, $CDCl_3$) δ 8.04-8.09 (m, 8H), 7.44-7.50 (m, 12H), 7.05 (s, 2H); ^{13}C NMR (100 MHz, $CDCl_3$) δ 159.7, 145.7, 144.3, 132.4, 131.7, 131.3, 130.8, 129.8, 129.6, 129.4, 129.0, 128.5, 128.3, 119.6; IR (ATR): 3054, 1514, 1476, 1453, 1398, 1275, 1223, 1121, 1091, 1063, 1030, 1000, 974, 943, 819, 754, 738, 692, 675, 660, 617 cm^{-1}; HRMS (EI): exact mass calculated for $C_{32}H_{22}BF_2N_3$ $[M+Na]^+$ 520.1772, found 520.1772

5,5-difluoro-1,3,7,9-tetrakis(4-methoxyphenyl)-5H-4l4,5l4-dipyrrolo[1,2-c:2',1'-f][1,3,5,2]triazaborinine (4b)

3b (450 mg, 1 Eq, 790 µmol) was dissolved in 20 mL of toluene in a 100 mL RB flask. Triethylamine (22.0 mL, 200 Eq, 158 mmol) was added to the reaction mixture followed by dropwise addition of boron trifluoride diethyl etherate (22.4 mL, 230 Eq, 182 mmol). The reaction mixture was then heated to 70°C for 2 hrs. The solvent was reduced and purified via column chromatography (DCM to 10% MeOH/DCM). The solvent was removed and subsequent solid sample was washed with DI water and filtered to yield 370 mg (76%) of a dark blue solid. ^{1}H NMR (400 MHz, $CDCl_3$) δ 8.03-8.07 (m, 8H), 6.97-7.01 (m, 8H), 6.92 (s, 2H), 3.89 (s, 6H), 3.88 (s, 6H); ^{13}C NMR (100 MHz, $CDCl_3$) δ 161.7, 160.7, 157.7, 145.1, 142.7, 131.6, 131.4, 130.8, 130.6, 125.5, 124.3, 114.4, 113.8, 55.4, 55.3; IR (ATR): 3000, 2932, 2833, 1598, 1489, 1469, 1433, 1409, 1384, 1251,

1231, 1177, 1152, 1128, 1094, 1054, 1021, 972, 936, 828, 814, 787, 748, 592 cm^{-1}; HRMS (EI): exact mass calculated for $C_{36}H_{30}BF_2N_3O_4$ $[M+Na]^+$ 640.2195, found 640.2185

1,3,7,9-tetrakis(3,5-dimethoxyphenyl)-5,5-difluoro-5H-4l4,5l4-dipyrrolo[1,2-c:2',1'-f][1,3,5,2]triazaborinine (4c)

Boron trifluoride diethyl etherate (1.07 mL, 15.0 Eq, 8.70 mmol) was slowly added into the mixture of dry CH_2Cl_2 (30 mL), 3b (400 mg, 1 Eq, 580 µmol) and DIPEA (2.63 mL, 26 Eq, 15.1 mmol), which then reacted at 25 °C for 4 h. The solvent was reduced and purified via column chromatography (DCM to 10% MeOH/DCM) The eluent was evaporated to yield 0.340 mg (80%) of pure product as a dark blue solid. ^{1}H NMR (400 MHz, $CDCl_3$) δ 7.24-7.25 (d, *J* = 4Hz, 4H), 7.13-7.14 (d, *J* = 4 Hz, 4H), 7.00 (s, 2H), 6.59-6.60 (t, *J* = 4 Hz, 2H), 6.53-6.54 (t, *J* = 4 Hz, 2H), 3.85 (s, 12H), 3.76 (s, 12H); ^{13}C NMR (100 MHz, $CDCl_3$) δ 160.8, 160.6, 159.2, 145.5, 144.4, 134.0, 133.1, 119.8, 107.6, 107.2, 103.8, 102.1, 55.5, 55.3; IR (ATR): 2998, 2934, 2836, 1590, 1509, 1455, 1427, 1387, 1300, 1270, 1203, 1154, 1107, 1062, 1053, 1033, 1013, 990, 941, 926, 906, 837, 820, 779, 756, 719, 704, 679 cm^{-1}; HRMS (EI): exact mass calculated for $C_{40}H_{38}BF_2N_3O_8$ $[M+Na]^+$ 760.2617, found 760.2609

5,5-difluoro-1,3,7,9-tetrakis(3,4,5-trimethoxyphenyl)-5H-4l4,5l4-dipyrrolo[1,2-c:2',1'-f][1,3,5,2]triazaborinine (4d)

3d (500 mg, 1 Eq, 617 µmol) was dissolved in 20 mL of toluene in a 100 mL RB flask. Triethylamine (17.2 mL, 200 Eq, 123 mmol) was added to the reaction mixture followed by dropwise addition of boron trifluoride diethyl etherate (17.5 mL, 230 Eq, 142 mmol). The reaction mixture was then heated to 70°C for 2 hrs. The solvent was reduced and purified with column chromatography (DCM to 10% MeOH/DCM). Eluent was removed via rotavap, and the solid sample was washed with DI water then filtered to

yield 0.411 g (78%) of a dark blue solid. ^{1}H NMR (400 MHz, $CDCl_3$) δ 7.37 (s, 4H), 7.19 (s, 4H), 6.95 (s, 2H), 3.95 (s, 6H), 3.93 (s, 18H), 3.77 (s, 12H); ^{13}C NMR (100 MHz, $CDCl_3$) δ 158.5, 153.3, 153.0, 145.4, 143.8, 140.9, 139.6, 128.0, 126.7, 107.6, 107.1, 106.4, 56.4, 56.3, 56.2, 56.0; IR (ATR): 2994, 2936, 2830, 1579, 1486, 1453, 1426, 1402, 1314, 1271, 1238, 1107, 1061, 1048, 1031, 993, 917, 812, 764, 718, 647 cm^{-1}; HRMS (EI): exact mass calculated for $C_{44}H_{46}BF_2N_3O_{12}$ $[M+Na]^+$ 880.3040, found 880.3030

4,4',4'',4'''-(5,5-difluoro-5H-4l4,5l4-dipyrrolo[1,2-c:2',1'-f][1,3,5,2]triazaborinine-1,3,7,9-tetrayl)tetrakis(N,N-dimethylaniline) (4e)

3e (600 mg, 1 Eq, 965 µmol) was dissolved in 20 mL of toluene in a 100 mL RB flask. Triethylamine (26.9 mL, 200 Eq, 193 mmol) was added to the reaction mixture followed by dropwise addition of boron trifluoride diethyl etherate (27.4 mL, 230 Eq, 222 mmol). The reaction mixture was then heated to 70°C for 2 hrs. The solvent was reduced and purified with column chromatography (DCM to 10% MeOH/DCM). Eluent was removed via rotavap and the solid sample was washed with DI water and then filtered to yield 0.354 g (55%) of a dark blue solid. ^{1}H NMR (400 MHz, $CDCl_3$) δ 8.07-8.10 (t, J = 4 Hz, 8H), 6.90 (s, 2H), 6.75-6.79 (t, J = 8 Hz, 8H), 3.06 (s, 24H); ^{13}C NMR (100 MHz, $CDCl_3$) δ 151.5, 150.7, 131.3, 130.5, 121.8, 114.8, 112.0, 111.8, 47.0, 40.4; IR (ATR): 2887, 2851, 2798, 1597, 1488, 1436, 1416, 1355, 1314, 1284, 1196, 1163, 1133, 1101, 1031, 1007, 974, 943, 804, 785, 738, 572 cm^{-1}; HRMS (EI): exact mass calculated for $C_{40}H_{42}BF_2N_7$ $[M+Na]^+$ 692.3460, found 692.3475

4,4'-(3,7-bis(4-(tert-butyl)phenyl)-5,5-difluoro-5H-4l4,5l4-dipyrrolo[1,2-c:2',1'-f][1,3,5,2]triazaborinine-1,9-diyl)bis(N,N-dimethylaniline) (4f)

3f (600 mg, 1 Eq, 926 µmol) was dissolved in 20 mL of toluene in a 100 mL RB flask. Triethylamine (25.8 mL, 200 Eq, 185 mmol) was added to the reaction mixture followed by dropwise addition of boron trifluoride diethyl etherate (26.3 mL, 230 Eq, 213 mmol).

The reaction mixture was then heated to 70°C for 2 hrs. The solvent was reduced and purified with column chromatography (DCM to 10% MeOH/DCM). Eluent was removed via rotavap and the solid sample was washed with DI water then filtered to yield 421 mg (65%) of a dark purple solid. ^{1}H NMR (400 MHz, $CDCl_3$) δ 8.07-8.09 (d, *J* = 8.4 Hz, 4H), 7.98-8.00 (d, *J* = 8.1 Hz, 4H), 7.47-7.49 (d, *J* = 8.1 Hz, 4H), 6.84 (s, 2H), 6.77-6.79 (d, *J* = 8.5 Hz, 4H), 3.08 (s, 12H), 1.36 (s, 18H); ^{13}C NMR (100 MHz, $CDCl_3$) δ 157.6, 153.5, 151.1, 145.5, 143.5, 130.9, 129.7, 129.3, 125.6, 121.4, 115.4, 112.1, 40.3, 35.0, 31.3; IR (ATR): 2956, 2901, 2861, 1653, 1600, 1548, 1485, 1440, 1408, 1380, 1323, 1268, 1101, 1062, 1031, 966, 941, 841, 802, 739 cm^{-1}; HRMS (APCI): exact mass calculated for $C_{44}H_{48}BF_2N_5$ $[M+H]^+$ 696.3971, found 696.4044

4,4'-(1,9-bis(4-(tert-butyl)phenyl)-5,5-difluoro-5H-4l4,5l4-dipyrrolo[1,2-c:2',1'-f][1,3,5,2]triazaborinine-3,7-diyl)bis(N,N-dimethylaniline) (4g)

3g (600 mg, 1 Eq., 926 µmol) was dissolved in 20 mL of toluene in a 100 mL RB flask. Triethylamine (25.8 mL, 200 Eq, 185 mmol) was added to the reaction mixture followed by dropwise addition of boron trifluoride diethyl etherate (26.3 mL, 230 Eq, 213 mmol). The reaction mixture was then heated to 70°C for 2 hrs. The solvent was reduced and purified with column chromatography (DCM to 10% MeOH/DCM). Eluent was removed via rotavap and the solid sample was washed with DI water then filtered to yield 226 mg (35%) of a dark blue solid. ^{1}H NMR (400 MHz, $CDCl_3$) δ 8.12-8.14 (d, *J* = 9.1 Hz, 4H), 8.01-8.03 (d, *J* = 8.5 Hz, 4H), 7.46-7.48 (d, *J* = 8.5 Hz, 4H), 7.05 (s, 2H), 6.77-6.79 (d, *J* = 8.7 Hz, 4H), 3.09 (s, 12H), 1.39 (s, 18H); ^{13}C NMR (100 MHz, $CDCl_3$) δ 156.4, 151.8, 145.3, 141.0, 131.7, 130.5, 129.1, 125.4, 119.4, 117.5, 111.9, 40.2, 34.9, 31.4; IR (ATR): 2950, 2859, 1653, 1596, 1558, 1507, 1492, 1460, 1418, 1365, 1317, 1283, 1158, 1068, 1009, 974, 866, 808, 773, 750 cm^{-1}; HRMS (APCI): exact mass calculated for $C_{44}H_{48}BF_2N_5$ $[M+H]^+$ 696.3971, found 696.4042

3,7-bis(4-(tert-butyl)phenyl)-5,5-difluoro-1,9-bis(3,4,5-trimethoxyphenyl)-5H-4l4,5l4- dipyrrolo[1,2-c:2',1'-f][1,3,5,2]triazaborinine (4h)

3h (250 mg, 1 Eq, 337 µmol) was dissolved in 20 mL of toluene in a 100 mL 2- neck RB flask under N2. Triethylamine (6.82 g, 9.40 mL, 200 Eq, 67.4 mmol) was added to the reaction mixture followed by dropwise addition of boron trifluoride diethyl etherate (11.0 g, 9.56 mL, 230 Eq, 77.5 mmol). The reaction mixture was then heated to 70°C for 2 hrs and monitored via TLC (100% DCM). The solvent was concentrated under reduced pressure using rotary evaporation, and the crude product was purified via column chromatography (100% DCM) to yield the desired product as a black solid (252 mg, 95%). ^{1}H NMR (400 MHz, $CDCl_3$) δ 8.03-8.05 (d, J = 8.9 Hz, 4H), 7.51-7.53 (d, J = 8.8 Hz, 4H), 7.19 (s, 4H), 6.98 (s, 2H), 3.92 (s, 6H), 3.77 (s, 12H), 1.37 (s, 18H); ^{13}C NMR (100 MHz, $CDCl_3$) δ 158.9, 154.6, 153.4, 145.6, 143.9, 139.6, 129.6, 128.8, 128.3, 125.9, 119.0, 106.8, 61.2, 56.1, 35.2, 31.3; IR (ATR): 2950, 2904, 2868, 2830, 1605, 1578, 1492, 1464, 1415, 1385, 1337, 1311, 1270, 1242, 1208, 1085, 1005, 810, 717 cm^{-1}; HRMS (ESI): exact mass calculated for $C_{46}H_{50}BF_2N_3O_6$ $[M+Na]^+$ 812.3658, found 812.3666

2,8-dibromo-5,5-difluoro-1,3,7,9-tetraphenyl-5H-4l4,5l4-dipyrrolo[1,2-c:2',1' f][1,3,5,2]triazaborinine (5a)

NBS (107 mg, 2 Eq, 603 µmol) in CH_2Cl_2 (2 mL) was slowly added into a mixture of dry CH_2Cl_2 (10 mL) and 4a (150 mg, 1 Eq, 302 µmol), which then reacted at 25°C for 6 h. Purified via column chromatography (DCM to 10% MeOH/DCM) to yield 90 mg (46%) of a dark blue solid. ^{1}H NMR (400 MHz, $CDCl_3$) δ 7.88-7.89 (m, 4H), 7.71-7.73 (m, 4H), 7.44-7.49 (m, 12H); ^{13}C NMR (100 MHz, $CDCl_3$) δ 158.5, 144.4, 142.5, 130.9, 130.6, 130.4, 130.3, 130.2, 129.6, 128.2, 128.1, 110.2; IR (ATR): 3052, 1525, 1513, 1498, 1444, 1379, 1132, 1079, 1040, 1026, 999, 958, 935, 917, 838, 802, 764, 691, 660, 632, 620, 604

cm^{-1}; HRMS (EI): exact mass calculated for $C_{32}H_{20}BBr_2F_2N_3$ $[M+Na]^+$ 675.9983, found 677.9953

2,8-dibromo-5,5-difluoro-1,3,7,9-tetrakis(4-methoxyphenyl)-5H-4l4,5l4-dipyrrolo[1,2-c:2',1'-f][1,3,5,2]triazaborinine (5b)

NBS (86.5 mg, 2 Eq, 486 µmol) was slowly added into the mixture of dry DCM (10 mL) and 4b (150 mg, 1 Eq, 243 µmol), which then reacted at 25°C for 10 minutes. The reaction mixture was washed with 1M NaOH (3x 10 mL) and the organic layer was subsequently dried with $MgSO_4$ and filtered. The solvent was removed via rotavap to yield 104 mg (55%) of a pure, dark blue solid. ^{1}H NMR (400 MHz, $CDCl_3$) δ 7.88-7.91 (d, *J* = 12 Hz, 4H), 7.74-7.76 (d, *J* = 8 Hz, 4H), 6.97-7.00 (m, 8H), 3.89 (s, 6H), 3.86 (s, 6H); ^{13}C NMR (100 MHz, $CDCl_3$) δ 161.5, 160.8, 157.1, 144.0, 142.0, 132.4, 123.5, 122.0, 113.6, 108.7, 55.4, 55.3; IR (ATR): 2958, 2933, 2835, 1600, 1483, 1462, 1426, 1381, 1248, 1167, 1135, 1048, 1022, 1010, 986, 830, 808, 796, 750, 736, 715, 703, 660, 630, 596, 571 cm^{-1}; HRMS (EI): exact mass calculated for $C_{36}H_{28}BBr_2F_2N_3O_4$ $[M+Na]^+$ 796.0405, found 798.0378

2,8-dibromo-5,5-difluoro-1,3,7,9-tetrakis(3,4,5-trimethoxyphenyl)-5H-4l4,5l4-dipyrrolo[1,2-c:2',1'-f][1,3,5,2]triazaborinine (5d)

NBS (62.3 mg, 2 Eq, 350 µmol) was slowly added into the mixture of dry DCM (10 mL) and 4d (150 mg, 1 Eq, 175 µmol), which then reacted at 25°C for 10 minutes. The reaction was washed with 1M NaOH (3x 10 mL) and the organic layer was subsequently dried with $MgSO_4$ and filtered. The solvent was removed via rotavap to yield 121 mg (68%) of a pure, dark blue solid. ^{1}H NMR (400 MHz, $CDCl_3$) δ 7.10 (s, 4H), 7.07 (s, 4H), 3.96 (s, 6H), 3.95 (s, 6H), 3.88 (s, 12H), 3.69 (s, 12H); ^{13}C NMR (100 MHz, $CDCl_3$) δ 157.4, 152.7, 152.5, 144.0, 142.4, 140.5, 139.6, 125.9, 124.3, 108.4, 108.3, 61.0, 60.9, 56.1, 56.0; IR (ATR): 2998, 2934, 2830, 1577, 1484, 1459, 1403, 1372, 1334, 1317,

1272, 1240, 1182, 1119, 1065, 1040, 995, 919, 830, 731, 720, 674, 649 cm^{-1}; HRMS (EI): exact mass calculated for $C_{44}H_{44}BBr_2F_2N_3O_{12}$ $[M+Na]^+$ 1014.1431, found 1016.1420

4,4',4'',4'''-(2,8-dibromo-5,5-difluoro-5H-4l4,5l4-dipyrrolo[1,2-c:2',1'-f][1,3,5,2]triazaborinine-1,3,7,9-tetrayl)tetrakis(N,N-dimethylaniline) (5e)

NBS (79.7 mg, 2 Eq, 448 µmol) was slowly added into the mixture of dry DCE (10 mL) and 4e (150 mg, 1 Eq, 224 µmol), which then reacted at 25°C for 10 minutes. The reaction was washed with 1 M NaOH (3x 10 mL) and the organic layer was subsequently dried with $MgSO_4$ and filtered. The solvent was removed via rotavap to yield 61 mg (33%) of a pure, dark blue solid. ^{1}H NMR (400 MHz, $CDCl_3$) δ 7.96-7.98 (d, *J* = 8 Hz, 4H), 7.77-7.79 (d, *J* = 8 Hz, 4H), 6.71-6.78 (m, 8H), 3.06 (s, 12H), 3.04 (s, 12H); ^{13}C NMR (100 MHz, $CDCl_3$) δ 151.5, 150.8, 150.7, 132.4, 131.3, 130.5, 121.9, 120.1, 112.1, 111.8, 111.4, 110.9, 40.4, 40.3, 40.2, 40.1; IR (ATR): 2961, 2849, 2796, 1595, 1474, 1414, 1350, 1312, 1261, 1194, 1159, 1133, 1096, 1044, 1029, 1007, 969, 940, 793, 722 cm^{-1}; HRMS (EI): exact mass calculated for $C_{40}H_{40}BBr_2F_2N_7$ $[M+H]^+$ 826.1851, found 828.1824

2,8-dibromo-3,7-bis(4-(tert-butyl)phenyl)-5,5-difluoro-1,9-bis(3,4,5 trimethoxyphenyl)-5H4l4,5l4-dipyrrolo[1,2-c:2',1'-f][1,3,5,2]triazaborinine (5h)

NBS (477.3 mg, 2 Eq, 2.682 mmol) was slowly added into the mixture of dry DCE (10 mL) and 4h (1.059 g, 1 Eq, 1.341 mmol), which then reacted at 25°C for 10 minutes. The reaction was washed with 1 M NaOH (3x 10 mL) and the organic layer was subsequently dried with $MgSO_4$ and filtered. The solvent was removed via rotavap to yield 529 mg (42%) of a pure, dark blue solid). ^{1}H NMR (400 MHz, $CDCl_3$) δ 7.68-7.70 (d, J = 8.4 Hz, 4H), 7.48-7.50 (d, J = 8.5 Hz, 4H), 7.11 (s, 4H), 3.94 (s, 6H), 3.69 (s, 12H), 1.35 (s, 18H); ^{13}C NMR (100 MHz, $CDCl_3$) δ 158.4, 154.3, 152.8, 144.2, 142.2, 139.6, 130.3,

126.6, 126.2, 125.1, 109.9, 108.5, 61.1, 56.1, 35.1, 31.3; IR (ATR): 2958, 2905, 2867, 2833, 1579, 1491, 1464, 1411, 1377, 1336, 1290, 1269, 1240, 1168, 1121, 1063, 1015, 837, 713 cm^{-1}; HRMS (ESI): exact mass calculated for $C_{46}H_{48}BBr_2F_2N_3O_6$ $[M+Na]^+$ 968.1868, found 968.1868

5,5-dimethyl-1,3,7,9-tetrakis(3,4,5-trimethoxyphenyl)-5H-4l4,5l4-dipyrrolo[1,2-c:2',1'-f][1,3,5,2]triazaborinine (6d)

4d (200 mg, 1 Eq, 0.233 mmol) was dissolved in dry THF (10 mL). Under N_2(g), 3M methylmagnesium bromide in Et_2O (1.17 mL, 15 Eq., 3.50 mmol) was added into the flask slowly. The reaction mixture was stirred vigorously for 30 min. The RB flask was subsequently lowered into an ice bath and a sat. NH_4Cl(aq.) solution was added dropwise until no bubbles and heat were generated. DCM was added to the aqueous phase to extract the crude product. The combined organic layers were washed with brine and was dried with $MgSO_4$. The solvent was reduced via rotavap and purified via column chromatography (1:1 Hexane:Ethyl Acetate) to yield 39 mg (20%) of a dark blue solid. ^{1}H NMR (400 MHz, $CDCl_3$) δ 7.18 (s, 4H), 6.76 (s, 4H), 6.73 (s, 4H), 3.92 (s, 6H), 3.90 (s, 6H), 3.87 (s, 12H), 3.75 (s, 12H), 0.04 (s, 6H); ^{13}C NMR (100 MHz, $CDCl_3$) δ 158.8, 153.3, 152.7, 143.3, 141.6, 139.0, 138.9, 129.7, 128.7, 119.9, 107.0, 106.5, 61.2, 61.1, 56.4, 56.0; IR (ATR): 2934, 2827, 1579, 1486, 1449, 1408, 1379, 1338, 1312, 1271, 1235, 1119, 1097, 1054, 1025, 996, 943, 822, 796, 761, 726 cm^{-1}; HRMS (APCI): exact mass calculated for $C_{46}H_{52}BN_3O_{12}$ $[M+H]^+$ 850.3722, found 850.3720

4,4',4'',4'''-(5,5-dimethyl-5H-4l4,5l4-dipyrrolo[1,2-c:2',1'-f][1,3,5,2]triazaborinine-1,3,7,9-tetrayl)tetrakis(N,N-dimethylaniline) (6e)

4e (350 mg, 1 Eq., 0.523 mmol) was dissolved in dry DCM (10 mL). Under N_2(g), 3M methylmagnesium bromide (2.61 mL, 15 Eq., 7.84 mmol) was added into the flask slowly. The reaction mixture was stirred vigorously for 30 min. The RB flask was

lowered into an ice bath and a sat. NH_4Cl(aq.) solution was added dropwise until no bubbles and heat were generated. DCM was added to the aqueous phase to extract the crude product. The combined organic layers were washed with brine and was dried with $MgSO_4$. The solvent was reduced via rotavap to yield 137 mg (40%) of a pure, dark blue solid. ^{1}H NMR (400 MHz, $CDCl_3$) δ 8.03-8.05 (d, *J* = 8 Hz, 4H), 7.55-7.57 (d, *J* = 8 Hz, 4H), 6.77-6.79 (d, *J* = 8 Hz, 4H), 6.68-6.70 (d, *J* = 8 Hz, 4H), 6.67 (s, 2H), 3.04 (s, 12H), 3.00 (s, 12H), 0.12 (s, 6H); ^{13}C NMR (100 MHz, $CDCl_3$) δ 157.3, 150.6, 150.3, 143.4, 140.3, 131.0, 130.3, 122.7, 122.5, 116.8, 112.2, 111.1, 40.5, 40.4; IR (ATR): 2891, 2853, 2801, 1711, 1603, 1497, 1439, 1357, 1283, 1195, 1167, 1126, 1094, 1020, 946, 922, 817, 805, 751 cm^{-1}; HRMS (APCI): exact mass calculated for $C_{42}H_{48}BN_7$ $[M+H]^+$ 662.4142, found 662.4160

2.39: CHARACTERIZATION

^{1}H NMR DATA

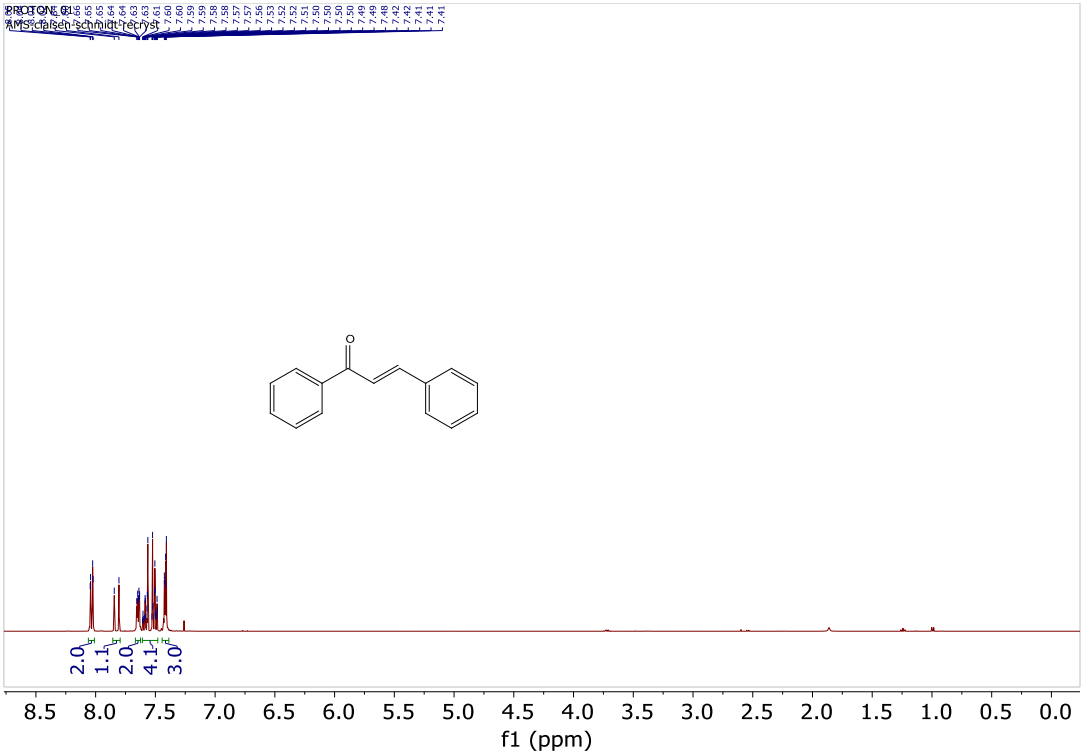

Figure 2.29: ^{1}H NMR of Compound **1a** in $CDCl_3$

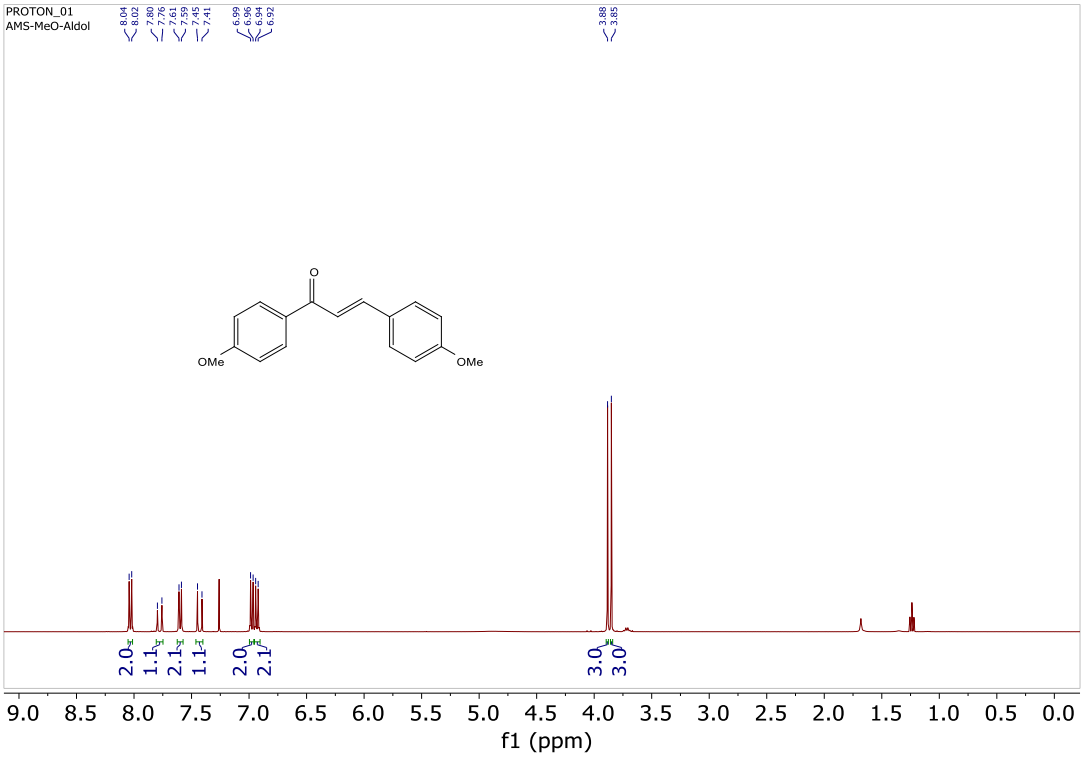

Figure 2.30: ^{1}H NMR of Compound **1b** in $CDCl_3$

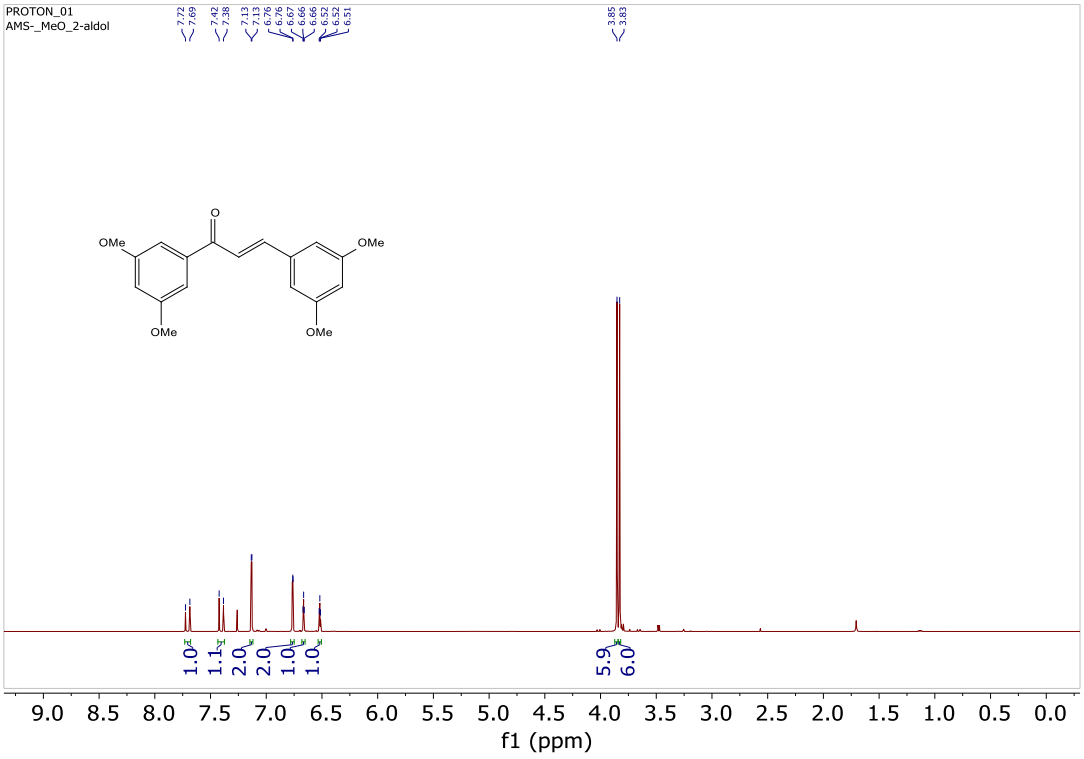

Figure 2.31: ^{1}H NMR of Compound **1c** in $CDCl_3$

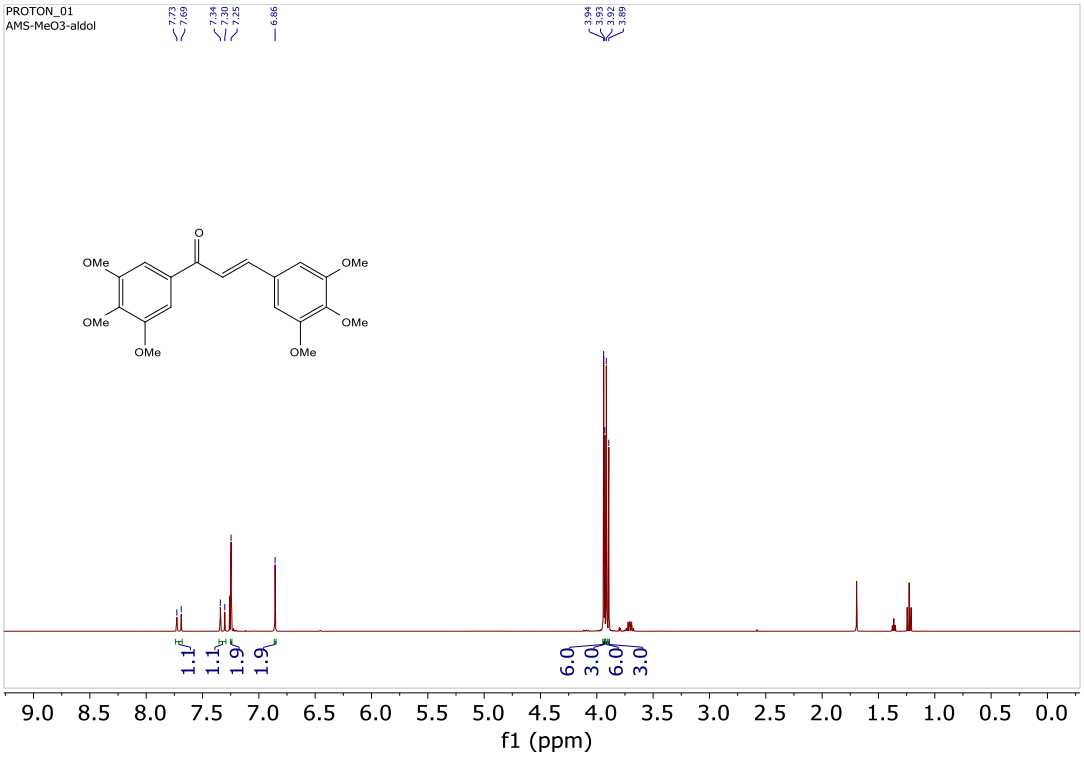

Figure 2.32: ^{1}H NMR of compound **1d** in $CDCl_3$

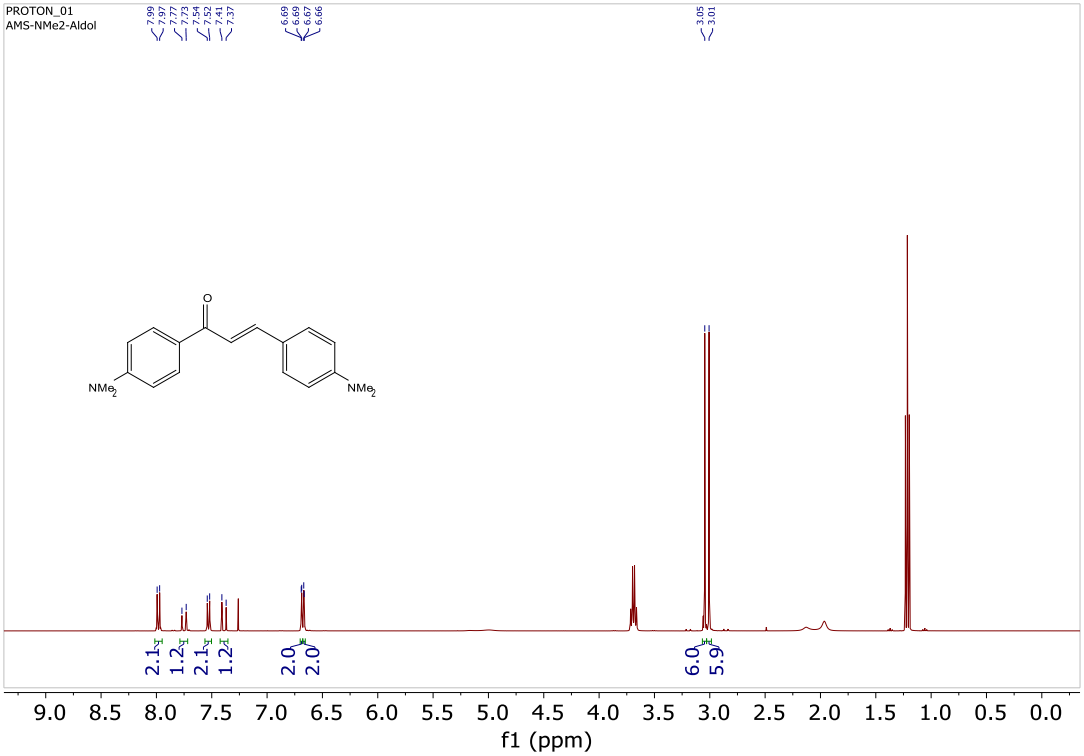

Figure 2.33: ^{1}H NMR of Compound **1e** in $CDCl_3$

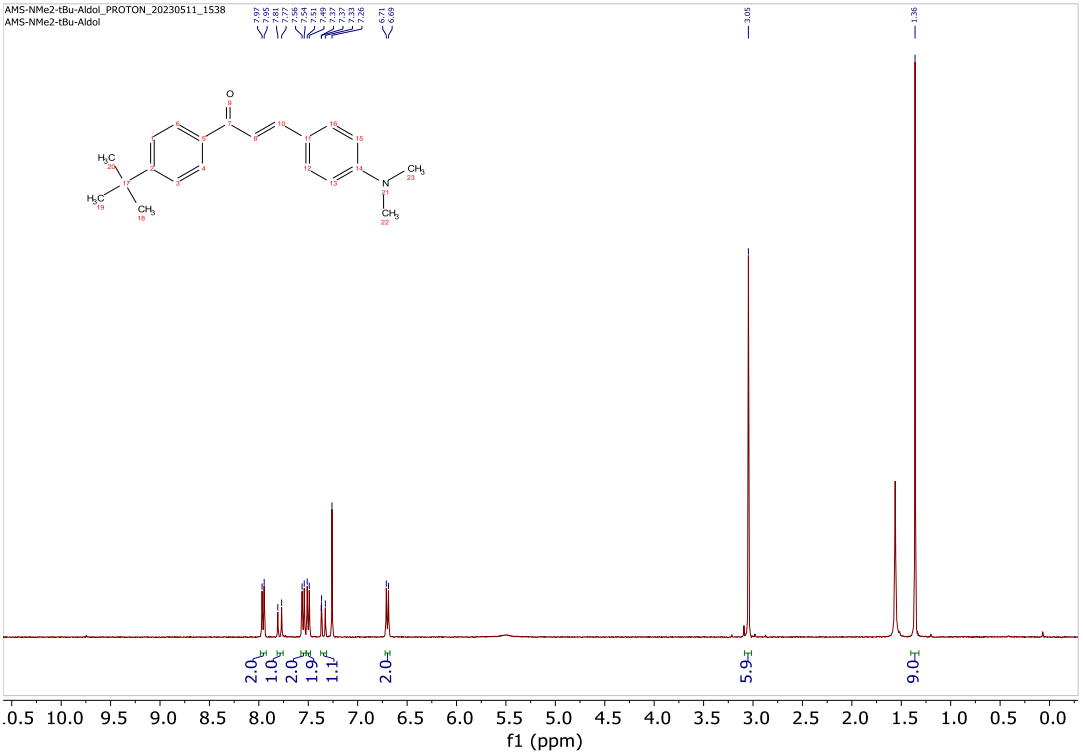

Figure 2.34: ^{1}H NMR of Compound **1f** in $CDCl_3$

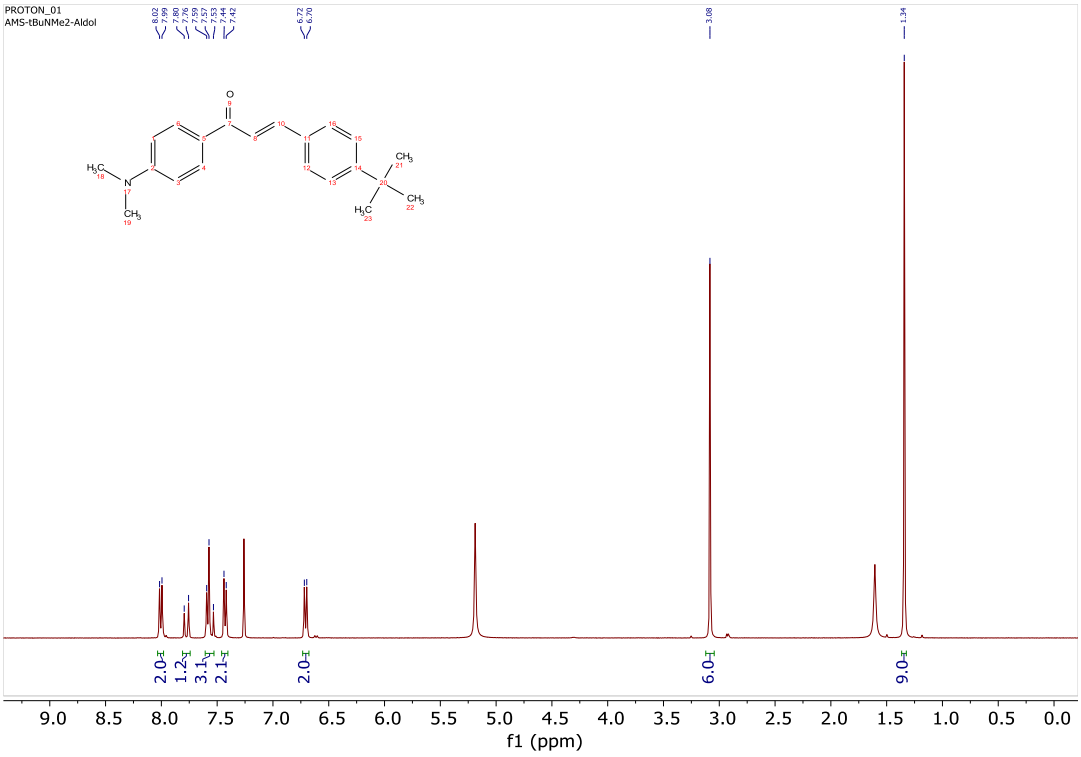

Figure 2.35: ^{1}H NMR of Compound **1g** in $CDCl_3$

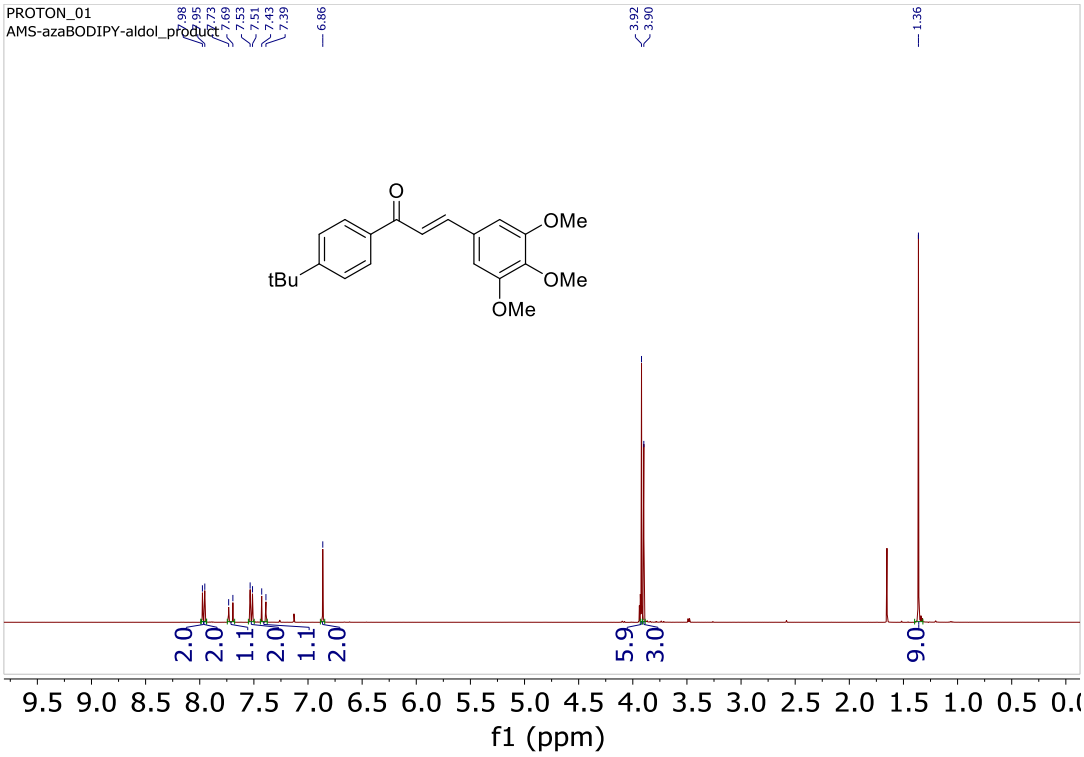

Figure 2.36: ^{1}H NMR of Compound **1h** in $CDCl_3$

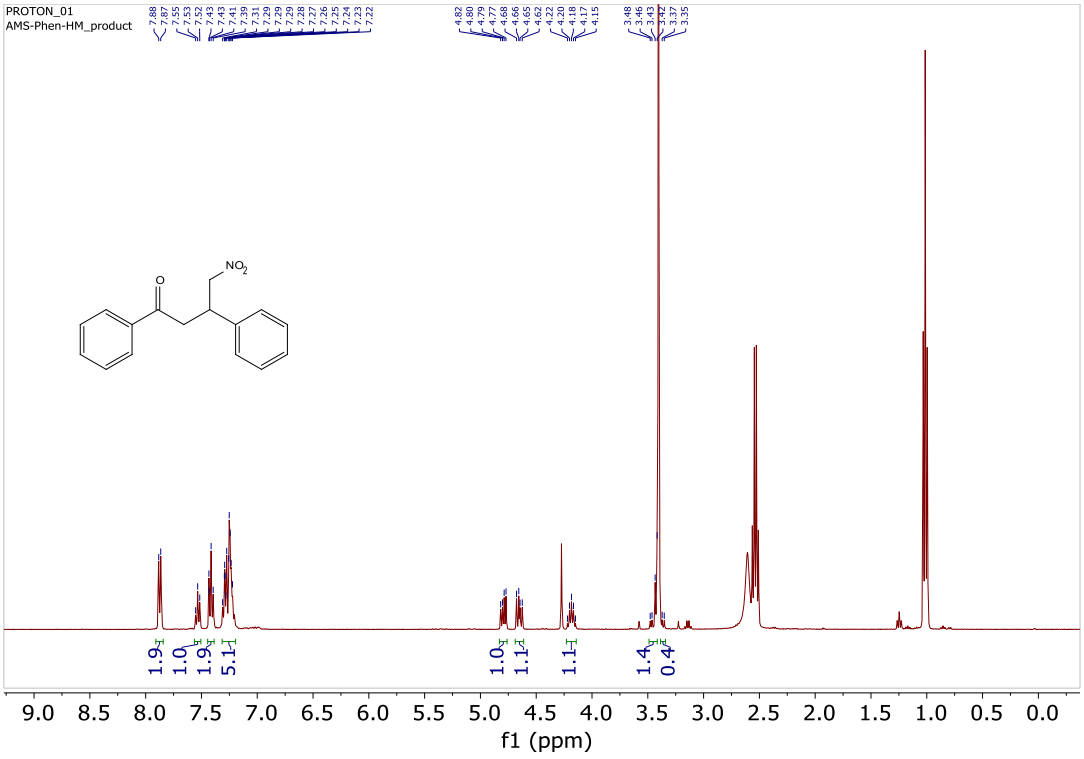

Figure 2.37: ^{1}H NMR of Compound **2a** in $CDCl_3$

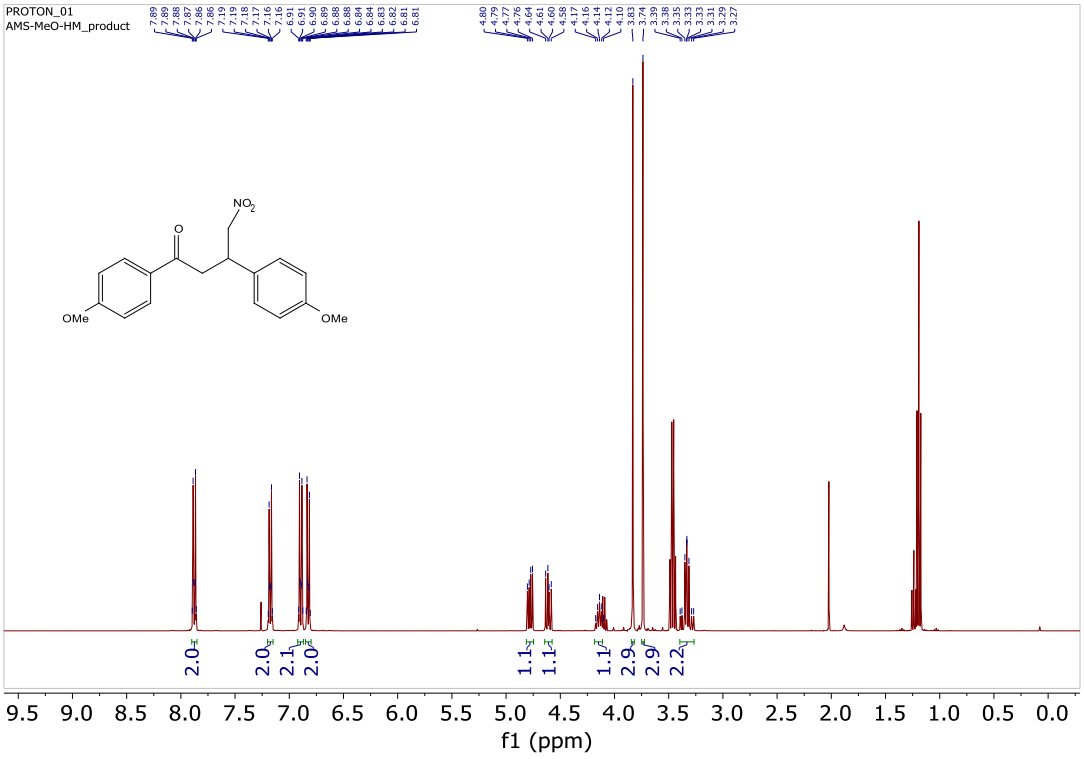

Figure 2.38: ^{1}H NMR of Compound **2b** in $CDCl_3$

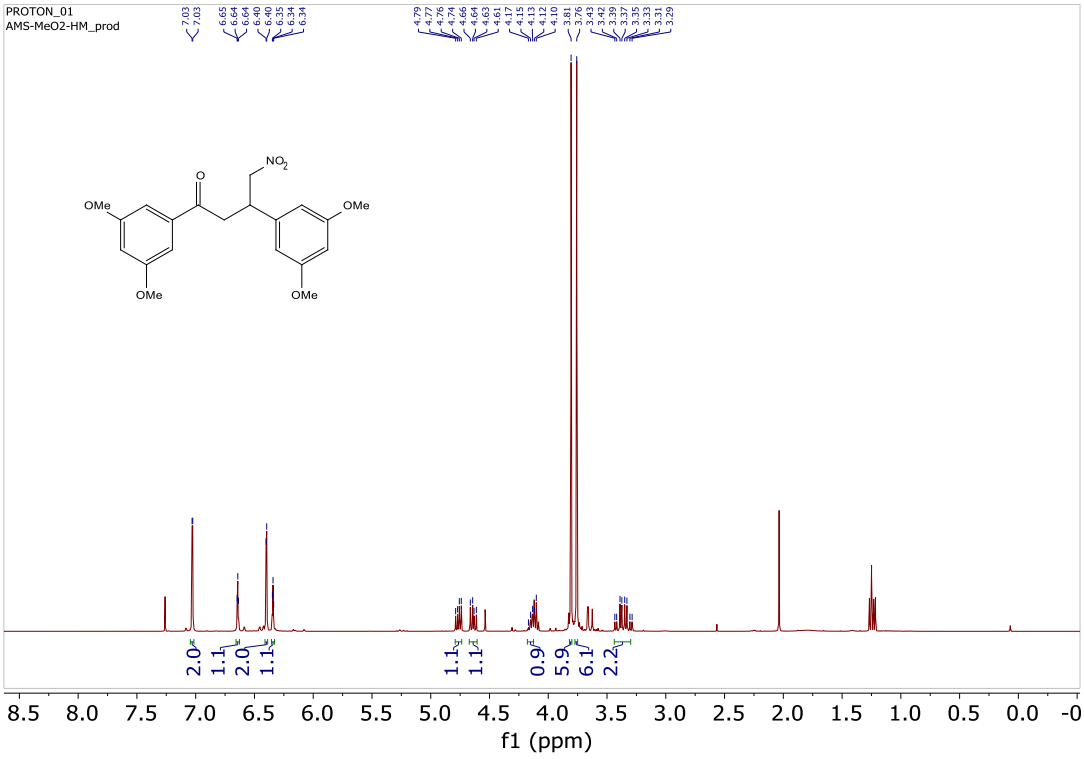

Figure 2.39: ^{1}H NMR of Compound **2c** in $CDCl_3$

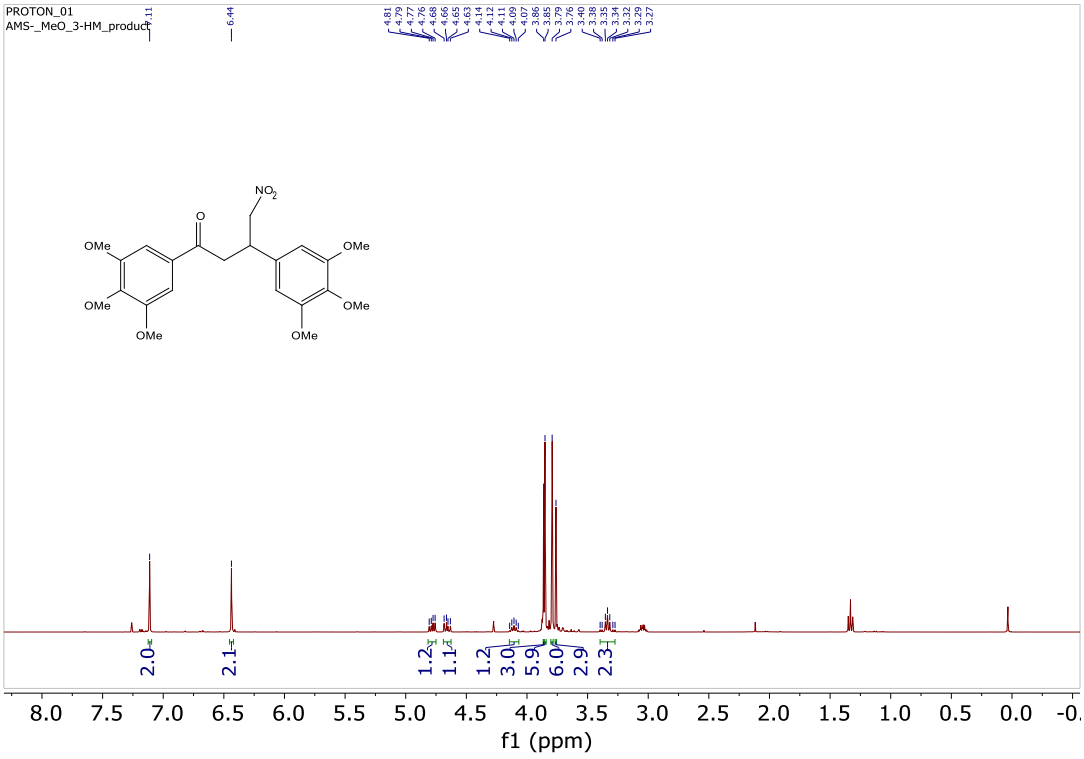

Figure 2.40: ^{1}H NMR of Compound **2d** in $CDCl_3$

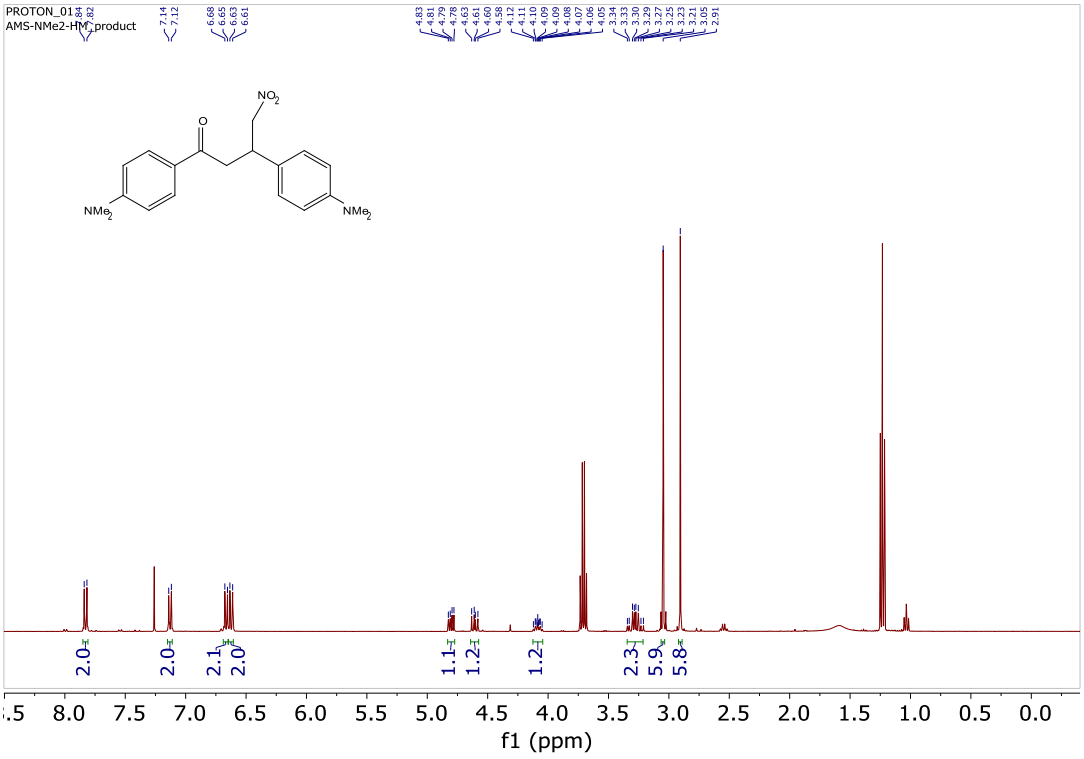

Figure 2.41: ^{1}H NMR of Compound **2e** in $CDCl_3$

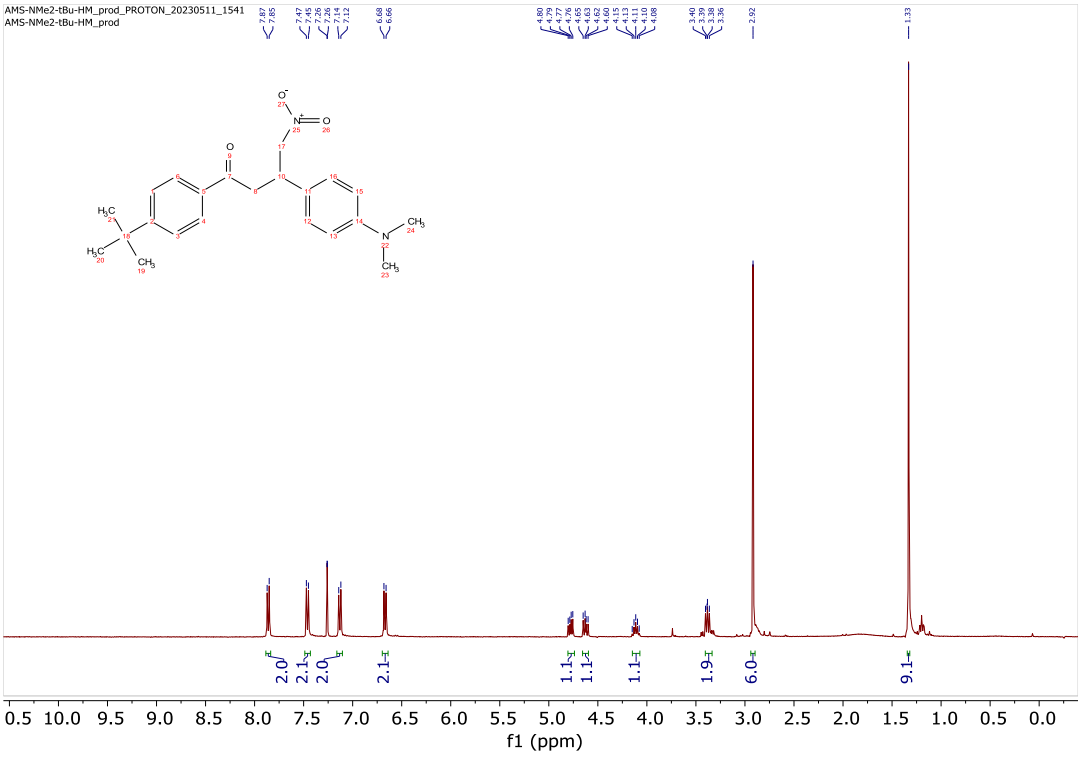

Figure 2.42: ^{1}H NMR of Compound **2f** in $CDCl_3$

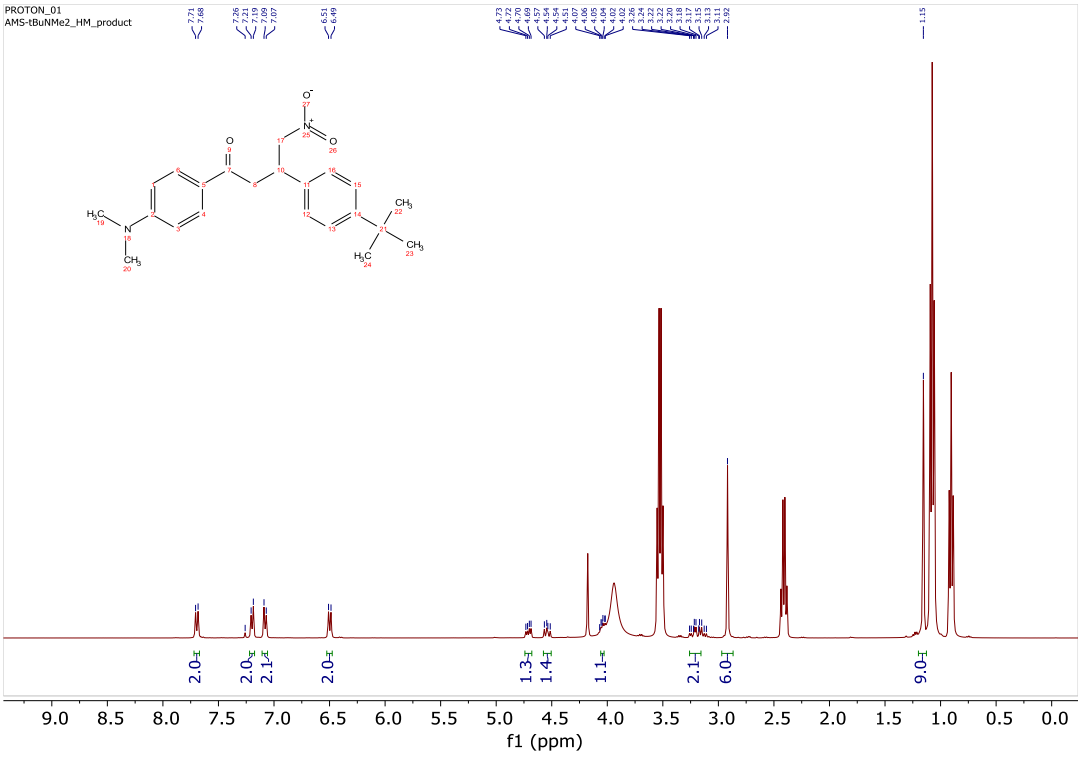

Figure 2.43: ^{1}H NMR of Compound **2g** in $CDCl_3$

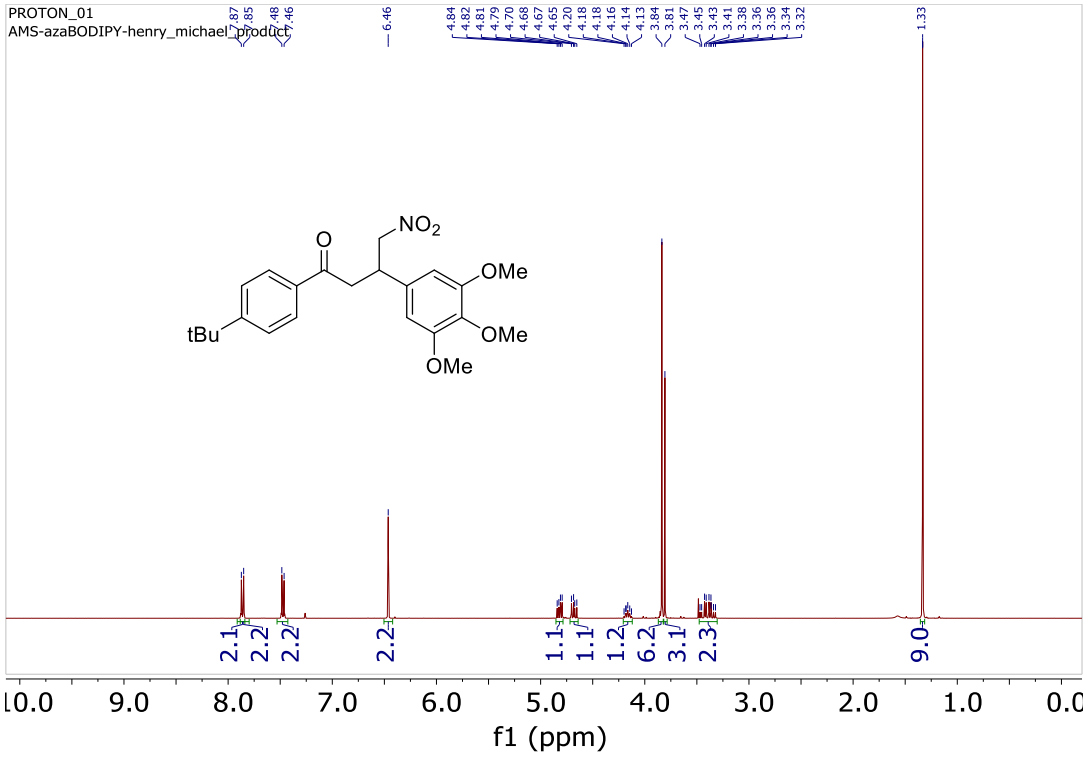

Figure 2.44: ^{1}H NMR of Compound **2h** in $CDCl_3$

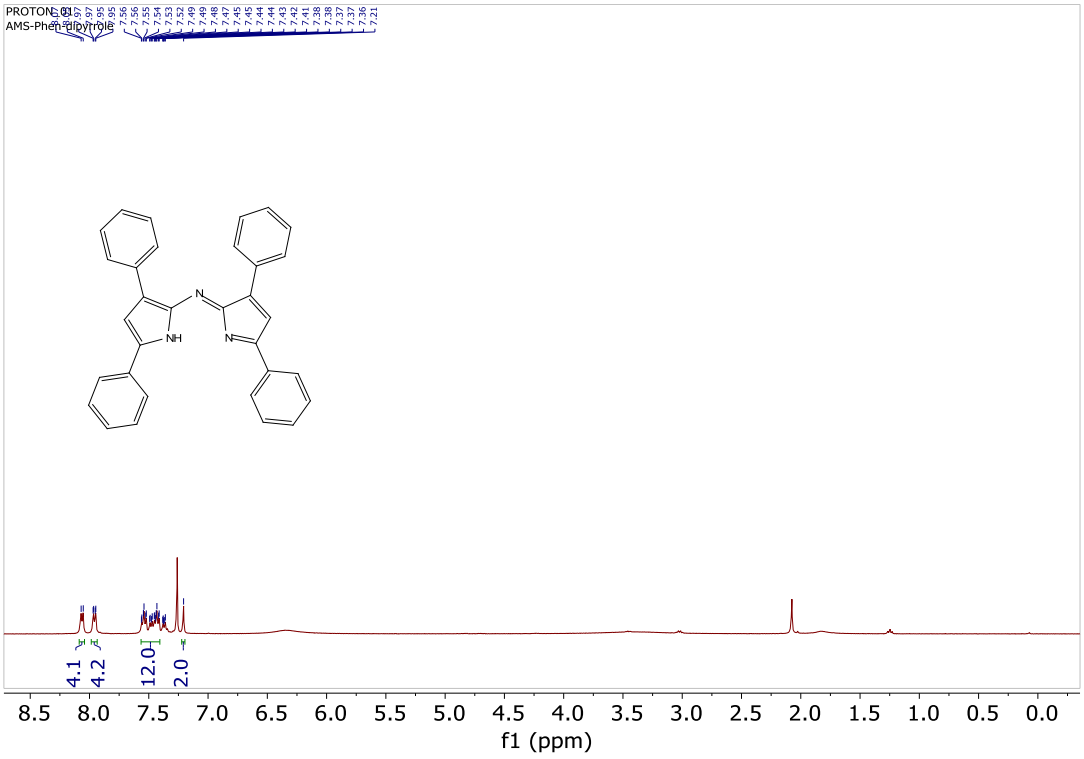

Figure 2.45: ^{1}H NMR of Compound **3a** in $CDCl_3$

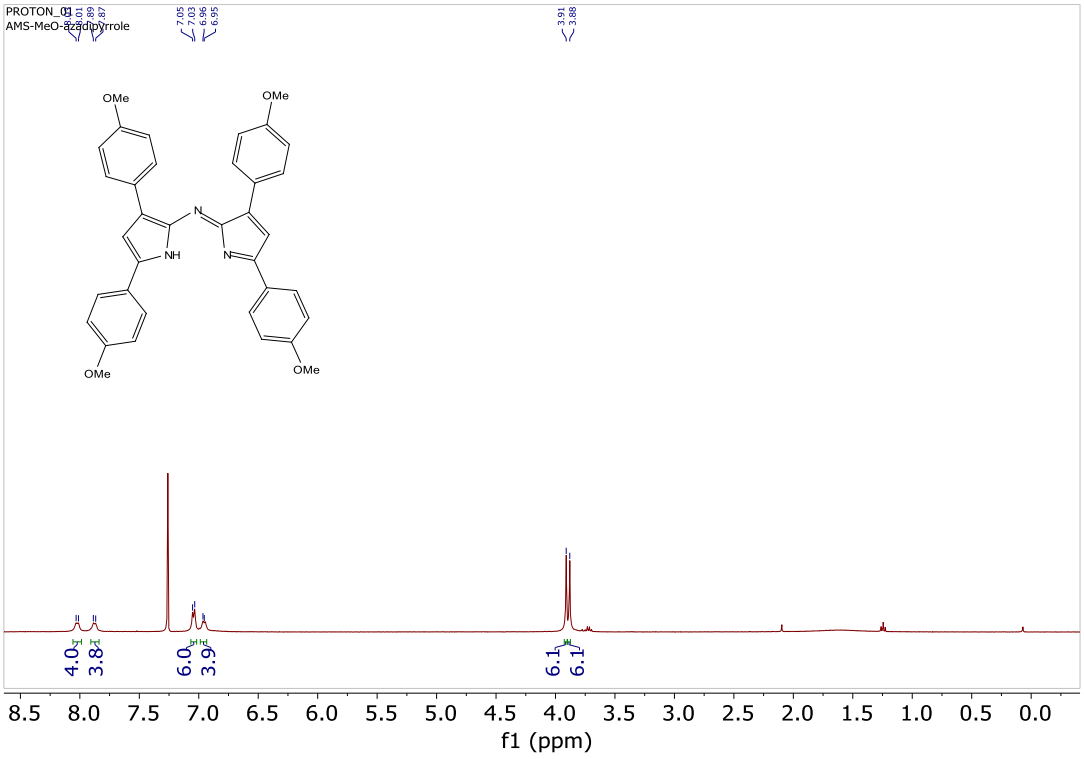

Figure 2.46: ^{1}H NMR of Compound **3b** in $CDCl_3$

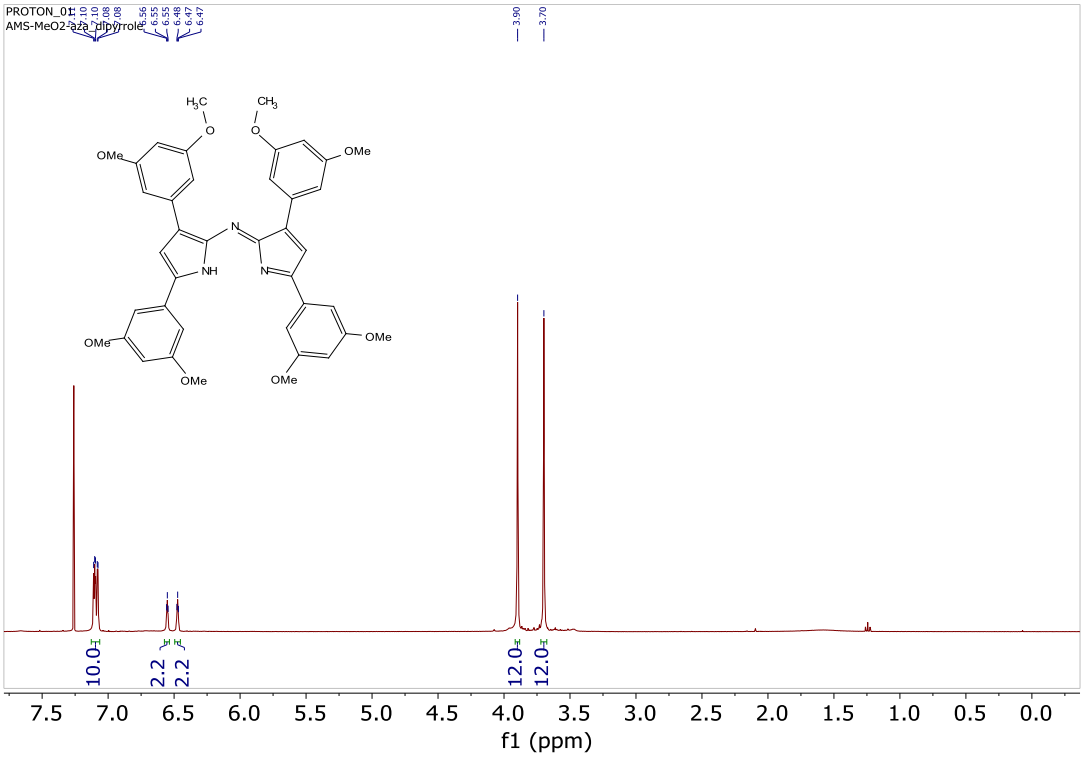

Figure 2.47: ^{1}H NMR of Compound **3c** in $CDCl_3$

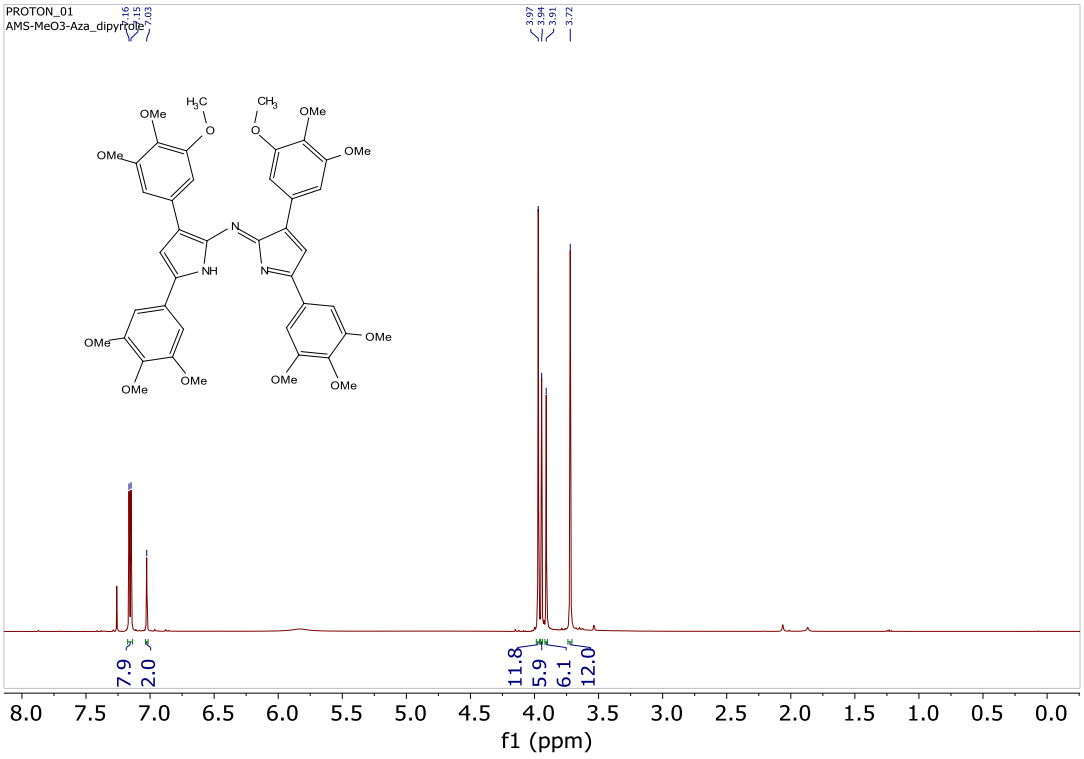

Figure 2.48: ^{1}H NMR of compound **3d** in $CDCl_3$

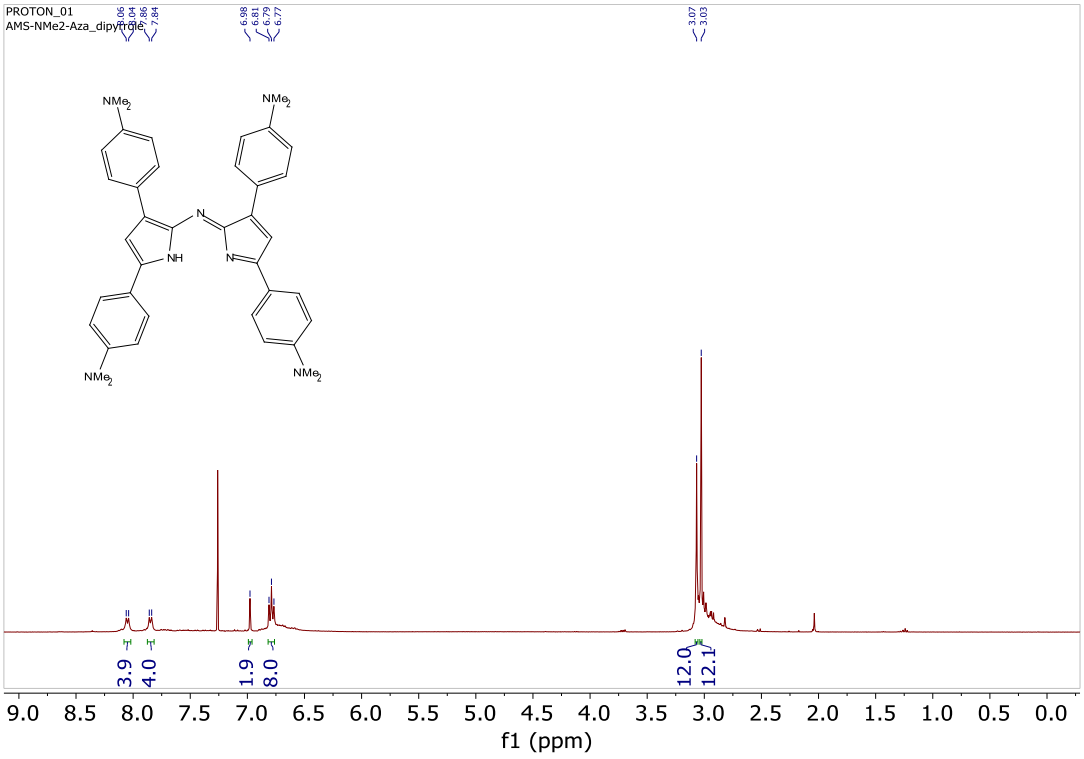

Figure 2.49: ^{1}H NMR of Compound **3e** in $CDCl_3$

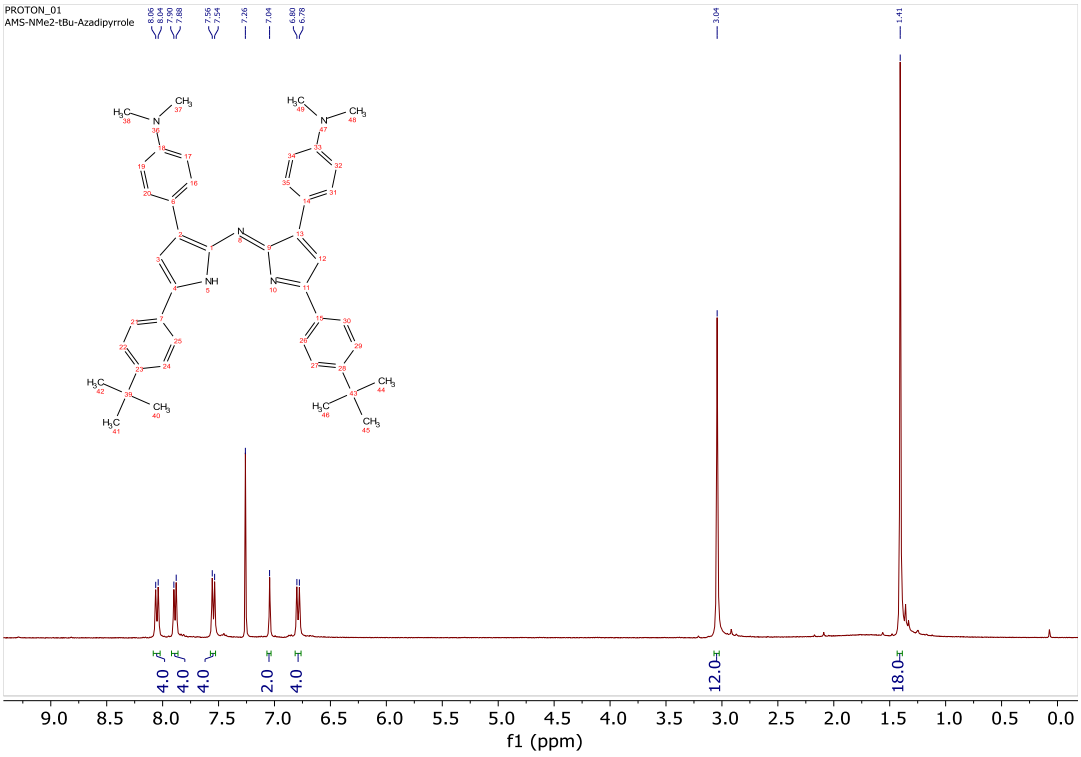

Figure 2.50: ^{1}H NMR of Compound **3f** in $CDCl_3$

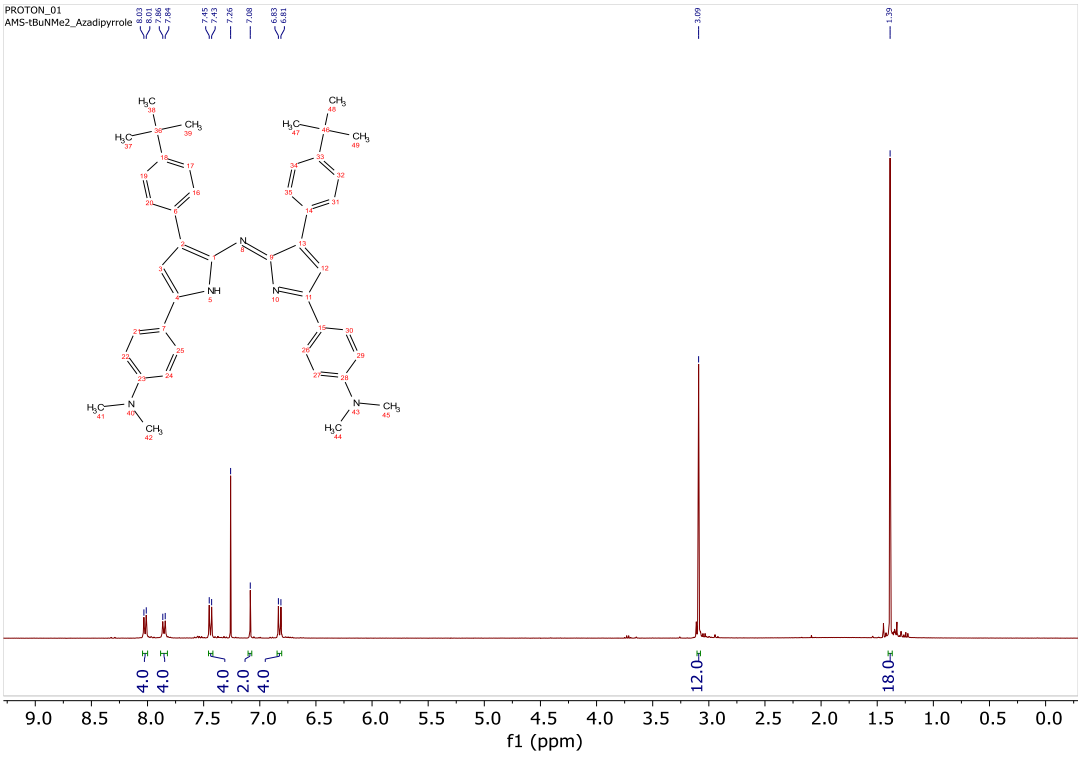

Figure 2.51: ^{1}H NMR of Compound **3g** in $CDCl_3$

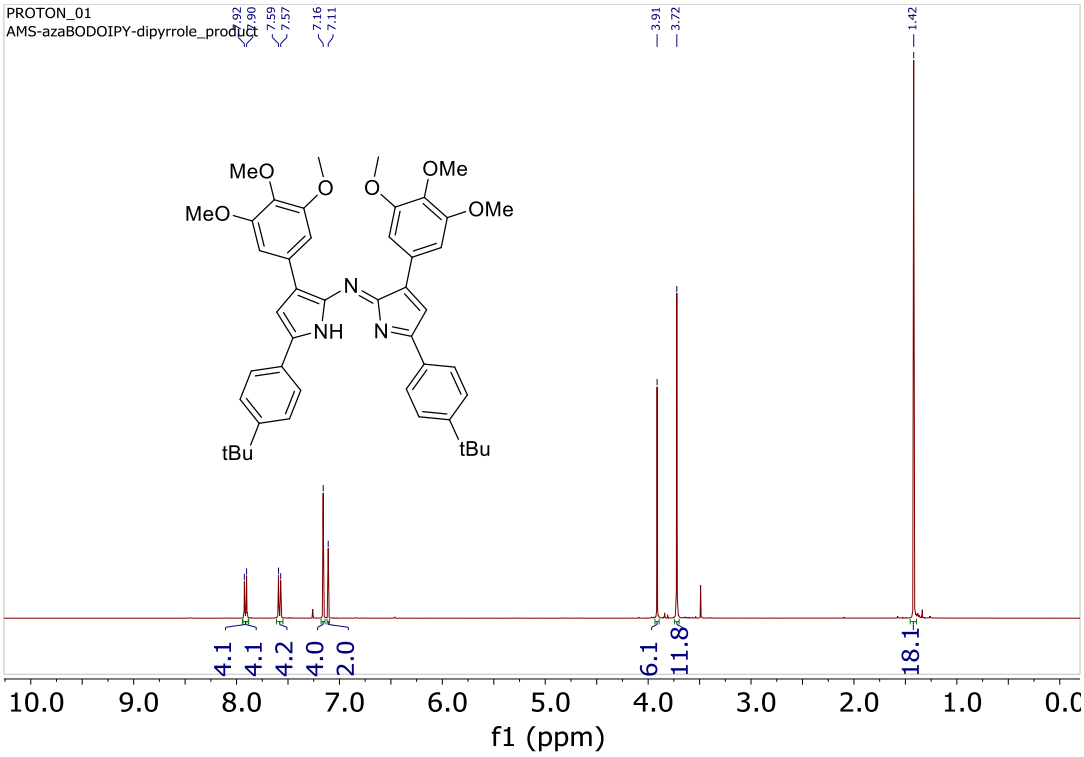

Figure 2.52: ^{1}H NMR of Compound **3h** in $CDCl_3$

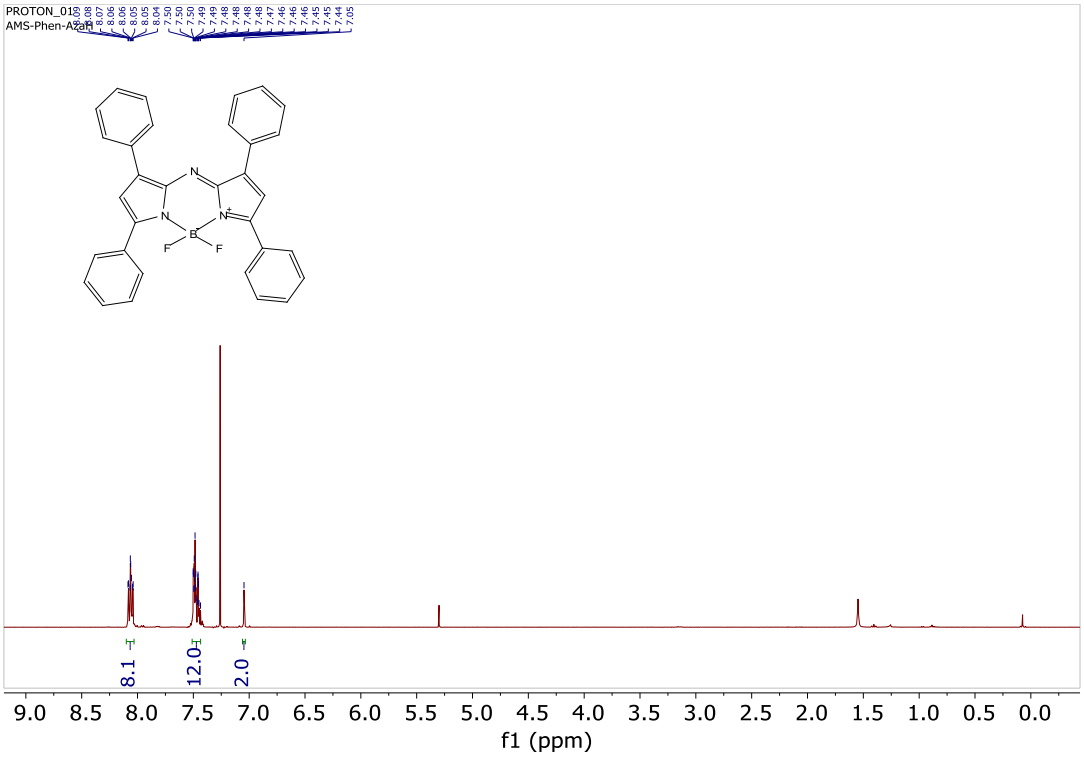

Figure 2.53: ^{1}H NMR of Compound **4a** in $CDCl_3$

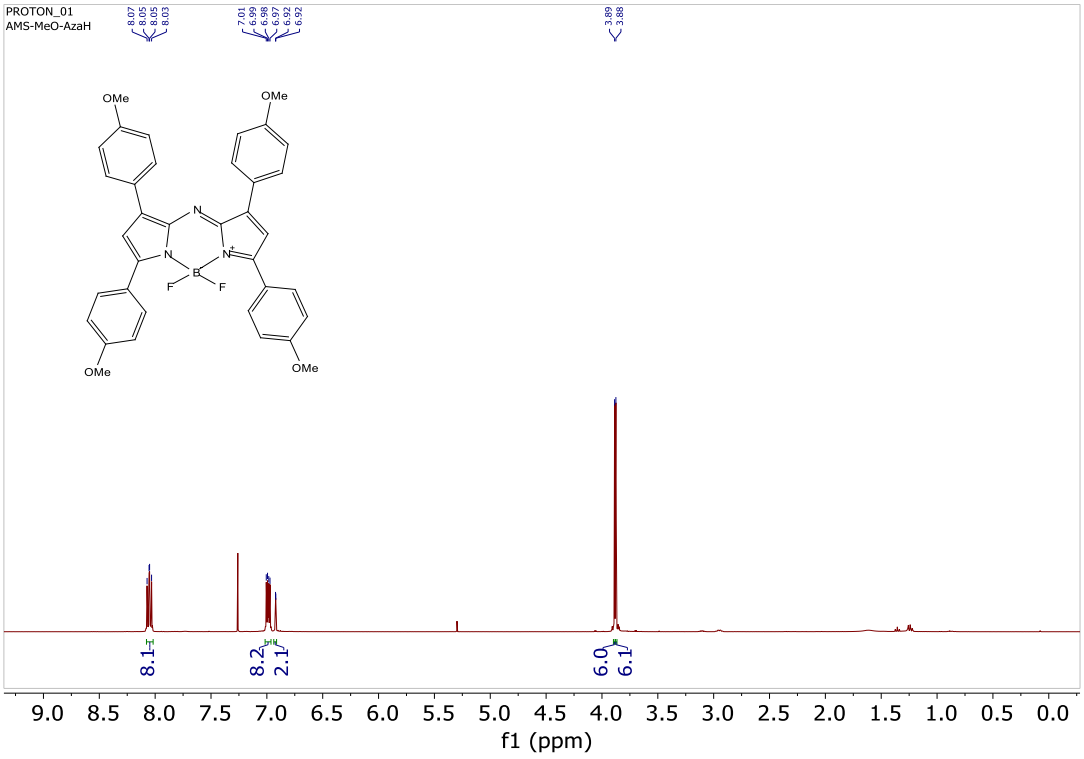

Figure 2.54: ^{1}H NMR of Compound **4b** in $CDCl_3$

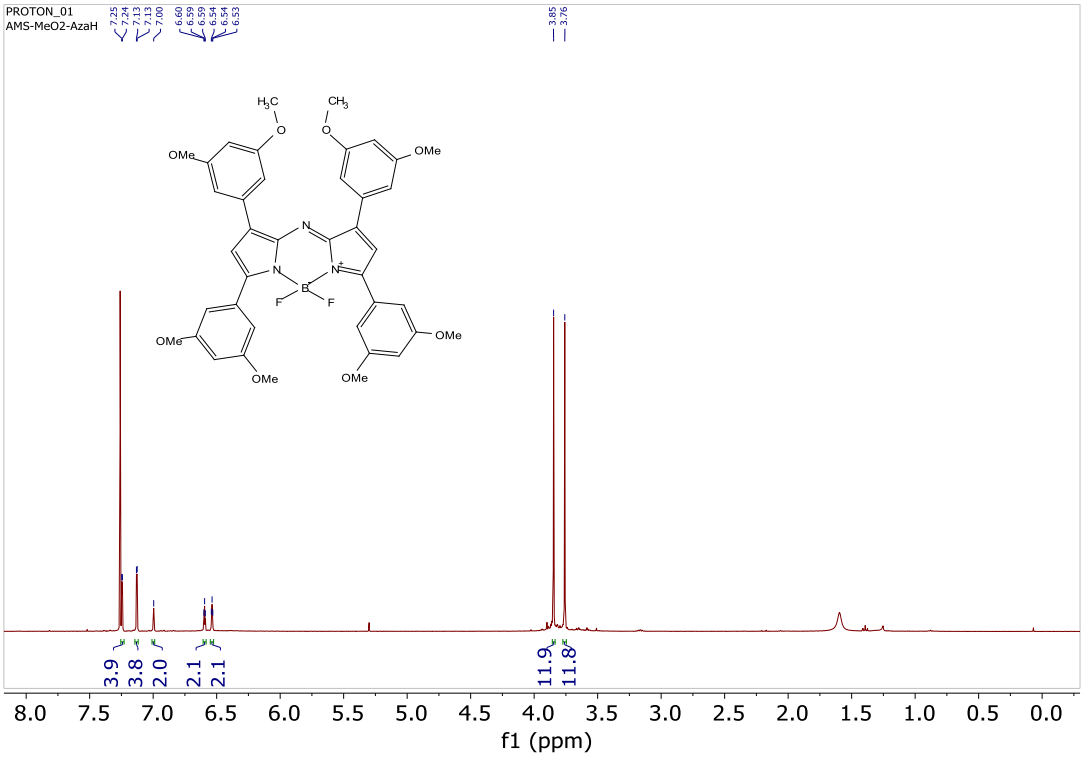

Figure 2.55: ^{1}H NMR of Compound **4c** in $CDCl_3$

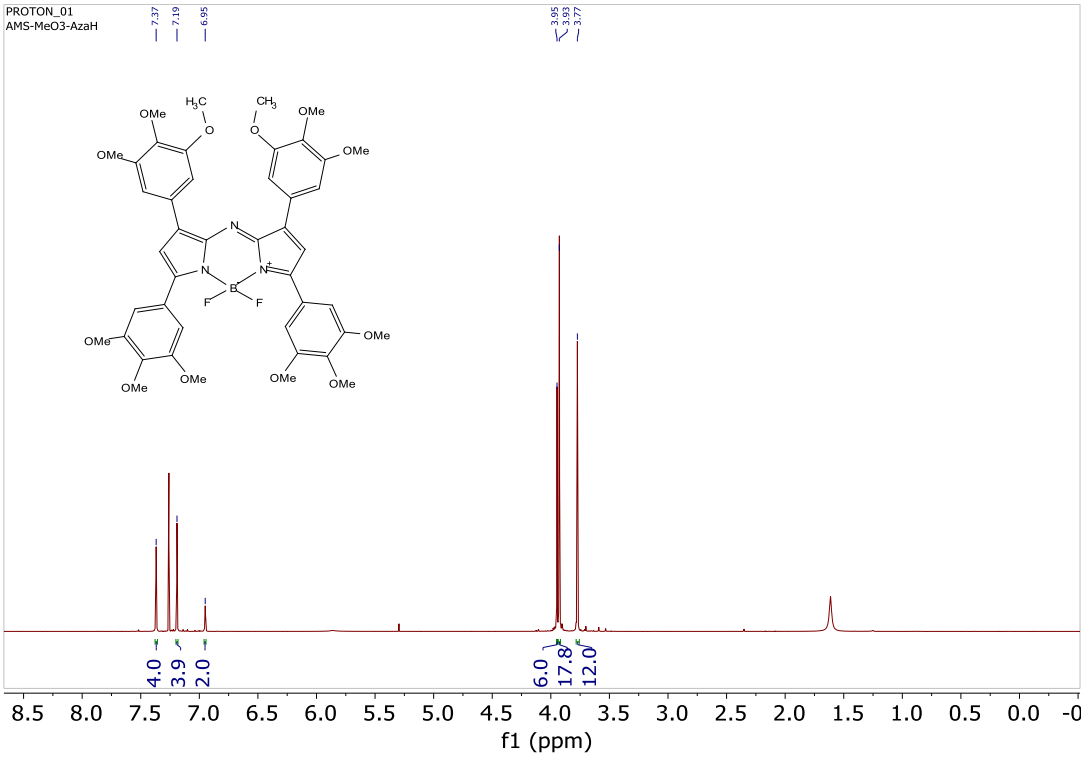

Figure 2.56: ^{1}H NMR of Compound **4d** in $CDCl_3$

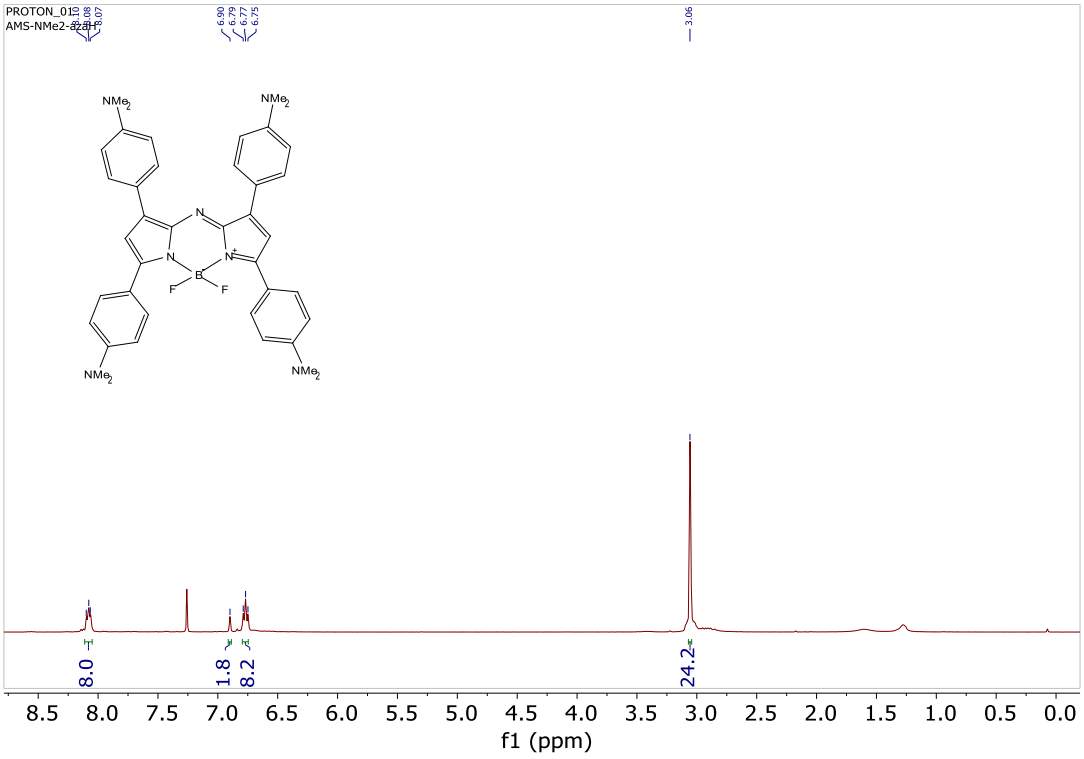

Figure 2.57: ^{1}H NMR of Compound **4e** in $CDCl_3$

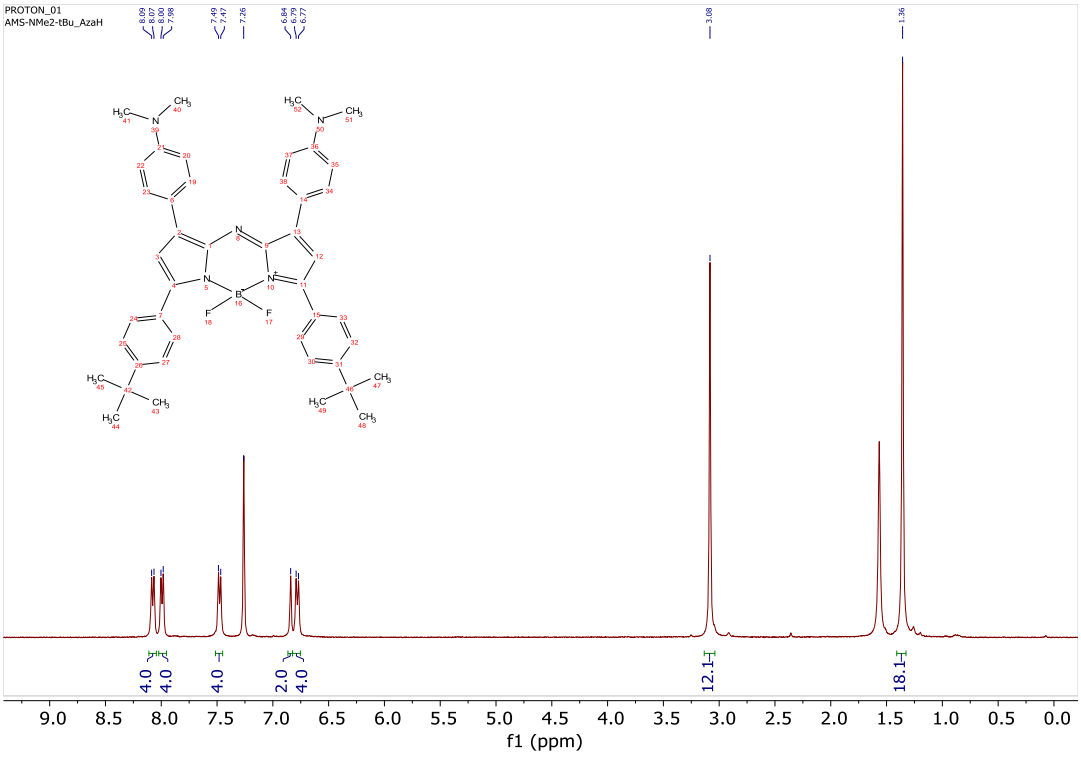

Figure 2.58: ^{1}H NMR of Compound **4f** in $CDCl_3$

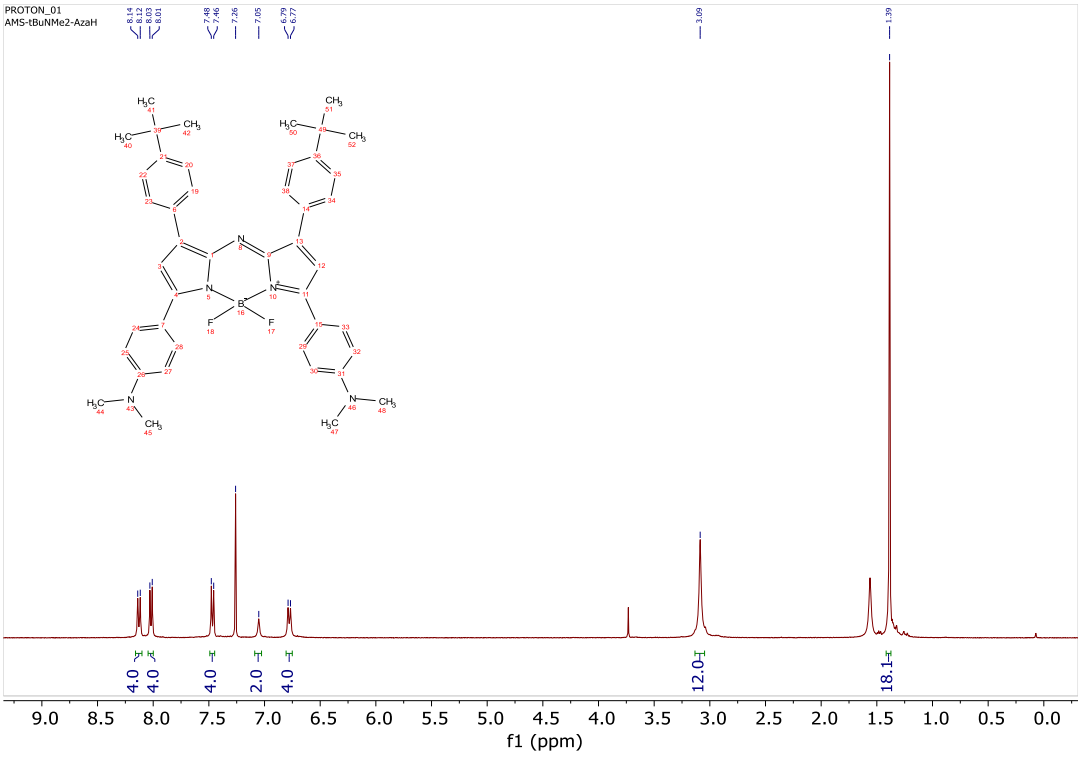

Figure 2.59: ^{1}H NMR of Compound **4g** in $CDCl_3$

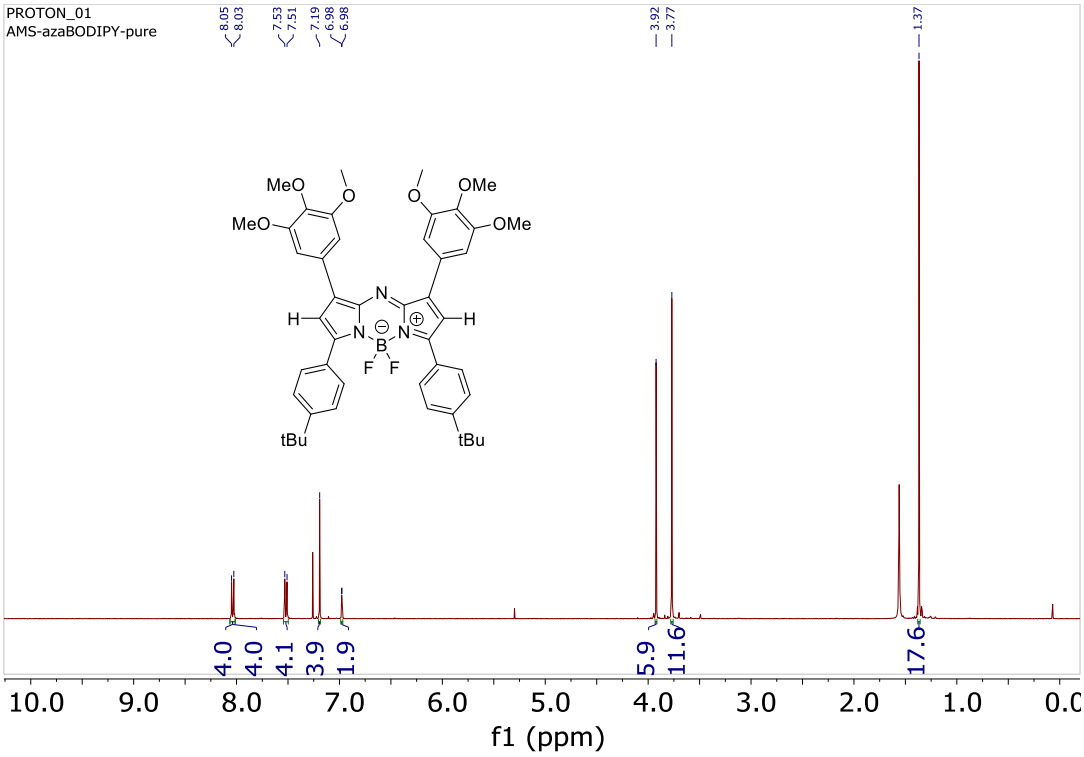

Figure 2.60: ^{1}H NMR of Compound **4h** in $CDCl_3$

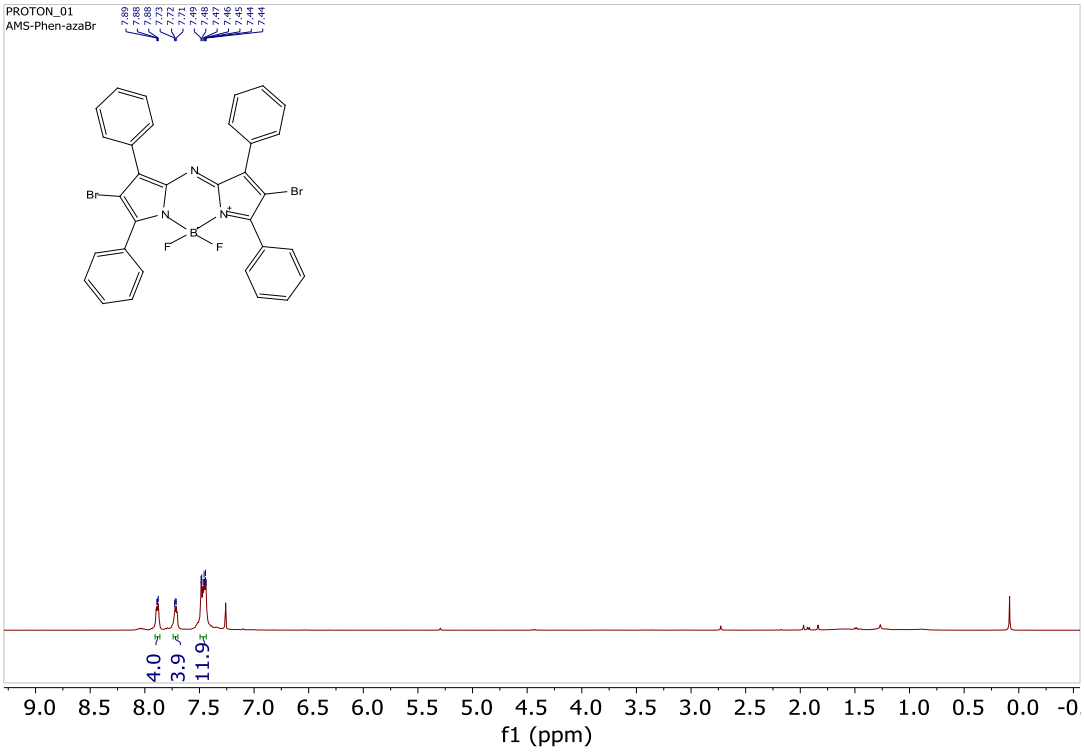

Figure 2.61: ^{1}H NMR of Compound **5a** in $CDCl_3$

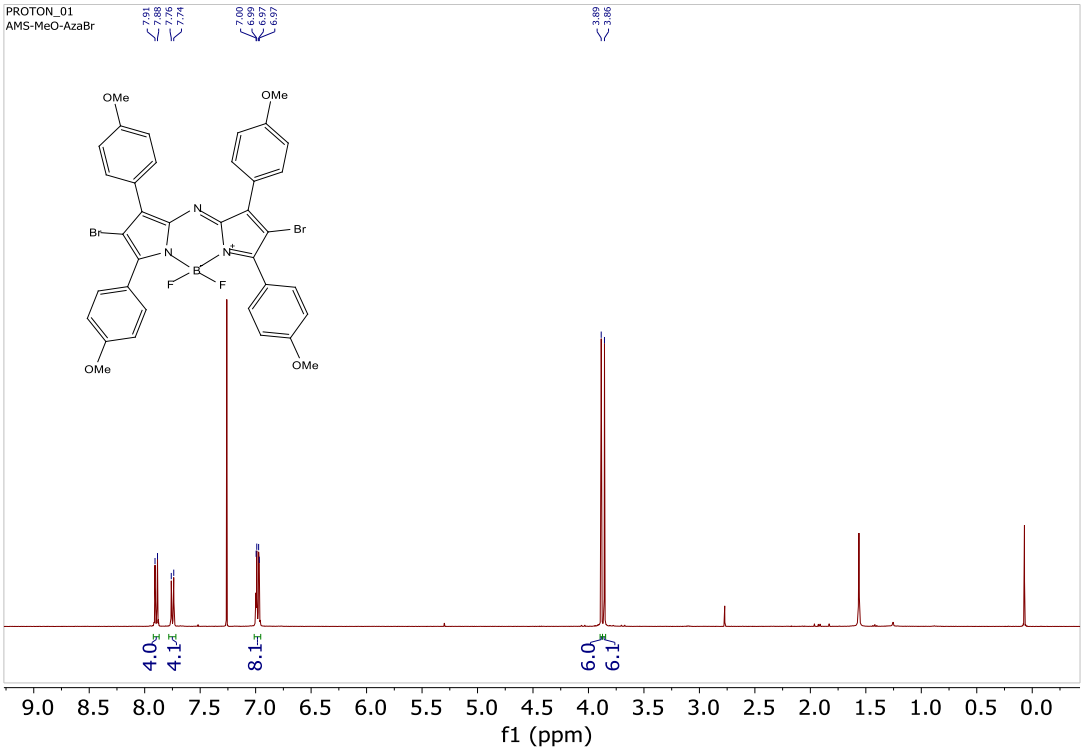

Figure 2.62: ^{1}H NMR of Compound **5b** in $CDCl_3$

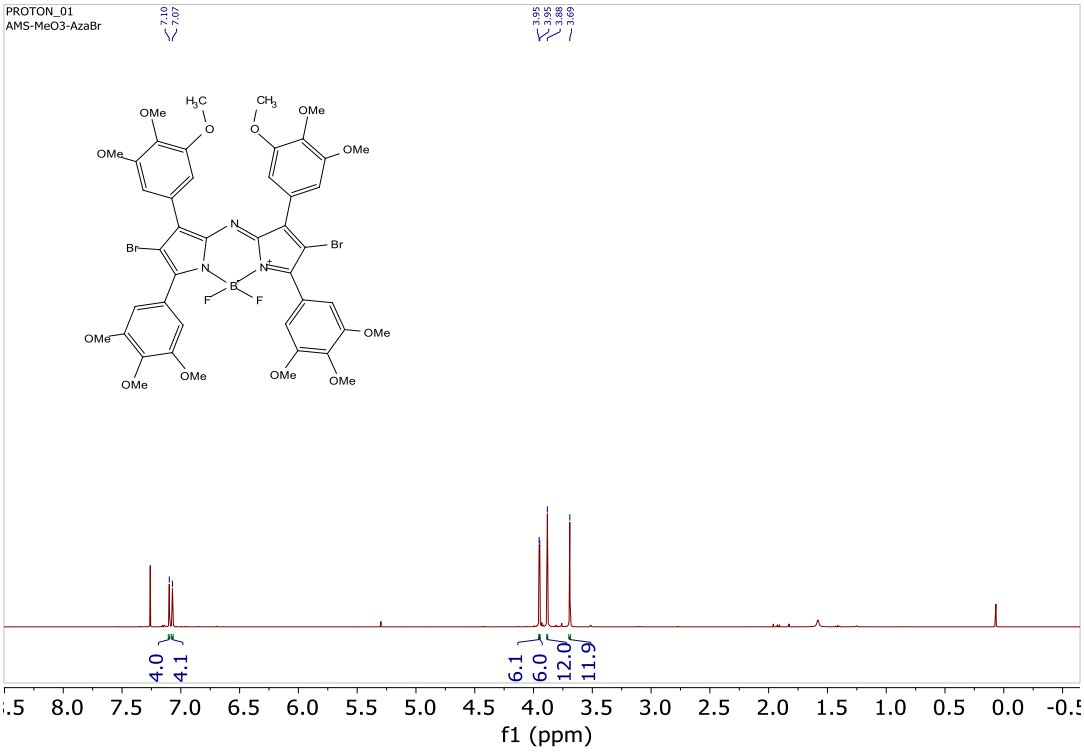

Figure 2.63: ^{1}H NMR of Compound **5d** in $CDCl_3$

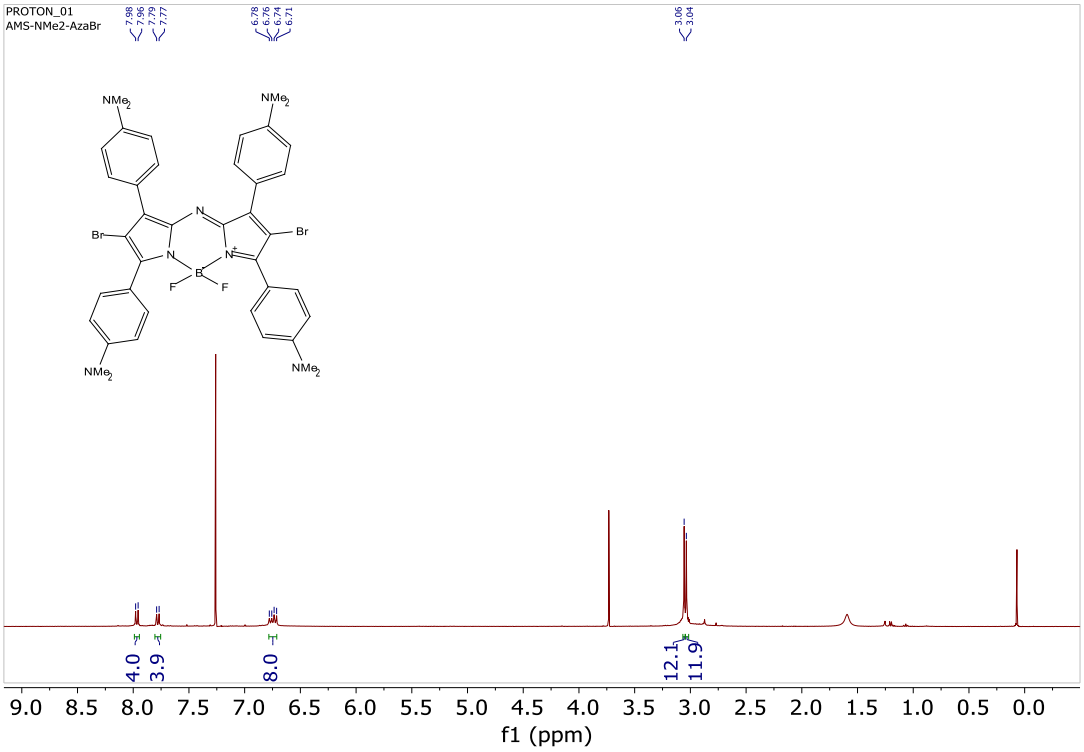

Figure 2.64: ^{1}H NMR of Compound **5e** in $CDCl_3$

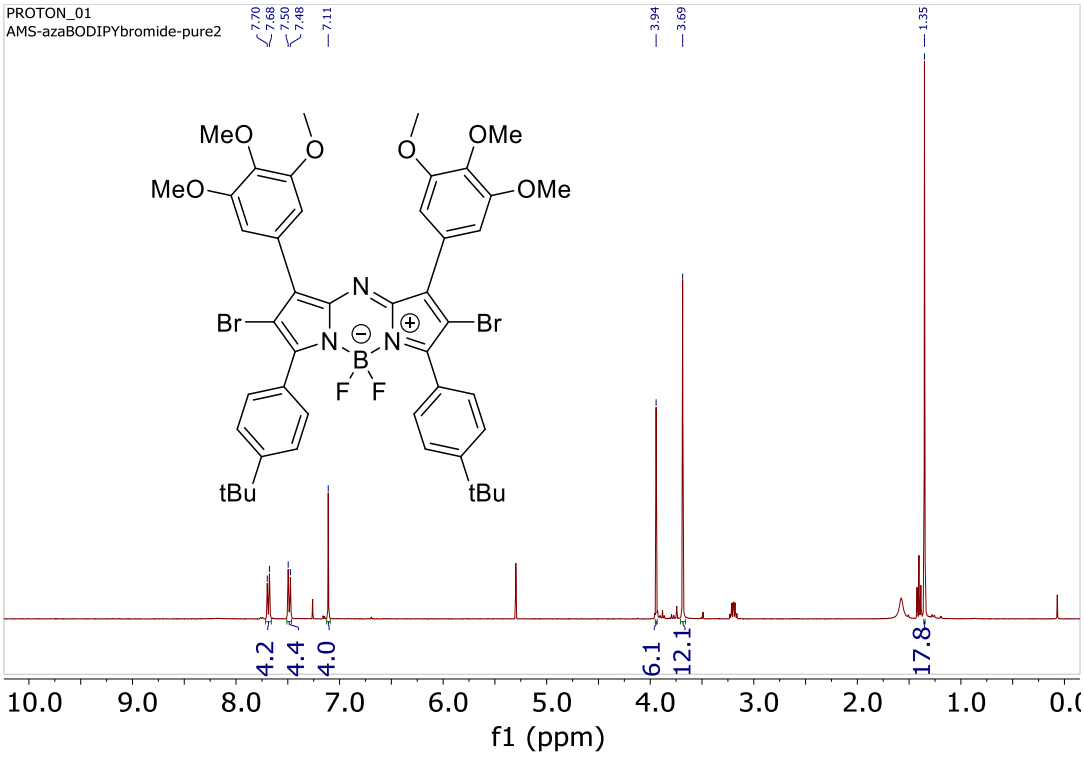

Figure 2.65: ^{1}H NMR of Compound **5h** in $CDCl_3$

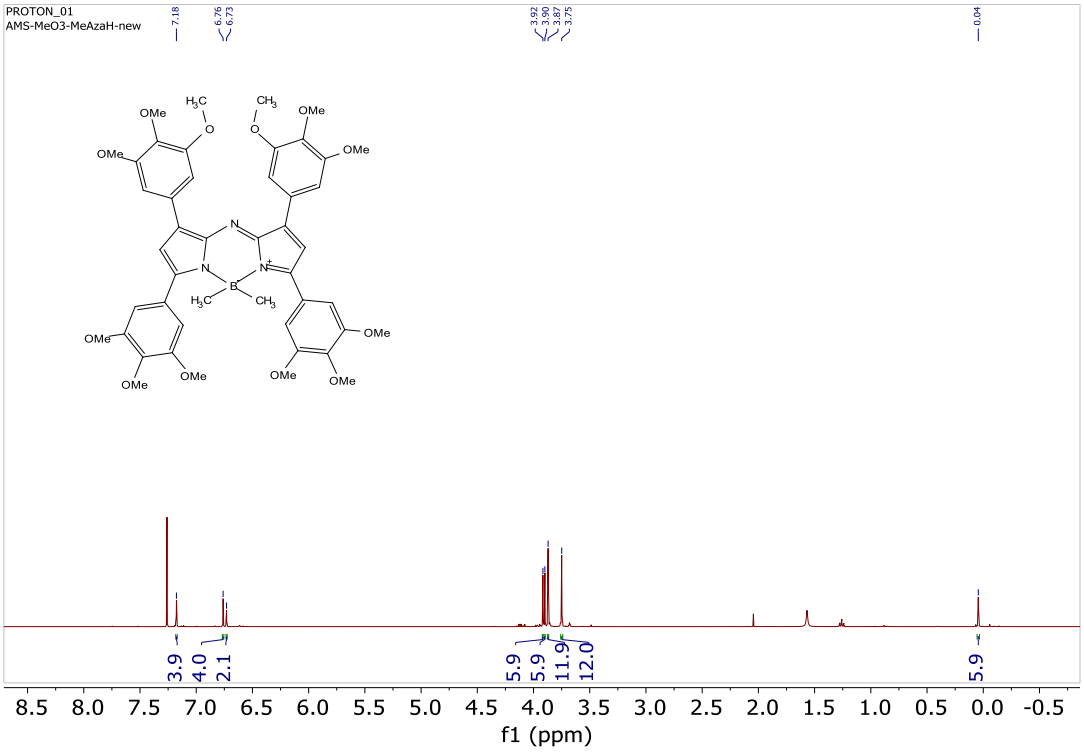

Figure 2.66: ^{1}H NMR of Compound **6d** in $CDCl_3$

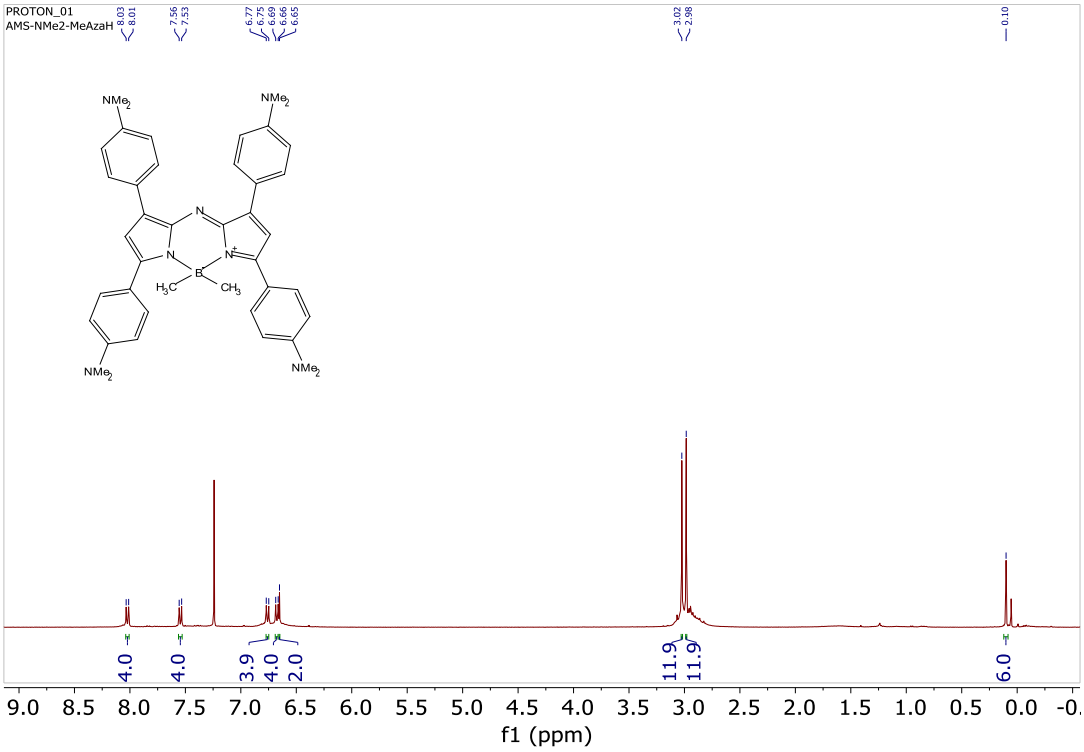

Figure 2.67: ^{1}H NMR of Compound **6e** in $CDCl_3$

2.4: CONCLUSION

The incoprotation of electron-donating groups on aza-BODIPY dyes was demonstrated to be an effective strategy to simultaneosly red-shift and improve the efficiency of light-based polymerizations. Systematic kinetic and optoelectronic characterizations of a series of aza-BODIPY derivatives unveiled critical structure property insights for far-red and near-IR photopolymerizations. Real time ATR-FTIR with custom bottom-up irradiation was used to quantitatively characterize polymerization rate, showing that increasing the quantity of electron-donating groups on aza-BODIPY dyes resulted in faster polymerization rates upon exposure to far-red and near-IR light. Transient absorption spectroscopy confirmed the precesnce of excited charge-transfer states within our near-IR dyes rather than triplet states even upon bromination. The efficiency of this charge transfer could be tuned by adjusting the substituent position on the aza-BODIPY core, which had a direct impact on the rate of photopolymerization. In addition, the aza-BODIPY derivatives were shown to provide unprecedented photopolymerization rates (complete conversion within ~60 s) given extremely low far-red light intensity (~0.66 mW/cm^2), as well as with low near-IR light intensity at 850 nm and 940 nm (~55 mW/cm^2). Additionally, a NIR-azaBODIPY was utilized for the first time to successful print with NIR light from an LED. These results are particularly exciting to inform the future development of more efficient NIR photoredox catalysts that absorb beyond 780 nm, as well as to establish the potential Aza-BODIPYs possess as promising canditates for visible and NIR additive manufacturing.

2.5: REFERENCES

(1) Kocaarslan, A.; Tabanli, S.; Eryurek, G.; Yagci, Y. Near-Infrared Free-Radical and Free-Radical-Promoted Cationic Photopolymerizations by In-Source Lighting Using Upconverting Glass. *Angew. Chemie - Int. Ed.* **2017**, *56* (46), 14507–14510.

(2) Fagnani, D. E.; Tami, J. L.; Copley, G.; Clemons, M. N.; Getzler, Y. D. Y. L.; McNeil, A. J. 100th Anniversary of Macromolecular Science Viewpoint: Redefining Sustainable Polymers. *ACS Macro Lett.* **2021**, *10* (1), 41–53.

(3) Lee, Y.; Boyer, C.; Kwon, M. S. Visible-Light-Driven Polymerization towards the Green Synthesis of Plastics. *Nat. Rev. Mater.* **2021**.

(4) Dumur, F. Recent Advances on Photoinitiating Systems Designed for Solar Photocrosslinking Polymerization Reactions. *Eur. Polym. J.* **2023**, *189*, 111988.

(5) Wallin, T. J.; Pikul, J.; Shepherd, R. F. 3D Printing of Soft Robotic Systems. *Nat. Rev. Mater.* **2018**, *3* (6), 84–100.

(6) Ligon, S. C.; Liska, R.; Stampfl, J.; Gurr, M.; Mülhaupt, R. Polymers for 3D Printing and Customized Additive Manufacturing. *Chem. Rev.* **2017**, *117* (15), 10212–10290.

(7) Bagheri, A.; Jin, J. Photopolymerization in 3D Printing. *ACS Appl. Polym. Mater.* **2019**, *1* (4), 593–611.

(8) Truby, R. L.; Lewis, J. A. Printing Soft Matter in Three Dimensions. *Nature* **2016**, *540* (7633), 371–378.

(9) Murphy, C. A.; Lim, K. S.; Woodfield, T. B. F. Next Evolution in Organ-Scale Biofabrication: Bioresin Design for Rapid High-Resolution Vat Polymerization. *Adv. Mater.* **2022**, *34* (20), 2107759.

(10) Zou, X.; Zhu, J.; Zhu, Y.; Yagci, Y.; Liu, R. Photopolymerization of Macroscale Black 3D Objects Using Near-Infrared Photochemistry. *ACS Appl. Mater. Interfaces* **2020**, *12* (52), 58287–58294.

(11) Lu, P.; Ahn, D.; Yunis, R.; Delafresnaye, L.; Corrigan, N.; Boyer, C.; Barner-Kowollik, C.; Page, Z. A. Wavelength-Selective Light-Matter Interactions in Polymer Science. *Matter* **2021**, *4* (7), 2172–2229.

(12) Atchison, J.; Kamila, S.; Nesbitt, H.; Logan, K. A.; Nicholas, D. M.; Fowley, C.; Davis, J.; Callan, B.; McHale, A. P.; Callan, J. F. Iodinated Cyanine Dyes: A New Class of Sensitisers for Use in NIR Activated Photodynamic Therapy (PDT). *Chem. Commun.* **2017**, *53* (12), 2009–2012.

(13) Borjigin, T.; Schmitt, M.; Giacoletto, N.; Rico, A.; Bidotti, H.; Nechab, M.; Zhang, Y.; Graff, B.; Morlet-Savary, F.; Xiao, P.; Dumur, F.; Lalevée, J. The Blue-LED-

Sensitive Naphthoquinone-Imidazolyl Derivatives as Type II Photoinitiators of Free Radical Photopolymerization. *Adv. Mater. Interfaces* **2023**, *10*, 2202352.

(14) Pang, Y.; Jiao, H.; Zou, Y.; Strehmel, B. The NIR-Sensitized Cationic Photopolymerization of Oxetanes in Combination with Epoxide and Acrylate Monomers. *Polym. Chem.* **2021**, *12* (40), 5752–5759.

(15) Wang, Q.; Popov, S.; Strehmel, V.; Gutmann, J. S.; Strehmel, B. NIR-Sensitized Hybrid Radical and Cationic Photopolymerization of Several Cyanines in Combination with Diaryliodonium Bis(Trifluoromethyl)Sulfonyl Imide. *Polym. Chem.* **2022**, *14* (2), 116–125.

(16) Topa-Skwarczyńska, M.; Galek, M.; Jankowska, M.; Morlet-Savary, F.; Graff, B.; Lalevée, J.; Popielarz, R.; Ortyl, J. Development of the First Panchromatic BODIPY-Based One-Component Iodonium Salts for Initiating the Photopolymerization Processes. *Polym. Chem.* **2021**, *12* (47), 6873–6893.

(17) Ma, Q.; Liu, S.; Le Dot, M.; Mokbel, H.; Zhang, Y.; Graff, B.; Lalevée, J. Imidazole Based Dual Photo/Thermal Initiators for Highly Efficient Radical Polymerization under Air with a Metal-Free Approach. *Polym. Chem.* **2021**, *12* (44), 6386–6391.

(18) Dumur, F. The Future of Visible Light Photoinitiators of Polymerization for Photocrosslinking Applications. *Eur. Polym. J.* **2023**, *187* (December 2022).

(19) Trotta, J. T.; Fors, B. P. Organic Catalysts for Photocontrolled Polymerizations. *Synlett* **2016**, *27* (5), 702–713.

(20) Ahn, D.; Stevens, L. M.; Zhou, K.; Page, Z. A. Rapid High-Resolution Visible Light 3D Printing. *ACS Cent. Sci.* **2020**, *6* (9), 1555–1563.

(21) Ahn, D.; Stevens, L. M.; Zhou, K.; Page, Z. A. Additives for Ambient 3D Printing with Visible Light. *Adv. Mater.* **2021**, *33* (44), 2104906.

(22) Stevens, L. M.; Tagnon, C.; Page, Z. A. "Invisible" Digital Light Processing 3D Printing with Near Infrared Light. *ACS Appl. Mater. Interfaces* **2022**, *14* (20), 22912–22920.

(23) Corrigan, N.; Yeow, J.; Judzewitsch, P.; Xu, J.; Boyer, C. Seeing the Light: Advancing Materials Chemistry through Photopolymerization. *Angew. Chemie - Int. Ed.* **2019**, *58* (16), 5170–5189.

(24) Xiao, P.; Zhang, J.; Dumur, F.; Tehfe, M. A.; Morlet-Savary, F.; Graff, B.; Gigmes, D.; Fouassier, J. P.; Lalevée, J. Visible Light Sensitive Photoinitiating Systems: Recent Progress in Cationic and Radical Photopolymerization Reactions under Soft Conditions. *Prog. Polym. Sci.* **2015**, *41* (C), 32–66.

(25) Bonardi, A. H.; Dumur, F.; Grant, T. M.; Noirbent, G.; Gigmes, D.; Lessard, B. H.; Fouassier, J. P.; Lalevée, J. High Performance Near-Infrared (NIR) Photoinitiating Systems Operating under Low Light Intensity and in the Presence of Oxygen. *Macromolecules* **2018**, *51* (4), 1314–1324.

(26) Bonardi, A.; Bonardi, F.; Noirbent, G.; Dumur, F.; Dietlin, C.; Gigmes, D.; Fouassier, J. P.; Lalevée, J. Different NIR Dye Scaffolds for Polymerization Reactions under NIR Light. *Polym. Chem.* **2019**, *10* (47), 6505–6514.

(27) Zhou, J.; Pitzer, L.; Ley, C.; Rölle, T.; Allonas, X. A Highly Sensitive Photoinitiating System Based on Pre-Associated Ion-Pairs for NIR Radical Photopolymerization of Optically Clear Materials. *Polym. Chem.* **2022**, *13* (47), 6475–6483.

(28) Stafford, A.; Ahn, D.; Raulerson, E. K.; Chung, K. Y.; Sun, K.; Cadena, D. M.; Forrister, E. M.; Yost, S. R.; Roberts, S. T.; Page, Z. A. Catalyst Halogenation Enables Rapid and Efficient Polymerizations with Visible to Far-Red Light. *J. Am. Chem. Soc.* **2020**, *142* (34), 14733–14742.

(29) Xu, Y., Zhao, M., Zou, L., Wu, L., Xie, M., Yang, T., Liu, S., Huang, W., Zhao, Q. Highly Stable and Multifunctional Aza-BODIPY-Based Phototherapeutic Agent for Anticancer Treatment. *ACS Appl. Mater. Interfaces* **2018**, *10* (51), 44234-44335.

(30) Obloza, M., Lapok, L., Pedzinski, T., Stadnicka, K., Nowakowska, M. Synthesis, Photophysics and Redox Properties of Aza-BODIPY Dyes with Electron-Donating Groups. *ChemPhysChem* **2019**, *20* (19), 2482-2497

(31) Sheng, W.; Wu, Y.; Yu, C.; Bobadova-Parvanova, P.; Hao, E.; Jiao, L. Synthesis, Crystal Structure, and the Deep Near-Infrared Absorption/Emission of Bright AzaBODIPY-Based Organic Fluorophores. *Org. Lett*. **2018**, *20* (9), 2620−2623.

(32) Adarsh, N.; Avirah, R. R.; Ramaiah, D. Tuning Photosensitized Singlet Oxygen Generation Efficiency of Novel Aza-BODIPY Dyes. *Org. Lett*. **2010**, *12* (24), 5720−5723.

(33) Zhao, J.; Xu, K.; Yang, W.; Wang, Z.; Zhong, F. The Triplet Excited State of Bodipy: Formation, Modulation and Application. *Chem. Soc. Rev.* **2015**, *44* (24), 8904–8939.

(34) Lu, P.; Chung, K. Y.; Stafford, A.; Kiker, M.; Kafle, K.; Page, Z. A. Boron Dipyrromethene (BODIPY) in Polymer Chemistry. *Polym. Chem.* **2021**, *12* (3), 327–348.

(35) Lakshmi, V.; Rajeswara Rao, M.; Ravikanth, M. Halogenated Boron-Dipyrromethenes: Synthesis, Properties and Applications. *Org. Biomol. Chem.* **2015**, *13* (9), 2501–2517.

(36) Allen, M. J.; Page, Z. A. Tracking Photocuring via ATR-FT-IR with Illumination through the ATR Element. Spectrosc. Appl. Noteb. **2020**, *35* (2), 78

(37) Le, A. K.; Bender, J. A.; Arias, D. H.; Cotton, D. E.; Johnson, J. C.; Roberts, S. T. Singlet Fission Involves an Interplay between Energetic Driving Force and

Electronic Coupling in Perylenediimide Films. *J. Am. Chem. Soc*. **2018**, *140* (2), 814–826.

(38) Azzaro, M. S.; Le, A. K.; Wang, H.; Roberts, S. T. Ligand-Enhanced Energy Transport in Nanocrystal Solids Viewed with Two-Dimensional Electronic Spectroscopy. *J. Phys. Chem. Lett*. **2019**, *10* (18), 5602–5608.

(39) Thorat, K. G.; Kamble, P.; Ray, A. K.; Sekar, N. Novel Pyrromethene Dyes with N-Ethyl Carbazole at the Meso Position: A Comprehensive Photophysical, Lasing, Photostability and TD-DFT Study. *Phys. Chem. Chem. Phys*. **2015**, *17* (26), 17221–17236.

Chapter 3: ThiopheneBODIPYs as Near-IR Photoredox Catalysts

(J. Mater. Chem. A, 2023, 11, 22259-22266)

3.1: INTRODUCTION

From small molecule transformations (photoredox catalysis[1], photolabile protecting groups[2], photobase and photoacid generation[3]) to the synthesis of large polymers[4], the utilization of light as an energy source to perform a myriad of chemical transformations has seen rapid growth in the past decade. Within the field of polymer chemistry, light based photopolymerizations provide a degree of spatiotemporal control and selectivity that traditional polymerization methods are unable to achieve[5-7]. This advantage has led to significant developments in the fields of adhesives, paints, coatings, patterning, photolithography and, more recently, 3D printing[8-13]. Additive manufacturing has seen significant technological advancements in recent years, however, there remain several key challenges to overcome. One such challenge is the limitation in the wavelength of light that can be utilized. While progress has been made to address this shortcoming[14], traditional methods of 3D printing still rely heavily on high energy, UV light to achieve rapid and efficient polymerization. Higher energy light sources negatively impact the scope of light-based 3D printing by limiting material compatibility due to degradation. In order to overcome this limitation, our group has focused on the systematic study and evaluation of the photosystems utilized in 3D printing in order to better optimize the catalysts for longer-wavelength polymerizations. Our previous work developed an efficient green light (530 nm) and far-red light (740 nm) photosystem utilizing a BODIPY and aza-BODIPY core, respectively[15]. Our focus has been centered on BODIPY dyes due to their high degree of tunability, high molar absorptivity, and excellent photostability[16]. Incorporating key design parameters from that previous work,

this work is focused on the development of a fast and efficient system in the near-IR (>780 nm). To that end, we synthesized a series of thiophene-fused BODIPYs in order to both red-shift and, ideally, capitalize on the heavy-atom effect of the sulfur atom, to achieve rapid photopolymerizations at much longer wavelengths of light.

ThiopheneBODIPYs have found their niche application in the field of photodynamic therapy[17-19], where they have demonstrated efficient ISC, good singlet oxygen generation, as well as high molar absorptivities. As a NIR absorbing dye, they also have the advantage of deeper tissue penetration. These strong photoexcited state properties make them ideal candidates for utilization as photoredox catalysts for 3D printing. There are two main types of photosystems for photopolymerization: Type I and Type II. Type I photosystems consist of a photoinitiator that, upon irradiation, will undergo intramolecular bond homolysis to generate the reactive radical species needed to initiate polymerization. This process typically results in very fast initiation, however, is limited in scope due to requiring high energy UV or violet light. Common type I photoinitiators are acyl phosphine oxides like TPO[20]. Type II photosystems, on the other hand, involve an intermolecular process of either hydrogen bond abstraction or electron transfer. The photosystem consists of a photocatalyst that, upon irradiation, will interact with either a donor or donor/acceptor pair to generate the reactive radical species. Because of this, type II photosystems are able to be irradiated with longer wavelengths of light and have minimal side reactions, though tend to be slower than type I photosystems[21]. Traditionally, type II photosystems have been dominated by xanthenes[22] and cyanines[23-24] for blue/green and red/NIR light photopolymerizations, respectively. Fast and efficient photosystems have been developed throughout the visible spectrum[7,8,11,25], however, facile photopolymerizations in the NIR using low intensity light sources still remains a challenge. Lalevée and coworkers[26] have developed

numerous NIR dyes utilizing compounds such as squarines, squaryliums, porphyrins, and BODIPYs for NIR photopolymerizations that can reach a max conversion with rates as fast as 85 s. However, these dyes still require the use of high enery lasers at 400 mW/cm^2. A better understanding of these photosystems utilizing robust and systematic approaches is necessary in order to facilitate the development of new photocatalysts that can operate efficiently at these longer wavelengths of light with lower light intensities. To that end, we report unprecedented sensitivity to far-red and NIR light while maintaining excellent temporal control (no initial dark polymerization). The synthesized thiopheneBODIPYs showed excellent rates of polymerization (<60 s) utilizing LEDs centered at 850 nm and 940 nm with low light intensities of 20 mW/cm^2 and 33 mW/cm^2, respectively.

3.2: Results and Discussion

A series of phenyl substituted meso-CF_3 thiopheneBODIPYs were synthesized and systematically evaluated for their efficiency as photoredox catalysts for radical photopolymerizations (**Figure 3.1**). By incorporating the thiophene moiety onto the

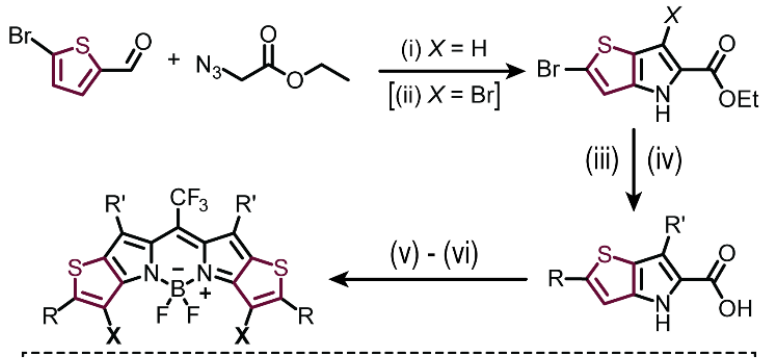

ThiopheneBODIPY-R(I)-X	R'	X	R = *p*OMePh
-Ph_2-H_4	H	H	
-Ph_2-Br_4	Br	Br	
-Ph_4-H_2	*p*OMePh	H	
-Ph_4-Br_2	*p*OMePh	Br	

Figure 3.1: General Synthesis of Meso-CF_3 ThiopheneBODIPY Series

BODIPY core, we aimed for two outcomes: efficient ISC to longer lived triplet excited states by utilizing an -S atom in lieu of a halogen heavy atom as well as to further redshift the photocatalyst into the near-IR. This longer-lived excited state, as we have previously demonstrated, can lead to more efficient photocatalysts and the subsequent redshift allows us to utilize longer wavelengths of light for rapid photopolymerizations. As we shall observe, our meso-CF_3 thiopheneBODIPYs, were able to achieve ISC to long-lived excited states though the respective excited state energies were not able to sensitize singlet oxygen. Despite this limitation, our BODIPYs showcase unprecedented reactivity with NIR LEDs at 780 nm and 850 nm. This unexpected result led us to explore the interplay and importance of not only excited state lifetime, but photoredox electron transfer efficiency. Upon synthesizing the above photocatalysts, we examined their photophysical properties (**Figure 3.2 & Table 3.1**). With the incorporation of methoxy-

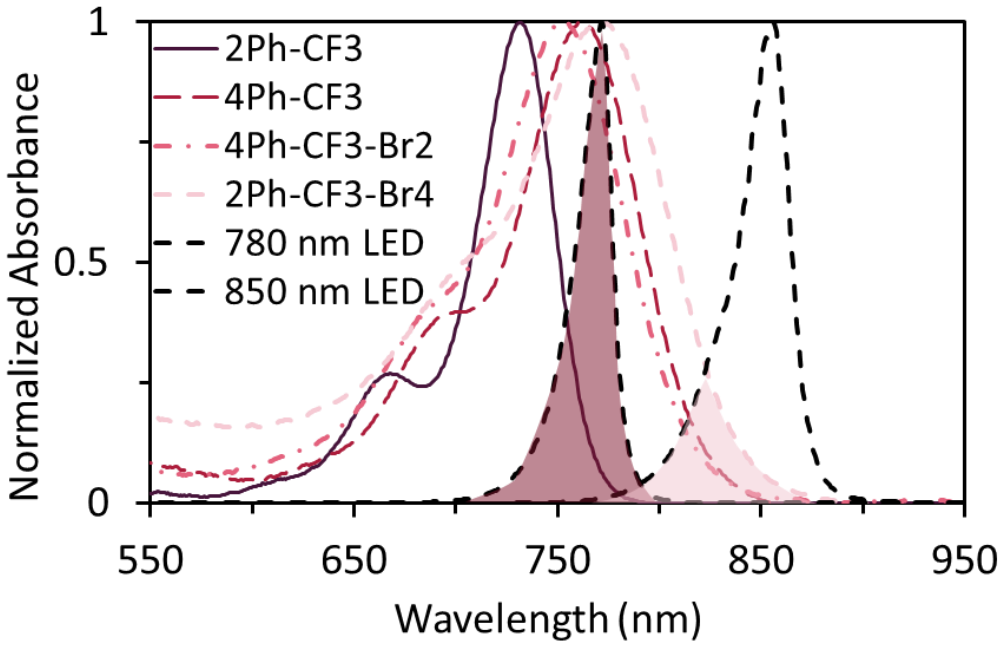

Figure 3.2: Absorbance Profiles of Meso-CF_3 ThiopheneBODIPYs in DCM Overlayed With 780 and 850 nm LEDs.

phenyl substituents, we were able to achieve maximum absorbances ranging from 731 – 768 nm with the -meso CF_3 BODIPYs. Interestingly, dibromination of the 4Ph-CF_3

BODIPY	λ_{max} (nm)	ε ($M^{-1}cm^{-1}$)	λ_{em} (nm)
2Ph-CF_3	730	161,000 ± 3000	754
2Ph-CF_3-Br_4	765	40,000 ± 2000	834
4Ph-CF_3	763	85,000 ± 2100	812
4Ph-CF_3-Br_2	748	46,000 ± 1000	816

Table 3.1: Optoelectronic Properties of the Meso-CF_3 ThiopheneBODIPY Photoredox Catalysts

derivative results in a slight blue-shift in maximum absorbance, whereas tetrabromination of the 2Ph-CF_3 derivative results in a red-shift in absorbance. In addition to absorbance, we were also able to measure the fluorescence of each thiopheneBODIPY. As can be seen in **Figure 3.2**, the respective absorbance profiles of the thiopheneBODIPYs overlay nicely with the emission profiles of our 780 and 850 nm LEDs enabling us to utilize them for near-IR photopolymerizations. With our photocatalysts in hand, we began evaluating their utility as near-IR initiators for radical polymerizations. Our resin composition is a type II photosystem consisting of our thiopheneBODIPYs, a donor borate salt (Borate V), acceptor iodonium salt (HNu 254), and isobornyl acrylate as the monomer. The rate of polymerization was monitored using the same photo-ATR FTIR setup from PIKE technologies that allows us to irradiate and measure the sample from the same surface (**Figure 3.3**).

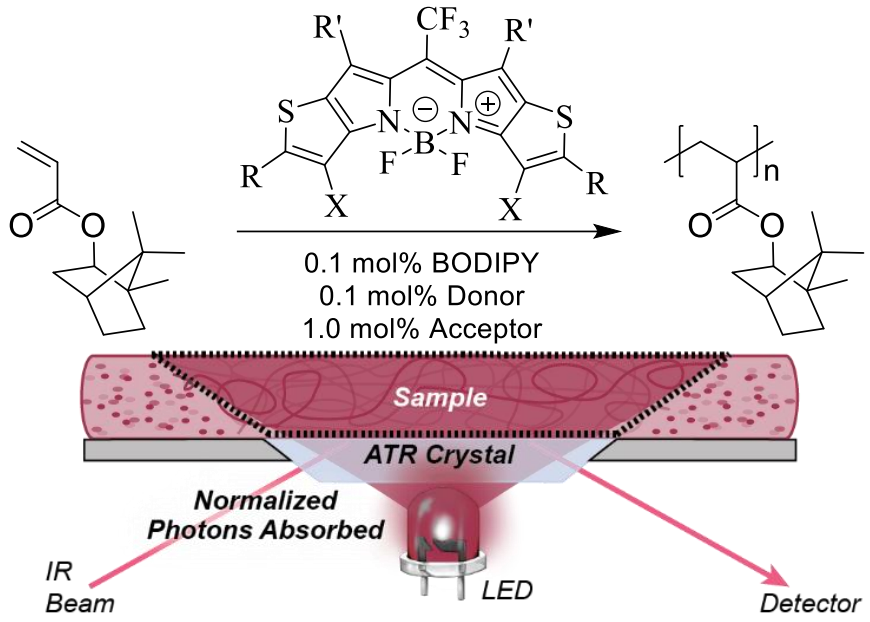

Figure 3.3: Monomer Resin Composition and Photo-ATR FTIR Setup

Utilizing a 780 nm LED, **Figures 3.4** and **3.5** show the rate of photopolymerization for 2Ph-CF_3 and 2Ph-CF_3-Br_4 at varying light intensities. The tetrabrominated derivative shows a significant increase in the rate of polymerization (~3.5-4x) compared to the non-brominated achieving max conversion within 20 s at 40 mW/cm^2 and able to go as low as 5 mW/cm^2 and still reach max conversion within 60 s. The nonbrominated derivative on the other hand is unable to reach max conversion even within 160 s. This improvement in rate is due to two factors: better overlap with the emission profile of the 780 nm LED and access to triplet excited states from bromination. The tetrabrominated 2Ph-CF_3-Br_4 derivative has a max absorbance at 765 nm whereas the nonbrominated 2Ph-CF_3 is at 730 nm. From the TA data in **Figure 3.6**, we observe a triplet excited state lifetime of 943 ns for 2Ph-CF_3-Br_4 whereas 2Ph-CF_3 does not show any triplet activity.

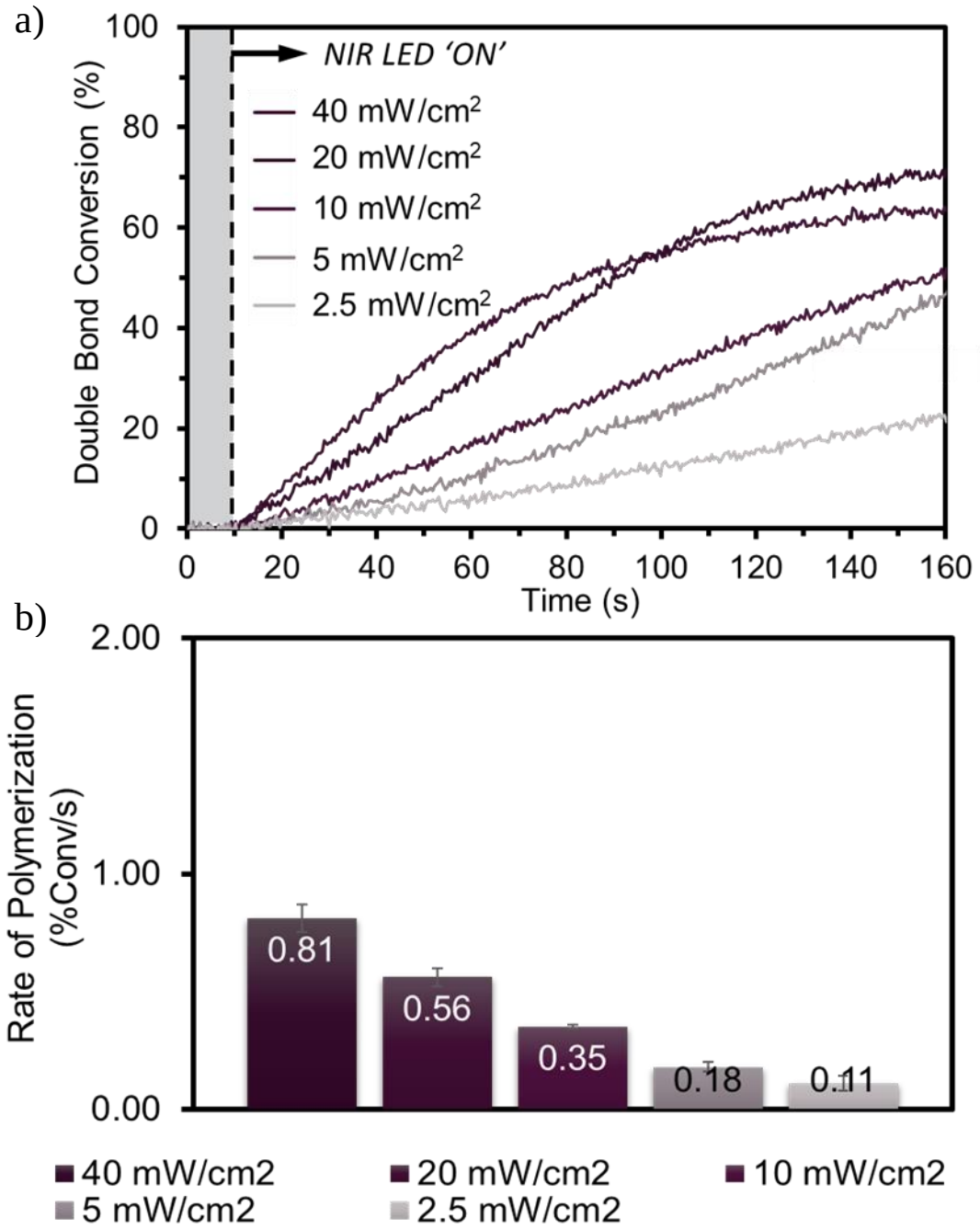

Figure 3.4: (a) Photopolymerization Rate of Isobornyl Acrylate With 0.1 mol% 2Ph-CF_3, 0.1 mol% Borate V, and 1.0 mol% HNu 254 Using a 780 nm LED at Varying Intensities. (b) Polymerization Rate in %Conversion/second at the Different LED Intensities. Error Bars Represent ± 1 Standard Deviation.

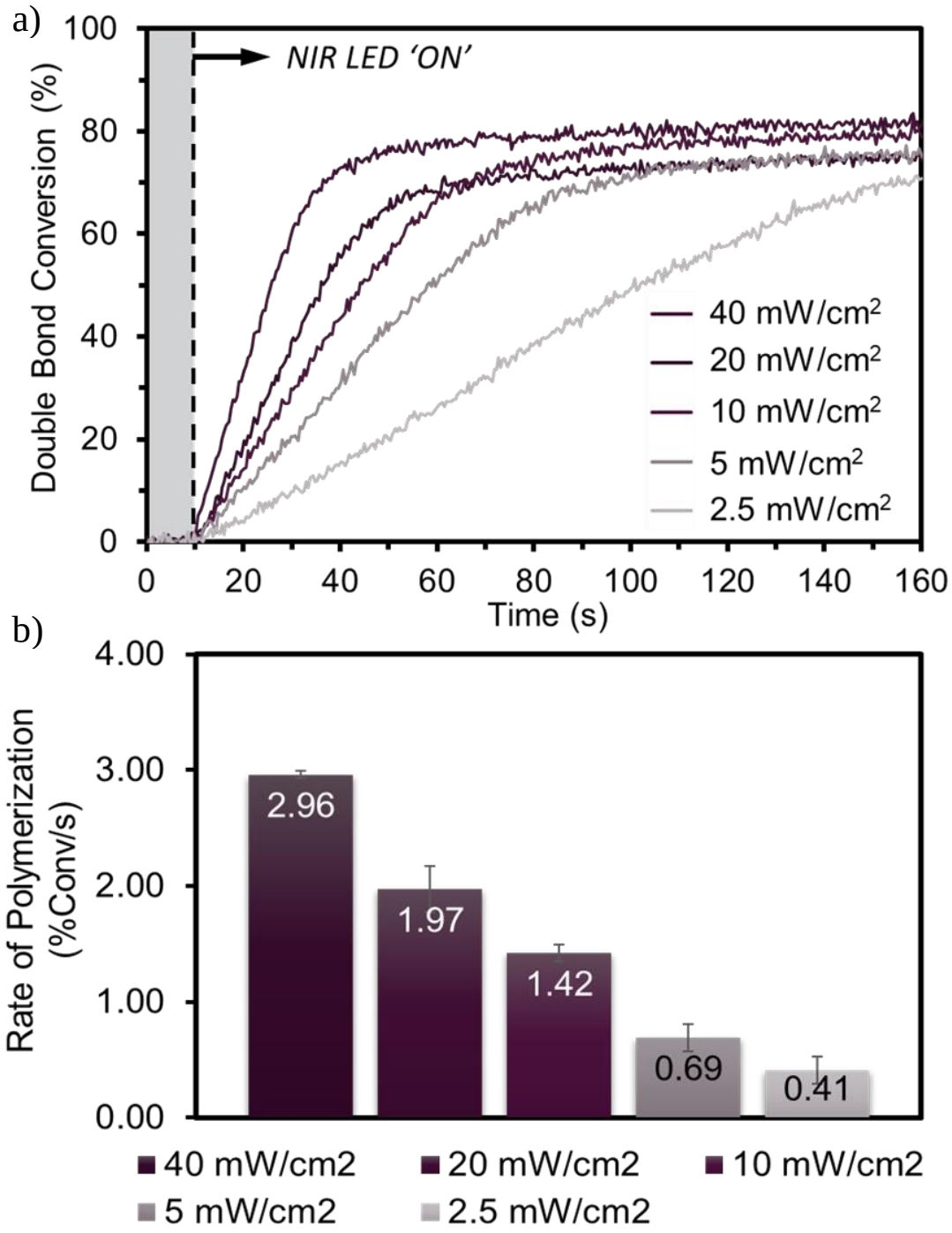

Figure 3.5: (a) Photopolymerization Rate of Isobornyl Acrylate With 0.1 mol% 2Ph-CF_3-Br_4, 0.1 mol% Borate V, and 1.0 mol% HNu 254 Using a 780 nm LED at Varying Intensities. (b) Polymerization Rate in %Conversion/second at the Different LED Intensities. Error Bars Represent ± 1 Standard Deviation.

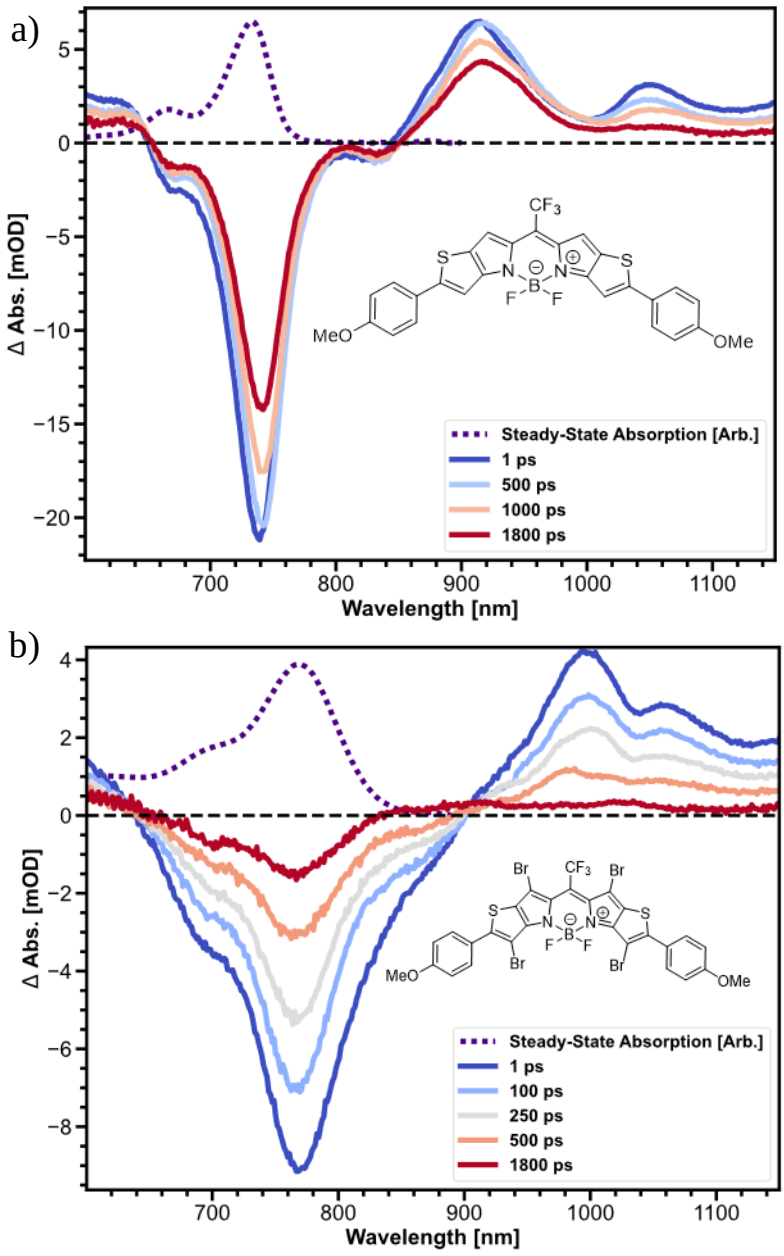

Figure 3.6: Femtosecond Transient Absorption Data for 2Ph-CF_3 (a) and 2Ph-CF_3-Br_4 (b) in Toluene.

Utilizing the red-shifted 4Ph-CF_3 and 4Ph-CF_3-Br_2 thiopheneBODIPYs, we can use an 850 nm LED to perform the photopolymerizations. In order to ensure that these polymerizations were occurring via NIR light, we used a 775 longpass (LP) filter to block

any emission below the NIR region and the subsequent impact on the LED emission profile can be seen in **Figure 3.15** in the experimental section. As can been seen in **Figures 3.7** and **3.8**, the 4Ph-CF_3 and 4Ph-CF_3-Br_2 demonstrate similar efficiency utilizing an 850 nm LED with a 775 LP filter. The dibrominated derivative rate is slightly faster achieving max conversion within 20 s at 40 mW/cm^2 and 70 s at 10 mW/cm^2 whereas the nonbrominated derivative achieves max conversion within 40 s at 40 mW/cm^2 and within 120 s at 10 mW/cm^2. The rate enhancement with bromination is ~1.2x times faster than nonbromination. This increase in efficiency can be explained via the long-lived triplet excited state of 4Ph-CF_3-Br_2 and the faster rate of ISC. Halogenation enhances its ability to undergo ISC relative to nonbromination. From the TA data in **Figure 3.9**, we observe a triplet excited state lifetime of 9.5 μs and a triplet yield of 5.5%.

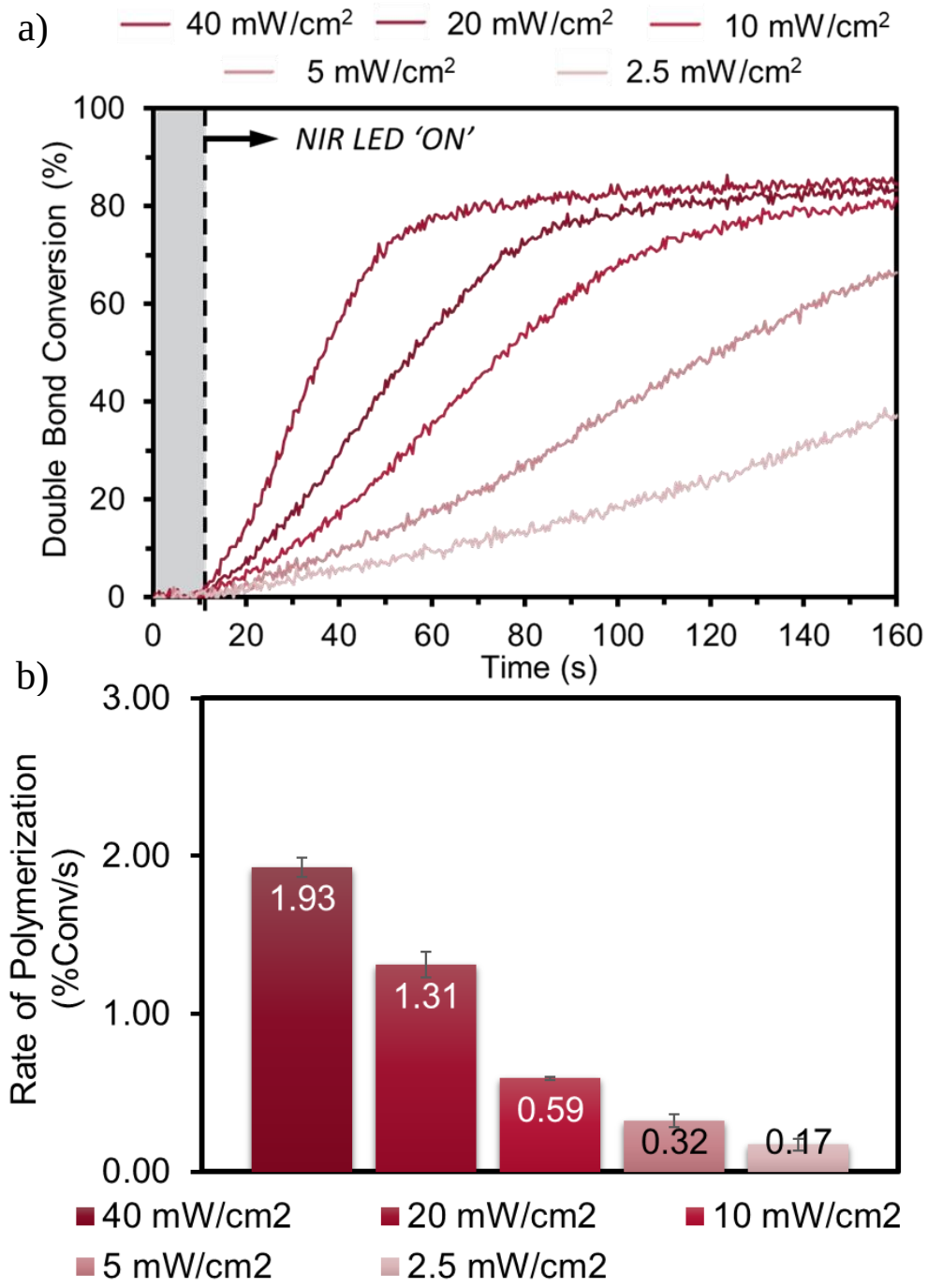

Figure 3.7: (a) Photopolymerization Rate of Isobornyl Acrylate With 0.1 mol% 2Ph-CF_3-Br_4, 0.1 mol% Borate V, and 1.0 mol% HNu 254 Using a 780 nm LED at Varying Intensities. (b) Polymerization Rate in %Conversion/second at the Different LED Intensities. Error Bars Represent ± 1 Standard Deviation.

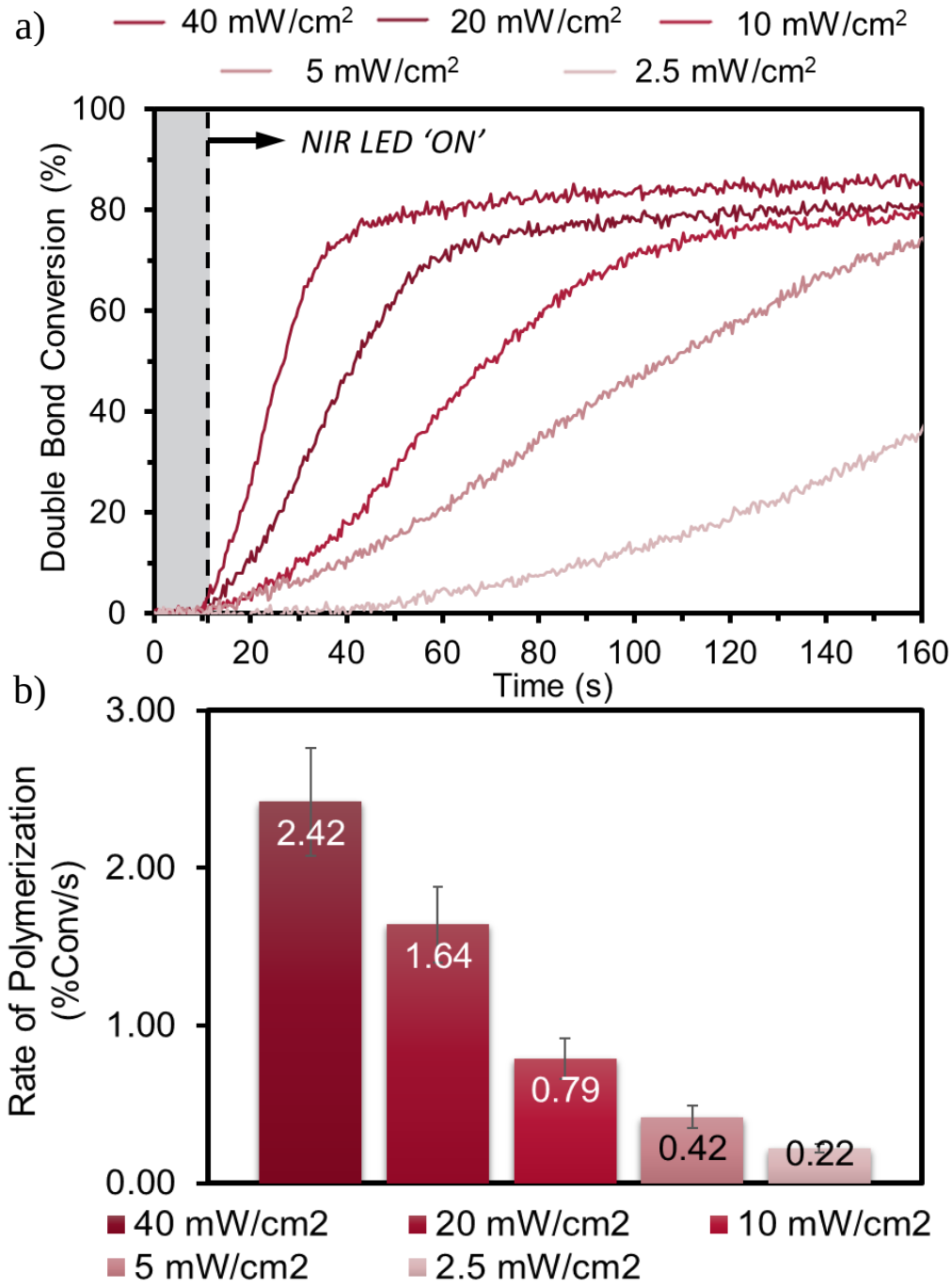

Figure 3.8: (a) Photopolymerization Rate of Isobornyl Acrylate With 0.1 mol% 2Ph-CF_3-Br_4, 0.1 mol% Borate V, and 1.0 mol% HNu 254 Using a 780 nm LED at Varying Intensities. (b) Polymerization Rate in %Conversion/second at the Different LED Intensities. Error Bars Represent ± 1 Standard Deviation.

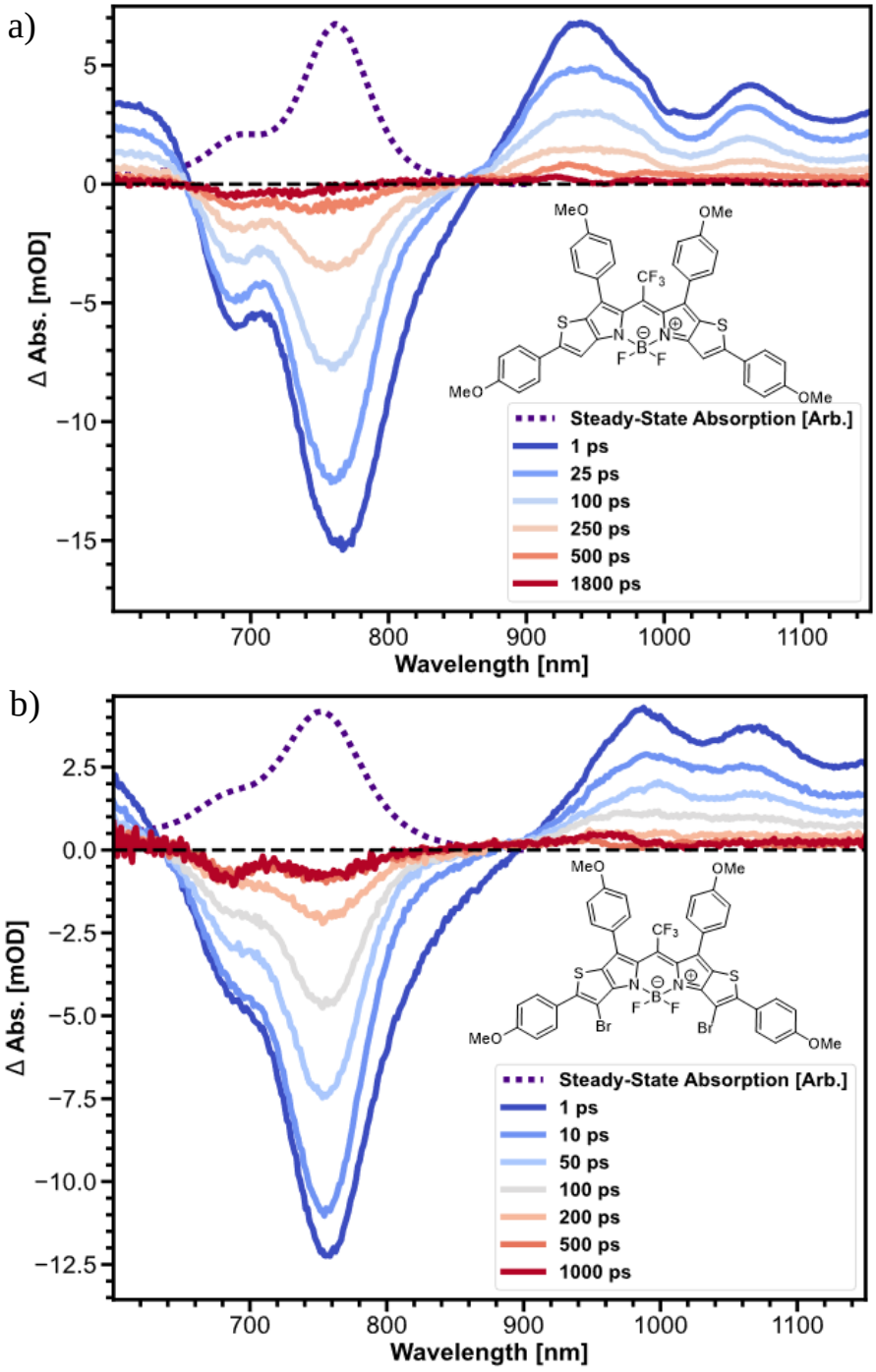

Figure 3.9: Femtosecond Transient Absorption Data for 4Ph-CF_3 (a) and 4Ph-CF_3-Br_4 (b) in Toluene.

In addition to examining the impact of light intensity on photopolymerization efficiency, we also evaluated the 4Ph-CF_3 and 4Ph-CF_3-Br_2 thiopheneBODIPYs by equalizing the total number of photons absorbed between them as we have done previously. This was done in order to account for the differing absorbance profiles of the photocatalysts. From this we can ascertain the relative efficiency that is intrinsic to the structure of the photocatalyst, rather than the catalyst simply having a better absorption cross-section with the LED emission profile. As we can see in **Figure 3.10**, the rate of photopolymerization at 850 nm for 4Ph-CF_3-Br_2 is slightly faster than the nonbrominated

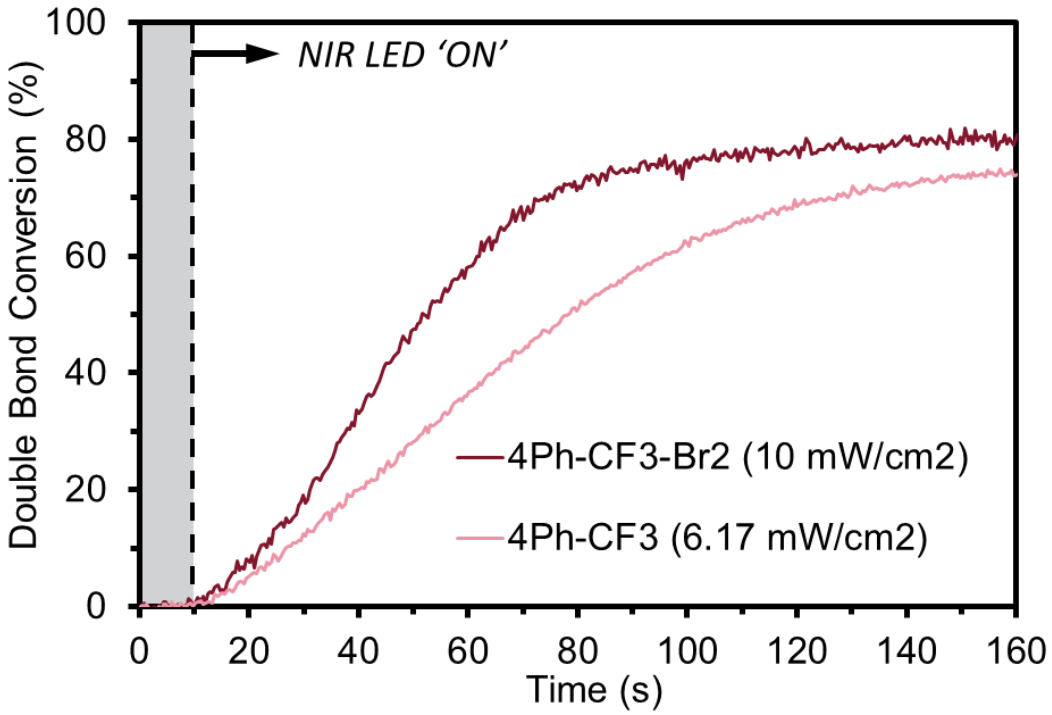

Figure 3.10: Photopolymerization of Isobornyl Acrylate With 4Ph-CF_3 and 4Ph-CF_3-Br_2 ThiopheneBODIPYs Using an 850 nm LED With a 775 LP Filter at Equal Photon flux. Resin Formulation: 0.1 mol% BODIPY, 0.1 mol% Borate V, and 1.0 mol% HNu 254

4Ph-CF_3. This rate enhancement can be rationalized based on the ability for the brominated derivative to form low energy long-lived triplet excited states. We do not observe as drastic of a rate enhancement as we have previously explored with the mesitylBODIPYs in Chapter 1 and azaBODIPYs in Chapter 2 due to how low in energy the excited state is, but it is enough to give it a slight advantage over nonbromination.

We also evaluated the ability for the thiopheneBODIPYs to polymerize polar monomers as our previous NIR derivatives in Chapter 2 struggled to polymerize due to the CT excited state we were accessing. As can be seen in **Figure 3.11**, the 4Ph-CF_3 thiopheneBODIPY has no trouble polymerizing 2-hydroxyethylacrylate at 850 nm.

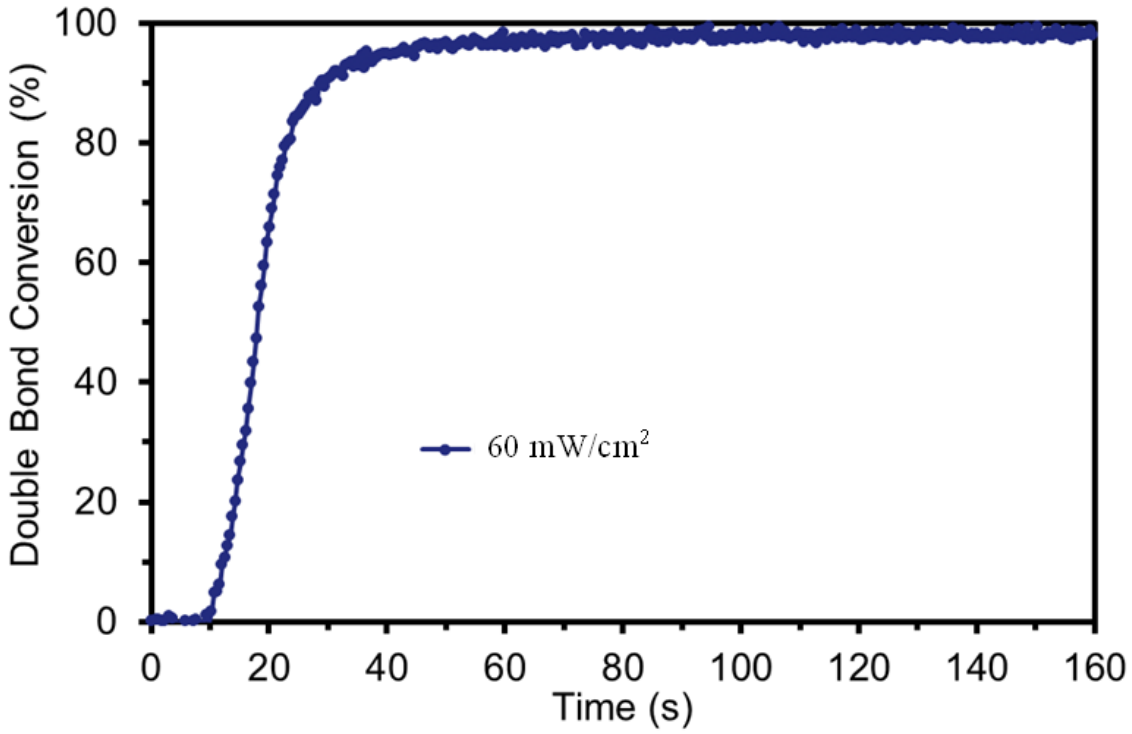

Figure 3.11: Photopolymerization of 2-hydroxyethylacrylate (HEA) With 4Ph-CF_3 ThiopheneBODIPYs Using an 850 nm LED at 60 mW/cm^2. Resin Formulation: 0.1 mol% BODIPY, 0.1 mol% Borate V, and 1.0 mol% HNu 254

Additional optimization was also performed on the resin composition to further improve the rate of polymerization with NIR light. We sequentially increased the mol% of the donor co-initiator present from the original 0.1 mol% from our previous work all the way to 1.0 mol% to match the acceptor mol%. As can be seen in **Figure 3.12**, we observe a significant increase in the rate of photopolymerization using an 850 nm LED at

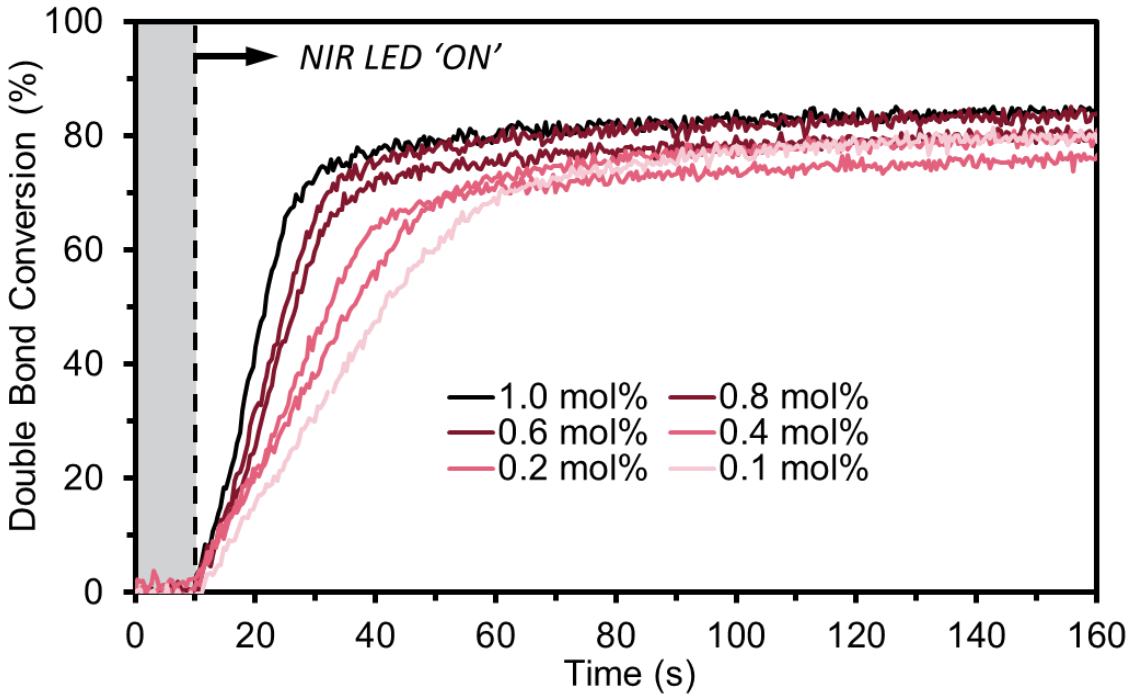

Figure 3.12: Photopolymerization of Isobornyl Acrylate With 4Ph-CF_3 ThiopheneBODIPY Using an 850 nm LED With a 775 LP Filter at 20 mW/cm^2. Resin Formulation: 0.1 mol% BODIPY, X mol% Borate V, and 1.0 mol% HNu 254

20 mW/cm^2 as we increase the concentration of donor present to match the concentration of acceptor at 1.0 mol%. We see a 3-fold increase in the initial rate of polymerization (1.31 %Conv/s at 0.1 mol% to 4.09 %Conv/s at 1.0 mol%) and reach max conversion in 20 s rather than 60 s using the original resin composition.

Lastly, we evaluated our thiopheneBODIPY photocatalyst against a commercially available cyanine dye (HNu 815) utilizing an equal number of photons absorbed at 850 nm and can be found in **Figure 3.13**. The mol% of photocatalyst was lowered to 0.05 mol% due to solubility issues with HNu 815 in isobornyl acrylate. The photon flux comparison of the cyanine and thiopheneBODIPY shows an improved rate (2x) in the intrinsic efficiency of the thiopheneBODIPY over the cyanine photocatalyst with the 4Ph-CF_3 derivative reaching max conversion in 20 s and the HNu 815 in 40 s. This result highlights the potential the thiopheneBODIPY core has in creating highly efficient NIR photoredox catalysts.

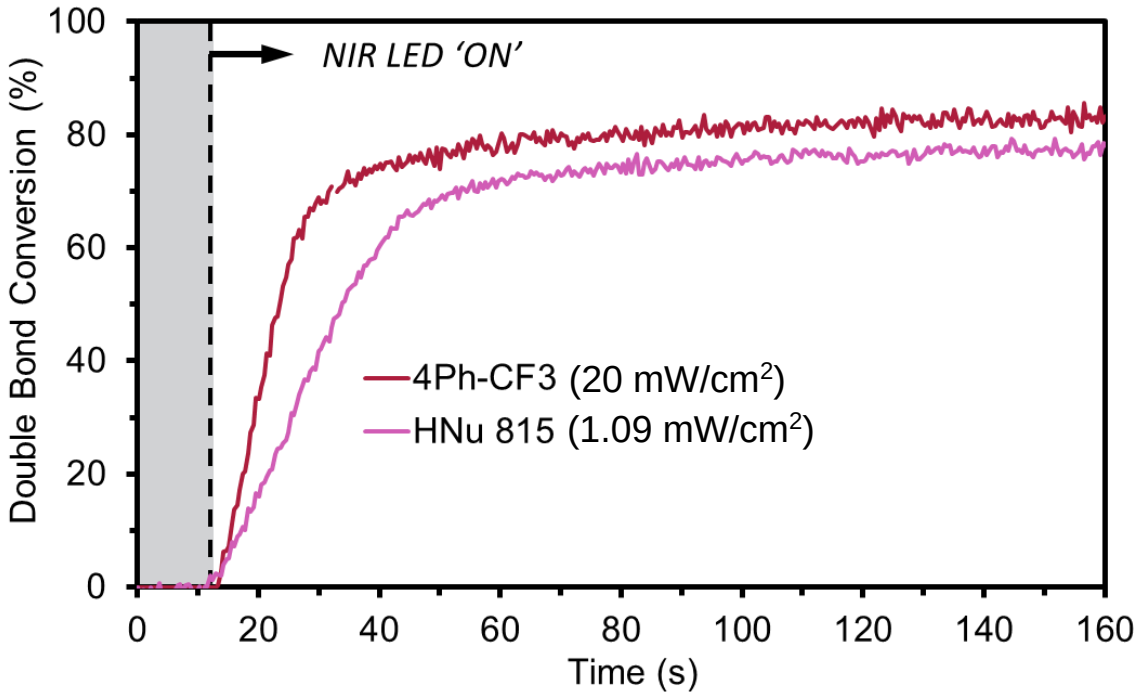

Figure 3.13: Photopolymerization of Isobornyl Acrylate With 4Ph-CF_3 ThiopheneBODIPY and HNu 815 Using an 850 nm LED With a 775 LP filter at Equal Photon Flux. Resin Formulation: 0.05 mol% BODIPY, 0.1 mol% Borate V, and 1.0 mol% HNu 254.

3.3: EXPERIMENTAL

3.31: MATERIALS

Chemicals: ethyl azidoacetate 95.0+% TCI America, trifluoroacetic acid 99.0+% TCI America, dichloromethane (DCM) 99.9%, anhydrous, sodium hydroxide (NaOH) (certified ACS), methanol (MeOH) (certified ACS), ethanol, anhydrous (EtOH), tetrahydrofuran (THF), and toluene (Certified ACS) were purchased from Fisher Scientific. 2-thiophenealdehyde and 5-bromo-2-formylthiophene were purchased from VWR. 4-methoxyphenylboronic acid ≥98% and trifluoroacetic anhydride ≥99% were purchased from Chem-Impex. sodium ethoxide 96%, sodium carbonate 98%, and bromine ≥99.8% were purchased from Alfa Aesar. triethylamine ≥99.5% was purchased from Sigma-Aldrich. Boron trifluoride diethyl etherate 98% was purchased from Oakwood Chemical. Tetrakis(triphenylphosphine)-palladium(0) 99% was purchased from Strem Chemicals. H-Nu 254, Onium Salt and Borate V were purchased from Spectra Group Limited, Inc. $CDCl_3$ 99.8% was purchased from Cambridge Isotope Laboratories. All chemicals were used as received without additional purification, unless otherwise noted.

3.32: EQUIPMENT AND INSTRUMENTATION

NUCLEAR MAGNETIC RESONANCE (NMR) SPECTROSCOPY

NMR spectra were recorded on an Agilent MR 400 MHz spectrometer utilizing $CDCl_3$ as the solvent. ^{1}H NMR were carried out coupled and referenced to the $CDCl_3$ chemical shift at 7.26 ppm. ^{13}C NMR were carried out decoupled and referenced to the $CDCl_3$ chemical shift at 77.16 ppm.

HIGH RESOLUTION MASS SPECTROMETRY (HRMS)

HRMS was performed on an Agilent Technologies 6530 Accurate-Mass Q-TOF LC/MS using ESI and the data was subsequently analyzed using Agilent MassHunter Qualitative Analysis Software.

REAL-TIME FOURIER-TRANSFORM INFRARED SPECTROSCOPY (RT-FTIR)

RT-FTIR was recorded utilizing an INVENIO-R FT-IR Spectrometer from Bruker (Figure S1) and controlled via OPUS Spectroscopy Software. A liquid nitrogen cooled (LN-MCT Mid) detector was used for measurements. A modified GladiATR Illuminate ATR accessory[27] from PIKE Technologies was used to analyze chemical composition and monitor photocuring of liquid resins upon exposure to light. Collimated LED light sources (740 nm-P/N LCS-0740-10-22, 810 nm-P/N LCS-0810-02-22, 850 nm-P/N LCS-0850-03-22, 940 nm-P/N LCS-0940-02-38) from Mightex Systems along with Lightguide Adapters were utilized to irradiate resins with visible light (see photopolymerization procedure for more details). LED Controller M/N SLC-MA02-U was used with a 3 mm liquid light guide (LLG-3- 4H).

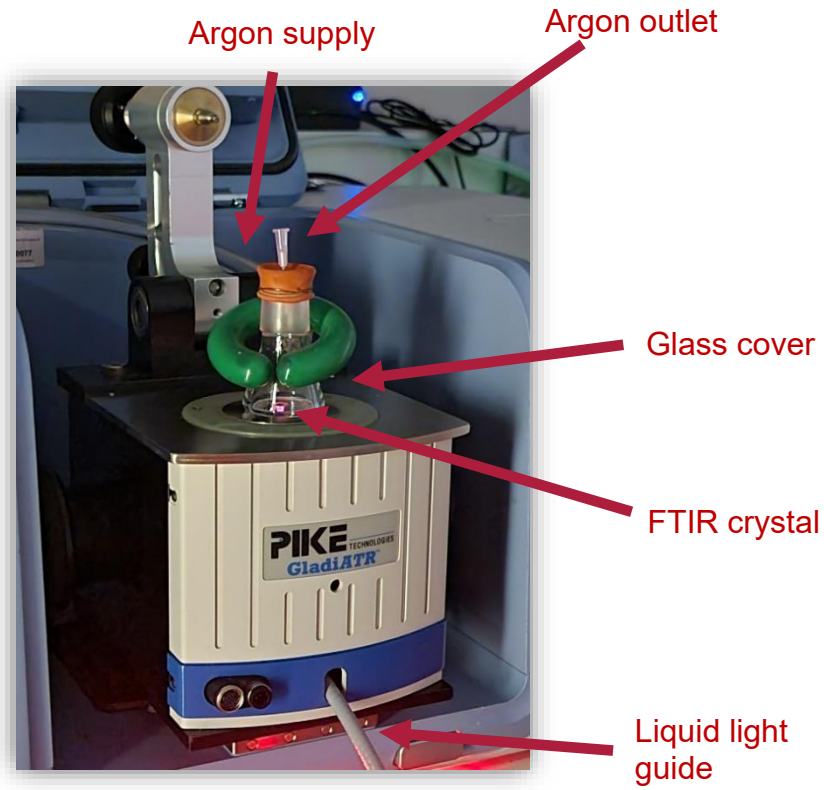

Figure 3.14: PhotoATR-FTIR Setup With Air-Free Glassware

3.33: STEADY-STATE OPTICAL CHARACTERIZATION

UV-visible absorption spectra were recorded on an Ocean Optics QE PRO-ABS Fiber Optic Spectrometer utilizing deuterium-tungsten halogen light sources (DH-2000-BAL). 600 µm fiberoptic cables (QP600-025-SR) were coupled to the detector with a slit width of 5 µm. Dilute absorption data was collected in acetonitrile utilizing quartz cuvettes and a qpod sample holder (QNW qpod2e). Thin-film absorption data was collected in the resin formulation (see photopolymerization conditions) utilizing the Ocean Optics Stage RTL-T.

3.34: TRANSIENT ABSORPTION CHARACTERIZATION

Transient absorption (TA) spectra that monitored photoexcited sample dynamics on femtosecond to sub-nanosecond timescales were performed using an experimental layout described in prior work.[28,29] Briefly, excitation and probe pulses were derived from the output of a Ti:sapphire regenerative amplifier (Coherent Legend Elite Duo: 3 kHz repetition rate, ~4.2 mJ, ~90 fs). Excitation pulses centered at 525 nm used to photoexcite Mes-BODIPY derivatives were produced by using the Ti:sapphire laser to pump a home-built noncollinear optical parametric amplifier (NOPA). Pulses centered at 645 nm used to excite aza-H and aza-Br were created by using a β-barium borate (BBO) crystal to frequency double the signal output of a commercial optical parametric amplifier (Light Conversion, TOPAS-prime). Spectrally-broad probe pulses were generated by seeding an OPA with the Ti:sapp, the output of the OPA at ~1200 nm was used to generate the continuum, which was centered from ~550 – 1150 nm. A computer controlled optical delay stage (Newport ILS300LM) was used to scan the time of arrival of the probe at the sample with respect to the pump. Pump-induced changes in probe transmission through each sample solution were detected using a Si CCD (Princeton Instruments, PyLoN 100BR) interfaced with a Czerny-Turner spectrometer (Acton Instruments SP-2556). Sample solutions were prepared by dissolving dry powder of each compound in acetonitrile. Sample solutions were housed in 1 mm path length quartz cuvettes and degassed using nitrogen prior to experiments.

3.35: ELECTRONIC CHARACTERIZATION

Cyclic voltammetry (CV) was performed in a nitrogen-filled VAC glovebox using a BioLogic SP-50e potentiostat. A single-compartment three-electrode cell was used with glassy carbon as the working electrode, a platinum wire as the counter electrode, and an

$Ag/AgNO_3$ (0.01 M) nonaqueous reference electrode calibrated versus Fc/Fc^+ in 0.1 M tetrabutylammonium hexafluorophosphate ($TBAPF_6$) dichloromethene solutions ($E_{½}(Fc/Fc^+)$ = 0.1 V vs Ag/Ag^+) with a 0.1 V/s scan rate. Oxidation onsets were utilized to calculate the highest occupied molecular orbital (HOMO) energy levels -(4.8 eV $–E_{ox}$ (Ferrocene) + E_{ox}) and reduction onsets to calculate the lowest unoccupied molecular orbital (LUMO) energy levels -(4.8 eV $–E_{ox}$ (Ferrocene) + E_{red})[30].

3.36: LED LIGHT SOURCES

All LEDs used were purchased from Mightex Systems. The product numbers for the four LEDs listed are 740 nm-P/N LCS-0740-10-22, 810 nm-P/N LCS-0810-02-22, 850 nm-P/N LCS-0850-03-22, 940 nm-P/N LCS-0940-02-38. The emission profile for each LED was measured using a calibrated UV-Vis Ocean Insight system. Irradiation intensities were measured with a Thorlabs PM100D photometer equipped with silicon-based photodiode power sensor (S120VC, Thorlabs). Emission profiles were recorded with a QE pro spectrometer, in which the LED was connected to the fiber optic system using a 3 mm 420 – 2000 nm liquid lightguide from Mightex Systems (serial #: LLG-03-59-340-0800-1). A 775 nm longpass filter from ThorLabs (R5000872535-21348) was used to ensure NIR light emission from the LEDs.

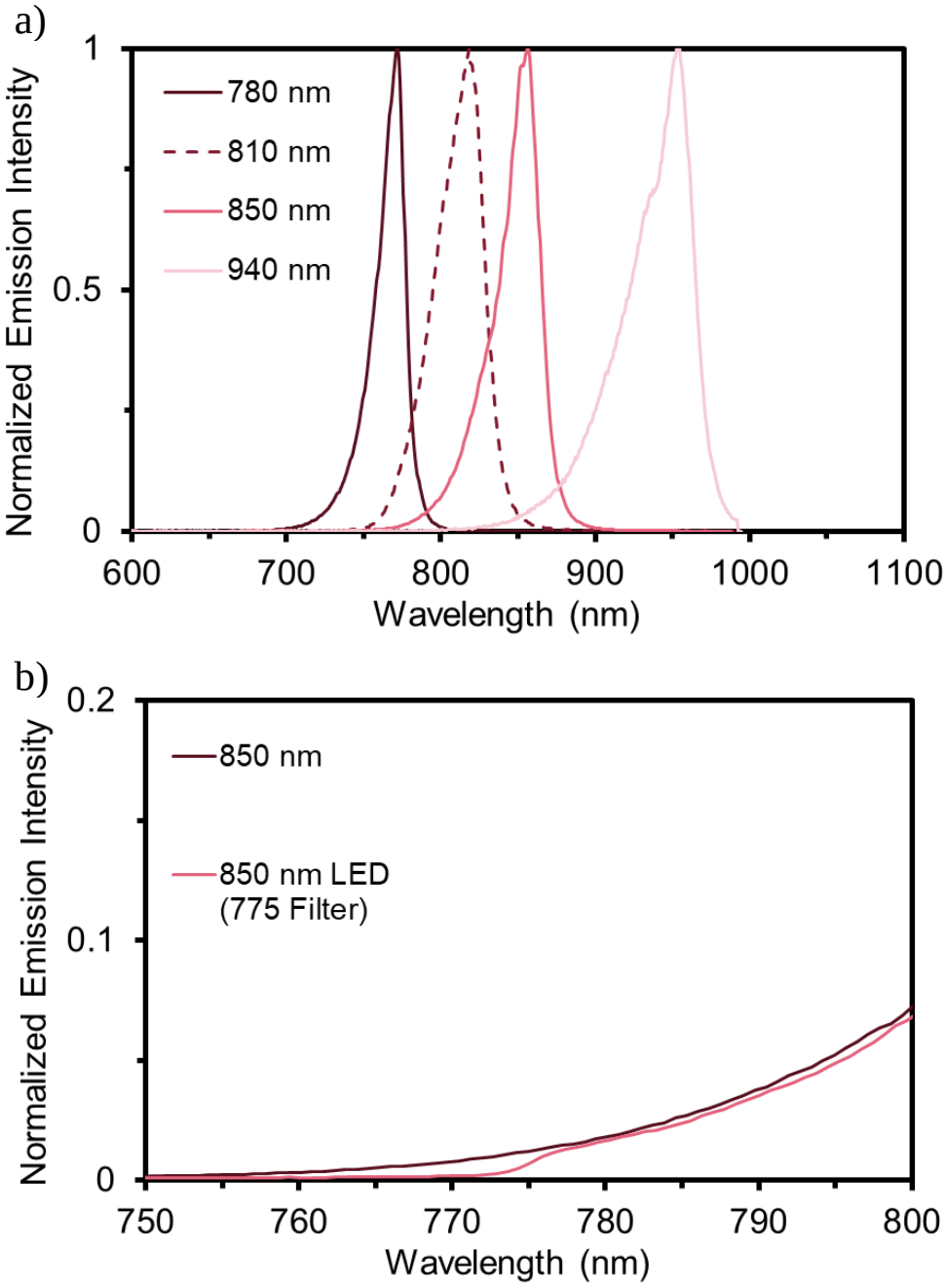

Figure 3.15: (a) LED Emission Profiles of Near-IR Light Sources (b) LED Emission Profile of 850 nm LED With and Without 775 LP filter.

3.37: SYNTHESIS

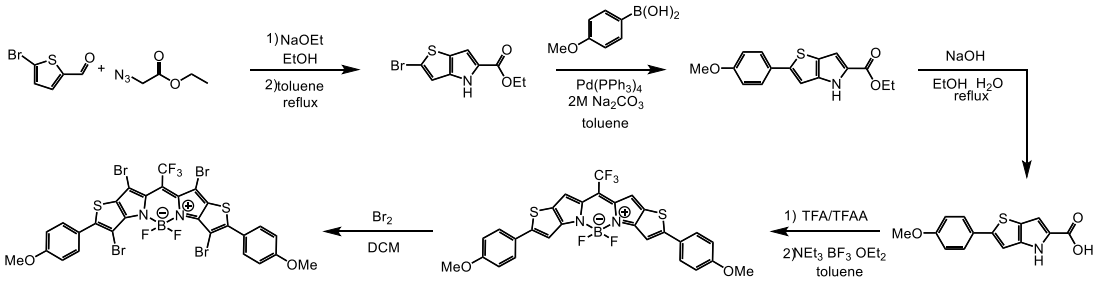

Figure 3.16: Synthesis of 2Ph-CF_3 and 2Ph-CF_3-Br_4 ThiopheneBODIPYs

ethyl 2-bromo-4H-thieno[3,2-b]pyrrole-5-carboxylate (1a)

sodium ethoxide (5.0 g, 4.40 Eq, 74 mmol) in 40 mL of ethanol was added dropwise to a mixture of 5-bromothiophene-2-carbaldehyde (3.2 g, 2.0 mL, 1 Eq, 17 mmol) and ethyl 2-azidoacetate (8.0 g, 7.2 mL, 3.70 Eq, 62 mmol) in 20 mL ethanol over 20 mins in an ice bath. The mixture was left to stir overnight. The reaction was quenched with NH_4Cl(sat) and extracted with ethyl acetate. Solvent was removed and the oil residue was dissolved in 30 mL toluene and refluxed for 1.5 hr. The mixture was cooled to room temp and solvent was removed under vacuum. The subsequent brown solid was purified via column chromatography (1:10 EtOAc:Hexanes) to yield a yellow solid (54%). ^{1}H NMR (400 MHz, $CDCl_3$) δ 9.06 (s, 1H), 7.04 (s, 1H), 7.02 (s, 1H), 4.33-4.39 (q, *J* = 7.1 Hz, 2H), 1.36-1.40 (t, *J* = 7.2 Hz, 3H); ^{13}C NMR (100 MHz, $CDCl_3$) δ 161.9, 139.4, 126.4, 124.9, 116.3, 114.6, 107.5, 61.0, 14.6; IR (ATR): 3270, 3060, 2974, 1677, 1525, 1469, 1444, 1384, 1283, 1181, 1092, 1016, 929, 926, 864, 839, 805, 757, 681 cm^{-1}; HRMS (APCI): exact mass calculated for $C_9H_8BrNO_2S$ $[M+H]^+$ 273.9459, found 273.9533

ethyl 2-(4-methoxyphenyl)-4H-thieno[3,2-b]pyrrole-5-carboxylate (1b)

ethyl 2-bromo-4H-thieno[3,2-b]pyrrole-5-carboxylate (700 mg, 1 Eq, 2.55 mmol) , $Pd(PPh_3)_4$ (49.3 mg, 0.0167 Eq, 42.6 µmol) , and (4-methoxyphenyl)boronic acid (776

mg, 2 Eq, 5.11 mmol) were added to a 100 mL 2-neck rb flask equipped with stir bar and condenser under argon. The reaction setup was placed under vacuum for 5 minutes, then refilled with argon. This process was repeated three times. Toluene (10 mL) and 2M Na_2CO_3 (10 mL) were degassed with argon for 10 minutes. The two solutions were added to the rb flask, stirred vigorously, and heated to 90 °C for 12 hr. After cooling down to room temperature, the reaction mixture was washed with brine. The organic layers were combined, dried over anhydrous $MgSO_4$, and evaporated to dryness under vacuum. The residue was column chromatographed (silica, hexane: dichloromethane = 1:2, v/v) to yield a yellow solid (90%). ^{1}H NMR (400 MHz, $CDCl_3$) δ 8.98 (s, 1H), 7.54-7.56 (d, *J* = 8.8 Hz, 2H), 7.11 (s, 1H), 7.07 (s, 1H), 6.92-6.94 (d, *J* = 8.8 Hz, 2H), 4.34-4.39 (q, *J* = 7.1 Hz, 2H), 3.85 (s, 3H), 1.39 (t, *J* = 7.1 Hz, 3H); ^{13}C NMR (100 MHz, $CDCl_3$) δ 161.6, 159.6, 148.1, 141.8, 127.9, 127.7, 127.1, 114.4, 114.2, 107.9, 106.0, 60.6, 55.4, 14.5; IR (ATR): 3305, 2919, 2850, 1667, 1604, 1536, 1510, 1461, 1400, 1275, 1250, 1194, 1110, 1070, 965, 934, 870, 824, 805, 758, 720, 697, 678, 630, 582 cm^{-1}; HRMS (APCI): exact mass calculated for $C_{16}H_{15}NO_3S$ $[M+H]^+$ 302.0773, found 302.0849

2-(4-methoxyphenyl)-4H-thieno[3,2-b]pyrrole-5-carboxylic acid (1c)

ethyl 2-(4-methoxyphenyl)-4H-thieno[3,2-b]pyrrole-5-carboxylate (350 mg, 1 Eq, 1.16 mmol) was dissolved in EtOH (10 mL). sodium hydroxide (0.72 g, 15.6 Eq, 18.1 mmol) in water (5 mL) was added and refluxed for 1 hr. The reaction was cooled to room temperature and then chilled in an ice bath and subsequently acidified with concentrated HCl. The precipitate was filtered, washed with water, and dried under vacuum to yield a brownish-green solid (86%). ^{1}H NMR (400 MHz, DMSO) δ 11.95 (s, 1H), 7.60-7.62 (d, *J* = 2.0 Hz, 1H), 7.24 (s, 1H), 7.02 (s, 1H), 6.97-7.00 (d, *J* = 8.8 Hz, 2H), 3.79 (s, 3H); ^{13}C NMR (100 MHz, DMSO) δ 162.2, 159.1, 145.8, 142.4, 127.4, 127.0, 126.7, 121.8, 114.6, 107.2, 107.0, 55.3; IR (ATR): 3397, 2921, 2851, 1653, 1606, 1567, 1515, 1502,

1485, 1421, 1404, 1393, 1337, 1294, 1179, 1111, 1032, 1013, 936, 821, 797, 721, 631, 601 cm^{-1}; HRMS (APCI): exact mass calculated for $C_{14}H_{11}NO_3S$ $[M+H]^+$ 274.0460, found 274.0533

5,5-difluoro-2,8-bis(4-methoxyphenyl)-11-(trifluoromethyl)-5H-4l4,5l4-thieno[2',3':4,5]pyrrolo[1,2-c]thieno[2',3':4,5]pyrrolo[2,1-f][1,3,2]diazaborinine (1d)

2-(4-methoxyphenyl)-4H-thieno[3,2-b]pyrrole-5-carboxylic acid (590 mg, 1 Eq, 2.16 mmol) was dissolved in TFA (20 mL) and heated to 40 °C for 15 min in a 100 mL pressure flask (intense red color appeared). Subsequently, trifluoroacetic anhydride (6 mL) was added and the temperature was then raised to 80 °C with continued stirring for 1 hr. The resulting deep blue reaction solution was then allowed to cool to room temperature and poured into an aqueous $NaHCO_3$ solution containing crushed ice. The resultant precipitate was then filtered and dried in vacuo. The dry solid was then dissolved in toluene (30 mL) and stirred for 5 min at room temperature under a nitrogen atmosphere. Next, boron trifluoride dietherate (2 mL) and DIPEA (1 mL) were added and the reaction mixture was stirred at 80ºC for 1 h under N_2. The crude mixture was washed with brine and following evaporation of the solvent, the crude product was recrystallized using THF:MeOH in a -20ºC freezer overnight to yield a dark black solid (17%). ^1H NMR (400 MHz, $CDCl_3$) δ 7.68-7.70 (d, *J* = 8.8 Hz, 4H), 7.33 (s, 2H), 7.27 (s, 2H), 6.97-6.99 (d, *J* = 8.8 Hz, 4H), 3.87 (s, 6H); ^{13}C NMR (100 MHz, $CDCl_3$) δ 162.8, 162.0, 128.5, 126.8, 118.3, 114.9, 107.9, 77.4, 55.7, 29.9; IR (ATR): 3368, 2919, 1569, 1536, 1517, 1469, 1413, 1337, 1308, 1284, 1200, 1071, 1026, 970, 955, 918, 826, 800, 759, 732, 673, 595 cm^{-1}; HRMS (APCI): exact mass calculated for $C_{28}H_{18}BF_5N_2O_2S_2$ $[M+Na]^+$ 607.0721, found 607.0712

3,7,10,12-tetrabromo-5,5-difluoro-2,8-bis(4-methoxyphenyl)-11-(trifluoromethyl)-5H-4l4,5l4-thieno[2',3':4,5]pyrrolo[1,2-c]thieno[2',3':4,5]pyrrolo[2,1-f][1,3,2]diazaborinine (1e)

5,5-difluoro-2,8-bis(4-methoxyphenyl)-11-(trifluoromethyl)-5H-4l4,5l4-thieno[2',3':4,5]pyrrolo[1,2-c]thieno[2',3':4,5]pyrrolo[2,1-f][1,3,2]diazaborinine (60 mg, 1 Eq, 0.10 mmol) was dissolved in DCM (5 mL). bromine (0.20 g, 63 μL, 12 Eq, 1.2 mmol) in 5 mL DCM was added dropwise and stirred at 40°C overnight. The reaction mixture was neutralized with aqueous Na_2CO_3 solution, and the aqueous layer was separated from the organic layer. The aqueous layer was further extracted with diethyl ether and the combined organic layers were dried over anhydrous Na_2SO_4 and the solvents removed by evaporation to yield a dark black solid (36%). ^{1}H NMR (400 MHz, $CDCl_3$) δ 7.77-7.79 (d, *J* = 8.8 Hz, 4H), 7.01-7.03 (d, *J* = 8.8 Hz, 4H), 3.90 (s, 6H); ^{13}C NMR (100 MHz, $CDCl_3$) δ 162.0, 161.5, 157.0, 155.1, 131.0, 130.4, 129.6, 126.0, 125.2, 114.6, 114.5, 77.4, 55.7; IR (ATR): 2920, 2837, 1597, 1567, 1508, 1452, 1435, 1389, 1356, 1297, 1162, 1117, 1096, 1053, 1025, 985, 954, 754, 730, 598 cm^{-1}; HRMS (APCI): exact mass calculated for $C_{28}H_{14}BBr_4F_5N_2O_2S_2$ $[M+H]^+$ 896.7243, found 896.8773

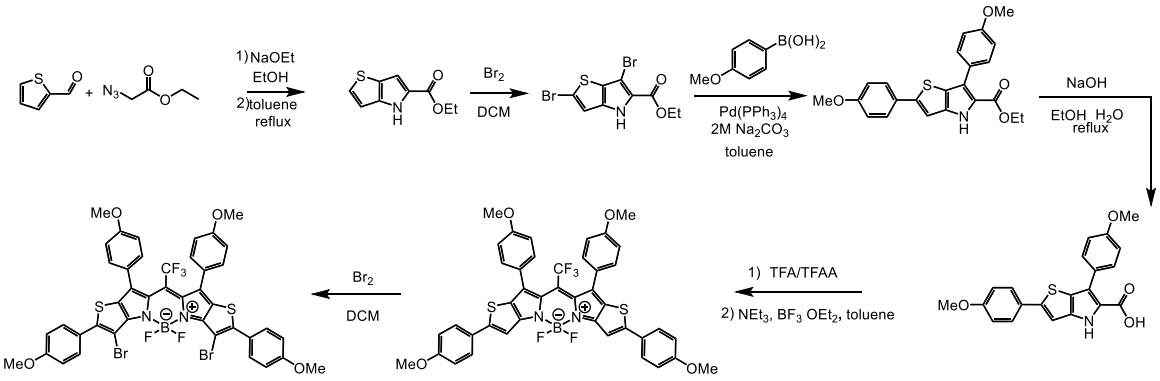

Figure 3.17: Synthesis of 4Ph-CF_3 and 4Ph-CF_3-Br_2 ThiopheneBODIPYs

ethyl 4H-thieno[3,2-b]pyrrole-5-carboxylate (2a)

sodium ethoxide (6.4 g, 4.40 Eq, 94 mmol) in 40 mL of ethanol was added dropwise to a mixture of thiophene-2-carbaldehyde (2.4 g, 2.0 mL, 1 Eq, 21 mmol) and ethyl 2-azidoacetate (10 g, 9.1 mL, 3.70 Eq, 79 mmol) in 20 mL ethanol over 20 mins in an ice bath. The mixture was left to stir overnight. The reaction was quenched with NH_4Cl(sat) and extracted with ethyl acetate. The organic layer was dried with $MgSO_4$, filtered and volume reduced under vacuum. The oil residue was dissolved in 30 mL toluene and refluxed for 1.5 hr. The mixture was cooled to room temp and solvent removed under vacuum to yield an orange solid (40%). ^{1}H NMR (400 MHz, $CDCl_3$) δ 9.11 (s, 1H), 7.32-7.33 (d, *J* = 5.3 Hz, 1H), 7.14-7.15 (d, *J* = 1.7 Hz, 1H), 6.95-6.97 (d, *J* = 5.3 Hz, 1H), 4.34-4.40 (q, *J* = 7.1 Hz, 2H), 1.37-1.41 (t, *J* = 7.1 Hz, 3H); ^{13}C NMR (100 MHz, $CDCl_3$) δ 161.6, 141.2, 129.4, 126.8, 114.3, 111.1, 107.5, 60.7, 14.5; IR (ATR): 3418, 2986, 2958, 1665, 1539, 1475, 1452, 1370, 1305, 1243, 1085, 1017, 868, 761, 726, 688 cm^{-1}; HRMS (APCI): exact mass calculated for $C_9H_9NO_2S$ $[M+H]^+$ 196.0354, found 196.0422

ethyl 2,6-dibromo-4H-thieno[3,2-b]pyrrole-5-carboxylate (2b)

ethyl 4H-thieno[3,2-b]pyrrole-5-carboxylate (200 mg, 1 Eq, 1.02 mmol) was dissolved in 80 mL DCM and a solution of bromine (327 mg, 106 µL, 2 Eq, 2.05 mmol) in 30 mL DCM was added dropwise. The solution was stirred for 1 hr. The reaction mixture was subsequently evaporated to dryness under vacuum. The solid residue obtained was recrystallized from an ethanol/water mixture to yield a brown solid (99%). ^{1}H NMR (400 MHz, $CDCl_3$) δ 9.17 (s, 1H), 7.03 (s, 1H), 4.37-4.43 (q, *J* = 7.1 Hz, 2H), 1.40-1.43 (t, *J* = 7.1 Hz, 3H); ^{13}C NMR (100 MHz, $CDCl_3$) δ 161.0, 137.8, 127.6, 123.1, 117.2, 115.0, 95.4, 61.4, 14.5; IR (ATR): 3280, 2981, 2901, 1542, 1529, 1476, 1465, 1404, 1386, 1291, 1259, 1193, 1178, 1088, 1036, 1017, 974, 930, 879, 862, 799, 696, 655 cm^{-1}; HRMS (APCI): exact mass calculated for $C_9H_7Br_2NO_2S$ $[M+H]^+$ 351.8564, found 353.8614

ethyl 2,6-bis(4-methoxyphenyl)-4H-thieno[3,2-b]pyrrole-5-carboxylate (2c)

ethyl 2,6-dibromo-4H-thieno[3,2-b]pyrrole-5-carboxylate (700 mg, 1 Eq, 1.98 mmol) , $Pd(PPh_3)_4$ (38.3 mg, 0.0167 Eq, 33.1 µmol) , and (4-methoxyphenyl)boronic acid (904 mg, 3 Eq, 5.95 mmol) were added to a 100 mL 2-neck rb flask equipped with stir bar and condenser under argon. The reaction setup was placed under vacuum for 5 minutes, then refilled with argon. This process was repeated three times. Toluene (10 mL) and 2M Na_2CO_3 (10 mL) were degassed with argon for 10 minutes. The two solutions were added to the rb flask, stirred vigorously, and heated to 90 °C for 12 hr. After cooling down to room temperature, the reaction mixture was washed with brine. Organic layers were combined, dried over anhydrous $MgSO_4$, and evaporated to dryness under vacuum. The residue was column chromatographed (silica, hexane: dichloromethane = 1:2, v/v) to yield a brown solid (94%). ^{1}H NMR (400 MHz, $CDCl_3$) δ 9.05 (s, 1H), 7.69-7.71 (d, *J* = 8.8 Hz, 2H), 7.54-7.56 (d, *J* = 8.8 Hz, 2H), 7.08 (s, 1H), 6.97-6.99 (d, *J* = 8.8 Hz, 2H), 6.92-6.94 (d, *J* = 8.8 Hz, 2H), 4.29-4.34 (q, *J* = 7.1 Hz, 2H), 3.87 (s, 3H), 3.84 (s, 3H),

1.30-1.33 (t, *J* = 7.1 Hz, 3H); ^{13}C NMR (100 MHz, $CDCl_3$) δ 161.5, 159.8, 159.1, 148.5, 140.1, 130.8, 127.9, 127.2, 126.2, 124.5, 120.5, 114.5, 114.3, 113.6, 106.2, 60.6, 55.5, 55.4, 14.5; IR (ATR): 3270, 2982, 2934, 1663, 1607, 1575, 1503, 1464, 1405, 1384, 1283, 1200, 1176, 1111, 1031, 933, 868, 807, 686 cm^{-1}; HRMS (APCI): exact mass calculated for $C_{23}H_{21}NO_4S$ $[M+Na]^+$ 430.1089, found 430.1085

2,6-bis(4-methoxyphenyl)-4H-thieno[3,2-b]pyrrole-5-carboxylic acid (2d)

ethyl 2,6-bis(4-methoxyphenyl)-4H-thieno[3,2-b]pyrrole-5-carboxylate (600 mg, 1 Eq, 1.47 mmol) was dissolved in EtOH (10 mL). sodium hydroxide (1.6 g, 27 Eq, 39.8 mmol) in water (5 mL) was added and refluxed for 1 hr. The reaction was cooled to room temperature and then chilled in an ice bath and subsequently acidified with concentrated HCl. The precipitate was filtered, washed with water and dried under vacuum to yield a brownish-green solid (94%). ^{1}H NMR (400 MHz, $CDCl_3$) δ 9.13 (s, 1H), 7.70-7.72 (d, *J* = 8.3 Hz, 2H), 7.55-7.57 (d, *J* = 8.6 Hz, 2H), 7.09 (s, 1H), 6.99-7.01 (d, *J* = 8.6 Hz, 2H), 6.92-6.94 (d, *J* = 8.5 Hz, 2H), 3.87 (s, 3H), 3.85 (s, 3H); ^{13}C NMR (100 MHz, DMSO) δ 162.5, 159.2, 158.2, 145.5, 140.1, 130.2, 127.3, 127.2, 126.7, 126.4, 126.2, 125.3, 114.6, 114.4, 113.5, 107.3, 55.3, 55.1; IR (ATR): 3411, 2933, 2837, 1644, 1606, 1573, 1526, 1487, 1452, 1419, 1357, 1292, 1247, 1177, 1113, 1031, 984, 935, 801, 609 cm^{-1}; HRMS (APCI): exact mass calculated for $C_{21}H_{17}NO_4S$ $[M+H]^+$ 380.0878, found 380.0949

5,5-difluoro-2,8,10,12-tetrakis(4-methoxyphenyl)-11-(trifluoromethyl)-5H-4l4,5l4-thieno[2',3':4,5]pyrrolo[1,2-c]thieno[2',3':4,5]pyrrolo[2,1-f][1,3,2]diazaborinine (2e)

2,6-bis(4-methoxyphenyl)-4H-thieno[3,2-b]pyrrole-5-carboxylic acid (300 mg, 1 Eq, 791 μmol) was dissolved in TFA (22 g, 15 mL, 2.5e+2 Eq, 0.19 mol) at 40°C in a pressure flask. An intense green color appeared. TFAA (6 g, 4 mL, 4e+1 Eq, 0.03 mol) was added at 40°C and the temperature was then raised to 80°C and continued stirring for 1 hr. Then, the reaction was quenched with saturated aqueous solution of Na_2CO_3 and

extracted with ethyl acetate and washed with water and brine. The solution was dried over anhydrous $MgSO_4$ and the solvent was evaporated to give a green solid. The solid was dried and dissolved in dry toluene (30 mL) and heated to 85°C under a nitrogen atmosphere. NEt_3 (1 mL) was added and stirred for 10 min. 2 mL of $BF_3 \cdot OEt_2$ was added and continued stirring for 1 hr. Then, it was cooled to room temperature and quenched with water and extracted with DCM. The solvent was evaporated to obtain a crude mixture, which was purified via recrystallization in THF:MeOH to yield a dark black solid (12%). ^{1}H NMR (400 MHz, $CDCl_3$) δ 7.65-7.67 (d, *J* = 8.8 Hz, 4H), 7.35-7.37 (d, *J* = 8.5 Hz, 6H), 6.95-6.98 (dd, *J* = 8.8, 3.4 Hz, 8H), 3.88 (s, 6H), 3.86 (s, 6H); ^{13}C NMR (100 MHz, $CDCl_3$) δ 162.0, 161.8, 159.9, 157.9, 130.4, 128.3, 127.3, 127.0, 114.8, 113.8, 108.4, 77.4, 55.7, 55.4, 47.4; IR (ATR): 2933, 2837, 1602, 1572, 1517, 1498, 1469, 1409, 1383, 1299, 1249, 1172, 1134, 1091, 1060, 1027, 927, 829, 762, 687, 604 cm^{-1}; HRMS (APCI): exact mass calculated for $C_{42}H_{30}BF_5N_2O_4S_2$ $[M+Na]^+$ 819.1558, found 819.1549

3,7-dibromo-5,5-difluoro-2,8,10,12-tetrakis(4-methoxyphenyl)-11-(trifluoromethyl)-5H-4l4,5l4-thieno[2',3':4,5]pyrrolo[1,2-c]thieno[2',3':4,5]pyrrolo[2,1-f][1,3,2]diazaborinine (2f)

5,5-difluoro-2,8,10,12-tetrakis(4-methoxyphenyl)-11-(trifluoromethyl)-5H-4l4,5l4-thieno[2',3':4,5]pyrrolo[1,2-c]thieno[2',3':4,5]pyrrolo[2,1-f][1,3,2]diazaborinine (40 mg, 1 Eq, 50 μmol) was dissolved in DCM (10 mL). bromine (24 mg, 7.8 μL, 3 Eq, 0.15 mmol) in 5 mL DCM was added while stirring vigorously at 40°C and left overnight. The reaction was quenched with a solution of Na_2CO_3 and the aqueous layer was further extracted with diethyl ether. The organic layer was dried with $MgSO_4$, and the solvent was removed under vacuum to yield a dark black solid (83%). ^{1}H NMR (400 MHz, $CDCl_3$) δ 7.73-7.75 (d, *J* = 8.8 Hz, 4H), 7.32-7.34 (d, *J* = 8.5 Hz, 4H), 6.96-7.00 (m, 8H), 3.88 (s, 6H), 3.86 (s, 6H); ^{13}C NMR (100 MHz, $CDCl_3$) δ 161.4, 160.2, 159.7, 156.4,

130.9, 130.5, 130.2, 130.0, 129.9, 126.6, 126.4, 114.3, 114.2, 114.0, 77.4, 55.6, 55.5; IR (ATR): 2961, 2917, 2848, 1600, 1571, 1495, 1451, 1438, 1375, 1294, 1256, 1222, 1170, 1143, 1085, 1010, 868, 792, 756, 728, 696, 633 cm^{-1}; HRMS (APCI): exact mass calculated for $C_{42}H_{28}BBr_2F_5N_2O_4S_2$ $[M+H]^+$ 974.9769, found 976.9749

3.38: CHARACTERIZATION

^{1}H NMR DATA

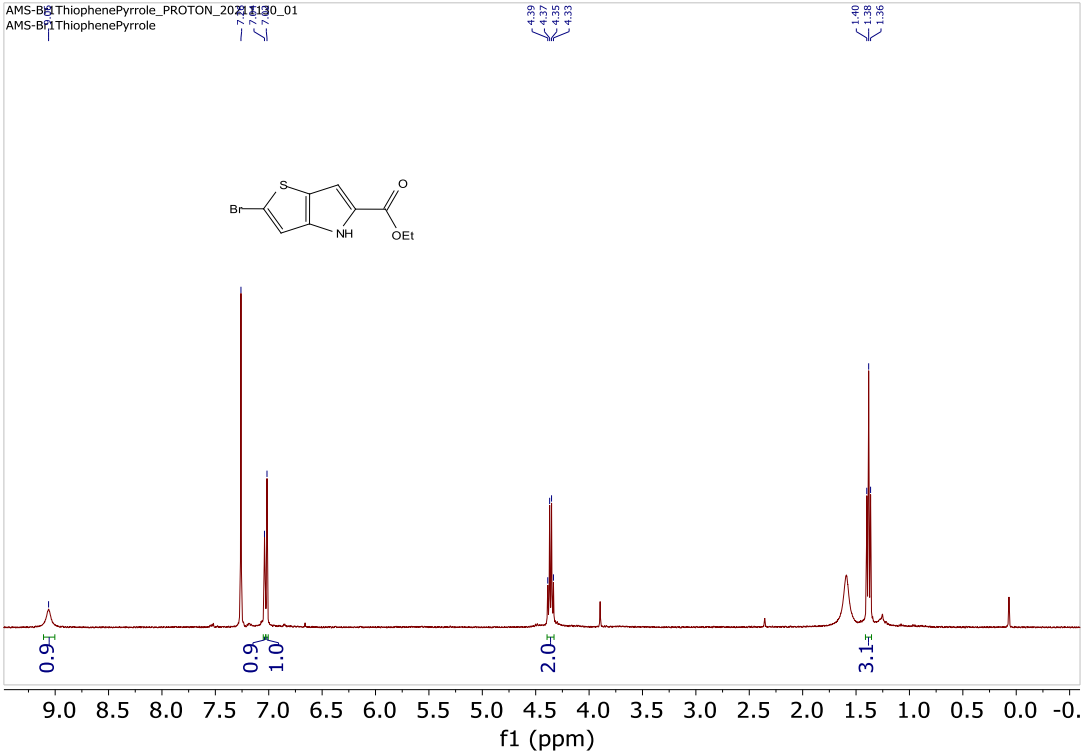

Figure 3.18: ^{1}H NMR of Compound **1a** in $CDCl_3$

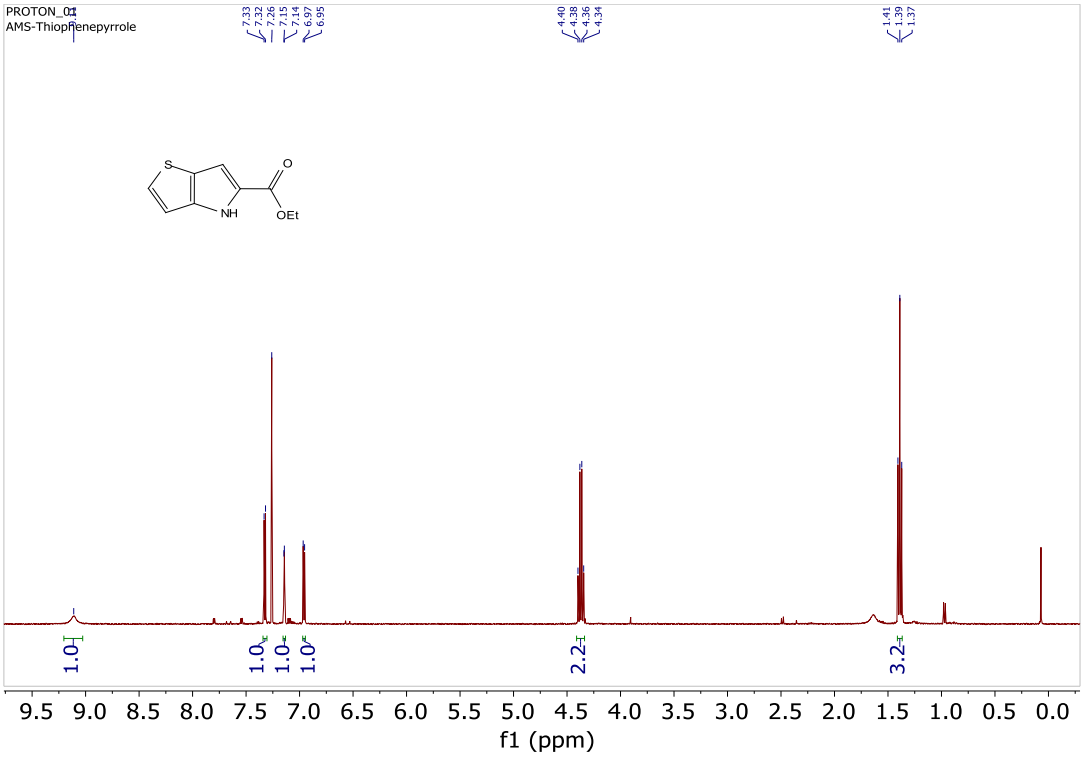

Figure 3.19: ^{1}H NMR of Compound **2a** in $CDCl_3$

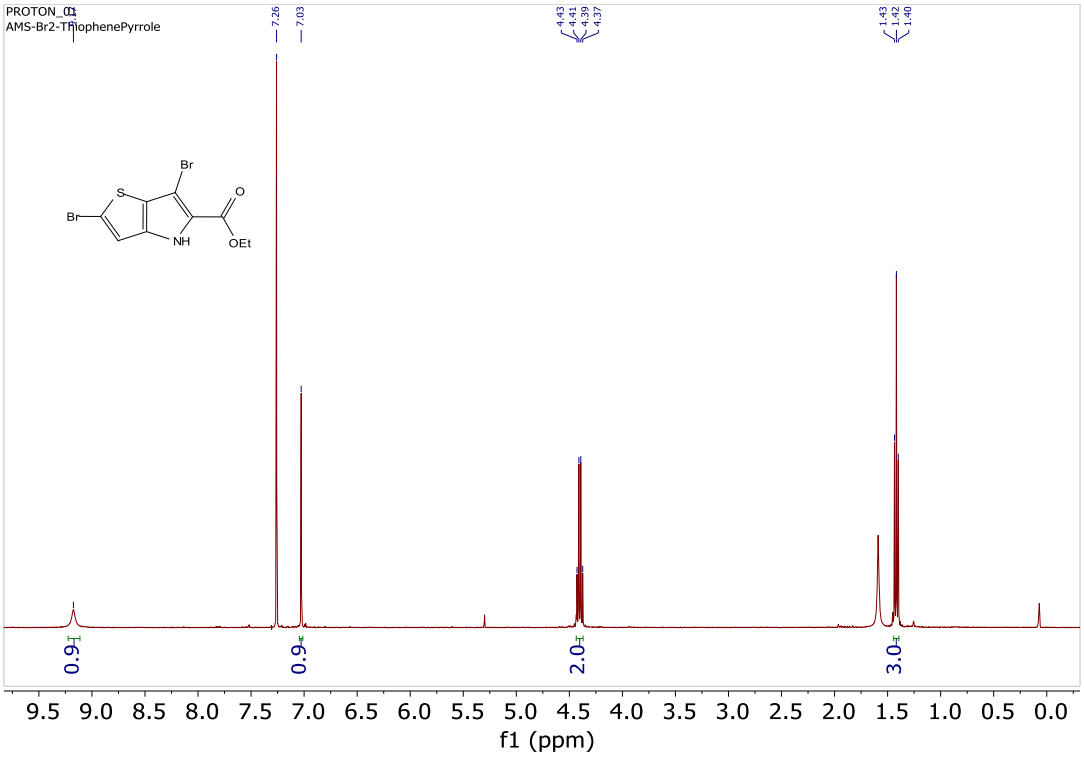

Figure 3.20: ^{1}H NMR of Compound **2b** in $CDCl_3$

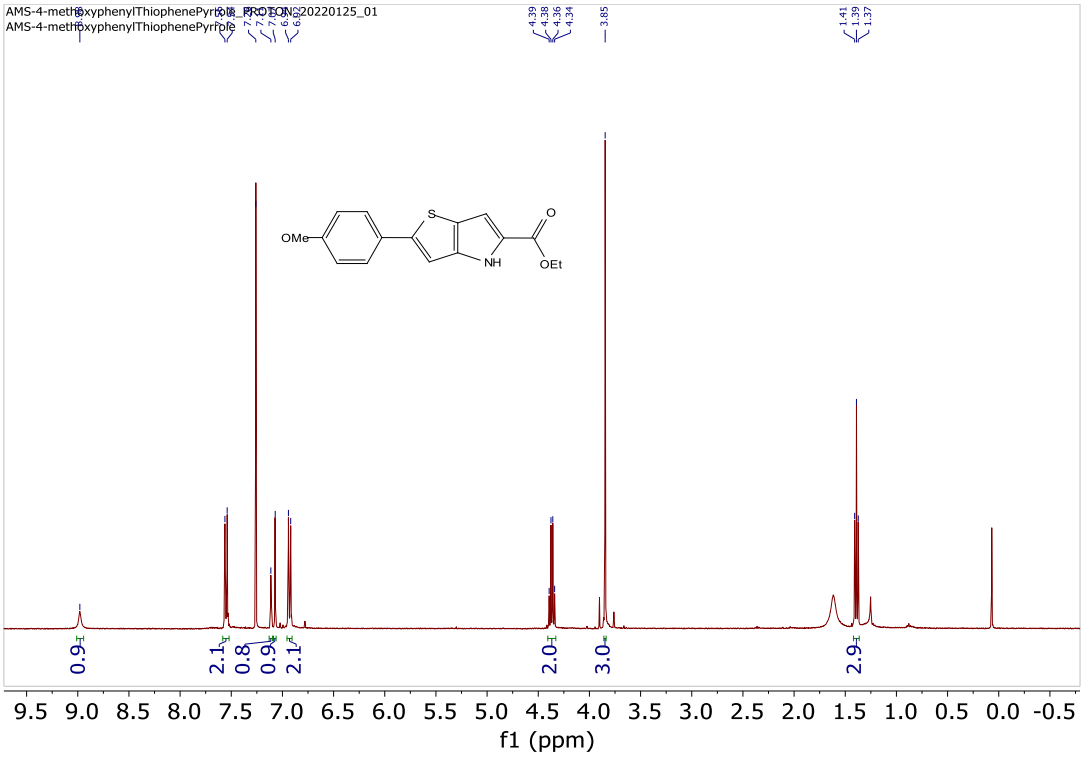

Figure 3.21: ^{1}H NMR of Compound **1b** in $CDCl_3$

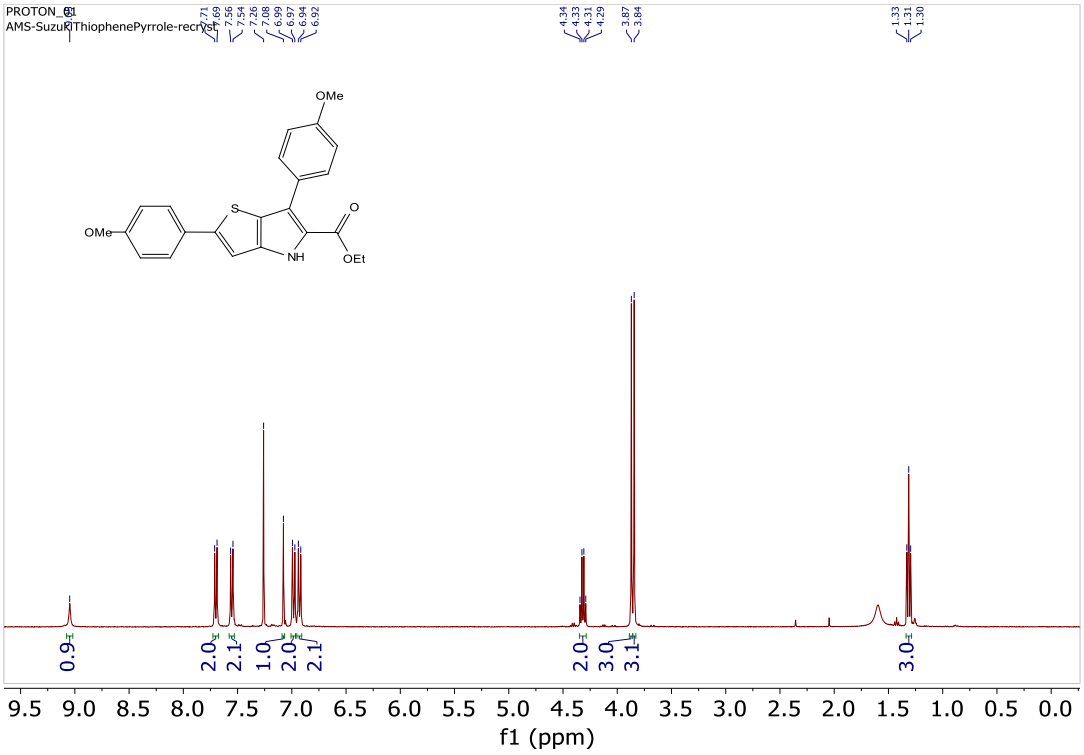

Figure 3.22: ^{1}H NMR of Compound **2c** in $CDCl_3$

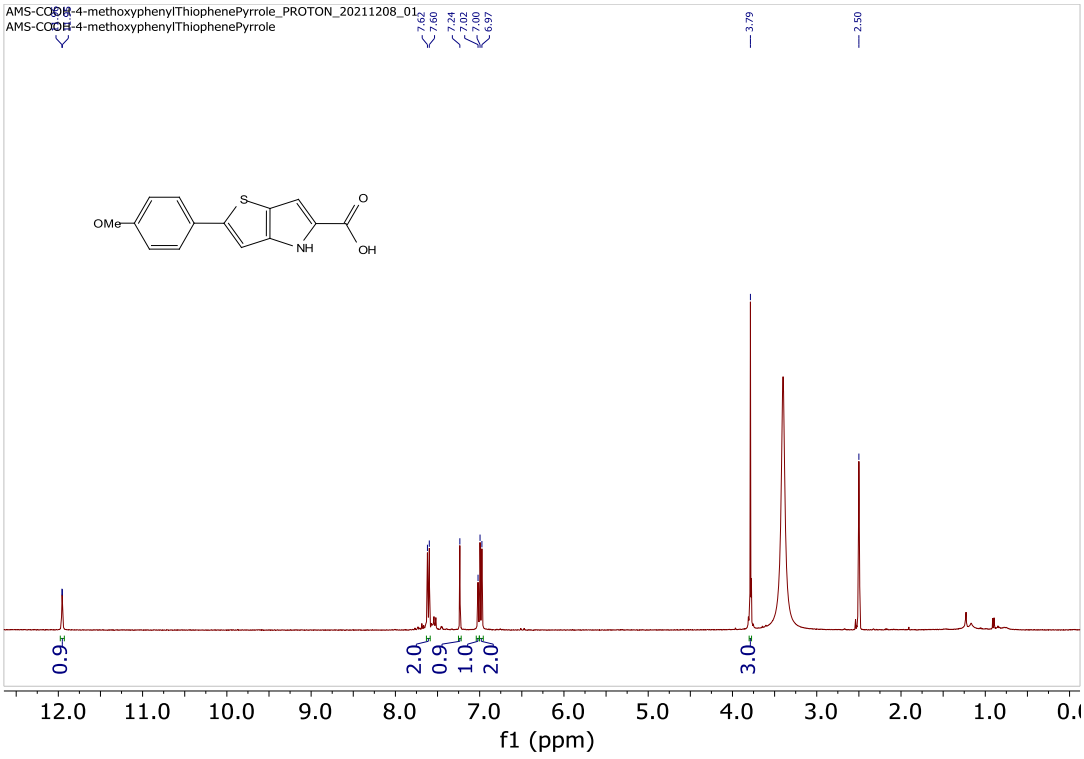

Figure 3.23: ^{1}H NMR of Compound **1c** in $CDCl_3$

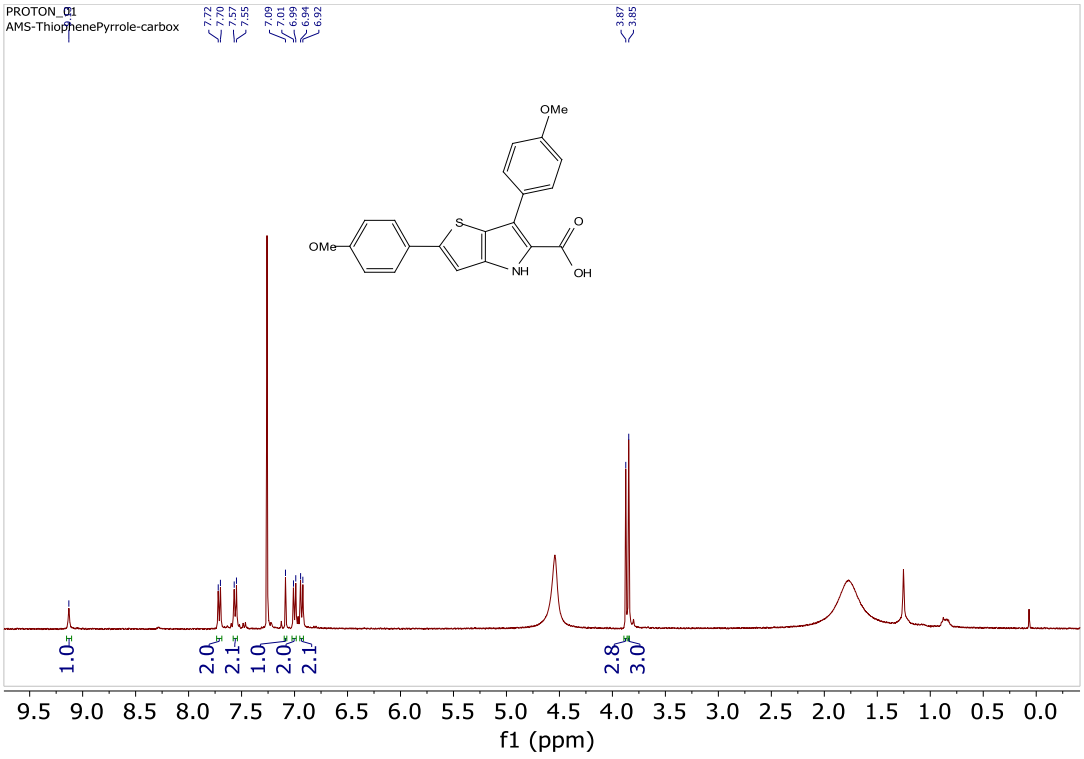

Figure 3.24: ^{1}H NMR of Compound **2d** in $CDCl_3$

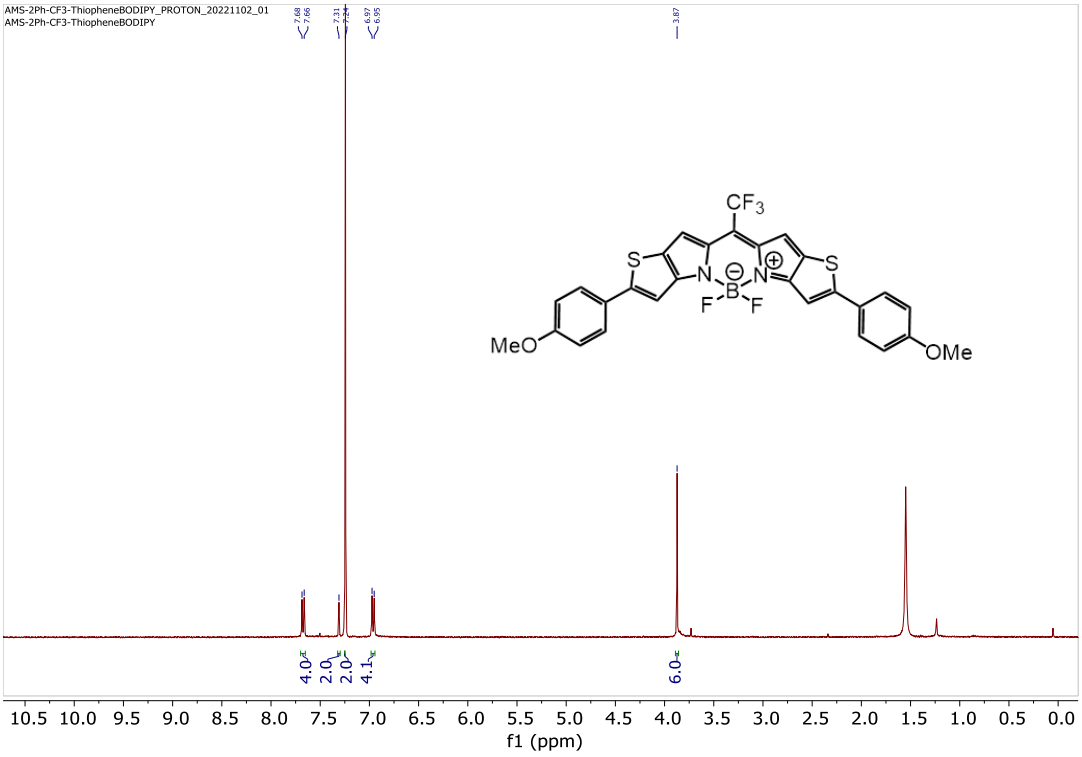

Figure 3.25: ^{1}H NMR of Compound **1d** in $CDCl_3$

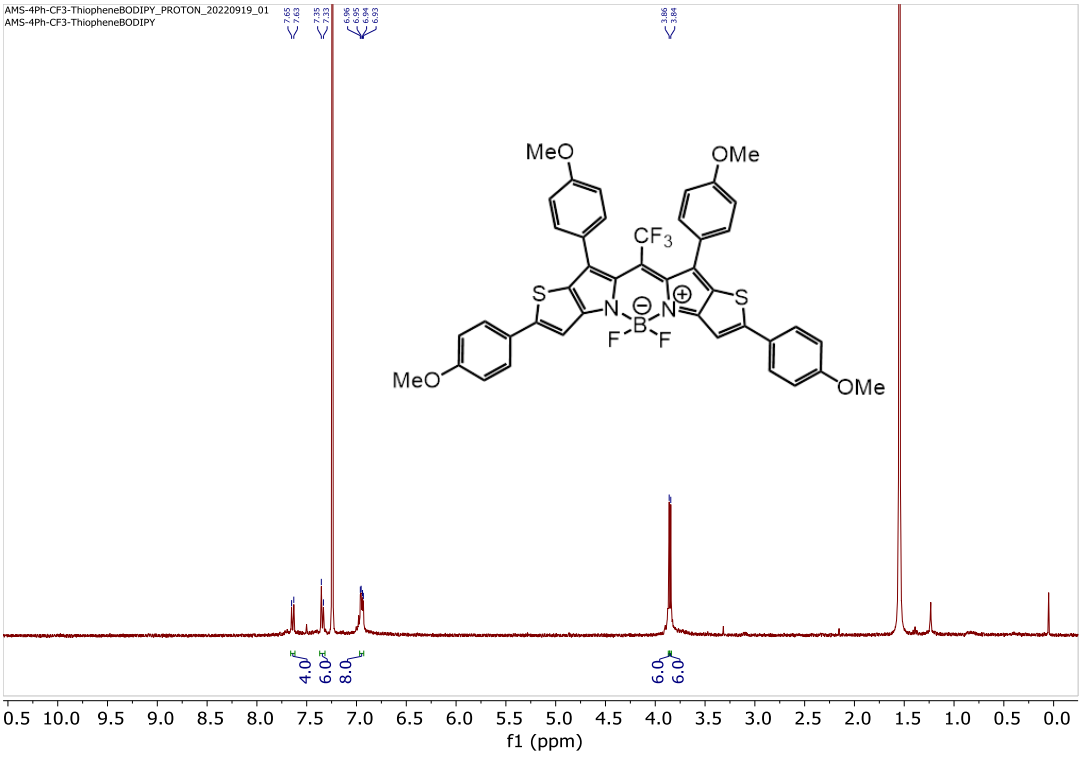

Figure 3.26: ^{1}H NMR of Compound **2e** in $CDCl_3$

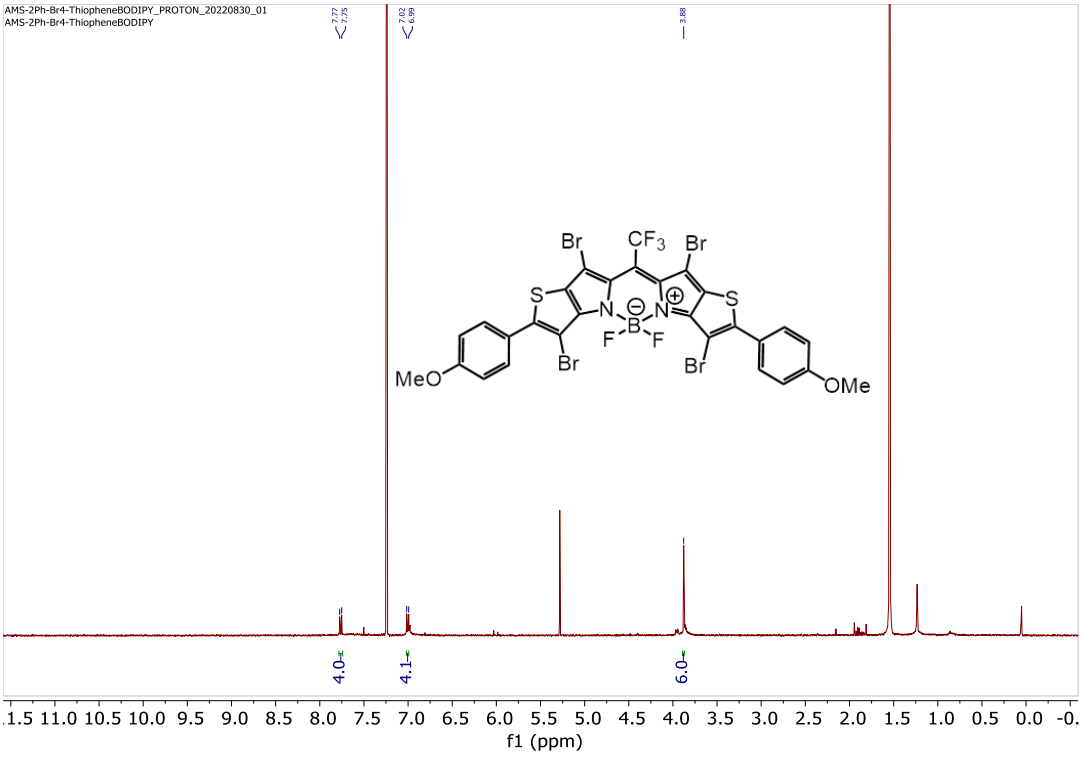

Figure 3.27: ^{1}H NMR of Compound **1e** in $CDCl_3$

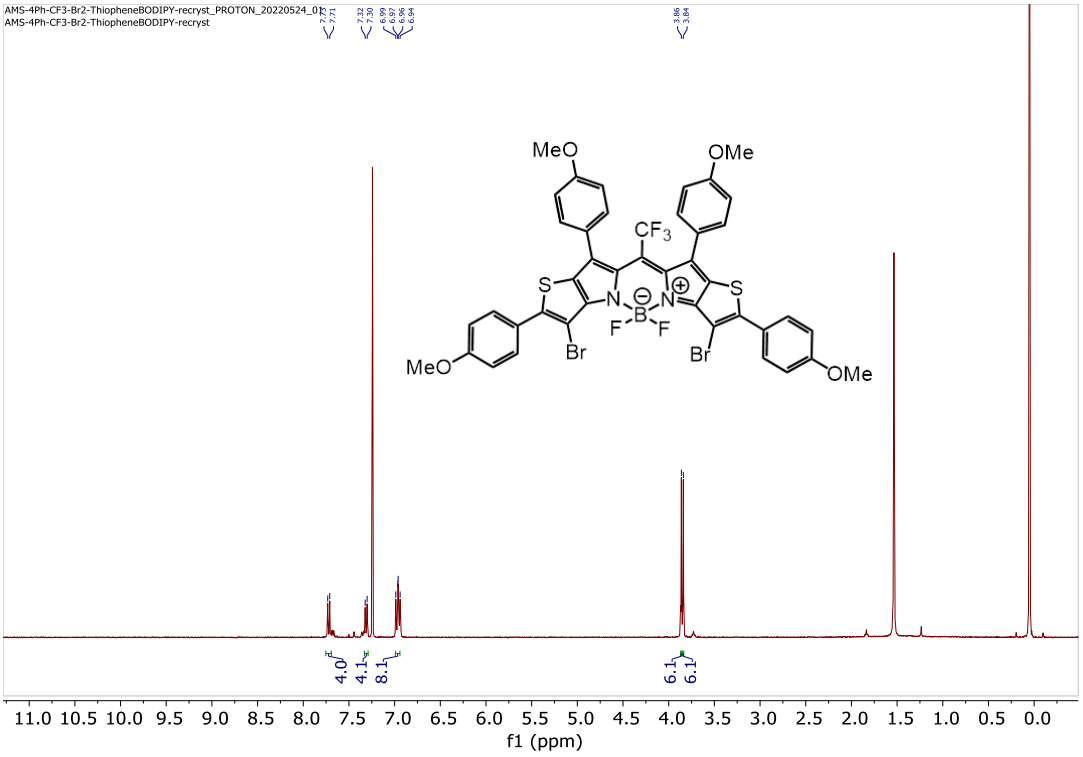

Figure 3.28: ^{1}H NMR of Compound **2f** in $CDCl_3$

3.4: CONCLUSION

The incorporation of the -thiophene moiety onto BODIPY dyes was demonstrated to be an effective strategy to achieve efficient near-IR light driven polymerizations. Systematic optoelectronic characterization of a series of thiopheneBODIPY derivatives unveiled another important aspect for improving photopolymerization rate in electron transfer efficiency. Transient absorption spectroscopy demonstrated that these thiopheneBODIPY derivatives possess very short-lived excited states without additional bromination, yet despite this short lifetime, can achieve rapid photopolymerization with NIR light at low light intensities. Real time ATR-FTIR with custom bottom-up irradiation was used to characterize polymerization rate, showing that halogenation of the thiopheneBODIPY dyes resulted in a 1.2-3.6x faster polymerization rate upon exposure to NIR light. Cyclic voltammetry in conjunction with absorbance/fluorescence studies suggested that electron donation into the photoexcited thiopheneBODIPY dyes (i.e., reductive quenching) was the primary mechanistic pathway for radical generation. Furthermore, additional optimization to the monomer resin was shown to provide unprecedented photopolymerization rates (complete conversion within ~10 s) given a low NIR light intensity (20 mW/cm^2). These results are particularly exciting and provide another characteristic to consider in the future development of NIR photocatalysts.

3.5: REFERENCES

(1) Shaw, M., Twilton, J., MacMillan, D. Photoredox Catalysis in Organic Chemistry. *J. Org. Chem*. **2016**, *81*, 6898

(2) Hansen, M., Velema, W., Lerch, M., Szymanski, W., Feringa, B. Wavelength-Selective Cleavage of Photoprotecting Groups: Strategies and Applications in Dynamic Systems**.** *Chem. Soc. Rev*., **2015**, *44*, 3358

(3) Zivic, N., Kuroishi, P., Dumur, F., Gigmes, D., Dove, A., Sardon, H. Recent Advances and Challenges in the Design of Organic Photoacid and Photobase Generators for Polymerizations. *Angew. Chem. Int. Ed*. **2019**, *58*, 10410

(4) Trotta, J., Fors, B. Organic Catalysts for Photocontrolled Polymerizations. *Synlett*. **2016**, *27*, 702

(5) Ma. Y., Kottisch, V., McLoughlin, E., Rouse, Z., Supej, M., Baker, S., Fors, B. Photoswitching Cationic and Radical Polymerizations: Spatiotemporal Control of Thermoset Properties. *J. Am. Chem. Soc.* **2021**, *143*, 50, 21200

(6) Doerr, A., Burroughs, J., Gitter, S., Yang, X., Boydston, A., Long, B. Advances in Polymerizations Modulated by External Stimuli**.** *ACS Catal.* **2020**, *10* (24), 14457

(7) Zhang, X., Cox, L., Wen, Z., Xi, W., Ding, Y., Bowman, C. Implementation of Two Distinct Wavelengths to Induce Multistage Polymerization in Shape Memory Materials and Nanoimprint Lithography. *Polymer*. **2018**, *156*, 162

(8) Bao, Y. Recent Trends in Advanced Photoinitiators for Vat Photopolymerization 3D Printing. *Macromol. Rapid Commun*. **2022**, *43* (14), 2200202

(9) Sandmeier, M., Paunović, N., Conti, R., Hofmann, L., Wang, J., Luo, Z., Masania, K., Wu, N., Kleger, N., Coulter, F., Studart, A., Grützmacher, H., Leroux, J., Bao, Y. Solvent-Free Three-Dimensional Printing of Biodegradable Elastomers Using Liquid Macrophotoinitiators. *Macromolecules* **2021**, *54* (17), 7830

(10) Estabrook, D., Sletten, E. Printing Precise Materials with Visible Light. *ACS Cent. Sci.* **2020**, *6* (9), 1482

(11) Ma, Q., Liu, S., Le Dot, M., Mokbel, H., Zhang, Y., Graff, B., Lalevée, J. Imidazole Based Dual Photo/Thermal Initiators for Highly Efficient Radical Polymerization Under Air With a Metal-Free Approach. *Polym. Chem*., **2021**, *12*, 6386

(12) Camposeo, A.; Persano, L.; Farsari, M.; Pisignano, D. Additive Manufacturing: Applications and Directions in Photonics and Optoelectronics. *Adv. Opt. Mater*. **2019**, *7* (1), 1800419

(13) Jung, K.; Corrigan, N.; Ciftci, M.; Xu, J.; Seo, S. E.; Hawker, C. J.; Boyer, C. Designing with Light: Advanced 2D, 3D, and 4D Materials. *Adv. Mater*. **2020**, *32* (18), 1903850

(14) Ahn, D., Stevens, L., Zhou, K., Page, Z. Rapid High-Resolution Visible Light 3D Printing. *ACS Cent. Sci*. **2020**, *6* (9), 1555

(15) Stafford, A., Ahn, D., Raulerson, E., Chung, K., Sun, K., Cadena, D., Forrister, E., Yost, S., Roberts, S., Page, Z. Catalyst Halogenation Enables Rapid and Efficient Polymerizations with Visible to Far-Red Light. *J. Am. Chem. Soc.* **2020**, *142* (34), 14733

(16) Lu, P., Chung, K., Stafford, A., Kiker, M., Kafle, K., Page, Z. Boron Dipyrromethene (BODIPY) in Polymer Chemistry. *Polym. Chem*., **2021**, *12*, 327

(17) Wang, J., Li, J., Chen, N., Wu, Y., Hao, E., Wei, Y., Mu, X., Jiao, L. Synthesis, Structure and Properties of Thiophene-Fused BODIPYs and AzaBODIPYs as Near-Infrared Agents. *New J. Chem*. **2016**, *40*, 5966

(18) Awuah, S. G., Das, S. K., D'Souza, F., You, Y. Thieno–Pyrrole-Fused BODIPY Intermediate as a Platform to Multifunctional NIR Agents**.** *Chem. Asian J*. **2013**,*8*, 3123

(19) Awuah, S. G., Polreis, J., Biradar, V., You, Y. Singlet Oxygen Generation by Novel NIR BODIPY Dyes. *Org. Lett.* **2011**, *13* (15), 3884

(20) Lee, K., Corrigan, N., Boyer, C. Rapid High-Resolution 3D Printing and Surface Functionalization via Type I Photoinitiated RAFT Polymerization**.** *Angew. Chem. Int. Ed*. **2021**, *60* (16), 8839

(21) Dadashi-Silab, S., Doran, S., Yagci, Y. Photoinduced Electron Transfer Reactions for Macromolecular Syntheses. *Chem. Rev*. **2016**, *116* (17), 10212

(22) Corrigan, N., Shanmugam, S., Xu, J., Boyer, C. Photocatalysis in Organic and Polymer Synthesis. *Chem. Soc. Rev*., **2016**, *45* (22), 6165

(23) Pang, Y., Fan, S., Wang, Q., Oprych, D., Feilen, A., Reiner, K., Keil, D., Slominksy, Y., Popov, S., Zou, Y., Strehmel, B. NIR-Sensitized Activated Photoreaction between Cyanines and Oxime Esters: Free-Radical Photopolymerization. *Ange. Chem. .Int. Ed*. **2020**, *59*, 11440

(24) Strehmel, B., Schmitz, C., Kütahya, C., Pang, Y., Drewitz, A., Mustroph, H. Photophysics and Photochemistry of NIR Absorbers Derived From Cyanines: Key to New Technologies Based on Chemistry 4.0. *Beilstein J. Org. Chem*. **2020**, *16*, 415

(25) Breloy, L., Brezová, V., Barbieriková, Z., Ito, Y., Akimoto, J., Chiappone, A., Abbad-Andaloussi, S., Malval, J., Versace, D. Methacrylated Quinizarin Derivatives for Visible-Light Mediated Photopolymerization: Promising Applications in 3D-Printing Biosourced Materials under LED@405 nm. *ACS Appl. Polym. Mater.* **2022**, *4* (1), 210

(26) Bonardi, A., Bondardi, F., Noirbent, G., Dumur, F., Dietlin, C., Gigmes, D., Fouassier, J., Lalevée, J. Different NIR Dye Scaffolds for Polymerization Reactions Under NIR Light. *Polym. Chem*. **2019**, *10*, 6505

(27) Allen, M. J.; Page, Z. A. Tracking Photocuring via ATR-FT-IR with Illumination through the ATR Element. *Spectrosc. Appl. Noteb*. **2020**, *35* (2), 78.

(28) Le, A. K.; Bender, J. A.; Arias, D. H.; Cotton, D. E.; Johnson, J. C.; Roberts, S. T. Singlet Fission Involves an Interplay between Energetic Driving Force and Electronic Coupling in Perylenediimide Films. *J. Am. Chem. Soc*. **2018**, *140* (2), 814–826.

(29) Azzaro, M. S.; Le, A. K.; Wang, H.; Roberts, S. T. Ligand-Enhanced Energy Transport in Nanocrystal Solids Viewed with Two-Dimensional Electronic Spectroscopy. *J. Phys. Chem. Lett*. **2019**, *10* (18), 5602–5608.

(30) Thorat, K. G.; Kamble, P.; Ray, A. K.; Sekar, N. Novel Pyrromethene Dyes with N-Ethyl Carbazole at the Meso Position: A Comprehensive Photophysical, Lasing, Photostability and TD-DFT Study. *Phys. Chem. Chem. Phys*. **2015**, *17* (26), 17221–17236.

Chapter 4: Thionaphthalimides as Heavy-Atom Free Photoredox Catalysts

4.1: INTRODUCTION

The utilization of light in chemical processes has seen rapid expansion in the last decade through developments in photocatalysis[1-6], photon up conversion[7-9], and photodynamic therapy[10-12]. Light-driven reactions have become an asset for many unique chemical transformations and in applications ranging from solar cells[13] to additive manufacturing[14]. Through these studies, key structural features of efficient photocatalysts have been identified and systematically examined. One challenge that arises in the development of efficient photocatalysts and photosensitizers is absorption strength and excited state lifetime. In order to efficiently utilize the excited state energy, the quantity of excited states generated as well as their ability to persist longer and avoid unproductive decay/relaxation pathways is crucial. To that end, numerous polypyridiyl based Ru- or Ir-catalysts have been developed due to their strong light absorption and efficient intersystem crossing (ISC) mechanism[15-21]. Despite their utility, late transition metal complexes suffer from concerns regarding toxicity, cost, and abundance[22-26]. As such, organic photocatalysts and photosensitizers have received significant attention for their versatility compared to metal-based systems.

Typically, organic chromophores suffer from fast, spin-allowed S1-S0 decay that outcompetes ISC[10]. To overcome this, strategies based on halogen heavy atoms[27-28], radical pair recombination[29], and twisted π-conjugation[11,30] have been developed to increase the rate of triplet formation. Akin to heavy metals, concerns of cytotoxicity with respect to halogen heavy atoms led to the desire to develop heavy-atom free photocatalysts that possess high triplet quantum yields, low cytotoxicity, and a high

molar extinction coefficient at longer wavelengths (600-800 nm). To that end, thiobases become one primary avenue of research due to the thiocarbonyl groups ability to efficiently undergo ISC and generate excited triplet states[31-37].

Xiao and coworkers[38], for example, have demonstrated this effect brilliantly through a single- atom replacement approach to generating highly efficient PDT photosensitizers across the visible spectrum with singlet oxygen quantum yields ranging from 0.64 to 1. Given the ability for these thiolated photosensitizers to access triplet excited states, we aimed to utilize this structural modification in order to generate highly efficient photoredox catalysts for photopolymerizations and small molecule photoredox reactions.

As we have previously demonstrated, the ability to access long-lived triplet excited states can greatly enhance polymerization rates[28] and thus these compounds possess significant potential to be an alternative to halogenation in generating efficient photoredox catalysts. To that end, a series of thionaphthalimide dyes were synthesized and subsequently characterized using real- time ATR-FTIR to analyze photopolymerization efficiency. Additionally, the photocatalysts were tested in two small molecule photoredox reactions, a photo aza-henry reaction and a photodebromination to demonstrate the redox versatility of these compounds. We report high sensitivity to green light while maintaining excellent temporal control (no initial dark polymerization). The synthesized thionaphthalimides showed excellent rates of polymerization (< 30 s) utilizing LEDs centered at 530 nm with low light intensities of 10 mW/cm^2 as well as near quantitative conversion of a small molecule photo aza-henry reaction.

4.2: RESULTS AND DISCUSSION

Inspired by the work of Yoon and coworkers[18] on the utilization of thionaphthalimides for singlet oxygen generation, we sought to evaluate these photosensitizers as photoredox catalysts in both radical photopolymerizations and small molecule redox reactions. A series of thionaphthalimides with -H, -OMe, and -NMe_2 substitution were synthesized, and the general synthetic procedure can be seen in **Figure 4.1**. The derivatives were synthesized from the initial -H or -Br naphthalic anhydride via reaction with n-butylamine to yield the naphthalimide, followed by nucleophilic aromatic substitution with either sodim methoxide or dimethylamine and lastly, thiolation of the carbonyls with lawesson's reagent.

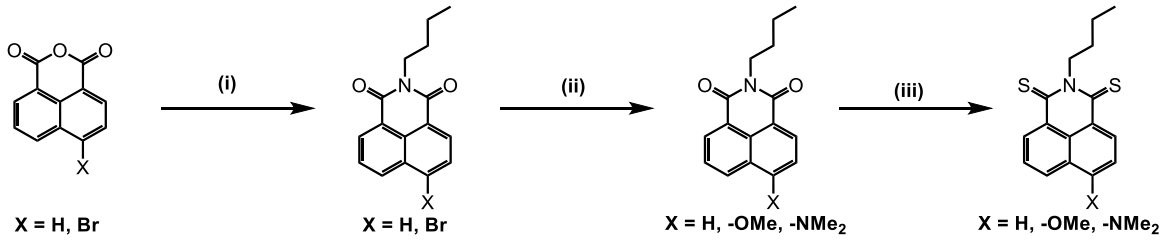

Figure 4.1: General Synthesis of Thionaphthalimides (See Synthesis section for complete reaction scheme)

Upon synthesis completion, the optoelectronic properties of these compounds were characterized and can be found in **Figure 4.2** and **Table 4.1**. Akin to our azaBODIPYs in Chapter 2, as we increase the strength of the electron donating group, we see a red-shift in maximum absorbance from 437 nm to 571 nm. As Yoon and coworkers demonstrated, these thionaphthalimides can efficiently undergo ISC to triplet excited states capable of sensitizing oxygen to singlet oxygen with quantum yields of 0.32, 0.74

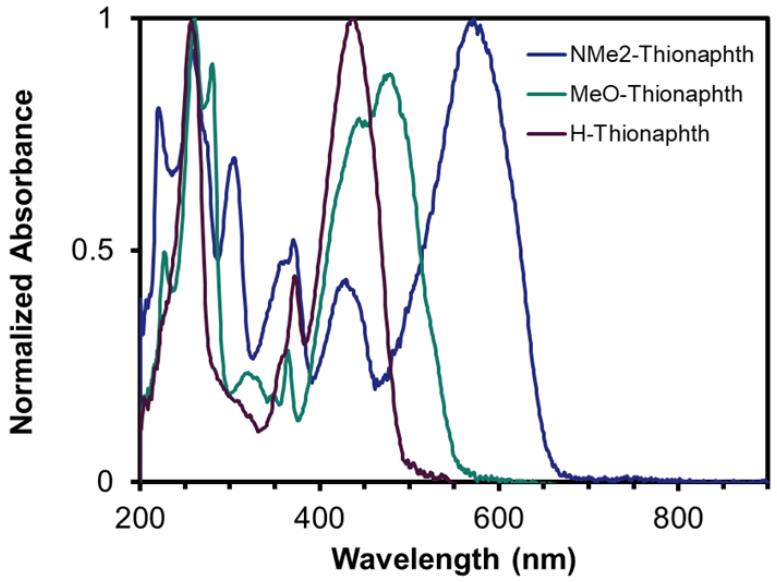

Figure 4.2: Normalized Absorbance Profiles of Thionaphthalimide Series in Acetonitrile

Compound	λ_{max} (nm)	ε ($M^{-1}cm^{-1}$)	E_{ox} (V)	E_{red} (V)	HOMO (eV)	LUMO (eV)
H-Thionaph	437	22610 ± 910	0.907	-1.016	-5.61	-3.68
MeO-Thionaph	478	17400 ± 800	0.750	-1.097	-5.45	-3.60
NMe_2-Thionaph	571	19200 ± 1100	0.500	-1.125	-5.20	-3.57

Table 4.1: Optoelectronic Properties of the Thionaphthalimide Photoredox Catalysts

and ~1.0 for -H, -OMe, NMe_2 respectively[18]. Given the max absorbance of NMe_2-Thionaphth and the highly efficient singlet oxygen quantum yields, this compound provides the ideal framework for comparison with our halogenated BODIPYs in Chapter 1 as an alternative to halogenation for improving photoredox catalyst efficiency.

Utilizing the same resin formulation as previously discussed: 0.1 mol% PC, 0.1 mol% donor (Borate V), and 1.0 mol% acceptor (HNu 254), we evaluated the efficiency of photopolymerization using a 530 nm LED and our photo-ATR FTIR setup (**Figure 4.3**). Following a similar protocol of resin preparation, intensity sweeps for the non-

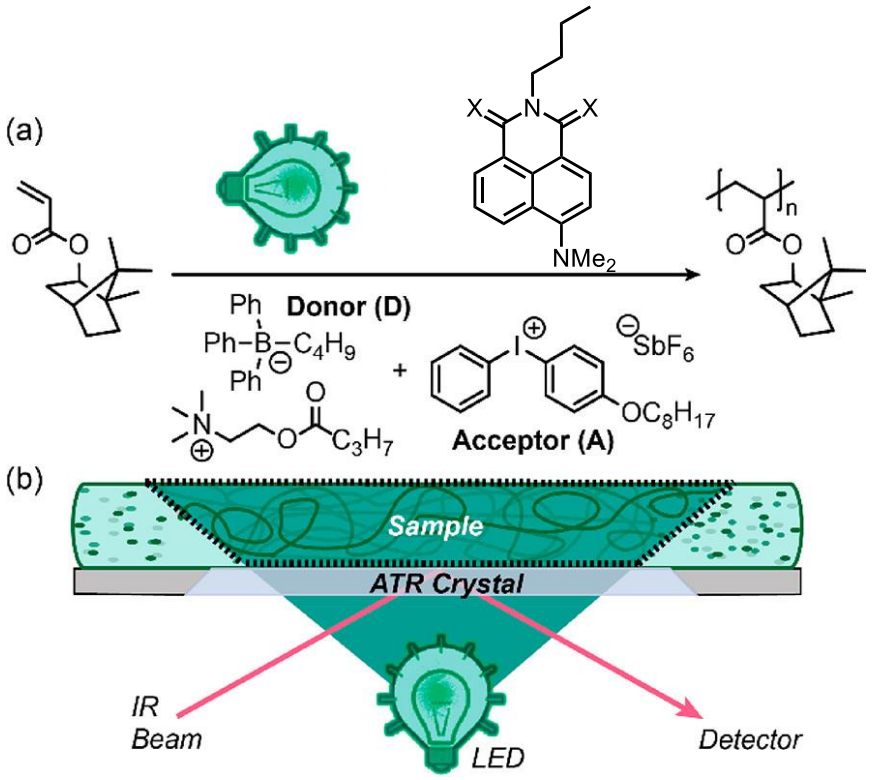

Figure 4.3: (a) Chemical Structures for the Different Components Within the Resin Formulation: Isobornyl Acrylate as Monomer, Borate V as Donor, and HNu 254 as Acceptor. (b) Schematic Illustration for the Custom Real Time ATR-FTIR Setup with Bottom-Up Irradiation.

thiolated (NMe_2-Naphth) and thiolated (NMe_2-Thionaphth) catalysts were collected and can be seen in **Figure 4.4** and **Figure 4.5**. We observe a significant increase in polymerization rate (~3-5x) with the thiocarbonyl present compared to just the carbonyl. The time to reach max conversion is 10 s at 40 mW/cm^2 and 30 s at 10 mW/cm^2 for

NMe_2-Thionaphth compared to 40 s at 40 mW/cm^2 and 150 s at 10 mW/cm^2 for NMe_2-Naphth. This result showcases that thiolation can be another alternative to halogenation in order to improve photocatalyst efficiency. The design principle is the same, increasing ISC rate to longer lived triplet excited states but avoids some of the negative drawbacks of halogenation like cost and cytotoxicity. That being said, these thionaphthalimide derivatives were not as efficient compared to our green light-BODIPY system in Chapter 1 as the polymerization rate begins to slow down significantly at 1 mW/cm^2, unable to reach max conversion within 160 s, whereas with **Mes-Br**, we can lower the intensity to 0.01 mW/cm^2 and still reach max conversion within 60 s. As such, we sought to explore other photosystems in which these photocatalysts can prove highly effective.

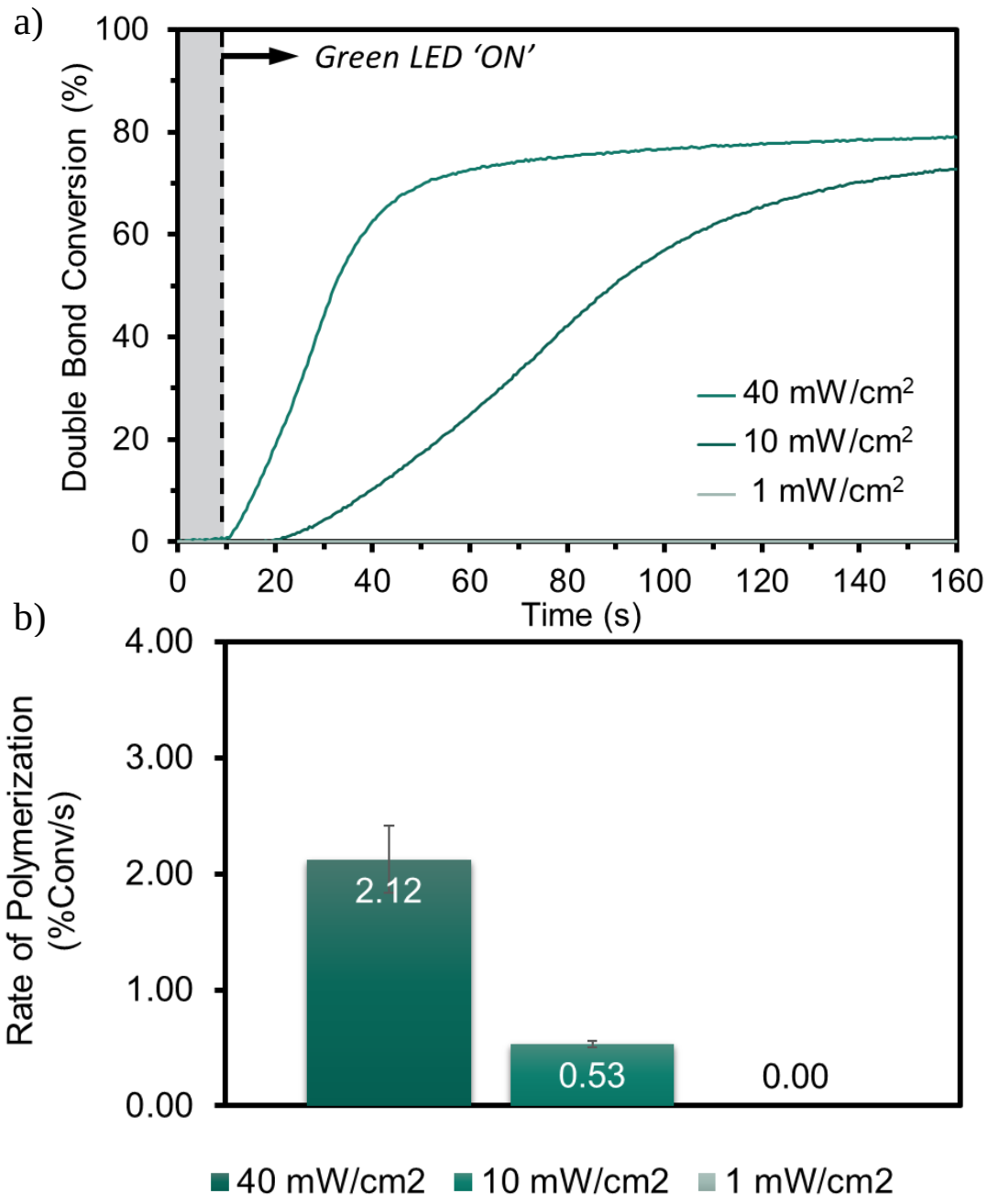

Figure 4.4: (a) Photopolymerization Rate of Isobornyl Acrylate With 0.1 mol% NMe_2-Naphth, 0.1 mol% Borate V, and 1.0 mol% HNu 254 Using a 530 nm LED at Varying Intensities. (b) Polymerization Rate in %Conversion/second at the Different LED Intensities. Error Bars Represent ± 1 Standard Deviation.

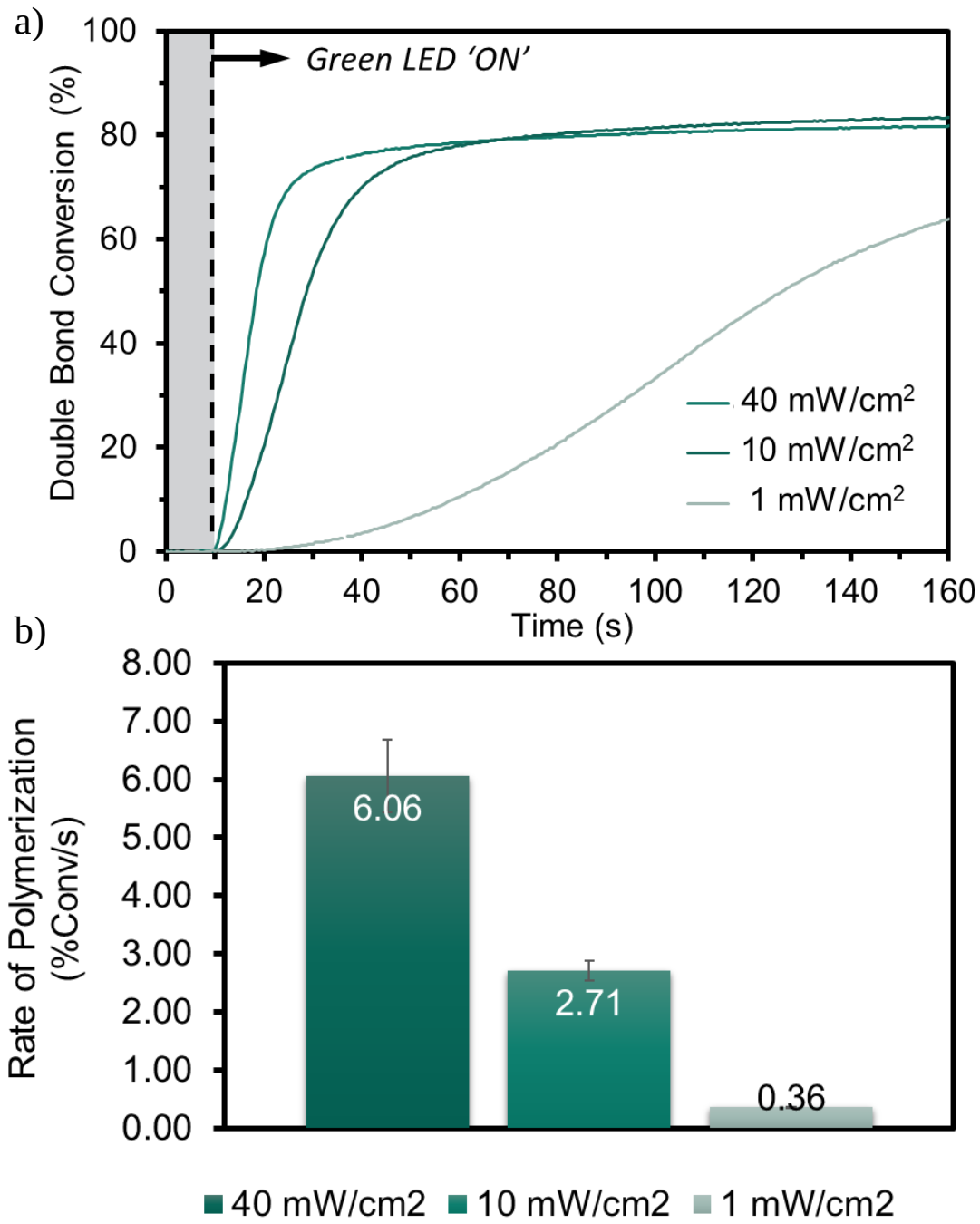

Figure 4.5: (a) Photopolymerization Rate of Isobornyl Acrylate With 0.1 mol% NMe_2-Thionaphth, 0.1 mol% Borate V, and 1.0 mol% HNu 254 Using a 530 nm LED at Varying Intensities. (b) Polymerization Rate in %Conversion/second at the Different LED Intensities. Error Bars Represent ± 1 Standard Deviation.

Looking towards small molecule photoreactions, Wu and coworkers[39] have demonstrated that a mono-thiolated naphthalimide can act as both a photooxidant and photoreductant in a photo aza-henry reaction and photodebromination. The first reaction we explored was the aza-henry photoreaction of a tetrahydroisoquinoline derivative and can be seen in **Figure 4.6**. The reaction was carried out in nitromethane and was

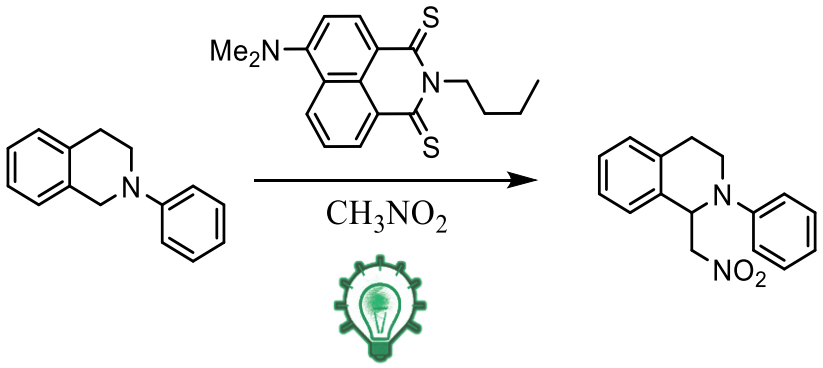

Figure 4.6: Photo Aza-Henry Reaction of N-phenyl-1,2,3,4-tetrahydroisoquinoline

irradiated for 4 hours using 1 mol% of photocatalyst, with aliquots taken every hour. In this reaction, the photocatalyst is acting as a photooxidant in order to oxidize the tetrahydroisoquinoline derivative as shown in **Figure 4.7**. The reaction was carried out in our custom photoreactor seen in **Figure 4.8**. This photoreactor is equiped with a fan in order to ensure the temperature of the reaction stays constant throughout the experiment.

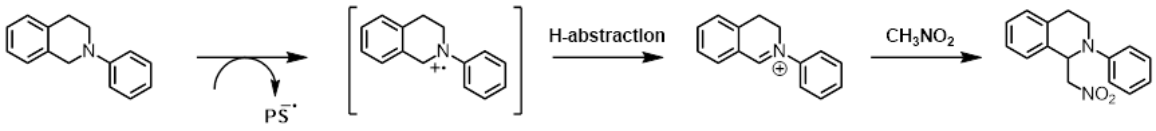

Figure 4.7: Mechanism of Photo Aza-Henry Reaction

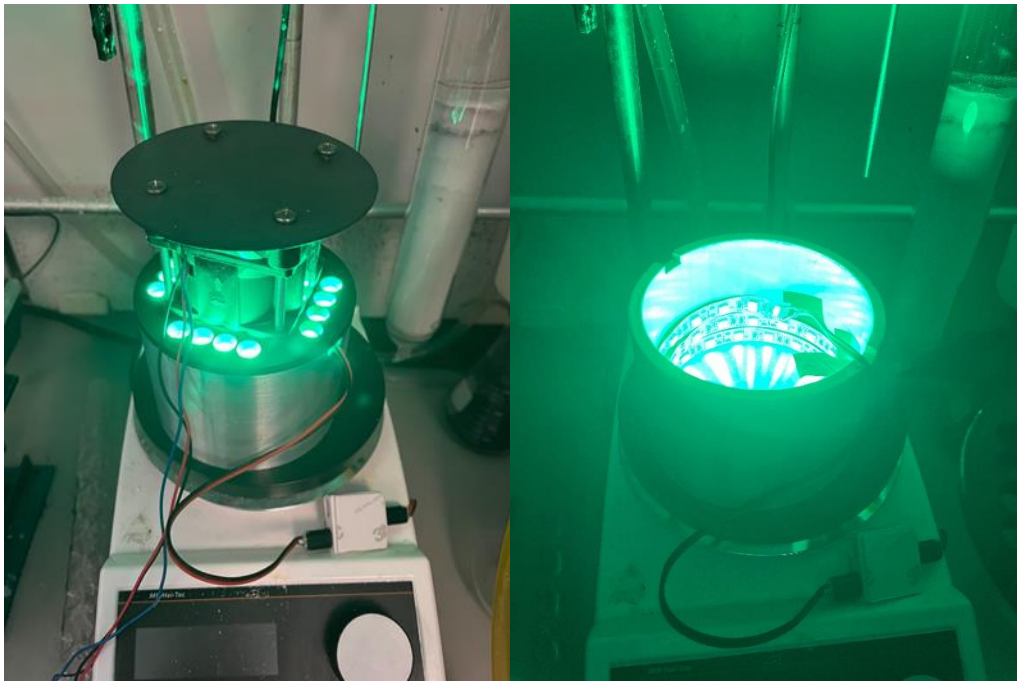

Figure 4.8: Photoreactor Setup with Fan and Stirplate Using Green LED Strips

NMR was used in order to determine the yield of final product with 2,5-dimethylfuran as the internal standard. The results of the NMR experiments can be found in **Figure 4.9**. The integration of the signal at 5.55 ppm (t, 1H), characteristic of the photoproduct, was compared to those of the internal standard (5.84 (s, 2H) and 2.25 ppm (s, 6H)) to calculate the amount of product generated. We see a linear trend in yield over the course of 4 hours reaching a final yield of 98%. For comparison, we also evaluated Eosin Y, a commercial dye, and our **Mes-Br** BODIPY dye in the same photoreaction under the same conditions (**Figure 4.10**). We observe only a 20% yield and 25% yield for Eosin Y and **Mes-Br**, respectively. NMe_2-Thionaphthalimide is a highly efficient photooxidant for this aza-henry photoreaction.

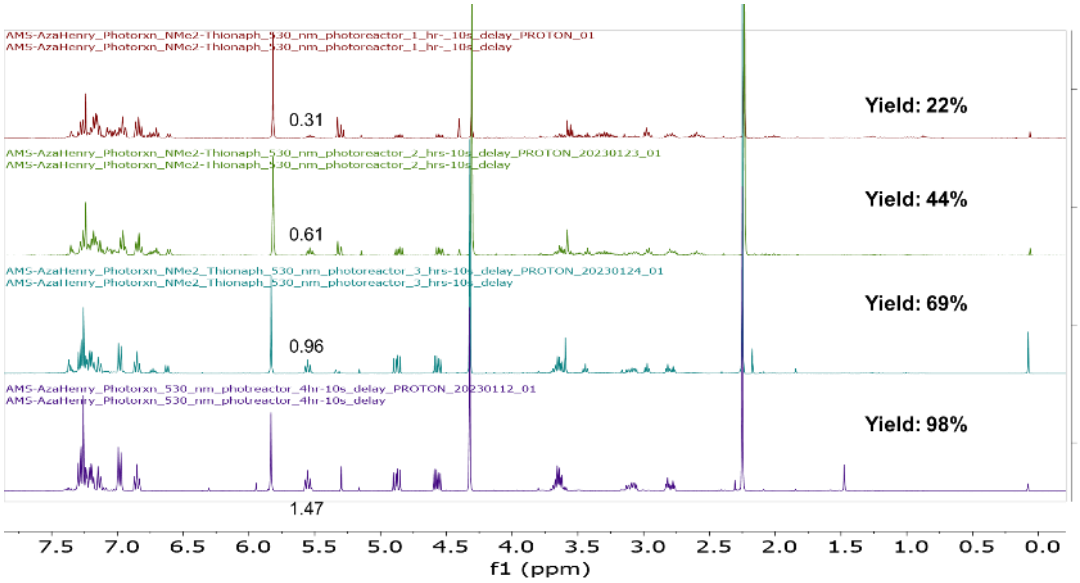

Figure 4.9: NMR Spectra of Photoreaction in $CDCl_3$ at 1 Hour Time Intervals Over 4 hours.

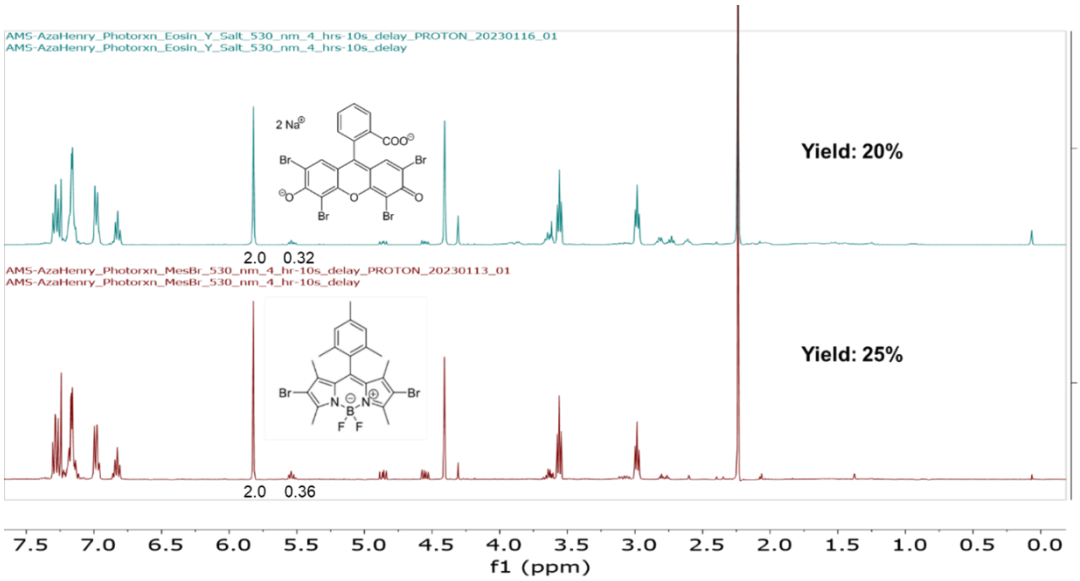

Figure 4.10: NMR Spectra of Photoreaction in $CDCl_3$ with Eosin Y and **Mes-Br** after 4 hours

The second reaction we explored was the photo-debromination of α-bromoacetophenone (**Figure 4.11**). The reaction was carried out in acetonitrile and was

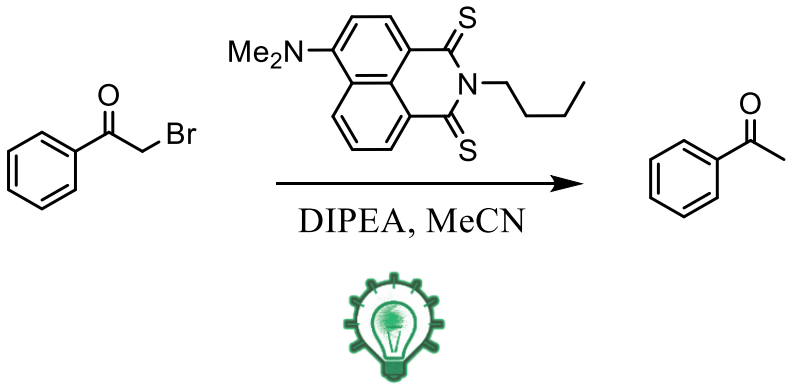

Figure 4.11: Photo-Debromination Reaction of α-bromoacetophenone

irradiated for 4 hours. In this reaction, the photocatalyst is instead acting as a photoreductant in order to reduce the α-bromoacetophenone as shown in **Figure 4.12**.

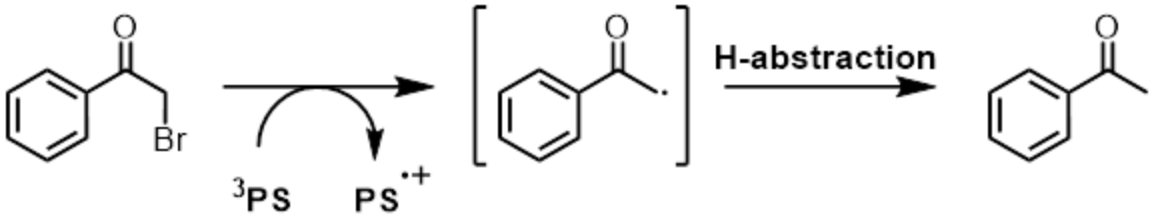

Figure 4.12: Mechanism of Photo-Debromination Reaction of α-bromoacetophenone

Utilizing the same photoreactor as above and the same internal standard, the yields of the reactions from NMR can be found in **Figure 4.13**. Eosin Y and **Mes-Br** were also evaluated in this debromination reaction.

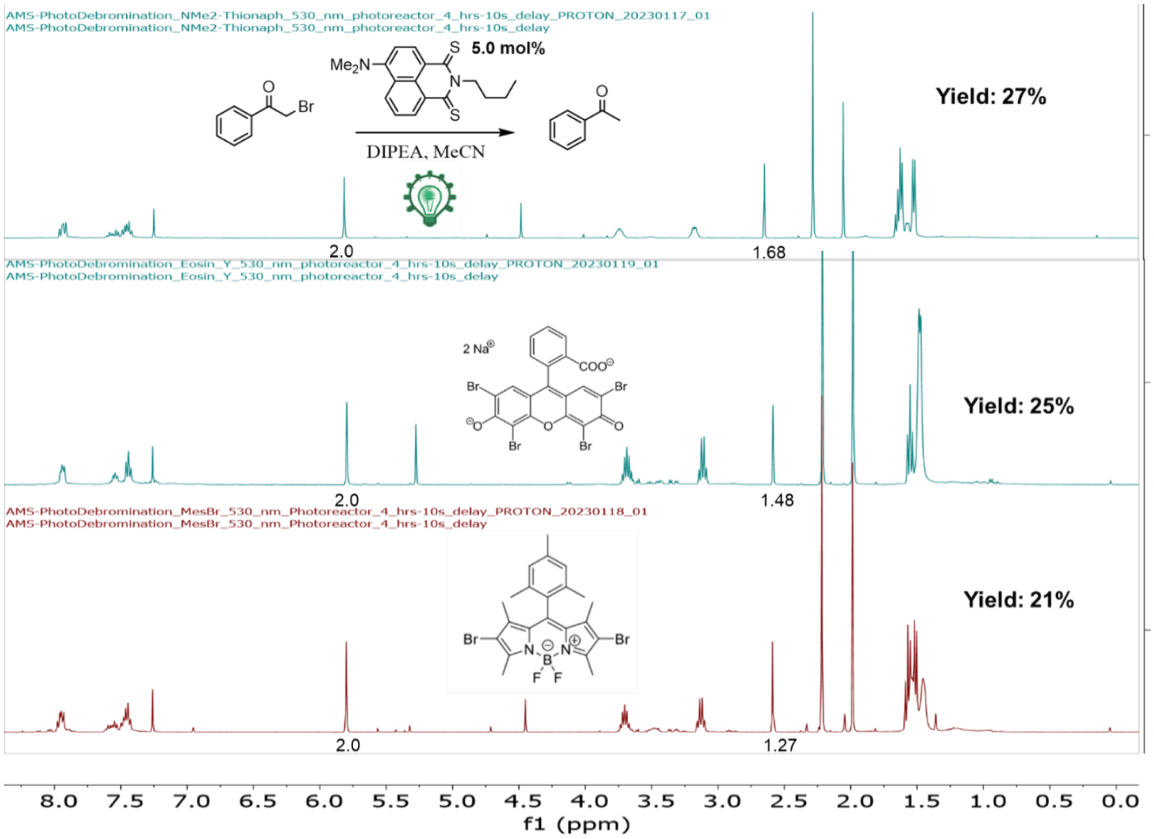

Figure 4.13: NMR Spectra of Debromination Photoreaction in $CDCl_3$ with NMe_2-Thionaphthalimide, Eosin Y and **Mes-Br** after 4 hours.

We observe a 27% yield for the NMe_2-Thionaphthalimide photocatalyst whereas Eosin Y and **Mes-Br** exhibit only a 25% and 21% yield after 4 hours, respectively. The three dyes all show similar efficiency for this photoreaction.

4.3: EXPERIMENTAL

4.31: MATERIALS

Chemicals: 1,8-naphthalic anhydride 98.0+%, 1,2,3,4-tetrahydroisoquinoline, N, N-diisopropylethylamine (DIPEA), and sodium methoxide were purchased from TCI America, butylamine 99.5%, copper(I) iodide 99.99%, iodobenzene, ethylene glycol anhydrous, and ethyl alcohol (EtOH) anhydrous ≥99.5% were purchased from Sigma-Aldrich, methanol (MeOH) (certified ACS), acetonitrile, dimethylamine 2M solution in THF, 2-methoxyethanol 99.0%, potassium phosphate tribasic, and cupric sulfate pentahydrate were purchased from Fischer Scientific, lawesson's reagent 99% and isopropanol 99.8% were purchased from Acros Organics, toluene anhydrous and nitromethane ≥98% were purchased from Alfa Aesar, 2-bromoacetophenone was purchased from Chem-Impex 6-bromobenzo[de]isochromene-1,3-dione was purchased from Ambeed Inc. H-Nu 254, Onium Salt and Borate V were purchased from Spectra Group Limited, Inc. $CDCl_3$ 99.8% was purchased from Cambridge Isotope Laboratories. All chemicals were used as received without additional purification, unless otherwise noted.

4.32: EQUIPMENT AND INSTRUMENTATION

NUCLEAR MAGNETIC RESONANCE (NMR) SPECTROSCOPY

NMR spectra were recorded on an Agilent MR 400 MHz spectrometer utilizing $CDCl_3$ as the solvent. ^{1}H NMR were carried out coupled and referenced to the $CDCl_3$ chemical shift at 7.26 ppm. ^{13}C NMR were carried out decoupled and referenced to the $CDCl_3$ chemical shift at 77.16 ppm.

HIGH RESOLUTION MASS SPECTROMETRY (HRMS)

HRMS was performed on an Agilent Technologies 6530 Accurate-Mass Q-TOF LC/MS using ESI and the data was subsequently analyzed using Agilent MassHunter Qualitative Analysis Software.

REAL-TIME FOURIER-TRANSFORM INFRARED SPECTROSCOPY (RT-FTIR)

RT-FTIR was recorded utilizing an INVENIO-R FT-IR Spectrometer from Bruker (Figure S1) and controlled via OPUS Spectroscopy Software. A liquid nitrogen cooled (LN-MCT Mid) detector was used for measurements. A modified GladiATR Illuminate ATR accessory[40] from PIKE Technologies was used to analyze chemical composition and monitor photocuring of liquid resins upon exposure to light. Collimated LED light sources (740 nm-P/N LCS-0740-10-22, 810 nm-P/N LCS-0810-02-22, 850 nm-P/N LCS-0850-03-22, 940 nm-P/N LCS-0940-02-38) from Mightex Systems along with Lightguide Adapters were utilized to irradiate resins with visible light (see photopolymerization procedure for more details). LED Controller M/N SLC-MA02-U was used with a 3 mm liquid light guide (LLG-3- 4H).

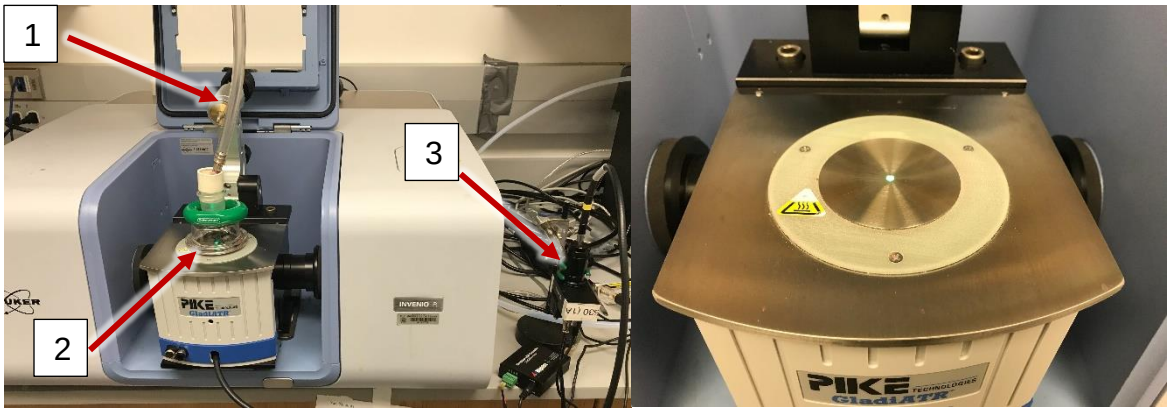

Figure 4.14: Photo-ATR FTIR Setup (1) Argon/Nitrogen Gas Line (2) Custom Glass Top With O-Ring to Create Oxygen Free Atmosphere (3) LED and Liquid Light Guide. Close-Up Image of Custom ATR Accessory With green LED On.

4.33: STEADY-STATE OPTICAL CHARACTERIZATION

UV-visible absorption spectra were recorded on an Ocean Optics QE PRO-ABS Fiber Optic Spectrometer utilizing deuterium-tungsten halogen light sources (DH-2000-BAL). 600 μm fiberoptic cables (QP600-025-SR) were coupled to the detector with a slit width of 5 μm. Dilute absorption data was collected in acetonitrile utilizing quartz cuvettes and a qpod sample holder (QNW qpod2e). Thin-film absorption data was collected in the resin formulation (see photopolymerization conditions) utilizing the Ocean Optics Stage RTL-T.

4.34: ELECTRONIC CHARACTERIZATION

Cyclic voltammetry (CV) was performed in a nitrogen-filled VAC glovebox using a BioLogic SP-50e potentiostat. A single-compartment three-electrode cell was used with glassy carbon as the working electrode, a platinum wire as the counter electrode, and an $Ag/AgNO_3$ (0.01 M) nonaqueous reference electrode calibrated versus Fc/Fc+ in 0.1 M tetrabutylammonium hexafluorophosphate ($TBAPF_6$) dichloromethene solutions

($E_{½}(Fc/Fc^{+})$ = 0.1 V vs Ag/Ag^{+}) with a 0.1 V/s scan rate. Oxidation onsets were utilized to calculate the highest occupied molecular orbital (HOMO) energy levels -(4.8 eV $–E_{ox}$ (Ferrocene) + E_{ox}) and reduction onsets to calculate the lowest unoccupied molecular orbital (LUMO) energy levels -(4.8 eV $–E_{ox}$ (Ferrocene) + E_{red})[41].

4.35: LED LIGHT SOURCES

All LEDs used were purchased from Mightex Systems. The emission profile for the LED was measured using a calibrated UV-Vis Ocean Insight system. Irradiation intensities were measured with a Thorlabs PM100D photometer equipped with silicon-based photodiode power sensor (S120VC, Thorlabs). Emission profiles were recorded with a QE pro spectrometer, in which the LED was connected to the fiber optic system using a 3 mm liquid lightguide from Mightex Systems (serial #: LLG-03-59-340-0800-1).

4.36: SYNTHESIS

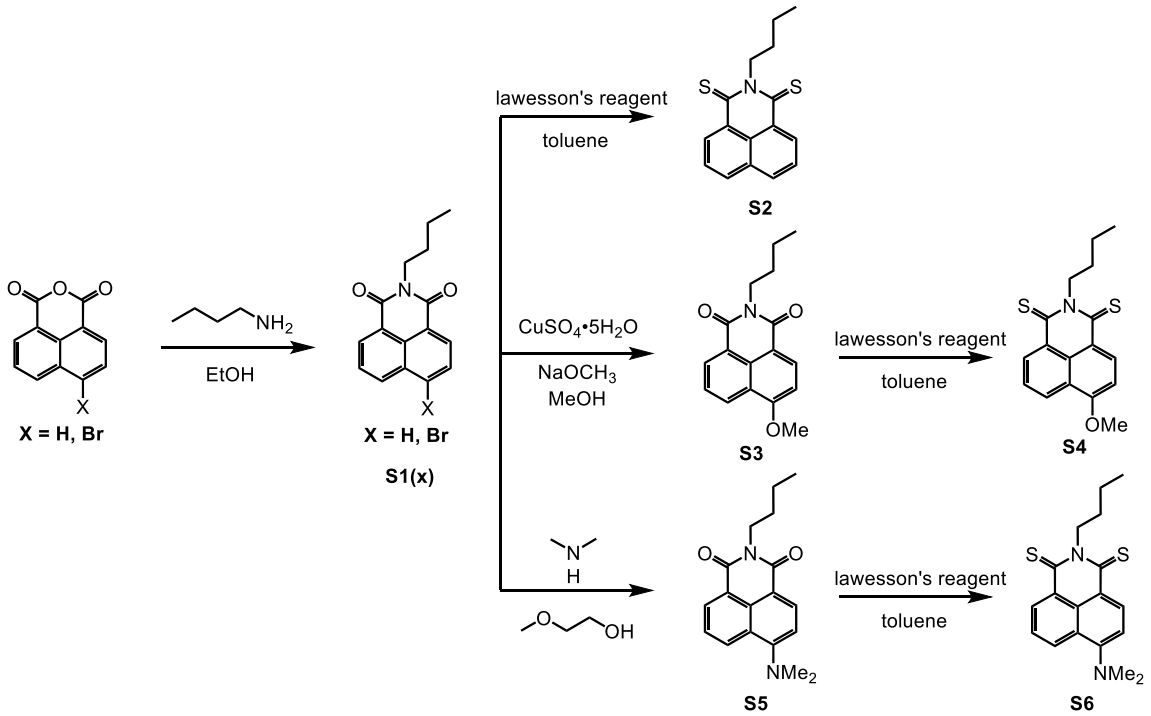

Figure 4.15: Synthesis of Thionaphthalimide Series

2-butyl-1H-benzo[de]isoquinoline-1,3(2H)-dione (S1a)

A mixture of 1H,3H-benzo[de]isochromene-1,3-dione (0.813 g, 1 Eq, 4.10 mmol) and butan-1-amine (306 mg, 0.41 mL, 1.02 Eq, 4.18 mmol) in ethanol (30 mL) was refluxed for 5 hrs. After the reaction was completed, the reaction mixture was evaporated in vacuum and dried to obtain 944 mg (91%) of a solid product. ^{1}H NMR (400 MHz, $CDCl_3$) δ 8.60-8.62 (d, *J* = 7.3 Hz, 2H), 8.20-8.22 (d, *J* = 8.2 Hz, 2H), 7.74-7.78 (t, *J* = 7.8 Hz, 2H), 4.17-4.21 (m, 2H), 1.69-1.76 (m, 2H), 1.41-1.50 (q, *J* = 7.5 Hz, 2H), 0.96-1.00 (t, *J* = 7.3 Hz, 3H); ^{13}C NMR (100 MHz, $CDCl_3$) δ 164.3, 133.9, 131.6, 131.2, 128.2, 127.0, 122.8, 40.3, 30.3, 20.5, 14.0; IR (ATR): 2973, 2947, 2868, 1696, 1655, 1622, 1588, 1466, 1437, 1414, 1386, 1259, 1194, 1114, 1070, 936, 869, 796, 779 cm^{-1}; HRMS (APCI): exact mass calculated for $C_{16}H_{15}NO_2$ $[M+H]^+$ 254.1103, found 254.1178

6-bromo-2-butyl-1H-benzo[de]isoquinoline-1,3(2H)-dione (S1b)

A mixture of 6-bromo-1H,3H-benzo[de]isochromene-1,3-dione (0.813 g, 1 Eq, 2.93 mmol) and butan-1-amine (0.219 g, 0.30 mL, 1.02 Eq, 2.99 mmol) in ethanol (30 mL) was refluxed for 5 hrs. After the reaction was completed, the reaction mixture was evaporated in vacuum and dried to obtain 975 mg (100%) of a solid product. ^{1}H NMR (400 MHz, $CDCl_3$) δ 8.65-8.67 (dd, *J* = 7.3, 1.1 Hz, 1H), 8.56-8.59 (dd, *J* = 8.5, 1.2 Hz, 1H), 8.41-8.43 (d, *J* = 7.8 Hz, 1H), 8.04-8.06 (d, *J* = 7.9 Hz, 1H), 7.83-7.87 (dd, *J* = 8.5, 7.3 Hz, 1H), 4.16-4.19 (m, 2H), 1.68-1.75 (q, *J* = 7.7 Hz, 2H), 1.40-1.49 (m, 2H), 0.96-1.00 (t, *J* = 7.4 Hz, 3H); ^{13}C NMR (100 MHz, $CDCl_3$) δ 163.7, 133.3, 132.1, 131.3, 131.2, 130.7, 130.3, 129.1, 128.2, 123.3, 122.4, 40.5, 30.3, 20.5, 14.0; IR (ATR): 3070, 2956, 2870, 1697, 1649, 1588, 1567, 1501, 1458, 1434, 1398, 1153, 1101, 1043, 1027, 994, 969, 938, 872, 854, 845, 814, 780, 749, 703 cm^{-1}; HRMS (APCI): exact mass calculated for $C_{16}H_{14}BrNO_2$ $[M+H]^+$ 332.0208, found 332.0283

2-butyl-1H-benzo[de]isoquinoline-1,3(2H)-dithione (S2)

2-butyl-1H-benzo[de]isoquinoline-1,3(2H)-dione (S1a) (0.120 g, 1 Eq, 474 µmol), lawesson's reagent (0.610 g, 3.18 Eq, 1.51 mmol) were dissolved in toluene (20 mL). The mixture was refluxed under nitrogen for 24 hrs. After the reaction mixture was cooled down to room temperature, the solvent was evaporated under reduced pressure, and the residue was subsequently purified by column chromatography on silica gel using n-hexane /DCM as eluent to yield 38 mg (28%) of solid product. ^{1}H NMR (400 MHz, $CDCl_3$) δ 8.90-8.92 (d, *J* = 8.7 Hz, 2H), 8.13-8.15 (d, *J* = 7.9 Hz, 2H), 7.60-7.64 (t, *J* = 7.9 Hz, 2H), 5.31-5.35 (m, 2H), 1.87-1.95 (m, 2H), 1.43-1.50 (q, *J* = 7.5 Hz, 2H), 0.99-1.02 (t, *J* = 7.4 Hz, 3H); ^{13}C NMR (100 MHz, $CDCl_3$) δ 191.2, 138.1, 133.4, 131.6, 129.6, 127.5, 123.5, 55.0, 27.5, 20.2, 14.0; IR (ATR): 2953, 2924, 2864, 1615, 1567, 1510, 1456, 1427, 1417, 1354, 1337, 1312, 1270, 1247, 1190, 1152, 1105, 1050, 947, 935, 834, 804, 761, 612 cm^{-1}; HRMS (APCI): exact mass calculated for $C_{16}H_{15}NS_2$ $[M+H]^+$ 286.0646, found 286.0720

2-butyl-6-methoxy-1H-benzo[de]isoquinoline-1,3(2H)-dione (S3)

To a 100 mL flask, 6-bromo-2-butyl-1H-benzo[de]isoquinoline-1,3(2H)-dione (S1b) (0.664 g, 1 Eq, 2.00 mmol), CuSO4•5H2O (10 mol%), and sodium methanolate (0.108 g, 1.00 Eq, 2.00 mmol) in methanol (20 mL) was refluxed for 8 hrs. The crude product was evaporated under vacuum and to the residue was added HCl (1M, 30 mL) to crystallize out 349 mg (62%) of solid product. ^{1}H NMR (400 MHz, $CDCl_3$) δ 8.60-8.62 (dd, *J* = 7.3, 1.2 Hz, 1H), 8.55-8.57 (m, 2H), 7.68-7.72 (dd, *J* = 8.4, 7.3 Hz, 1H), 7.04-7.06 (d, *J* = 8.3 Hz, 1H), 4.15-4.19 (m, 2H), 4.13 (s, 3H), 1.68-1.75 (m, 2H), 1.40-1.50 (m, 2H), 0.96-0.99 (t, *J* = 7.4 Hz, 3H); ^{13}C NMR (100 MHz, $CDCl_3$) δ 164.6, 164.1, 160.8, 133.5, 131.6, 129.4, 128.6, 126.0, 123.6, 122.5, 115.2, 105.3, 56.3, 40.2, 30.4, 20.5, 14.0; IR (ATR): 3021, 2955, 2870, 1689, 1649, 1621, 1591, 1577, 1512, 1463, 1452, 1433, 1386,

1291, 1233, 1165, 1114, 1049, 932, 824, 779, 647 cm^{-1}; HRMS (APCI): exact mass calculated for $C_{17}H_{17}NO_3$ $[M+H]^+$ 284.1208, found 284.1287

2-butyl-6-methoxy-1H-benzo[de]isoquinoline-1,3(2H)-dithione (S4)

2-butyl-6-methoxy-1H-benzo[de]isoquinoline-1,3(2H)-dione (S3) (0.14 g, 1 Eq, 0.49 mmol), lawesson's reagent (0.610 g, 3.1 Eq, 1.51 mmol) were dissolved in toluene (20 mL). The mixture was refluxed under nitrogen for 24 hrs. After the reaction mixture was cooled down to room temperature, the solvent was evaporated under reduced pressure, and the residue was purified by column chromatography on silica gel using n-hexane /DCM as eluent to yield 25 mg (16%) of solid product. ^{1}H NMR (400 MHz, $CDCl_3$) δ 8.94-8.98 (t, *J* = 8.2 Hz, 2H), 8.50-8.52 (d, *J* = 8.2 Hz, 1H), 7.55-7.61 (t, *J* = 8.0 Hz, 1H), 6.99-7.01 (d, *J* = 8.7 Hz, 1H), 5.34 (s, 2H), 4.12 (s, 3H), 1.87-1.95 (m, 2H), 1.43-1.52 (m, 2H), 0.98-1.00 (t, *J* = 7.4 Hz, 3H); ^{13}C NMR (100 MHz, $CDCl_3$) δ 191.2, 190.4, 161.2, 141.1, 138.7, 129.4, 128.3, 126.7, 124.7, 123.6, 122.9, 106.9, 56.5, 54.9, 27.5, 20.2, 14.0; IR (ATR): 2956, 2867, 1613, 1579, 1514, 1469, 1422, 1407, 1373, 1343, 1323, 1248, 1191, 1179, 1102, 1061, 1010, 997, 819, 756 cm^{-1}; HRMS (APCI): exact mass calculated for $C_{17}H_{17}NOS_2$ $[M+H]^+$ 316.0752, found 316.0825

2-butyl-6-(dimethylamino)-1H-benzo[de]isoquinoline-1,3(2H)-dione (S5)

dimethylamine (237 mg, 2.62 mL, 2 molar, 5.81 Eq, 5.25 mmol) was added dropwise to a solution of 6-bromo-2-butyl-1H-benzo[de]isoquinoline-1,3(2H)-dione (S1b) (300 mg, 1 Eq, 903 µmol) in 5 mL 2-methoxyethanol. The mixture was heated to reflux for 2 hrs, while monitored by TLC. After the reaction was completed, the solvent was reduced under vacuum. The solid product was subsequently washed with hexane to yield 151 mg (56%) of a yellow solid. ^{1}H NMR (400 MHz, $CDCl_3$) δ 8.57-8.58 (d, *J* = 6.9 Hz, 1H), 8.47-8.49 (d, *J* = 8.1 Hz, 1H), 8.44-8.46 (d, *J* = 8.6 Hz, 1H), 7.64-7.68 (t, *J* = 8.0 Hz, 1H), 7.12-7.14 (d, *J* = 8.2 Hz, 1H), 4.15-4.19 (m, 2H), 3.11 (s, 6H), 1.67-1.75 (m, 2H), 1.40-

1.49 (q, *J* = 7.5 Hz, 2H), 0.95-0.99 (t, *J* = 7.4 Hz, 3H); ^{13}C NMR (100 MHz, $CDCl_3$) δ 164.8, 164.2, 157.0, 132.7, 131.2, 131.1, 130.3, 125.4, 125.0, 123.3, 115.2, 113.5, 44.9, 40.2, 30.4, 20.5, 14.0; IR (ATR): 3053, 2993, 2958, 1681, 1610, 1578, 1522, 1446, 1408, 1387, 1348, 1275, 1203, 1088, 995, 943, 778, 755, 665 cm^{-1}; HRMS (APCI): exact mass calculated for $C_{18}H_{20}N_2O_2$ $[M+H]^+$ 297.1525, found 297.1601

2-butyl-6-(dimethylamino)-1H-benzo[de]isoquinoline-1,3(2H)-dithione (S6)

2-butyl-6-(dimethylamino)-1H-benzo[de]isoquinoline-1,3(2H)-dione (S5) (300 mg, 1 Eq, 1.01 mmol), lawesson's reagent (1.23 g, 3.0 Eq, 3.04 mmol) were dissolved in toluene (20 mL). The mixture was refluxed under nitrogen for 24 hrs. After the reaction mixture was cooled down to room temperature, the solvent was evaporated under reduced pressure and the residue was subsequently purified by column chromatography on silica gel using n-hexane /DCM as eluent to yield 59 mg (18%) of solid product. ^{1}H NMR (400 MHz, $CDCl_3$) δ 8.96-8.99 (dd, *J* = 7.7, 1.2 Hz, 1H), 8.87-8.89 (d, *J* = 8.8 Hz, 1H), 8.32-8.34 (dd, *J* = 8.3, 1.2 Hz, 1H), 7.51-7.55 (dd, *J* = 8.4, 7.7 Hz, 1H), 7.00-7.02 (d, *J* = 8.7 Hz, 1H), 5.37 (s, 2H), 3.16 (s, 6H), 1.88-1.96 (q, *J* = 7.6 Hz, 2H), 1.43-1.50 (m, 2H), 0.98-1.00 (t, *J* = 7.4 Hz, 3H); ^{13}C NMR (100 MHz, $CDCl_3$) δ 190.9, 189.4, 157.1, 140.5, 138.4, 131.3, 130.2, 125.9, 125.3, 123.6, 123.0. 114.2, 54.8, 44.8, 27.5, 20.2, 14.0; IR (ATR): 2953, 2922, 2851, 1666, 1644, 1597, 1572, 1502, 1409, 1372, 1338, 1297, 1254, 1177, 1100, 966, 929, 801, 751 cm^{-1}; HRMS (APCI): exact mass calculated for $C_{18}H_{20}N_2S_2$ $[M+H]^+$ 329.1068, found 329.1142

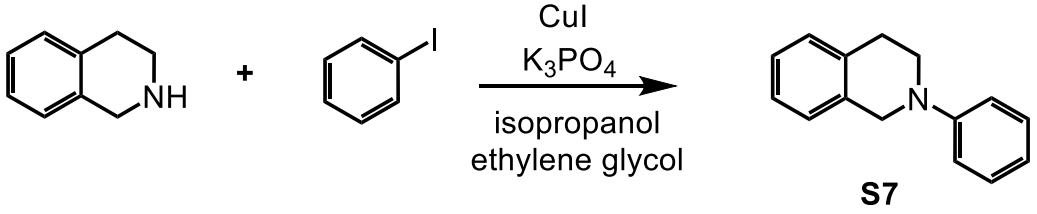

Figure 4.16: Synthesis of N-phenyl-1,2,3,4-tetrahydroisoquinoline

2-phenyl-1,2,3,4-tetrahydroisoquinoline (S7)

copper(I) iodide (200 mg, 1.0 mmol) and potassium phosphate (4.25 g, 20.0 mmol) were put into a Schlenk tube. The tube was evacuated and back filled with nitrogen. 2-propanol (10.0 mL), ethylene glycol (1.11 mL, 20.0 mmol), 1,2,3,4-tetrahydro-isoquinoline (2.0 mL, 15 mmol) and iodobenzene (1.12 mL, 10.0 mmol) were added. The reaction mixture was heated to 90 °C and reacted for 24 hrs. The mixture was then cooled to room temperature. Diethyl ether (20 mL) and water (20 mL) were then added and the organic layer was extracted by diethyl ether (2 × 20 mL). The combined organic phases were washed with brine and dried over $MgSO_4$. The solvent was removed by rotary evaporation and purified by column chromatography on silica gel (hexane/ethyl acetate=20:1) to yield 1.123 g (34%) of a white solid. ^{1}H NMR (400 MHz, $CDCl_3$) δ 7.28-7.32 (m, 2H), 7.15-7.20 (m, 4H), 7.00-7.01 (d, *J* = 8.0 Hz, 2H), 6.83-6.86 (t, *J* = 6.7 Hz, 1H), 4.42 (s, 2H), 3.56-3.59 (t, *J* = 5.9 Hz, 2H), 2.98-3.01 (t, *J* = 5.9 Hz, 2H); ^{13}C NMR (100 MHz, $CDCl_3$) δ 150,7, 135.0, 134.6, 129.3, 128.7, 126.7, 126.5, 126.2, 118.8, 115.3, 50.9, 46.6, 29.2; IR (ATR): 3022, 2903, 2823, 1698, 1597, 1575, 1501, 1460, 1431, 1337, 1292, 1110, 1030, 737, 690, 643 cm^{-1}; HRMS (APCI): exact mass calculated for $C_{15}H_{15}N$ $[M+H]^+$ 210.1205, found 210.1283

4.37: CHARACTERIZATION

^{1}H NMR DATA

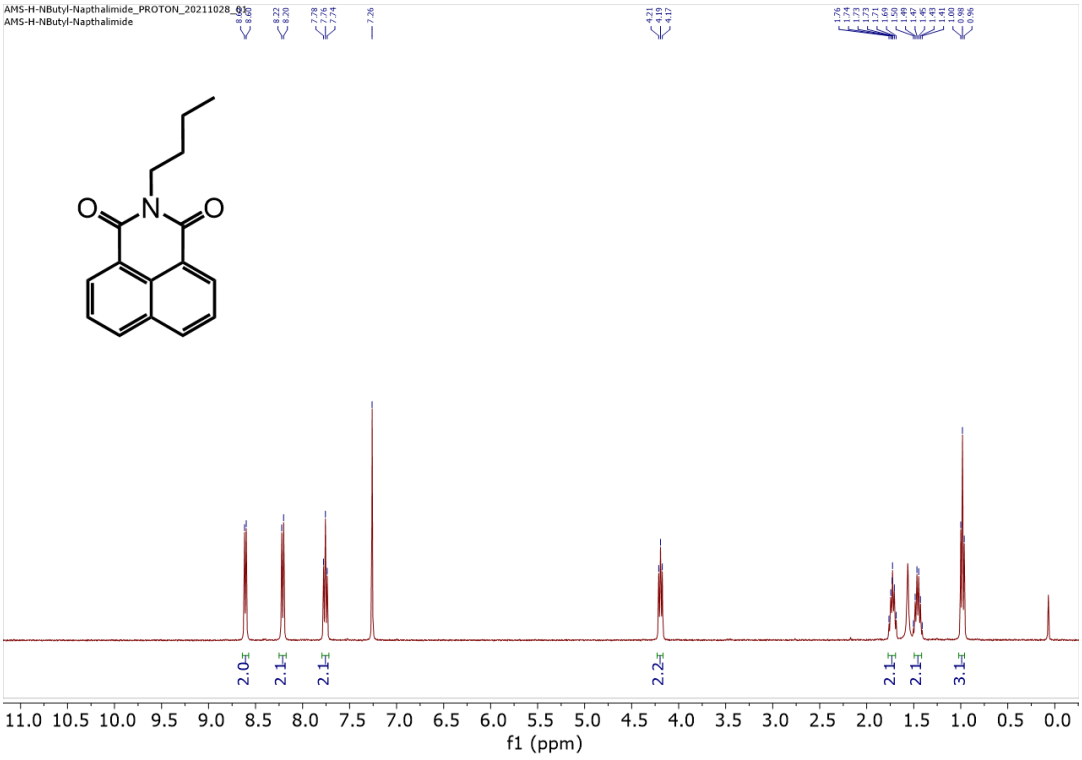

Figure 4.17: ^{1}H NMR of Compound **S1a** in $CDCl_3$

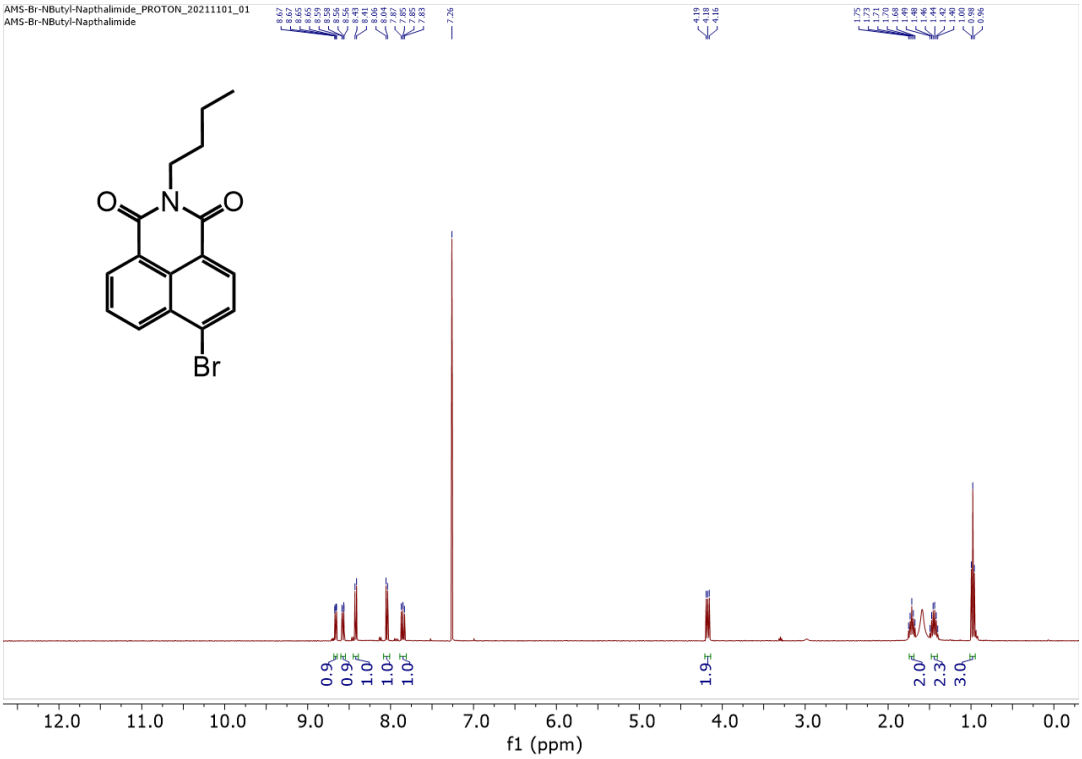

Figure 4.18: ^{1}H NMR of Compound **S1b** in $CDCl_3$

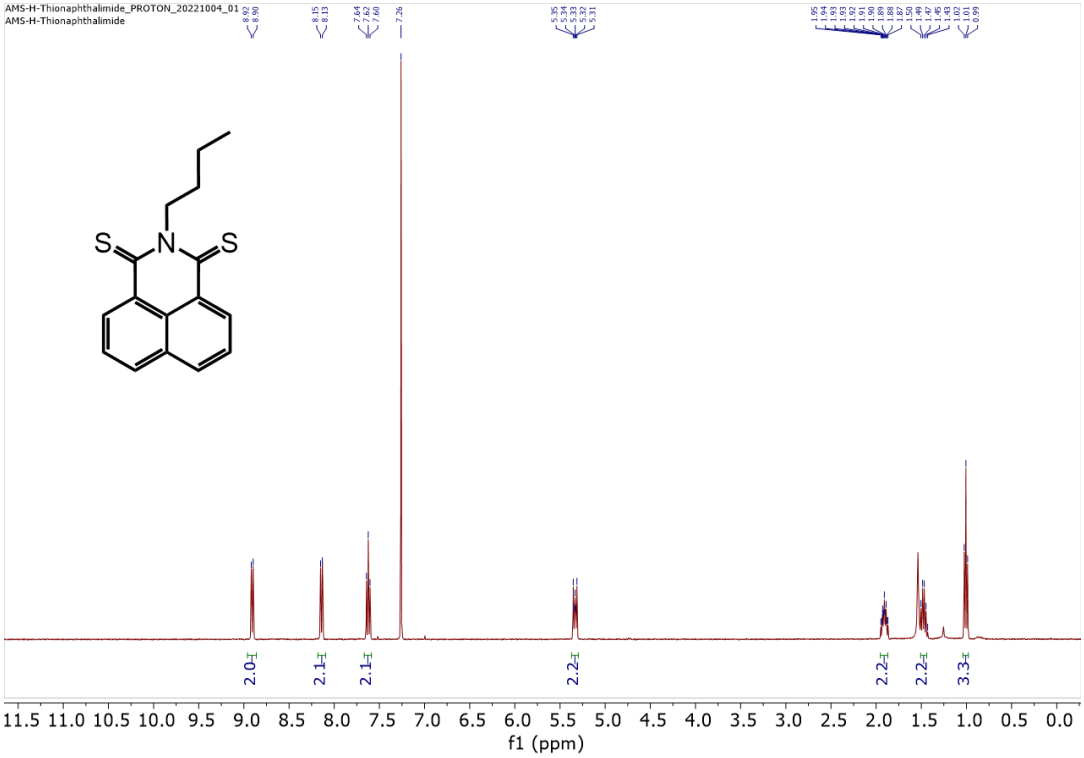

Figure 4.19: ^{1}H NMR of Compound S**2** in $CDCl_3$

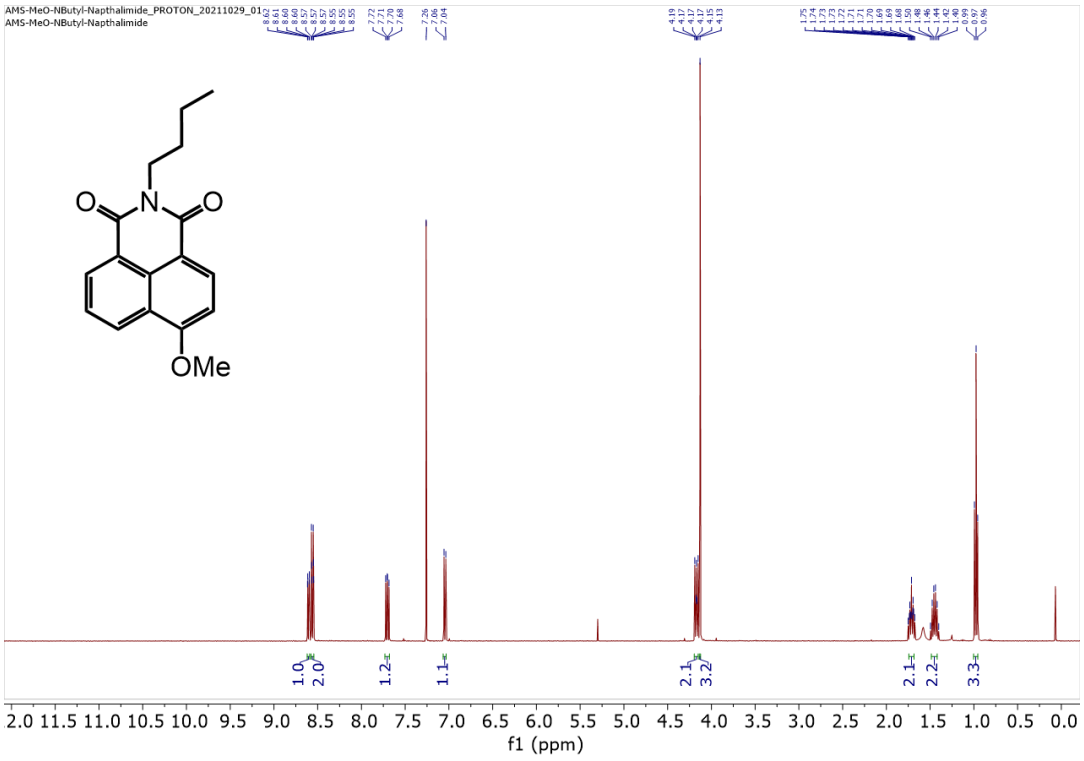

Figure 4.20: ^{1}H NMR of Compound **S3** in $CDCl_3$

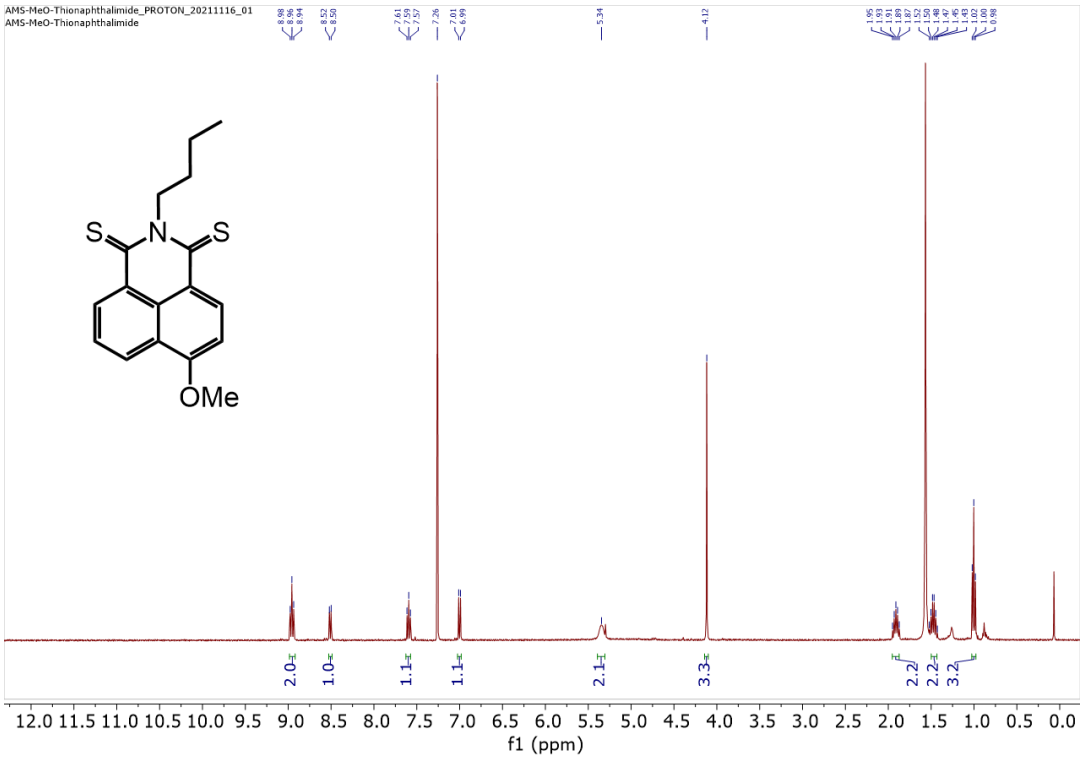

Figure 4.21: ^{1}H NMR of Compound **S4** in $CDCl_3$

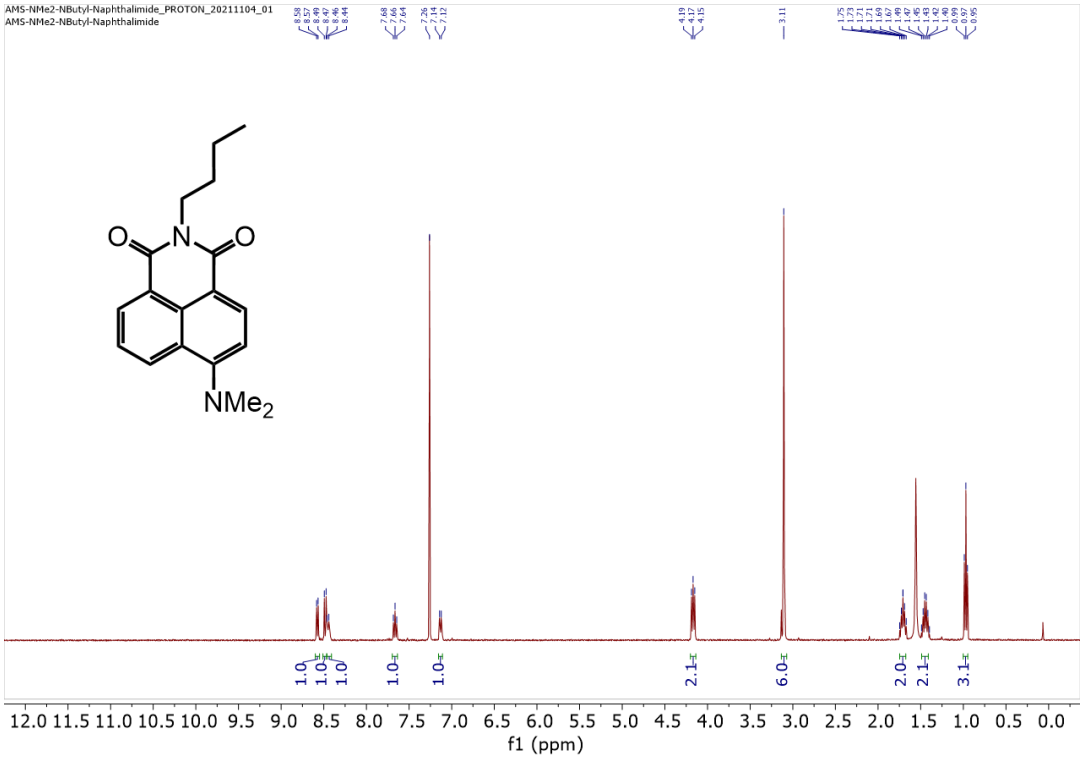

Figure 4.22: ^{1}H NMR of Compound **S5** in $CDCl_3$

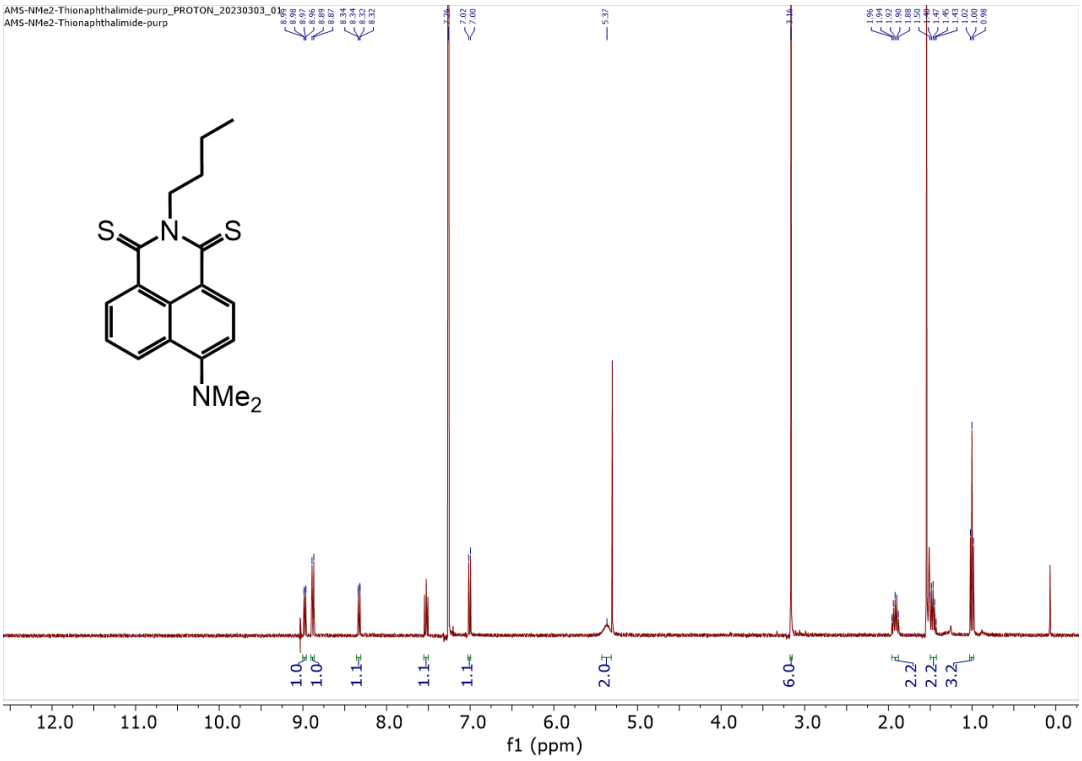

Figure 4.23: ^{1}H NMR of Compound **S6** in $CDCl_3$

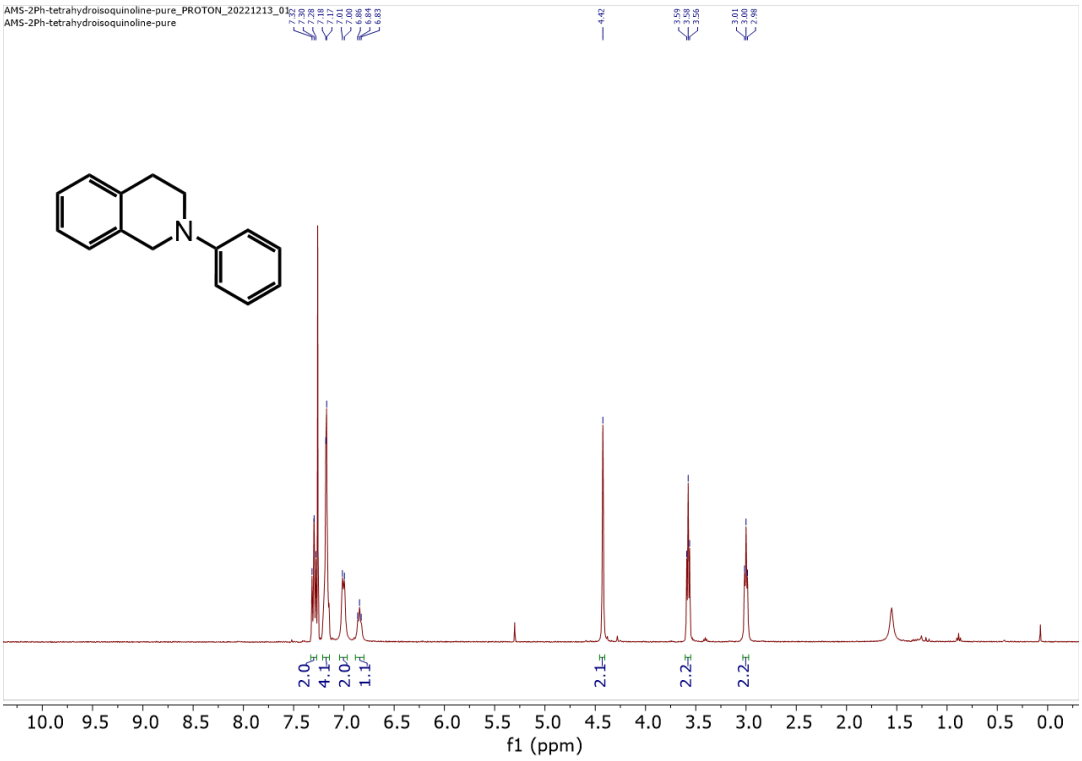

Figure 4.24: ^{1}H NMR of Compound **S7** in $CDCl_3$

4.4: CONCLUSION

Thiolation of naphthalimide dyes was demonstrated to be an effective strategy to improve the efficiency of light-driven polymerizations and small molecule photoredox reactions. Systematic kinetic and optoelectronic characterizations of a thionaphthalimide series revealed the utility of the sulfur atom as a heavy-atom alternative to halogens. Real time ATR-FTIR with custom bottom-up irradiation was used to quantitatively characterize polymerization rate, showing that thiolation of the carbonyls resulted in 3–5× higher polymerization rates upon exposure to green light. Additionally, the thionaphthalimide was able to achieve near quantitative conversion (98%) of a photo-henry reaction, outperforming a brominated BODIPY and commercial Eosin Y. The presence of the sulfur atom results in faster intersystem crossing rates, which corresponds to higher triplet yields and longer excited state lifetimes. This, in turn, improves photocatalytic efficiency by increasing the number of collisions that occur per photon absorbed between the dye in the excited state and an initiator. These results are particularly exciting to continue to inform the future development of more efficient photoredox catalysts as it provides an alternative method to achieve longer lived excited states without having to utilize halogen heavy atoms. This can extend the utility of photopolymers to include the formation of biocompatible tissue scaffolds where previously the cytotoxicity of halogen substitution was problematic.

4.5: REFERENCES

(1) Romero, N., Nicewicz, D. A. Organic Photoredox Catalysis *Chemical Reviews*, **2016**, *116* (17), 10075-10166

(2) Sideri, I. K., Voutyritsa, E., Kokotos, C. G. Photoorganocatalysis, Small Organic Molecules and Light in the Service of Organic Synthesis: The Awakening of a Sleeping Giant. *Organic and Biomolecular Chemistry*, **2018**, *16* (25), 4596-4614

(3) Rawat, D., Kumar, R., Subbarayappa, A. Visible-Light Induced Phosphonation of Quinoxalines and Quinoxalin-2(1H)-ones Under Aerobic Metal-Free Conditions. *Green Chemistry*, **2020**, *22* (18), 6170-6175

(4) Xuan, J., He, X., Xiao, W. Visible Light-Promoted Ring-Opening Functionalization of Three-Membered Carbo- And Heterocycles. *Chemical Society Reviews*, **2020**, *49* (9), 2546-2556

(5) Reed, N. L., Yoon, T. P. Oxidase Reactions in Photoredox Catalysis. *Chemical Society Reviews*, **2021**, *50* (5), 2954-2967

(6) Prier, C. K., Rankic, D. A., MacMillan, D. W. C. Visible Light Photoredox Catalysis with Transition Metal Complexes: Applications in Organic Synthesis. *Chemical Reviews*, **2013**, *113* (7), 5322-5363

(7) Singh-Rachford, T. N., Castellano, F. N. Photon Upconversion Based on Sensitized Triplet-Triplet Annihilation. *Coordination Chemistry Reviews*, **2010**, *254* (21-22), 2560-2573

(8) Dias, F. B., Santos, J., Graves, D. R., Data, P., Nobuyasu, R. S., Fox, M. A., Batsanov, A. S., Palmeira, T., Berberan-Santos, M. N., Bryce, M. R., Monkman, A. P. Transition metal-involved photon upconversion. *Advanced Science*, **2016**, *3* (12) 1-25

(9) Huang, L., Kakadiaris, E., Vaneckova, T., Huang, K., Vaculovicova, M., Han, G. Designing next generation of photon upconversion: Recent advances in organic triplet-triplet annihilation upconversion nanoparticles. *Biomaterials*, **2019**, *201*, 77-86

(10) Zhao, J., Wanhua, W., Sun, J., Guo, S. Triplet photosensitizers: From molecular design to applications *Chemical Society Reviews*, **2013**, *42* (12), 5323-5351

(11) Nguyen, V., Yan, Y., Zhao, J., Yoon, J. Heavy-Atom-Free Photosensitizers: From Molecular Design to Applications in the Photodynamic Therapy of Cancer. *Accounts of Chemical Research*, **2021**, *54* (1), 207-220

(12) Tang, J., Wang, L., Loredo, A., Cole, C., Xiao, H. Single-atom replacement as a general approach towards visible-light/near-infrared heavy-atom-free

photosensitizers for photodynamic therapy. *Chemical Science*, **2020**, *11* (26), 6701-6708

(13) Hu, Z., Wang, J., Ma, X., Gao, J., Xu, C., Yang, K., Wang, Z., Zhang, J., Zhang, F. A critical review on semitransparent organic solar cells. *Nano Energy*, **2020**, *78*, 1-20

(14) Ahn, D., Stevens, L., Zhou, K., Page, Z. Rapid High-Resolution Visible Light 3D Printing. *ACS Central Science*, **2020**, *6* (9), 1555-1563

(15) Arias-Rotondo, D. M., McCusker, J. K. The photophysics of photoredox catalysis: A roadmap for catalyst design. *Chemical Society Reviews*, **2016**, *45* (21), 5803-5820

(16) Shaw, M. H., Twilton, J., MacMillan, D. W. C. Photoredox Catalysis in Organic Chemistry. *Journal of Organic Chemistry*, **2016**, *81* (16), 6898-6926

(17) Skubi, K., Blum, T. R., Yoon, T. P. Dual Catalysis Strategies in Photochemical Synthesis. *Chemical Reviews*, **2016**, *116* (17), 10035-10074

(18) Nguyen, V., Qi, S., Kim, S., Kwon, N., Gyoungmi, K., Yim, Y., Park, S., Yoon, J. An Emerging Molecular Design Approach to Heavy-Atom-Free Photosensitizers for Enhanced Photodynamic Therapy under Hypoxia. *J. Am. Chem. Soc*. **2019**, *141*, 16243-16248

(19) Cakmak, Y.; Kolemen, S.; Duman, S.; Dede, Y.; Dolen, Y.; Kilic, B.; Kostereli, Z.; Yildirim, L. T.; Dogan, A. L.; Guc, D.; Akkaya, E. U. Designing Excited States: Theory-Guided Access to Efficient Photosensitizers for Photodynamic Action. *Angew. Chem., Int. Ed*. **2011**, *50*, 11937−11941

(20) Zhao, J.; Chen, K.; Hou, Y.; Che, Y.; Liu, L.; Jia, D. Recent progress in heavy atom-free organic compounds showing unexpected intersystem crossing (ISC) ability. *Org. Biomol. Chem*. **2018**, *16*, 3692−3701.

(21) Mai, S.; Pollum, M.; Martinez-Fernandez, L.; Dunn, N.; Marquetand, P.; Corral, I.; Crespo-Hernandez, C. E.; Gonzalez, L. The origin of efficient triplet state population in sulfur-substituted nucleobases. *Nat. Commun*. **2016**, *7*, 13077.

(22) Behm, K., McIntosh, R. D. Application of Discrete First-Row Transition-Metal Complexes as Photosensitisers. *ChemPlusChem*, **2020**, *85* (12), 2611-2618

(23) Fan, W.; Huang, P.; Chen, X. Overcoming the Achilles' heel of photodynamic therapy. *Chem. Soc. Rev*. **2016**, *45*, 6488−6519.

(24) Li, X.; Yu, S.; Lee, D.; Kim, G.; Lee, B.; Cho, Y.; Zheng, B. Y.; Ke, M. R.; Huang, J. D.; Nam, K. T.; Chen, X.; Yoon, J. Facile Supramolecular Approach to Nucleic-Acid-Driven Activatable Nanotheranostics That Overcome Drawbacks of Photodynamic Therapy. *ACS Nano*. **2018**, *12*, 681−688.

(25) Jung, H. S.; Han, J.; Shi, H.; Koo, S.; Singh, H.; Kim, H. J.; Sessler, J. L.; Lee, J. Y.; Kim, J. H.; Kim, J. S. Overcoming the Limits of Hypoxia in Photodynamic

Therapy: A Carbonic Anhydrase IX-Targeted Approach. *J. Am. Chem. Soc*. **2017**, *139*, 7595−7602

(26) Patel, N. J., Chen, Y., Joshi, P., Pera, P., Baumann, H., Missert, J.R., Ohkubo, K., Fukuzumi, S., Nani, R.R., M. Schnermann, M. J., Chen, P., Zhu, J., Kadish, K. M., Pandey, R.K. Effect of Metalation on Porphyrin-Based Bifunctional Agents in Tumor Imaging and Photodynamic Therapy. *Bioconjugate Chem*., **2016**, *27*, 667–680

(27) Zhou, J., Stojanovic, L., Berezin, A., Battisti, T., Gill, A., Kariuki, B., Bonifazi, D., Crespo-Otero, R., Wasielewski, M. R., Wu, Y. Organic room-temperature phosphorescence from halogen-bonded organic frameworks: hidden electronic effects in rigidified chromophores. *Chemical Science*, **2021**, *12* (2), 767-773

(28) Stafford, A., Ahn, D., Raulerson, E. K., Chung, K., Sun, K., Cadena, D. M., Forrister, E. M., Yost, S. R., Roberts, S., Page, Z. Catalyst Halogenation Enables Rapid and Efficient Polymerizations with Visible to Far-Red Light. *Journal of the American Chemical Society*, **2020**, *142* (34), 14733-14742

(29) Sartor, S. M., Chrisman, C. H., Pearson, R. M., Miyake, G. M., Damrauer, N. H. Designing High-Triplet-Yield Phenothiazine Donor-Acceptor Complexes for Photoredox Catalysis. *Journal of Physical Chemistry A*, **2020**, *124* (5), 817-823

(30) Uddin, A., Allen, S., Rylski, A., O'Dea, C., Ly, J., Grusenmeyer, T., Roberts, S., Page, Z. Do The Twist: Efficient Heavy-Atom-Free Visible Light Polymerization Facilitated by Spin-Orbit Charge Transfer Inter-system Crossing. *Angewandte Chemie – International Edition*, **2023**, *62* (22), 1-8

(31) Palmer, J. R., Wells, K. A., Yarnell, J. E., Favale, J. M., Castellano, F. N. Visible-Light-Driven Triplet Sensitization of Polycyclic Aromatic Hydrocarbons Using Thionated Perinones. *Journal of Physical Chemistry Letters*, **2020**, *11* (13), 5092-5099

(32) Ortiz-Rodriguez, L. A., Joehn, S. J., Loredo, A., Wang, L., Xiao, H., Cresp-Hernandez, C. Electronic relaxation pathways in heavy-atom-free photosensitizers absorbing near-infrared radiation and exhibiting high yields of singlet oxygen generation. *Journal of the American Chemical Society*, **2021**, *143* (7), 2676-2681

(33) Pham, T. C., Heo, S., Nguyen, V., Lee, M., Yoon, J., Lee, S. Molecular Design toward Heavy-Atom-free Photosensitizers Based on the C= S Bond and their Dual Functions in Hypoxia Photodynamic Cancer Therapy and ClO-Detection. *ACS Applied Materials and Interfaces*, **2021**, *13* (12), 13949-13957

(34) Massey, A.; Xu, Y. Z.; Karran, P. Photoactivation of DNA thiobases as a potential novel therapeutic option. *Curr. Biol*. **2001**, *11*, 1142−1146.

(35) Pollum, M.; Jockusch, S.; Crespo-Hernandez, C. E. 2,4-Dithiothymine as a potent UVA chemotherapeutic agent. *J. Am. Chem. Soc*. **2014**, *136*, 17930−17933.

(36) Ashwood, B.; Pollum, M.; Crespo-Hernandez, C. E. Photochemical and Photodynamical Properties of Sulfur-Substituted Nucleic Acid Bases. *Photochem. Photobiol*. **2019**, *95*, 33−58.

(37) Hussain, M.; Zhao, J.; Yang, W.; Zhong, F.; Karatay, A.; Yaglioglu, H. G.; Yildiz, E. A.; Hayvali, M. Intersystem crossing and triplet excited state properties of thionated naphthalenediimide derivatives. *J. Lumin*. **2017**, *192*, 211−217.

(38) Tang, J., Wang, L., Loredo, A., Cole, C., Xiao, H. Single-atom replacement as a general approach towards visible-light/near-infrared heavy-atom-free photosensitizers for photodynamic therapy. *Chem. Sci*. **2020**, *11*, 6701

(39) Wright, A., Kariuki, B., Wu, Y. Triplet-Forming Thionated Donor-Acceptor Chromophores for Electrochemically Amphoteric Photosensitization. *Eur. J. Org. Chem*. **2021**, 4647–4652

(40) Allen, M. J.; Page, Z. A. Tracking Photocuring via ATR-FT-IR with Illumination through the ATR Element. *Spectrosc. Appl. Noteb*. **2020**, *35* (2), 78.

(41) Thorat, K. G.; Kamble, P.; Ray, A. K.; Sekar, N. Novel Pyrromethene Dyes with N-Ethyl Carbazole at the Meso Position: A Comprehensive Photophysical, Lasing, Photostability and TD-DFT Study. *Phys. Chem. Chem. Phys*. **2015**, *17* (26), 17221–17236.

Bibliography

Aguado, B. A.; Grim, J. C.; Rosales, A. M.; Watson-Capps, J. J.; Anseth, K. S. Engineering Precision Biomaterials for Personalized Medicine. *Sci. Transl. Med*. **2018**, *10*, 8645.

Camposeo, A.; Persano, L.; Farsari, M.; Pisignano, D. Additive Manufacturing: Applications and Directions in Photonics and Optoelectronics. *Adv. Opt. Mater*. **2019**, *7* (1), 1800419.

Wallin, T. J.; Pikul, J.; Shepherd, R. F. 3D Printing of Soft Robotic Systems. *Nat. Rev. Mater*. **2018**, *3* (6), 84−100.

Zhang, J.; Xiao, P. 3D Printing of Photopolymers. *Polym. Chem*. **2018**, *9* (13), 1530−1540.

Jung, K.; Corrigan, N.; Ciftci, M.; Xu, J.; Seo, S. E.; Hawker, C. J.; Boyer, C. Designing with Light: Advanced 2D, 3D, and 4D Materials. *Adv. Mater*. **2020**, *32*, 1903850.

Lim, K. S.; Galarraga, J. H.; Cui, X.; Lindberg, G. C. J.; Burdick, J. A.; Woodfield, T. B. F. Fundamentals and Applications of Photo-Cross-Linking in Bioprinting. *Chem. Rev*. **2020**. *120* (19), 10662-10694

Yu, C.; Schimelman, J.; Wang, P.; Miller, K. L.; Ma, X.; You, S.; Guan, J.; Sun, B.; Zhu, W.; Chen, S. Photopolymerizable Biomaterials and Light-Based 3D Printing Strategies for Biomedical Applications. *Chem. Rev*. **2020**. *120* (19) 10695-10743

Willson, C. G.; Dammel, R. R.; Reiser, A. Photoresist Materials: A Historical Perspective. In Advances in Resist Technology and Processing XIV; SPIE, **1997**; Vol. 3049, p 28.

Kozawa, T.; Santillan, J. J.; Itani, T. Relationship between Resolution Blur and Stochastic Defect of Chemically Amplified Resists Used for Extreme Ultraviolet Lithography. *J. Photopolym. Sci. Technol*. **2019**, *32* (1), 161−167.

MacDonald, S. A.; Ito, H.; Willson, C. G. Advances in the Design of Organic Resist Materials. *Microelectron. Eng*. **1983**, *1* (4), 269−293.

Ito, H.; Willson, C. G.; Frechet, J. M. J. New UV Resists with Negative or Positive Tone. In Digest of Technical Papers - Symposium on VLSI Technology; **1982**; pp 86−87.

Dumur, F. Recent Advances on Visible Light Metal-Based Photocatalysts for Polymerization under Low Light Intensity. *Catalysts* **2019**, *9*, 736.

Bagheri, A.; Jin, J. Photopolymerization in 3D Printing. *ACS Appl. Polym. Mater*. **2019**, *1* (4), 593−611.

Corrigan, N.; Yeow, J.; Judzewitsch, P.; Xu, J.; Boyer, C. Seeing the Light: Advancing Materials Chemistry through Photopolymerization. *Angew. Chem., Int. Ed*. **2019**, *58* (16), 5170−5189.

Strehmel, B.; Schmitz, C.; Cremanns, K.; Göttert, J. Photochemistry with Cyanines in the Near Infrared: A Step to Chemistry 4.0 Technologies. *Chem. - Eur. J*. **2019**, *25* (56), 12855− 12864.

Xiao, P.; Zhang, J.; Dumur, F.; Tehfe, M. A.; Morlet-Savary, F.; Graff, B.; Gigmes, D.; Fouassier, J. P.; Lalevee, J. Visible Light́ Sensitive Photoinitiating Systems: Recent Progress in Cationic and Radical Photopolymerization Reactions under Soft Conditions. *Prog. Polym. Sci*. **2015**, *41* (C), 32−66.

Chatani, S.; Kloxin, C. J.; Bowman, C. N. The Power of Light in Polymer Science: Photochemical Processes to Manipulate Polymer Formation, Structure, and Properties. *Polym. Chem*. **2014**, *5* (7), 2187−2201.

Shanmugam, S.; Xu, J.; Boyer, C. Light-Regulated Polymerization under Near-Infrared/Far-Red Irradiation Catalyzed by Bacteriochlorophyll A. *Angew. Chem*. **2016**, *128* (3), 1048−1052.

Corrigan, N.; Xu, J.; Boyer, C. A Photoinitiation System for Conventional and Controlled Radical Polymerization at Visible and NIR Wavelengths. *Macromolecules*. **2016**, *49* (9), 3274−3285.

Wu, Z.; Jung, K.; Boyer, C. Effective Utilization of NIR Wavelengths for Photo-Controlled Polymerization: Penetration Through Thick Barriers and Parallel Solar Syntheses. *Angew. Chem*. **2020**, *132* (5), 2029−2033.

Zhang, Z.; Corrigan, N.; Bagheri, A.; Jin, J.; Boyer, C. A Versatile 3D and 4D Printing System through Photocontrolled RAFT Polymerization. *Angew. Chem*. **2019**, *131* (50), 18122−18131.

Haas, M.; Radebner, J.; Eibel, A.; Gescheidt, G.; Stueger, H. Recent Advances in Germanium-Based Photoinitiator Chemistry. *Chem. - Eur. J*. **2018**, *24* (33), 8258−8267.

Schroeder, W. F.; Vallo, C. I. Effect of Different Photoinitiator Systems on Conversion Profiles of a Model Unfilled Light-Cured Resin. *Dent. Mater*. **2007**, *23* (10), 1313−1321.

Corrigan, N.; Shanmugam, S.; Xu, J.; Boyer, C. Photocatalysis in Organic and Polymer Synthesis. *Chem. Soc. Rev*. **2016**, *45* (22), 6165−6212.

Dadashi-Silab, S.; Doran, S.; Yagci, Y. Photoinduced Electron Transfer Reactions for Macromolecular Syntheses. *Chem. Rev*. **2016**, *116* (17), 10212−10275.

Strehmel, B.; Schmitz, C.; Brömme, T.; Halbhuber, A.; Oprych, D.; Gutmann, J. S. Advances of near Infrared Sensitized Radical and Cationic Photopolymerization:

From Graphic Industry to Traditional Coatings. *J. Photopolym. Sci. Technol*. **2016**, *29* (1), 111−121.

Bonardi, A. H.; Dumur, F.; Grant, T. M.; Noirbent, G.; Gigmes, D.; Lessard, B. H.; Fouassier, J. P.; Lalevee, J. High Performance´ Near-Infrared (NIR) Photoinitiating Systems Operating under Low Light Intensity and in the Presence of Oxygen. *Macromolecules*. **2018**, *51* (4), 1314−1324.

Bonardi, A.; Bonardi, F.; Noirbent, G.; Dumur, F.; Dietlin, C.; Gigmes, D.; Fouassier, J. P.; Lalevee, J. Different NIR Dye Scaffolds´ for Polymerization Reactions under NIR Light. *Polym. Chem*. **2019**, *10* (47), 6505−6514.

Shiraishi, A.; Kimura, H.; Oprych, D.; Schmitz, C.; Strehmel, B. Comparison between NIR and UV-Sensitized Radical and Cationic Reactivity of Iodonium Salts Comprising Anions with Different Coordination Behavior. *J. Photopolym. Sci. Technol*. **2017**, *30* (6), 633−638.

Schmitz, C.; Halbhuber, A.; Keil, D.; Strehmel, B. NIR Sensitized Photoinitiated Radical Polymerization and Proton Generation with Cyanines and LED Arrays. *Prog. Org. Coat*. **2016**, *100*, 32−46.

Schmitz, C.; Pang, Y.; Gülz, A.; Glaser, M.; Horst, J.; Ja¨ger, M.;¨ Strehmel, B. New High-Power LEDs Open Photochemistry for NearInfrared- Sensitized Radical and Cationic Photopolymerization. *Angew. Chem*. **2019**, *131* (13), 4445−4450.

Lu, H.; MacK, J.; Yang, Y.; Shen, Z. Structural Modification Strategies for the Rational Design of Red/NIR Region BODIPYs. *Chem. Soc. Rev*. **2014**, *43* (13), 4778−4823.

Loudet, A.; Burgess, K. BODIPY Dyes and Their Derivatives: Syntheses and Spectroscopic Properties. *Chem. Rev*. **2007**, *107* (11), 4891−4932.

L. Thompson, B.; Heiden, Z. Redox Chemistry of BODIPY Dyes. In BODIPY Dyes - A Privilege Molecular Scaffold with Tunable Properties; **2019**.

Bonardi, A.; Bonardi, F.; Noirbent, G.; Dumur, F.; Dietlin, C.; Gigmes, D.; Fouassier, J. P.; Lalevee, J. Different NIR Dye Scaffolds´ for Polymerization Reactions under NIR Light. *Polym. Chem*. **2019**, *10* (47), 6505−6514.

Telitel, S.; Blanchard, N.; Schweizer, S.; Morlet-Savary, F.; Graff, B.; Fouassier, J. P.; Lalevee, J. BODIPY Derivatives and Boranil´ as New Photoinitiating Systems of Cationic Polymerization Exhibiting a Tunable Absorption in the 400−600 Nm Spectral Range. *Polymer*. **2013**, *54* (8), 2071−2076.

Telitel, S.; Lalevee, J.; Blanchard, N.; Kavalli, T.; Tehfe, M. A.;´ Schweizer, S.; Morlet-Savary, F.; Graff, B.; Fouassier, J. P. Photopolymerization of Cationic Monomers and Acrylate/Divinylether Blends under Visible Light Using Pyrromethene Dyes. *Macromolecules*. **2012**, *45* (17), 6864−6868.

Costa, P.; Sandrin, D.; Scaiano, J. C. Real-Time Fluorescence Imaging of a Heterogeneously Catalysed Suzuki−Miyaura Reaction. *Nat. Catal*. **2020**, *3*, 427−437.

Qiu, H.; Gao, Y.; Boott, C. E.; Gould, O. E. C.; Harniman, R. L.; Miles, M. J.; Webb, S. E. D.; Winnik, M. A.; Manners, I. Uniform Patchy and Hollow Rectangular Platelet Micelles from Crystallizable Polymer Blends. *Science* (Washington, DC, U. S.) **2016**, *352* (6286), 697−701.

Haldar, U.; Lee, H. Il. BODIPY-Derived Polymeric Chemosensor Appended with Thiosemicarbazone Units for the Simultaneous Detection and Separation of Hg(II) Ions in Pure Aqueous Media. *ACS Appl. Mater. Interfaces*. **2019**, *11* (14), 13685−13693.

Kamkaew, A.; Lim, S. H.; Lee, H. B.; Kiew, L. V.; Chung, L. Y.; Burgess, K. BODIPY Dyes in Photodynamic Therapy. *Chem. Soc. Rev*. **2013**, *42* (1), 77−88.

Miao, X.; Hu, W.; He, T.; Tao, H.; Wang, Q.; Chen, R.; Jin, L.; Zhao, H.; Lu, X.; Fan, Q.; Huang, W. Deciphering the Intersystem Crossing in Near-Infrared BODIPY Photosensitizers for Highly Efficient Photodynamic Therapy. *Chem. Sci*. **2019**, *10* (10), 3096− 3102.

Zhao, J.; Xu, K.; Yang, W.; Wang, Z.; Zhong, F. The Triplet Excited State of Bodipy: Formation, Modulation and Application. *Chem. Soc. Rev*. **2015**, *44* (24), 8904−8939.

Koziar, J. C.; Cowan, D. O. Photochemical Heavy-Atom Effects. *Acc. Chem. Res*. **1978**, *11*, 334−341.

Allen, M. J.; Page, Z. A. Tracking Photocuring via ATR-FT-IR with Illumination through the ATR Element. Spectrosc. *Appl. Noteb*. **2020**, *35* (2), 78.

Boens, N.; Verbelen, B.; Ortiz, M. J.; Jiao, L.; Dehaen, W. Synthesis of BODIPY Dyes through Postfunctionalization of the Boron Dipyrromethene Core. *Coord. Chem. Rev*. **2019**, *399*, 213024.

Wang, X. F.; Yu, S. S.; Wang, C.; Xue, D.; Xiao, J. BODIPY Catalyzed Amide Synthesis Promoted by BHT and Air under Visible Light. *Org. Biomol. Chem*. **2016**, *14* (29), 7028−7037.

Lovell, L. G.; Berchtold, K. A.; Elliott, J. E.; Lu, H.; Bowman, C. N. Understanding the Kinetics and Network Formation of Dimethacrylate Dental Resins. *Polym. Adv. Technol*. **2001**, *12* (6), 335−345.

Thermal Transitions of Homopolymers: Glass Transition & Melting Point https://www.sigmaaldrich.com/technical-documents/ articles/materials-science/polymer-science/thermal-transitions-ofhomopolymers.html.

Würth, C.; Grabolle, M.; Pauli, J.; Spieles, M.; Resch-Genger, U. Relative and Absolute Determination of Fluorescence Quantum Yields of Transparent Samples. *Nat. Protoc*. **2013**, *8* (8), 1535−1550.

Polykarpov, A. Y.; Neckers, D. C. Tetramethylammonium Phenyltrialkylborates in the Photoinduced Electron Transfer Reaction with Benzophenone. Generation of Alkyl Radicals and Their Addition to Activated Alkenes. *Tetrahedron Lett*. **1995**, *36* (31), 5483−5486.

Romanczyk, P. P.; Kurek, S. S. Reliable Reduction Potentials of Diaryliodonium Cations and Aryl Radicals in Acetonitrile from HighLevel Ab Initio Computations. *Electrochim. Acta*. **2020**, *351*, 136404.

Romanczyk, P. P.; Kurek, S. S. The Reduction Potential of Diphenyliodonium Polymerisation Photoinitiator Is Not − 0.2 V vs. SCE. A Computational Study. *Electrochim. Acta*. **2017**, *255*, 482−485.

Marenich, A. V.; Cramer, C. J.; Truhlar, D. G. Universal Solvation Model Based on Solute Electron Density and on a Continuum Model of the Solvent Defined by the Bulk Dielectric Constant and Atomic Surface Tensions. *J. Phys. Chem. B*. **2009**, *113* (18), 6378–6396.

Sabatini, R. P.; McCormick, T. M.; Lazarides, T.; Wilson, K. C.; Eisenberg, R.; McCamant, D. W. Intersystem Crossing in Halogenated Bodipy Chromophores Used for Solar Hydrogen Production. *J. Phys. Chem. Lett*. **2011**, *2* (3), 223−227.

Rachford, A. A.; Ziessel, R.; Bura, T.; Retailleau, P.; Castellano, F. N. Boron Dipyrromethene (Bodipy) Phosphorescence Revealed in [Ir(Ppy) 2(Bpy-C - C-Bodipy)]+. *Inorg. Chem*. **2010**, *49* (8), 3730− 3736.

Whited, M. T.; Djurovich, P. I.; Roberts, S. T.; Durrell, A. C.; Schlenker, C. W.; Bradforth, S. E.; Thompson, M. E. Singlet and Triplet Excitation Management in a Bichromophoric Near-InfraredPhosphorescent BODIPY-Benzoporphyrin Platinum Complex. *J. Am. Chem. Soc*. **2011**, *133* (1), 88−96.

Lee, Y.; Malamakal, R. M.; Chenoweth, D. M.; Anna, J. M. Halogen Bonding Facilitates Intersystem Crossing in Iodo-BODIPY Chromophores. *J. Phys. Chem. Lett*. **2020**, *11* (3), 877−884.

Wallin, T. J.; Pikul, J.; Shepherd, R. F. 3D Printing of Soft Robotic Systems. *Nat. Rev. Mater*. **2018**, *3* (6), 84−100.

Le, A. K.; Bender, J. A.; Arias, D. H.; Cotton, D. E.; Johnson, J. C.; Roberts, S. T. Singlet Fission Involves an Interplay between Energetic Driving Force and Electronic Coupling in Perylenediimide Films. *J. Am. Chem. Soc*. **2018**, *140* (2), 814–826.

Azzaro, M. S.; Le, A. K.; Wang, H.; Roberts, S. T. Ligand-Enhanced Energy Transport in Nanocrystal Solids Viewed with Two-Dimensional Electronic Spectroscopy. *J. Phys. Chem. Lett*. **2019**, *10* (18), 5602–5608.

Thorat, K. G.; Kamble, P.; Ray, A. K.; Sekar, N. Novel Pyrromethene Dyes with N-Ethyl Carbazole at the Meso Position: A Comprehensive Photophysical, Lasing, Photostability and TD-DFT Study. *Phys. Chem. Chem. Phys*. **2015**, *17* (26), 17221–17236.

Wang, X. F.; Yu, S. S.; Wang, C.; Xue, D.; Xiao, J. BODIPY Catalyzed Amide Synthesis Promoted by BHT and Air under Visible Light. *Org. Biomol. Chem*. **2016**, *14* (29), 7028–7037.

Lu, H.; MacK, J.; Yang, Y.; Shen, Z. Structural Modification Strategies for the Rational Design of Red/NIR Region BODIPYs. *Chem. Soc. Rev*. **2014**, *43* (13), 4778–4823.

Kocaarslan, A.; Tabanli, S.; Eryurek, G.; Yagci, Y. Near-Infrared Free-Radical and Free-Radical-Promoted Cationic Photopolymerizations by In-Source Lighting Using Upconverting Glass. *Angew. Chemie - Int. Ed.* **2017**, *56* (46), 14507–14510.

Fagnani, D. E.; Tami, J. L.; Copley, G.; Clemons, M. N.; Getzler, Y. D. Y. L.; McNeil, A. J. 100th Anniversary of Macromolecular Science Viewpoint: Redefining Sustainable Polymers. *ACS Macro Lett.* **2021**, *10* (1), 41–53.

Lee, Y.; Boyer, C.; Kwon, M. S. Visible-Light-Driven Polymerization towards the Green Synthesis of Plastics. *Nat. Rev. Mater.* **2021**.

Dumur, F. Recent Advances on Photoinitiating Systems Designed for Solar Photocrosslinking Polymerization Reactions. *Eur. Polym. J.* **2023**, *189*, 111988.

Wallin, T. J.; Pikul, J.; Shepherd, R. F. 3D Printing of Soft Robotic Systems. *Nat. Rev. Mater.* **2018**, *3* (6), 84–100.

Ligon, S. C.; Liska, R.; Stampfl, J.; Gurr, M.; Mülhaupt, R. Polymers for 3D Printing and Customized Additive Manufacturing. *Chem. Rev.* **2017**, *117* (15), 10212–10290.

Bagheri, A.; Jin, J. Photopolymerization in 3D Printing. *ACS Appl. Polym. Mater.* **2019**, *1* (4), 593–611.

Truby, R. L.; Lewis, J. A. Printing Soft Matter in Three Dimensions. *Nature* **2016**, *540* (7633), 371–378.

Murphy, C. A.; Lim, K. S.; Woodfield, T. B. F. Next Evolution in Organ-Scale Biofabrication: Bioresin Design for Rapid High-Resolution Vat Polymerization. *Adv. Mater.* **2022**, *34* (20), 2107759.

Zou, X.; Zhu, J.; Zhu, Y.; Yagci, Y.; Liu, R. Photopolymerization of Macroscale Black 3D Objects Using Near-Infrared Photochemistry. *ACS Appl. Mater. Interfaces* **2020**, *12* (52), 58287–58294.

Lu, P.; Ahn, D.; Yunis, R.; Delafresnaye, L.; Corrigan, N.; Boyer, C.; Barner-Kowollik, C.; Page, Z. A. Wavelength-Selective Light-Matter Interactions in Polymer Science. *Matter* **2021**, *4* (7), 2172–2229.

Atchison, J.; Kamila, S.; Nesbitt, H.; Logan, K. A.; Nicholas, D. M.; Fowley, C.; Davis, J.; Callan, B.; McHale, A. P.; Callan, J. F. Iodinated Cyanine Dyes: A New Class of Sensitisers for Use in NIR Activated Photodynamic Therapy (PDT). *Chem. Commun.* **2017**, *53* (12), 2009–2012.

Borjigin, T.; Schmitt, M.; Giacoletto, N.; Rico, A.; Bidotti, H.; Nechab, M.; Zhang, Y.; Graff, B.; Morlet-Savary, F.; Xiao, P.; Dumur, F.; Lalevée, J. The Blue-LED-Sensitive Naphthoquinone-Imidazolyl Derivatives as Type II Photoinitiators of Free Radical Photopolymerization. *Adv. Mater. Interfaces* **2023**, *10*, 2202352.

Pang, Y.; Jiao, H.; Zou, Y.; Strehmel, B. The NIR-Sensitized Cationic Photopolymerization of Oxetanes in Combination with Epoxide and Acrylate Monomers. *Polym. Chem.* **2021**, *12* (40), 5752–5759.

Wang, Q.; Popov, S.; Strehmel, V.; Gutmann, J. S.; Strehmel, B. NIR-Sensitized Hybrid Radical and Cationic Photopolymerization of Several Cyanines in Combination with Diaryliodonium Bis(Trifluoromethyl)Sulfonyl Imide. *Polym. Chem.* **2022**, *14* (2), 116–125.

Topa-Skwarczyńska, M.; Galek, M.; Jankowska, M.; Morlet-Savary, F.; Graff, B.; Lalevée, J.; Popielarz, R.; Ortyl, J. Development of the First Panchromatic BODIPY-Based One-Component Iodonium Salts for Initiating the Photopolymerization Processes. *Polym. Chem.* **2021**, *12* (47), 6873–6893.

Ma, Q.; Liu, S.; Le Dot, M.; Mokbel, H.; Zhang, Y.; Graff, B.; Lalevée, J. Imidazole Based Dual Photo/Thermal Initiators for Highly Efficient Radical Polymerization under Air with a Metal-Free Approach. *Polym. Chem.* **2021**, *12* (44), 6386–6391.

Dumur, F. The Future of Visible Light Photoinitiators of Polymerization for Photocrosslinking Applications. *Eur. Polym. J.* **2023**, *187* (December 2022).

Trotta, J. T.; Fors, B. P. Organic Catalysts for Photocontrolled Polymerizations. *Synlett* **2016**, *27* (5), 702–713.

Ahn, D.; Stevens, L. M.; Zhou, K.; Page, Z. A. Rapid High-Resolution Visible Light 3D Printing. *ACS Cent. Sci.* **2020**, *6* (9), 1555–1563.

Ahn, D.; Stevens, L. M.; Zhou, K.; Page, Z. A. Additives for Ambient 3D Printing with Visible Light. *Adv. Mater.* **2021**, *33* (44), 2104906.

Stevens, L. M.; Tagnon, C.; Page, Z. A. "Invisible" Digital Light Processing 3D Printing with Near Infrared Light. *ACS Appl. Mater. Interfaces* **2022**, *14* (20), 22912–22920.

Corrigan, N.; Yeow, J.; Judzewitsch, P.; Xu, J.; Boyer, C. Seeing the Light: Advancing Materials Chemistry through Photopolymerization. *Angew. Chemie - Int. Ed.* **2019**, *58* (16), 5170–5189.

Xiao, P.; Zhang, J.; Dumur, F.; Tehfe, M. A.; Morlet-Savary, F.; Graff, B.; Gigmes, D.; Fouassier, J. P.; Lalevée, J. Visible Light Sensitive Photoinitiating Systems:

Recent Progress in Cationic and Radical Photopolymerization Reactions under Soft Conditions. *Prog. Polym. Sci.* **2015**, *41* (C), 32–66.

Bonardi, A. H.; Dumur, F.; Grant, T. M.; Noirbent, G.; Gigmes, D.; Lessard, B. H.; Fouassier, J. P.; Lalevée, J. High Performance Near-Infrared (NIR) Photoinitiating Systems Operating under Low Light Intensity and in the Presence of Oxygen. *Macromolecules* **2018**, *51* (4), 1314–1324.

Bonardi, A.; Bonardi, F.; Noirbent, G.; Dumur, F.; Dietlin, C.; Gigmes, D.; Fouassier, J. P.; Lalevée, J. Different NIR Dye Scaffolds for Polymerization Reactions under NIR Light. *Polym. Chem.* **2019**, *10* (47), 6505–6514.

Zhou, J.; Pitzer, L.; Ley, C.; Rölle, T.; Allonas, X. A Highly Sensitive Photoinitiating System Based on Pre-Associated Ion-Pairs for NIR Radical Photopolymerization of Optically Clear Materials. *Polym. Chem.* **2022**, *13* (47), 6475–6483.

Stafford, A.; Ahn, D.; Raulerson, E. K.; Chung, K. Y.; Sun, K.; Cadena, D. M.; Forrister, E. M.; Yost, S. R.; Roberts, S. T.; Page, Z. A. Catalyst Halogenation Enables Rapid and Efficient Polymerizations with Visible to Far-Red Light. *J. Am. Chem. Soc.* **2020**, *142* (34), 14733–14742.

Xu, Y., Zhao, M., Zou, L., Wu, L., Xie, M., Yang, T., Liu, S., Huang, W., Zhao, Q. Highly Stable and Multifunctional Aza-BODIPY-Based Phototherapeutic Agent for Anticancer Treatment. *ACS Appl. Mater. Interfaces* **2018**, *10* (51), 44234-44335.

Obloza, M., Lapok, L., Pedzinski, T., Stadnicka, K., Nowakowska, M. Synthesis, Photophysics and Redox Properties of Aza-BODIPY Dyes with Electron-Donating Groups. *ChemPhysChem* **2019**, *20* (19), 2482-2497

Sheng, W.; Wu, Y.; Yu, C.; Bobadova-Parvanova, P.; Hao, E.; Jiao, L. Synthesis, Crystal Structure, and the Deep Near-Infrared Absorption/Emission of Bright AzaBODIPY-Based Organic Fluorophores. *Org. Lett*. **2018**, *20* (9), 2620−2623.

Adarsh, N.; Avirah, R. R.; Ramaiah, D. Tuning Photosensitized Singlet Oxygen Generation Efficiency of Novel Aza-BODIPY Dyes. *Org. Lett*. **2010**, *12* (24), 5720−5723.

Zhao, J.; Xu, K.; Yang, W.; Wang, Z.; Zhong, F. The Triplet Excited State of Bodipy: Formation, Modulation and Application. *Chem. Soc. Rev.* **2015**, *44* (24), 8904–8939.

Lu, P.; Chung, K. Y.; Stafford, A.; Kiker, M.; Kafle, K.; Page, Z. A. Boron Dipyrromethene (BODIPY) in Polymer Chemistry. *Polym. Chem.* **2021**, *12* (3), 327–348.

Lakshmi, V.; Rajeswara Rao, M.; Ravikanth, M. Halogenated Boron-Dipyrromethenes: Synthesis, Properties and Applications. *Org. Biomol. Chem.* **2015**, *13* (9), 2501–2517.

Allen, M. J.; Page, Z. A. Tracking Photocuring via ATR-FT-IR with Illumination through the ATR Element. Spectrosc. Appl. Noteb. **2020**, *35* (2), 78

Le, A. K.; Bender, J. A.; Arias, D. H.; Cotton, D. E.; Johnson, J. C.; Roberts, S. T. Singlet Fission Involves an Interplay between Energetic Driving Force and Electronic Coupling in Perylenediimide Films. *J. Am. Chem. Soc*. **2018**, *140* (2), 814–826.

Azzaro, M. S.; Le, A. K.; Wang, H.; Roberts, S. T. Ligand-Enhanced Energy Transport in Nanocrystal Solids Viewed with Two-Dimensional Electronic Spectroscopy. *J. Phys. Chem. Lett*. **2019**, *10* (18), 5602–5608.

Thorat, K. G.; Kamble, P.; Ray, A. K.; Sekar, N. Novel Pyrromethene Dyes with N-Ethyl Carbazole at the Meso Position: A Comprehensive Photophysical, Lasing, Photostability and TD-DFT Study. *Phys. Chem. Chem. Phys*. **2015**, *17* (26), 17221–17236.

Shaw, M., Twilton, J., MacMillan, D. Photoredox Catalysis in Organic Chemistry. *J. Org. Chem*. **2016**, *81*, 6898

Hansen, M., Velema, W., Lerch, M., Szymanski, W., Feringa, B. Wavelength-Selective Cleavage of Photoprotecting Groups: Strategies and Applications in Dynamic Systems**.** *Chem. Soc. Rev*., **2015**, *44*, 3358

Zivic, N., Kuroishi, P., Dumur, F., Gigmes, D., Dove, A., Sardon, H. Recent Advances and Challenges in the Design of Organic Photoacid and Photobase Generators for Polymerizations. *Angew. Chem. Int. Ed*. **2019**, *58*, 10410

Trotta, J., Fors, B. Organic Catalysts for Photocontrolled Polymerizations. *Synlett*. **2016**, *27*, 702

Ma. Y., Kottisch, V., McLoughlin, E., Rouse, Z., Supej, M., Baker, S., Fors, B. Photoswitching Cationic and Radical Polymerizations: Spatiotemporal Control of Thermoset Properties. *J. Am. Chem. Soc.* **2021**, *143*, 50, 21200

Doerr, A., Burroughs, J., Gitter, S., Yang, X., Boydston, A., Long, B. Advances in Polymerizations Modulated by External Stimuli**.** *ACS Catal.* **2020**, *10* (24), 14457

Zhang, X., Cox, L., Wen, Z., Xi, W., Ding, Y., Bowman, C. Implementation of Two Distinct Wavelengths to Induce Multistage Polymerization in Shape Memory Materials and Nanoimprint Lithography. *Polymer*. **2018**, *156*, 162

Bao, Y. Recent Trends in Advanced Photoinitiators for Vat Photopolymerization 3D Printing. *Macromol. Rapid Commun*. **2022**, *43* (14), 2200202

Sandmeier, M., Paunović, N., Conti, R., Hofmann, L., Wang, J., Luo, Z., Masania, K., Wu, N., Kleger, N., Coulter, F., Studart, A., Grützmacher, H., Leroux, J., Bao, Y. Solvent-Free Three-Dimensional Printing of Biodegradable Elastomers Using Liquid Macrophotoinitiators. *Macromolecules* **2021**, *54* (17), 7830

Estabrook, D., Sletten, E. Printing Precise Materials with Visible Light. *ACS Cent. Sci.* **2020**, *6* (9), 1482

Ma, Q., Liu, S., Le Dot, M., Mokbel, H., Zhang, Y., Graff, B., Lalevée, J. Imidazole Based Dual Photo/Thermal Initiators for Highly Efficient Radical Polymerization Under Air With a Metal-Free Approach. *Polym. Chem*., **2021**, *12*, 6386

Camposeo, A.; Persano, L.; Farsari, M.; Pisignano, D. Additive Manufacturing: Applications and Directions in Photonics and Optoelectronics. *Adv. Opt. Mater*. **2019**, *7* (1), 1800419

Jung, K.; Corrigan, N.; Ciftci, M.; Xu, J.; Seo, S. E.; Hawker, C. J.; Boyer, C. Designing with Light: Advanced 2D, 3D, and 4D Materials. *Adv. Mater*. **2020**, *32* (18), 1903850

Ahn, D., Stevens, L., Zhou, K., Page, Z. Rapid High-Resolution Visible Light 3D Printing. *ACS Cent. Sci.* **2020**, *6* (9), 1555

Stafford, A., Ahn, D., Raulerson, E., Chung, K., Sun, K., Cadena, D., Forrister, E., Yost, S., Roberts, S., Page, Z. Catalyst Halogenation Enables Rapid and Efficient Polymerizations with Visible to Far-Red Light. *J. Am. Chem. Soc.* **2020**, *142* (34), 14733

Lu, P., Chung, K., Stafford, A., Kiker, M., Kafle, K., Page, Z. Boron Dipyrromethene (BODIPY) in Polymer Chemistry. *Polym. Chem*., **2021**, *12*, 327

Wang, J., Li, J., Chen, N., Wu, Y., Hao, E., Wei, Y., Mu, X., Jiao, L. Synthesis, Structure and Properties of Thiophene-Fused BODIPYs and AzaBODIPYs as Near-Infrared Agents. *New J. Chem*. **2016**, *40*, 5966

Awuah, S. G., Das, S. K., D'Souza, F., You, Y. Thieno–Pyrrole-Fused BODIPY Intermediate as a Platform to Multifunctional NIR Agents**.** *Chem. Asian J*. **2013**,*8*, 3123

Awuah, S. G., Polreis, J., Biradar, V., You, Y. Singlet Oxygen Generation by Novel NIR BODIPY Dyes. *Org. Lett.* **2011**, *13* (15), 3884

Lee, K., Corrigan, N., Boyer, C. Rapid High-Resolution 3D Printing and Surface Functionalization via Type I Photoinitiated RAFT Polymerization**.** *Angew. Chem. Int. Ed*. **2021**, *60* (16), 8839

Dadashi-Silab, S., Doran, S., Yagci, Y. Photoinduced Electron Transfer Reactions for Macromolecular Syntheses. *Chem. Rev*. **2016**, *116* (17), 10212

Corrigan, N., Shanmugam, S., Xu, J., Boyer, C. Photocatalysis in Organic and Polymer Synthesis. *Chem. Soc. Rev*., **2016**, *45* (22), 6165

Pang, Y., Fan, S., Wang, Q., Oprych, D., Feilen, A., Reiner, K., Keil, D., Slominksy, Y., Popov, S., Zou, Y., Strehmel, B. NIR-Sensitized Activated Photoreaction between

Cyanines and Oxime Esters: Free-Radical Photopolymerization. *Ange. Chem. .Int. Ed*. **2020**, *59*, 11440

Strehmel, B., Schmitz, C., Kütahya, C., Pang, Y., Drewitz, A., Mustroph, H. Photophysics and Photochemistry of NIR Absorbers Derived From Cyanines: Key to New Technologies Based on Chemistry 4.0. *Beilstein J. Org. Chem*. **2020**, *16*, 415

Breloy, L., Brezová, V., Barbieriková, Z., Ito, Y., Akimoto, J., Chiappone, A., Abbad-Andaloussi, S., Malval, J., Versace, D. Methacrylated Quinizarin Derivatives for Visible-Light Mediated Photopolymerization: Promising Applications in 3D-Printing Biosourced Materials under LED@405 nm. *ACS Appl. Polym. Mater*. **2022**, *4* (1), 210

Bonardi, A., Bondardi, F., Noirbent, G., Dumur, F., Dietlin, C., Gigmes, D., Fouassier, J., Lalevée, J. Different NIR Dye Scaffolds for Polymerization Reactions Under NIR Light. *Polym. Chem*. **2019**, *10*, 6505

Allen, M. J.; Page, Z. A. Tracking Photocuring via ATR-FT-IR with Illumination through the ATR Element. *Spectrosc. Appl. Noteb*. **2020**, *35* (2), 78.

Le, A. K.; Bender, J. A.; Arias, D. H.; Cotton, D. E.; Johnson, J. C.; Roberts, S. T. Singlet Fission Involves an Interplay between Energetic Driving Force and Electronic Coupling in Perylenediimide Films. *J. Am. Chem. Soc*. **2018**, *140* (2), 814–826.

Azzaro, M. S.; Le, A. K.; Wang, H.; Roberts, S. T. Ligand-Enhanced Energy Transport in Nanocrystal Solids Viewed with Two-Dimensional Electronic Spectroscopy. *J. Phys. Chem. Lett*. **2019**, *10* (18), 5602–5608.

Thorat, K. G.; Kamble, P.; Ray, A. K.; Sekar, N. Novel Pyrromethene Dyes with N-Ethyl Carbazole at the Meso Position: A Comprehensive Photophysical, Lasing, Photostability and TD-DFT Study. *Phys. Chem. Chem. Phys*. **2015**, *17* (26), 17221–17236.

Romero, N., Nicewicz, D. A. Organic Photoredox Catalysis *Chemical Reviews*, **2016**, *116* (17), 10075-10166

Sideri, I. K., Voutyritsa, E., Kokotos, C. G. Photoorganocatalysis, Small Organic Molecules and Light in the Service of Organic Synthesis: The Awakening of a Sleeping Giant. *Organic and Biomolecular Chemistry*, **2018**, *16* (25), 4596-4614

Rawat, D., Kumar, R., Subbarayappa, A. Visible-Light Induced Phosphonation of Quinoxalines and Quinoxalin-2(1H)-ones Under Aerobic Metal-Free Conditions. *Green Chemistry*, **2020**, *22* (18), 6170-6175

Xuan, J., He, X., Xiao, W. Visible Light-Promoted Ring-Opening Functionalization of Three-Membered Carbo- And Heterocycles. *Chemical Society Reviews*, **2020**, *49* (9), 2546-2556

Reed, N. L., Yoon, T. P. Oxidase Reactions in Photoredox Catalysis. *Chemical Society Reviews*, **2021**, *50* (5), 2954-2967

Prier, C. K., Rankic, D. A., MacMillan, D. W. C. Visible Light Photoredox Catalysis with Transition Metal Complexes: Applications in Organic Synthesis. *Chemical Reviews*, **2013**, *113* (7), 5322-5363

Singh-Rachford, T. N., Castellano, F. N. Photon Upconversion Based on Sensitized Triplet-Triplet Annihilation. *Coordination Chemistry Reviews*, **2010**, *254* (21-22), 2560-2573

Dias, F. B., Santos, J., Graves, D. R., Data, P., Nobuyasu, R. S., Fox, M. A., Batsanov, A. S., Palmeira, T., Berberan-Santos, M. N., Bryce, M. R., Monkman, A. P. Transition metal-involved photon upconversion. *Advanced Science*, **2016**, *3* (12) 1-25

Huang, L., Kakadiaris, E., Vaneckova, T., Huang, K., Vaculovicova, M., Han, G. Designing next generation of photon upconversion: Recent advances in organic triplet-triplet annihilation upconversion nanoparticles. *Biomaterials*, **2019**, *201*, 77-86

Zhao, J., Wanhua, W., Sun, J., Guo, S. Triplet photosensitizers: From molecular design to applications *Chemical Society Reviews*, **2013**, *42* (12), 5323-5351

Nguyen, V., Yan, Y., Zhao, J., Yoon, J. Heavy-Atom-Free Photosensitizers: From Molecular Design to Applications in the Photodynamic Therapy of Cancer. *Accounts of Chemical Research*, **2021**, *54* (1), 207-220

Tang, J., Wang, L., Loredo, A., Cole, C., Xiao, H. Single-atom replacement as a general approach towards visible-light/near-infrared heavy-atom-free photosensitizers for photodynamic therapy. *Chemical Science*, **2020**, *11* (26), 6701-6708

Hu, Z., Wang, J., Ma, X., Gao, J., Xu, C., Yang, K., Wang, Z., Zhang, J., Zhang, F. A critical review on semitransparent organic solar cells. *Nano Energy*, **2020**, *78*, 1-20

Ahn, D., Stevens, L., Zhou, K., Page, Z. Rapid High-Resolution Visible Light 3D Printing. *ACS Central Science*, **2020**, *6* (9), 1555-1563

Arias-Rotondo, D. M., McCusker, J. K. The photophysics of photoredox catalysis: A roadmap for catalyst design. *Chemical Society Reviews*, **2016**, *45* (21), 5803-5820

Shaw, M. H., Twilton, J., MacMillan, D. W. C. Photoredox Catalysis in Organic Chemistry. *Journal of Organic Chemistry*, **2016**, *81* (16), 6898-6926

Skubi, K., Blum, T. R., Yoon, T. P. Dual Catalysis Strategies in Photochemical Synthesis. *Chemical Reviews*, **2016**, *116* (17), 10035-10074

Nguyen, V., Qi, S., Kim, S., Kwon, N., Gyoungmi, K., Yim, Y., Park, S., Yoon, J. An Emerging Molecular Design Approach to Heavy-Atom-Free Photosensitizers for

Enhanced Photodynamic Therapy under Hypoxia. *J. Am. Chem. Soc*. **2019**, *141*, 16243-16248

Cakmak, Y.; Kolemen, S.; Duman, S.; Dede, Y.; Dolen, Y.; Kilic, B.; Kostereli, Z.; Yildirim, L. T.; Dogan, A. L.; Guc, D.; Akkaya, E. U. Designing Excited States: Theory-Guided Access to Efficient Photosensitizers for Photodynamic Action. *Angew. Chem., Int. Ed*. **2011**, *50*, 11937−11941

Zhao, J.; Chen, K.; Hou, Y.; Che, Y.; Liu, L.; Jia, D. Recent progress in heavy atom-free organic compounds showing unexpected intersystem crossing (ISC) ability. *Org. Biomol. Chem*. **2018**, *16*, 3692−3701.

Mai, S.; Pollum, M.; Martinez-Fernandez, L.; Dunn, N.; Marquetand, P.; Corral, I.; Crespo-Hernandez, C. E.; Gonzalez, L. The origin of efficient triplet state population in sulfur-substituted nucleobases. *Nat. Commun*. **2016**, *7*, 13077.

Behm, K., McIntosh, R. D. Application of Discrete First-Row Transition-Metal Complexes as Photosensitisers. *ChemPlusChem*, **2020**, *85* (12), 2611-2618

Fan, W.; Huang, P.; Chen, X. Overcoming the Achilles' heel of photodynamic therapy. *Chem. Soc. Rev*. **2016**, *45*, 6488−6519.

Li, X.; Yu, S.; Lee, D.; Kim, G.; Lee, B.; Cho, Y.; Zheng, B. Y.; Ke, M. R.; Huang, J. D.; Nam, K. T.; Chen, X.; Yoon, J. Facile Supramolecular Approach to Nucleic-Acid-Driven Activatable Nanotheranostics That Overcome Drawbacks of Photodynamic Therapy. *ACS Nano*. **2018**, *12*, 681−688.

Jung, H. S.; Han, J.; Shi, H.; Koo, S.; Singh, H.; Kim, H. J.; Sessler, J. L.; Lee, J. Y.; Kim, J. H.; Kim, J. S. Overcoming the Limits of Hypoxia in Photodynamic Therapy: A Carbonic Anhydrase IX-Targeted Approach. *J. Am. Chem. Soc*. **2017**, *139*, 7595−7602

Patel, N. J., Chen, Y., Joshi, P., Pera, P., Baumann, H., Missert, J.R., Ohkubo, K., Fukuzumi, S., Nani, R.R., M. Schnermann, M. J., Chen, P., Zhu, J., Kadish, K. M., Pandey, R.K. Effect of Metalation on Porphyrin-Based Bifunctional Agents in Tumor Imaging and Photodynamic Therapy. *Bioconjugate Chem*., **2016**, *27*, 667–680

Zhou, J., Stojanovic, L., Berezin, A., Battisti, T., Gill, A., Kariuki, B., Bonifazi, D., Crespo-Otero, R., Wasielewski, M. R., Wu, Y. Organic room-temperature phosphorescence from halogen-bonded organic frameworks: hidden electronic effects in rigidified chromophores. *Chemical Science*, **2021**, *12* (2), 767-773

Stafford, A., Ahn, D., Raulerson, E. K., Chung, K., Sun, K., Cadena, D. M., Forrister, E. M., Yost, S. R., Roberts, S., Page, Z. Catalyst Halogenation Enables Rapid and Efficient Polymerizations with Visible to Far-Red Light. *Journal of the American Chemical Society*, **2020**, *142* (34), 14733-14742

Sartor, S. M., Chrisman, C. H., Pearson, R. M., Miyake, G. M., Damrauer, N. H. Designing High-Triplet-Yield Phenothiazine Donor-Acceptor Complexes for Photoredox Catalysis. *Journal of Physical Chemistry A*, **2020**, *124* (5), 817-823

Uddin, A., Allen, S., Rylski, A., O'Dea, C., Ly, J., Grusenmeyer, T., Roberts, S., Page, Z. Do The Twist: Efficient Heavy-Atom-Free Visible Light Polymerization Facilitated by Spin-Orbit Charge Transfer Inter-system Crossing. *Angewandte Chemie – International Edition*, **2023**, *62* (22), 1-8

Palmer, J. R., Wells, K. A., Yarnell, J. E., Favale, J. M., Castellano, F. N. Visible-Light-Driven Triplet Sensitization of Polycyclic Aromatic Hydrocarbons Using Thionated Perinones. *Journal of Physical Chemistry Letters*, **2020**, *11* (13), 5092-5099

Ortiz-Rodriguez, L. A., Joehn, S. J., Loredo, A., Wang, L., Xiao, H., Cresp-Hernandez, C. Electronic relaxation pathways in heavy-atom-free photosensitizers absorbing near-infrared radiation and exhibiting high yields of singlet oxygen generation. *Journal of the American Chemical Society*, **2021**, *143* (7), 2676-2681

Pham, T. C., Heo, S., Nguyen, V., Lee, M., Yoon, J., Lee, S. Molecular Design toward Heavy-Atom-free Photosensitizers Based on the C= S Bond and their Dual Functions in Hypoxia Photodynamic Cancer Therapy and ClO-Detection. *ACS Applied Materials and Interfaces*, **2021**, *13* (12), 13949-13957

Massey, A.; Xu, Y. Z.; Karran, P. Photoactivation of DNA thiobases as a potential novel therapeutic option. *Curr. Biol*. **2001**, *11*, 1142−1146.

Pollum, M.; Jockusch, S.; Crespo-Hernandez, C. E. 2,4-Dithiothymine as a potent UVA chemotherapeutic agent. *J. Am. Chem. Soc*. **2014**, *136*, 17930−17933.

Ashwood, B.; Pollum, M.; Crespo-Hernandez, C. E. Photochemical and Photodynamical Properties of Sulfur-Substituted Nucleic Acid Bases. *Photochem. Photobiol*. **2019**, *95*, 33−58.

Hussain, M.; Zhao, J.; Yang, W.; Zhong, F.; Karatay, A.; Yaglioglu, H. G.; Yildiz, E. A.; Hayvali, M. Intersystem crossing and triplet excited state properties of thionated naphthalenediimide derivatives. *J. Lumin*. **2017**, *192*, 211−217.

Tang, J., Wang, L., Loredo, A., Cole, C., Xiao, H. Single-atom replacement as a general approach towards visible-light/near-infrared heavy-atom-free photosensitizers for photodynamic therapy. *Chem. Sci*. **2020**, *11*, 6701

Wright, A., Kariuki, B., Wu, Y. Triplet-Forming Thionated Donor-Acceptor Chromophores for Electrochemically Amphoteric Photosensitization. *Eur. J. Org. Chem*. **2021**, 4647–4652

Allen, M. J.; Page, Z. A. Tracking Photocuring via ATR-FT-IR with Illumination through the ATR Element. *Spectrosc. Appl. Noteb*. **2020**, *35* (2), 78.

Thorat, K. G.; Kamble, P.; Ray, A. K.; Sekar, N. Novel Pyrromethene Dyes with N-Ethyl Carbazole at the Meso Position: A Comprehensive Photophysical, Lasing, Photostability and TD-DFT Study. *Phys. Chem. Chem. Phys*. **2015**, *17* (26), 17221–17236.